IRAQI JOURNAL OF APPLIED PHYSICS

The *Iraqi Journal of Applied Physics (IJAP)* is a peer reviewed journal of high quality devoted to the publication of original research papers from applied physics and their broad range of applications. IJAP publishes quality original research papers, comprehensive review articles, survey articles, book reviews, dissertation abstracts in physics and its applications in the broadest sense. It is intended that the journal may act as an interdisciplinary forum for Physics and its applications. Innovative applications and material that brings together diverse areas of Physics are particularly welcome. Review articles in selected areas are published from time to time. It aims to disseminate knowledge; provide a learned reference in the field; and establish channels of communication between academic and research experts, policy makers and executives in industry, commerce and investment institutions. IJAP is a quarterly specialized periodical dedicated to publishing original papers, letters and reviews in: Applied & Nonlinear Optics, Applied Mechanics & Thermodynamics, Digital & Optical Communications, Electronic Materials & Devices, Laser Physics & Applications, Plasma Physics & Applications, Quantum Physics & Spectroscopy, Semiconductors & Optoelectronics, Solid State Physics & Applications, Alternative & Renewable Energy, and Environmental Science & Technology.

ISSN (Print): 1813-2065, ISSN (Online): 2309-1673

Editorial Office:
P. O. Box 88052, Baghdad 12631, IRAQ
Mobile: +964 7832 360 114 (Telegram, Viber, WhatsApp)
Website: www.iraqiphysicsjournal.com
Emails: info@iraqiphysicsjournal.com, editor_ijap@yahoo.co.uk, ijap.editor@gmail.com,

SPONSORED AND PUBLISHED BY
AMERICAN QUALITY FOR SCIENTIFIC PUBLISHING INC.
1479 South De Gaulle Ct, Aurora, CO 80018, United States

IRAQI JOURNAL OF APPLIED PHYSICS

INSTRUCTIONS TO AUTHORS

CONTRIBUTIONS

Contributions to be published in this journal should be original research works, i.e., those not already published or submitted for publication elsewhere, individual papers or letters to editor.
Manuscripts should be submitted to the editor at the mailing address:

Iraqi Journal of Applied Physics, Editorial Board, P. O. Box 88052, Baghdad 12631, IRAQ
Mobile: +964 7832 360 114 (Telegram, Viber, WhatsApp)
Website: www.iraqiphysicsjournal.com
Email: info@iraqiphysicsjournal.com, editor_ijap@yahoo.co.uk, ijap.editor@gmail.com

MANUSCRIPTS

Two hard copies or a soft Word copy on a CD or DVD should be submitted to the Editor in the following configuration:

- **One-column** Double-spaced one-side A4 size with 2.5 cm margins of all sides
- Times New Roman font (16pt bold for title, 14pt bold for names, 12pt bold for headings, 12pt regular for text)
- Manuscripts presented in English only are accepted.
- English abstract not exceed 150 words
- 4 keywords (at least) should be maintained on (PACS preferred)
- Author(s) should express all quantities in SI units
- Equations should be written in equation form (*italic* and symbolic) NOT in plain text
- Tables and Figures should be separated from text and placed in new pages after the references
- Charts should be indicated by the software used for generating them (e.g., Excel, MATLAB, Grapher, etc.)
- Figures and diagrams can be submitted in original colored forms for assessment and they will be returned to authors after provide printable copies
- Only original or high-resolution scanner photos are accepted
- For electronic submission, articles should be formatted with MS-Word software
- Figures, charts, photos, images or pictures **SHOULD NOT** be grouped in Word file
- Figure caption should be written as plan text **NOT** inside a text box

AUTHOR NAMES AND AFFILIATIONS

It is IJAP policy that all those who have participated significantly in the technical aspects of a paper be recognized as co-authors or cited in the acknowledgments. In the case of a paper with more than one author, correspondence concerning the paper will be sent to the first author unless staff is advised otherwise.
Author name should consist of first name, middle initial, last name. The author affiliation should consist of the following, as applicable, in the order noted:
- Company or college (with department name or company division), Postal address, City, Governorate or State, zip code, Country name, contacting telephone number, and e-mail

REFERENCES

The references should be brought at the end of the article, and numbered in the order of their appearance in the paper. The reference list should be cited in accordance with the following examples:
[1] F.H. Al-Berkdar, D.N. Raouf and F.H. Hamza, "A Line Tuned TEM_{00} Mode CW CO_2 Laser", *Iraqi J. Appl. Phys.*, 1(1) (20025) 8-10.
[2] W. Demtröder, **"Atoms, Molecules, and Photons"**, Springer-Verlag (Berlin, 2006), Ch. 4, p. 130.
[3] Y. Lee, S.A. Korpela and R. Horne, "Structure of Multi-Cellular Natural Convection in a Tall Vertical Annulus", Proceedings of 7th International Heat Transfer Conference, U. Grigul et al., eds., Hemisphere (NY), 2 (1982) 221–226.
[5] M. Hashish, "Waterjet Technology Development", High Pressure Technology, PVP-Vol. 406 (2000) 135-140.
[6] D.W. Watson, "Thermodynamic Analysis", ASME Paper No. 97-GT-288 (1997).
[7] Z. Cheng, "Vibrational Discrete Action Theory", Ph.D. thesis, Columbia University, USA (2021).

PROOFS

Authors will receive proofs of papers and are requested to return one corrected copy as a WORD file on a compact disc (CD) or by email. New materials inserted in the original text without Editor's permission may cause rejection of paper unless the handling editor is informed.

COPYRIGHT FORM

Author(s) will be asked to sign the IJAP Copyright Form and hence transfer copyrights of the article to the Journal soon after acceptance of it. This will ensure the widest possible dissemination of information.

OFFPRINTS

Authors will receive electronic offprint free of charge and any additional reprints can be ordered.

SUBSCRIPTION AND ORDERS

Annual fees (4 issues per year) of subscription are:
50 US$ for individuals inside Iraq; **200** US$ for institutions inside Iraq; **100** US$ for individuals abroad; **300** US$ for institutions abroad.

IRAQI JOURNAL OF APPLIED PHYSICS
Vol. 19, No. 4C, December 2023, pp. 175-178

Investigation of Electrical, Optical Properties and Thermal Sensitivity of MEH-PPV/Ag Thin Films

Suha A. Jawad
Mustafa M.A. Hussein

Department of Physics, College of Science, University of Baghdad, Baghdad, IRAQ

Several concentrations of an ITO/MEH-PPV/Ag thin film were tested to see how temperature variation affected their resistance. The film was discovered to be a negative temperature coefficient sensor, meaning that as the temperature rises, the film's resistance drops. The experimental results of AC conductivity show the relationship between the impedance and the frequency is inversely proportional, and both values of the permittivity (ε′,ε″) are strong functions of frequency. Optical characteristics of MEH-PPV with varying Ag concentrations have been studied, and it was found that MEH-PPV/Ag has more robust UV-visible absorption spectra than pure MEH-PPV. Also, it was found that the absorbance and the absorption coefficient at the highest peak decreased with increasing silver weight percentages.

Keywords: MEH-PPV/Ag; Heat sensitivity; Hall Effect; AC conductivity
Received: 30 June 2023; **Revised:** 06 September 2023; **Accepted:** 13 September 2023

1. Introduction

Conjugated organic polymers' applications in optoelectronics and electronics, including photovoltaics, thin-film photovoltaics, and light-emitting diodes, have received significant attention during the past two decades. Since the discovery of electroluminescence (EL) in conjugated polymers by Burroughs et al. in 1990 [1], numerous efforts have been made to enhance the synthetic organic chemistry techniques that permit the variability of this material for these applications [2]. For their intended application, conjugated polymers' optical characteristics are particularly essential [3]. Poly [2-methoxy-5-(2-ethyl-hexyloxy)-1, 4-phenylene-vinylene] (MEH-PPV) is a conjugated polymer that is used as an active material in OLEDs [4]. It is used in many emitting devices because it is very stable and exhibits high electrical conductivity [5,6]. Composites composed of MEH-PPV and nanoparticles have been investigated as a way to extend the lifetime of OLEDs by providing them with stable active materials [7,8]. Using low particle concentrations, the composite film emits the same amount of light as the pure polymer. Recent evidence indicates that such composites have lower defect concentrations than polymer composites [9]. It is an electroluminescent conjugated polymer that offers improved processability compared to the original polymer poly (p-phenylenevinylene) [10]. MEH-PPV is used in many materials as a kind of active medium, as in photo-emitting diodes and electrochemical emitting cells (LEDS) [11,12]. Recent research has demonstrated that solvent annealing temperature, coating speed, and solution concentration are the most influential factors in determining the final physical properties of thin films [13]. Organic polymers with molecular orbitals distributed over the whole polymer chain are called "conjugated polymers". These orbitals are represented in chemical structural formulas by linked figures switching between single and double carbon bonds [14,15]. The versatility and applicability of thermos-responsive polymeric systems have led to great interest and a multitude of publications [16].

The primary purpose of this research is to study the electrical and optical characteristics of ITO/MEH-PPV/Ag thin films and use them to produce resistive thermal devices (RTDs) which are temperature sensors that take advantage of the change in the electrical resistance of some materials as a result of a change in their temperature.

2. Experimental

The basic materials used in this work are the orange color MEH-PPV bought from American Dye Source, Inc. (Canada) with 99.9% purity. The 99.99% pure silver metal powder used in this project was purchased from HIMEDIA, India laboratories PV Ltd. Also, the toluene solvent with 99.97% purity was bought from Thermo Fisher Scientific (France).

The polymer was prepared by dissolving 0.294 g of MEH-PPV powder in 18.934 g of toluene in a glass tube and stirred by magnetic stirring for at least 5 hours. Next, silver was added to the polymer in various weight ratios (0.01, 0.02, 0.03, and 0.04%), stirred for a few hours to be homogenize, and then deposited on glass slides and ITO slides (Fig. 1). Drop casting method was used to prepare films to study the Hall effect. Spin coating method used to produce films for other tests. The spin coating device rotates

at 1000 rpm then thin films were dried in a thermal oven set to 50°C for few minutes.

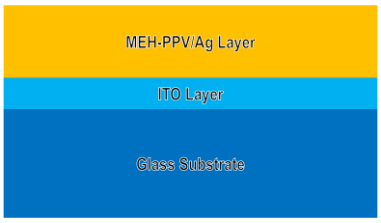

Fig. (1) Schematic view of the prepared samples

3. Results and Discussion

Analyzing the effect of the hall on the samples revealed that the addition of steroids (Ag) in various quantities increased tanker movement. The following percentages 0.01, 0.02, 0.03, and 0.04% were used in the analysis of the samples in this study. When Ag is added, conductivity begins to rise. As shown in table (1), the hall laboratories were discovered to be positive in the first sample and negative in the remaining samples because silver is a conductor, and when adding pure polymer, the surface of the pure matter was the vast majority of charging carrier is the gaps, so it is p-type while changing it. When adding, that is, increasing the number of electrons on the surface of the contaminated polymer so that the majority of shipping carriers are electrons, it has transformed to the n-type. According to this analysis, the pure sample is of p-type, whereas the drug samples are of n-type. Only by combining steroids and AG molecules can samples be utilized to create semiconductors of the p-type or n-type.

After the preparation of the thin films, the a.c. calculations of dielectric constant (ε') "real part" and (ε") "imaginary part" have been done in frequencies 100-1000Hz using the complex impedance as the following equation:

$$\varepsilon^* = \frac{1}{j\,\omega\,C_o\,Z^*} \qquad (1)$$

Electric permittivity (ε*) relates to complex impedance (Z*), ω is the angular frequency, and (C_0= t/Aωε$_0$) is the capacitance of free space

$$\varepsilon' = \frac{t}{A\,\omega\,\varepsilon_o}\left[\frac{Z''}{Z'+Z''}\right] \qquad (2)$$

$$\varepsilon'' = \frac{t}{A\,\omega\,\varepsilon_o}\left[\frac{Z'}{Z'+Z''}\right] \qquad (3)$$

Using the above equations, the real and imaginary parts of the dielectric permittivity are calculated. When we plot a graph between the real part versus *log f* where "ω=2πf" and the imaginary part versus *log f* it has proved that with increasing the frequency both (ε',ε") decrease, so it does with the impedances (Z', Z") versus frequency as shown in figures (2) and (3).

These graphs show the inverse relationship between the real and imaginary parts with frequency, which confirms the conclusion that we obtained from Hossam and his co-workers in 2015, where they also proved the inverse relationship [17].

Figure (4) shows the absorption spectra in the UV-visible region (350-980nm) of pure MEH-PPV polymer and the thin film formed by mixing silver with polymer with different weight ratios. The peaks of the largest absorption of pure MEH-PPV are located at 480 nm, which is attributable to the (π-π*) transition of the aromatic MEH-PPV polymer [18].

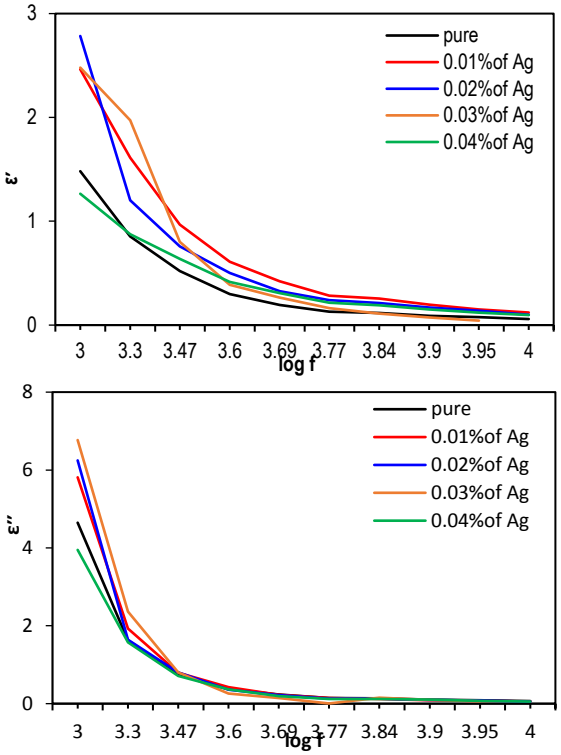

Fig. (2) Relation between the real and imaginary parts (ε', ε") with (log f), with different concentrations of Ag. When frequency increases both ε' and ε" decrease

When silver particles were added to the pure polymer, the absorbance values decreased as shown in table (2). These results confirm the results of Yahya (2012), who found that the pure polymer has a higher absorbency than the doped polymer [18].

Table (2) Absorbance of all samples of the thin film

Sample	Absorbance
MEH-PPV pure	4.6563
MEH-PPV/Ag0.01%	4.303
MEH-PPV/Ag0.02%	3.562
MEH-PPV/Ag0.03%	3.447
MEH-PPV/Ag0.04%	3.261

From the permeability, the absorption coefficient is calculated based on the Beer-Lambert equation as the following:

$$\alpha = 2.303\,(Abs/t) \qquad (4)$$

where *Abs* is the value of absorbance and *t* is the thickness of the film which is calculated to be 453.6 nm as will be discussed later in the next section

It was found that the absorption coefficient of the pure polymer was 46060, but it decreased when adding silver until it reached 44002 for the thin film MEH-PPV/Ag 0.04%, as shown in table (3). Figure (5) shows the plot of the absorption coefficient relative to the wavelength of all thin film samples.

 ISSN (print) 1813-2065, (online) 2309-1673

Table (3) Absorption coefficient of the MEH-PPV and MEH-PPV/Ag of all samples

Sample	Absorption coefficient α
MEH-PPV pure	46060
MEH-PPV/Ag 0.01%	46000
MEH-PPV/Ag 0.02%	45772
MEH-PPV/Ag 0.03%	44337
MEH-PPV/Ag 0.04%	44002

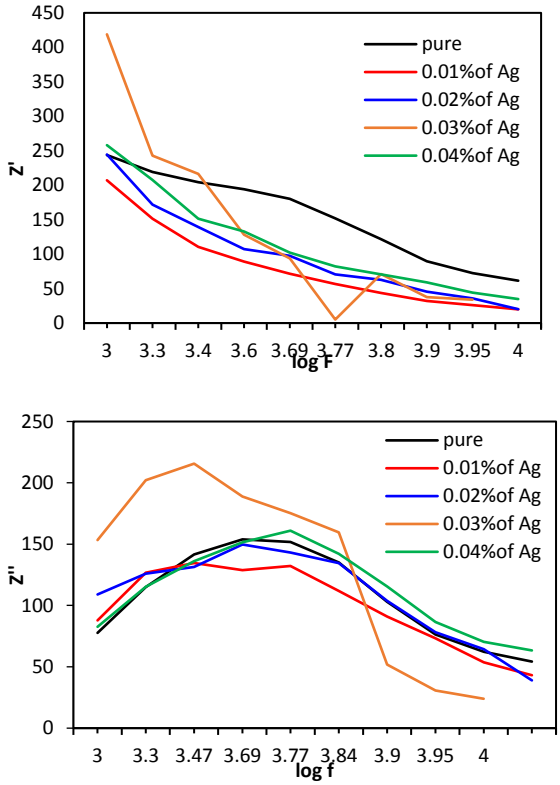

Fig. (3) The relation between the real and imaginary parts (Z', Z") with (log f), with different concentrations of Ag (a-e).When frequency increases both Z' and Z" decrease

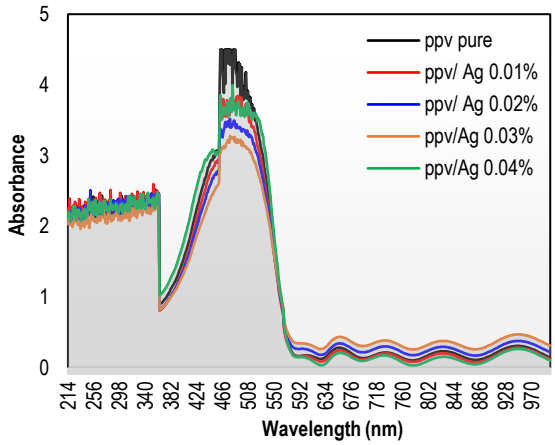

Fig. (4) UV-Vis absorption spectra of pure and MEH-PPV/Ag (0.01%, 0.02%, 0.03%, and 0.04%)

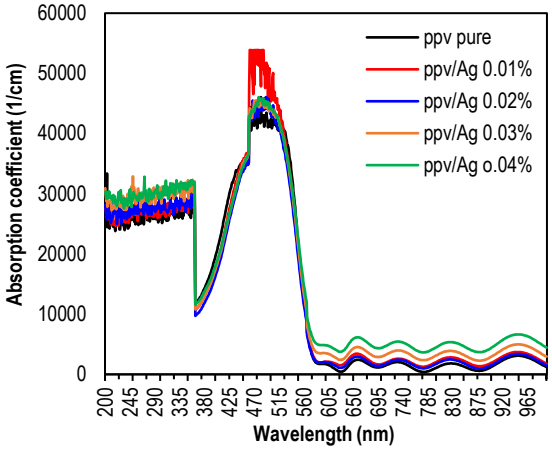

Fig. (5) Plot of the absorption coefficient relative to the wavelength of all thin film samples

To measure the thickness of the film, the atomic microscope was used. The thickness of the samples was determined by calculating the difference of the height between the highest and lowest spots of film. The sample thickness was 453.6 nm, as shown by AFM tests in Fig. (6).

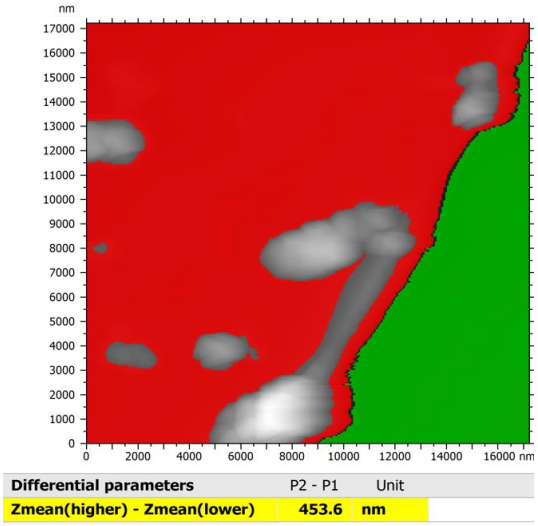

Fig. (6) AFM images showing thickness measurement of thin film samples

The application was obtained for the samples of the MEH-PPV/Ag thin films, and through the heat and resistance test, it is concluded that the prepared film is a temperature sensor as the film has negative heat coefficient type. Figure (7) demonstrates the film's resistance decreases as the temperature rises.

Martin and co-workers [19] have studied the temperature-dependent I-V characteristics, which somewhat supported the results of this work.

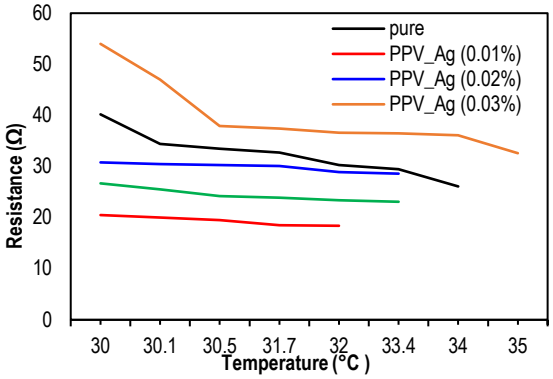

Fig. (7) The relationship between heat and resistance at different concentrations of thin film ITO/MEH-PPV/Ag (pure, 0.01, 0.02, 0.03, and 0.04%)

4. Conclusion

In this article, Ag-doped MEH-PPV polymer thin films at various Ag concentrations were prepared by spin coating deposited on ITO-coated glass substrates. These films were found to be n-type as Ag atom gives its extra electrons to the substance, thus converting it from p-type to n-type. Complex permittivity has been applied to investigate the frequency dependence of the dielectric constant and dielectric loss. With increasing frequency, both real and imaginary components of the polymer's dielectric constant decrease. As a result of the addition of silver, the optical characteristics demonstrated that the absorption coefficient in general decreased. This slight decrease is due to the inclusion of trace amounts of Ag. A thermal sensor was manufactured as the material used is thermally affected. When the temperature of the material increases, the resistance will decrease. This point is repeated in all percentages of silver added to MEH-PPV material.

References

[1] A. Alyamani et al., "Spectral, electrical and morphological properties of spin coated MEH-PPV and cresyl violet blended thin films for a light emitting diode", *Optik*, 127(4) (2016) 2331-2335.

[2] M S AlSalhi et al., "Recent Advances in Conjugated Polymers for Light Emitting Devices", *Int. J. Mol. Sci.*, 12(3) (2011) 2036-2054.

[3] J. G Rostra et al., "Thermo-optic response of MEH-PPV films incorporated to monolithic Fabry-Perot microresonators", *Dyes and Pigments*, 182 (2020) 108625.

[4] Galey, C. and H. Park, "Intermediate states during photodegradation in MEH-PPV solutions and thin films", *AIP Advances*, 9(10) (2019) 105010.

[5] S A Kumar et al., "Role of defective states in MgO nanoparticles on the photophysical properties and photostability of MEH-PPV/MgO nanocomposite", *Chem. Phys. Lett.*, 23 (2021) 22804-22816.

[6] Sharhan, S.I. and I.M. Ibrahim, "Fabrication and Characterization of Hybrid MEH-PPV/TiO_2 for Photodetector", *Iraqi J. Sci.*, 60 (4) (2019) 754-761.

[7] Carter, S., J. Scott, and P. Brock, " Enhanced luminance in polymer composite light emitting devices", *Appl. Phys. Lett.*, 71 (9) (1997) 1145-1147.

[8] S. E. Meftah et al., "Innovative organic MEH-PPV heterojunction device made by USP and PVD", *J. Electron. Mater.*, 50 (2021) 2287-2294.

[9] C.W. Lee et al., "Traps and performance of MEH-PPV/CdSe(ZnS) nanocomposite-based organic light-emitting diodes", *Nanotechnology*, 19(45) (2008) 455202.

[10] B.R. Moraes et al., "Surface-Enhanced Raman Scattering of MEH-PPV on Gold and Silver Nanoparticles", *J. Spectro.*, 2018 (2018) 6924758.

[11] R.J. Young and P.A. Lovell, **"Introduction to Polymers",** 3rd ed. CRC Press (2011), p. 688.

[12] N.K. Abbas, I.M. Ibrahim and M.A. Saleh "Characteristics of MEH-PPV/Si and MEH-PPV/PS Heterojunctions as NO_2 Gas Sensors", *Silicon,* 10 (2018) 1345–1350.

[13] F.A. Mahmoud et al., "Synthesis and Characterization of MEH-PPV for Solar Cell Application", *Egypt. J. Chem*, 59(5) (2016) 911-933.

[14] N.M. Jabbar, "Characterization of metal-doped MEH-PPV Thin films for gas sensor", M.Sc. thesis, University of Baghdad (2022).

[15] N.M. Jabbar and M.M.A. Hussein, "Structural and Morphological Characterization of MEH-PPV Nanocomposite Doped with $FeCl_3$", *Iraqi J. Phys.*, 20(3) (2022) 109-118.

[16] E.M. Frazar et al., "Multifunctional temperature-responsive polymers as advanced biomaterials and beyond", *J. Appl. Polym. Sci*., 137(25) (2020) 48770.

[17] R. Boumaraf, "Simulation de l'effet de la température et les défauts sur les caractéristiques électriques des diodes à base de GaAs", Université Mohamed Khider-Biskra (2015).

[18] N.Z. Yahya and M. Rusop, "Investigation on the optical and surface morphology of conjugated polymer MEH-PPV:ZnO nanocomposite thin films" *J. Nanomater.*, 2012 (2012) 1-8.

[19] S.J. Martin et al., "Modelling temperature-dependent current–voltage characteristics of an MEH-PPV organic light emitting device", *J. Phys. Cond. Matter*, 14(42) (2002) 9925.

Table (1) Hall parameters for MEH-PPV/Ag samples

Sample	Charge concentration $(cm)^{-3}$	Conductivity $(\Omega.cm)^{-1}$	Mobility (cm2/V. s)	Average Hall coefficient $(cm)^{-3}$	Resistivity (Ω.cm)	Type
pure	$1.01*10^{13}$	$2.54*10^{-5}$	15.7	$6.17*10^{5}$	$3.92*10^{4}$	P
0.01%	$-3.71*10^{13}$	$2.06*10^{-5}$	3.47	$-1.68*10^{5}$	$4.83*10^{4}$	N
0.02%	$-1.28*10^{13}$	$2.61*10^{-5}$	12.7	$-4.85*10^{5}$	$3.81*10^{4}$	N
0.03%	$-2.70*10^{12}$	$2.13*10^{-5}$	49.2	$-2.30*10^{6}$	$4.68*10^{4}$	N
0.04%	$-4.12*10^{12}$	$2.02*10^{-5}$	30.6	$-1.51*10^{6}$	$4.94*10^{4}$	N

 ISSN (print) 1813-2065, (online) 2309-1673

IRAQI JOURNAL OF APPLIED PHYSICS
Vol. 19, No. 4C, December 2023, pp. 179-186

Characterization and Antibacterial Activity of Titanium Dioxide Nanoparticles Prepared by Nd:YAG Pulsed-Laser Ablation

Mays W. Skakir
Awatif S. Jasim

Department of Physics, College of Science, University of Tikrit, Tikrit, IRAQ

A pulsed Nd:YAG laser with 1064nm wavelength and 100mJ energy was used to irradiate titanium plate placed in ethanol with different number of pulses (300, 350, 400, 450, and 500) to prepare titanium dioxide (TiO_2) nanoparticles. The formation of these nanoparticles was confirmed by the Fourier-transform infrared (FTIR) spectroscopy as the functional groups of TiO_2 were observed. The structural characterizations showed that the minimum nanoparticle size was 24.56 nm for low concentration and 24.50 nm for high concentration of nanoparticles in the solution. The antibacterial activity of the prepared nanoparticles was introduced against Gram positive (Streptococcus mutans) and Gram negative bacteria (Escherichia coli) and Candida albicans that were isolated from the oral cavity. These nanoparticles have shown reasonable ability to inhibit the growth of these microorganisms.

Keywords: Titanium dioxide; Laser ablation; Nanoparticles; Antibacterial activity
Received: 04 August 2023; **Revised:** 08 September 2023; **Accepted:** 15 September 2023

1. Introduction

Recently, metal oxide nanoparticles have attracted a lot of research interest due to their optical, mechanical, thermal, electrical, and magnetic properties [1-4]. Metal oxide nanoparticles can be employed as antibacterial agents due to their large surface area and morphologies those support their role against different type of bacteria, fungi, and other microorganisms [5-12]. In general, nanoparticles have several advantages as they have unique optical, magnetic, electronic, biological, and chemical properties compared to bulk materials due to their increased reaction surface area [13-17]. More specifically, metal oxide nanoparticles are used in flexible electronics and nano-circuits because of their superior electrical conductivity [18-20].

Titanium dioxide (TiO_2) is highly important in both theoretical and experimental field of research due to its interesting electronic structures and wide band gap (3.0-3.2 eV) which can be tuned by several processes [21-23]. It has wide range of industrial and technological applications as pigment, photocatalyst and UV absorption. Therefore, TiO_2 is an important compound suitable for fuel cells, solar cells, different sensors, pollution control system, waste management and self-cleaning glass coating materials along with food, cosmetic, paint, UV protector, etc. [24-30]. Nontoxicity, chemical stability, poor solubility and high refractive index are properties which add to its practical applicability [31,32].

Physical properties of TiO_2 not only depend on the phase structure but it depends also on the agglomerated microstructure, pores and particle size [33,34]. For different physical and chemical process like charge transfer, chemical reaction, photon absorption, etc., the molecules on the surface of a particles are more active than those stay inside. Hence surface offers more efficiency and TiO_2 nanoparticles with higher surface-to-volume ratio become extremely favorable from the application point of view [35,36].

Laser-produced nanoparticles have been widely used in industrial, biological, medical, and many other applications [37-40]. It has been discovered that the interactions of nanosecond laser pulses with a metal target placed inside a liquid medium can produce nanoparticles [41-44]. Using pulsed laser ablation in liquid (PLAL), low-cost, highly-pure metal oxide nanoparticles can be produced with uniform shapes and sizes [45,46]. The PLAL method includes several parameters by which the production of nanoparticles can be reasonably controlled. Some parameters are related to the laser sources such as laser wavelength, energy, power density, and repetition rate [47-50]. Other parameters are related to the solution or liquid medium such as chemical composition, viscosity, and temperature [51,52]. There are some parameters related to the experimental setup such as the distance between laser source and target, irradiation angle, and number of pulses per laser shot [53].

In this work, PLAL technique was used to prepare TiO_2 nanoparticles by irradiating Ti target immersed in ethanol with different numbers of laser pulses. The optical and structural characteristics of the prepared nanoparticles and their antibacterial activity against

some common types of bacteria and fungi were investigated.

2. Experimental Setup

A titanium (Ti) plate was placed at the bottom of a glass vessel containing 3 mL of ethanol (99.99% purity) filling up 1 cm above the Ti target. To perform the PLAL process, a HW9225L-12H Q-switched Nd:YAG laser operating at 1064nm with 9 ns pulse duration, 100 mJ maximum energy and 5 Hz repetition rate, was used. The laser source was 15 cm away from the Ti target. The number of laser pulses was varied to be 300, 350, 400, 450, and 500 in order to investigate the effect of this parameter on the characteristics of the prepared nanoparticles.

The characterization and measurement tests included x-ray diffraction (XRD), filed-emission scanning electron microscopy (FE-SEM), energy-dispersive x-ray spectroscopy (EDX), transmission electron microscopy (TEM), Fourier-transform infrared (FTIR) spectroscopy and UV-visible spectrophotometry. The antibacterial activity of the prepared nanoparticles was then tested against a strain of Gram-positive bacteria (*Streptococcus mutans*), a strain of Gram-negative bacteria (*Escherichia coli*), and *Candida albicaus* obtained from the oral cavity. The results were analyzed and charted using Origin 2018 software.

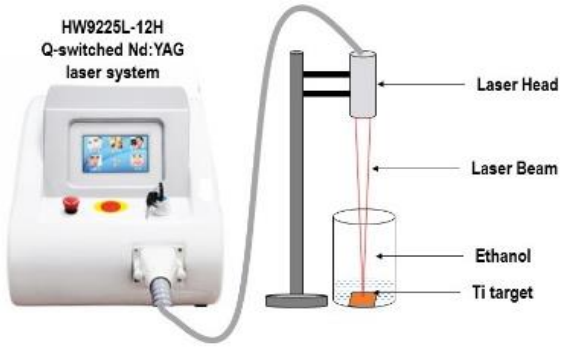

Fig. (1) Schematic diagram of PLAL setup used in this work

3. Results and Discussion

Figure (2) shows the UV-visible spectra of the TiO_2 nanoparticles prepared with different numbers of laser pulses. The absorbance at 300 nm increases regularly with increasing number of laser pulses used for the preparation of the nanoparticles. All samples exhibit identical behavior as the absorbance decreases as the wavelength is increased towards the visible region and then reach the minimum values in the NIR region. This absorption behavior may not be enough to identify the prepared material. Therefore, the determination of energy band gap may reasonably assist to do. Figure (3) shows the determination of energy band gap of the samples prepared with different numbers of pulses. The energy band gap is ranging in 3.1-3.18 eV, which is characteristic of TiO_2. However, additional characterization tests and measurements are required to confirm the formation of this material. It looks that the number of laser pulses used for preparing this material does not have strong effect on the energy band gap.

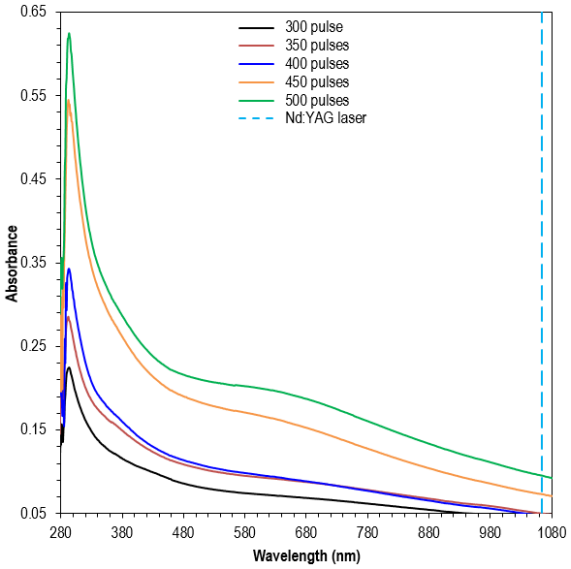

Fig. (2) UV-visible spectra of the samples prepared using different number of pulses

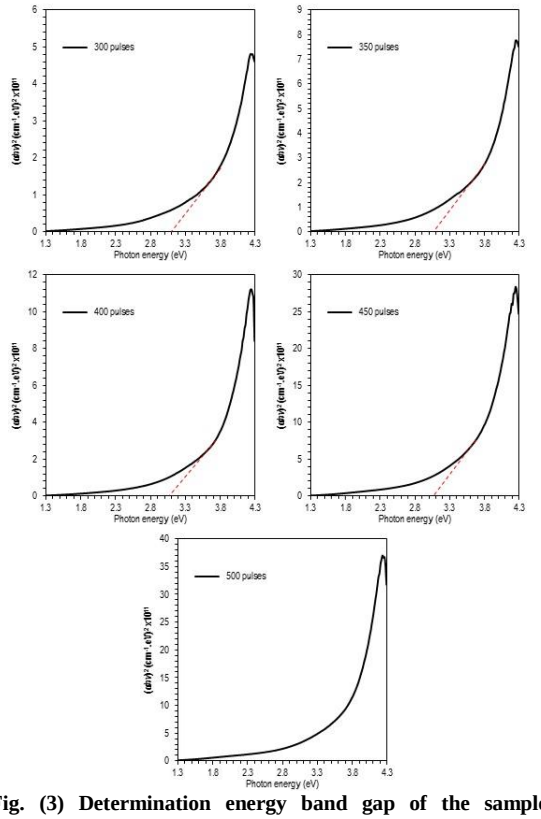

Fig. (3) Determination energy band gap of the samples prepared using different number of pulses

Figure (4) shows the FTIR spectra of the TiO_2 nanoparticles prepared with different numbers of laser pulses. First, the same functional groups are observed in all samples, which may indicate that the material is formed as a result of laser irradiation regardless the number of pulses. The peak seen at 408

 ISSN (print) 1813-2065, (online) 2309-1673

cm^{-1} is attributed to the Ti-O-Ti bonds in the TiO_2 lattice, while the peak at 446 cm^{-1} is ascribed to the Ti-O wagging. Other peaks observed at 883, 1049, 1087, 1652, and 3357 cm^{-1} are ascribed to C-C-O symmetric stretching, C-O stretching, C-C-O asymmetric stretching, and C-C stretching, respectively [54]. The broad bands seen within 1381-1453 and 2787-2872 cm^{-1} are attributed to C-H_n bending and scissors, and stretching, respectively, while the other broad band within 3357 cm^{-1} is ascribed to the O-H stretching in physisorbed water [55]. The peak observed at 1925 cm^{-1} is attributed to ethanol absorption overtone [56,57].

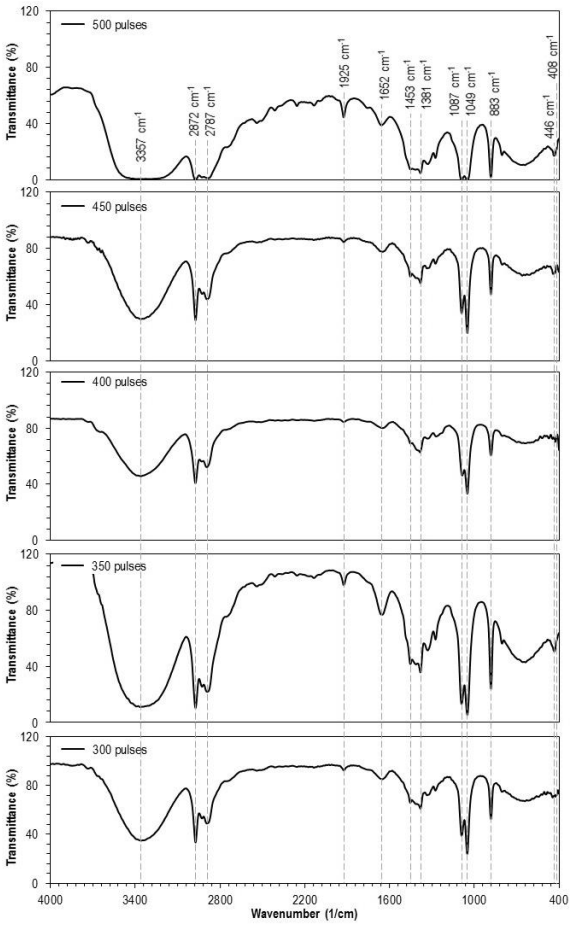

Fig. (4) FTIR spectra of TiO_2 NPs prepared with different numbers of laser pulses

Figure (5) indicates the XRD patterns of the samples prepared with two different numbers of pulses (300 and 500). It is clearly that both samples exhibit amorphous structures, which is a characteristic of nanoparticles. Correlating the results of UV-visible absorption, energy band gap, FTIR spectroscopy, and XRD patterns, the formation of TiO_2 nanoparticles can be sufficiently confirmed.

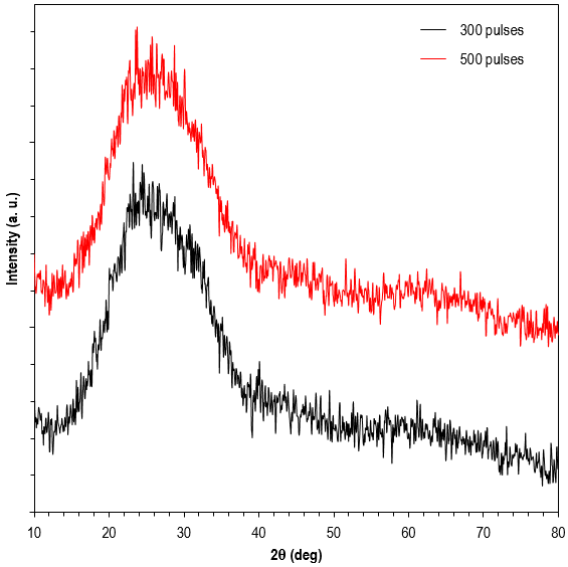

Fig. (5) XRD patterns of the TiO_2 nanoparticles prepared with two different number of pulses (300 and 500)

The morphologies of colloidal TiO_2 nanoparticles for both cases of concentrations (low and high) of these nanoparticles in ethanol were studied by TEM, as shown in Fig. (6). The aggregation of these nanoparticles is clear due to the thermal effect resulted from the high power density of laser pulse as well as from accumulation of thermal energy due to the relatively large number of pulses. Particles with sizes lower than 40 nm are clearly observed in both samples.

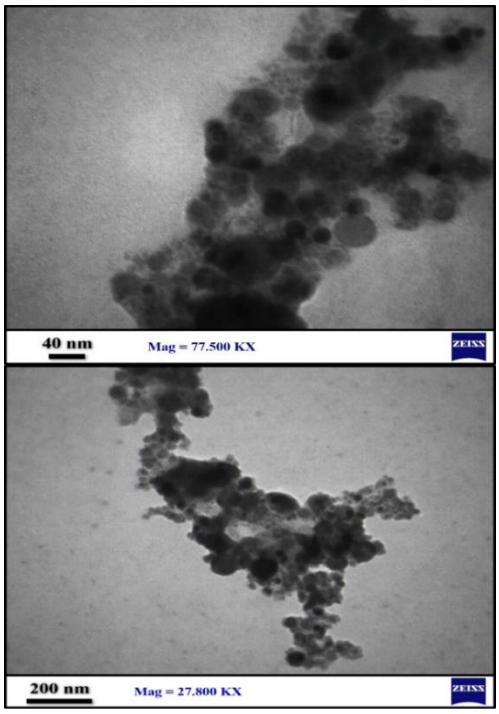

(a)

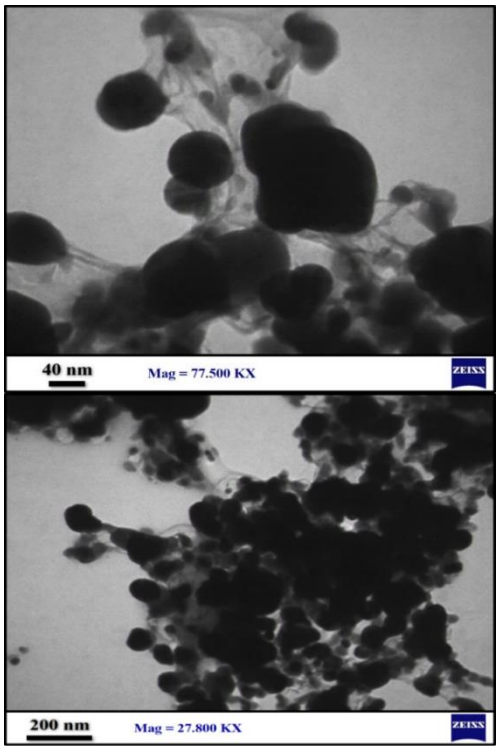

(b)

Fig. (6) TEM images of TiO_2 nanoparticles at different scales (40 and 200 nm) in (a) low concentration, and (b) high concentration of nanoparticles in ethanol

Figure (7) shows the surface morphology of TiO_2 nanoparticles for both cases of their concentrations in ethanol (low and high). The agglomeration seems to be a characteristic feature of theses nanoparticles whatever the number of laser pulses is. The average particle size was determined to be 24.5 nm for both samples. This result supports the TEM result.

The antibacterial activity of the prepared nanoparticles was analyzed using the disc diffusion method. The bacterial inoculums were first grown in LB broth for 24 hours at 28°C and 200 rpm. It was then re-suspended in LB medium until the optical density (OD) was adjusted to 0.1 at 600 nm, which corresponds to 10^8 colony-forming units (CFU)/mL. The spread plate technique was used, in which 100µL of each bacterial suspension was spread over nutrient agar medium. A set of four concentrations (50, 100, 150, and 200 µL) of the colloidal solution in the disc were prepared and used in the study. The four different concentrations of the nanoparticles in the respective discs were placed over the lawn of bacterial culture and standard. All the agar plates were incubated in the bacteriological incubator for 24 hours at 37°C. The zone of inhibition (ZOI) around the discs was determined with a measuring scale (mm).

Using broth medium techniques, it was discovered that the prepared nanoparticles have antibacterial activity against the pathogens *Streptococcus mutans*, *Escherichia coli*, and *Candida albicans*.

According to the results of the liquid medium testing, it can be observed that both types of pathogens experienced a decrease in the number of bacterial cells and the inhibition was concentration-dependent (figures 8 and 9). Gram-negative and Gram-positive bacteria are categorized according to their membrane structures. The electrostatic forces are thought to be responsible for the bioactivity and adhesion between bacteria and TiO_2 nanoparticles due to their opposing charges. Also, nanoparticles have a larger surface area available for interactions, which boosts their ability to inhibit bacteria and hence they cause cytotoxicity in microorganisms [58,59].

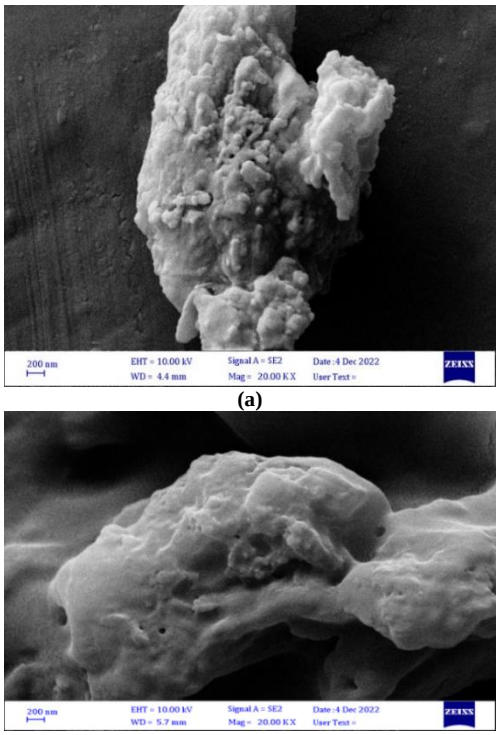

(a)

(b)

Fig. (7) FE-SEM images of the synthesized TiO_2 nanoparticles using 1064nm laser pulses for (a) low concentration and (b) high concentration of nanoparticles in ethanol

Although the exact mechanism of TiO_2 nanoparticles against microorganisms still unclear, they may possibly adhere to cell membranes and then penetrate inside, interact with phosphorus-containing substances like DNA to disrupt the replication process, or, more preferably, attack the respiratory chain. The effectiveness of this explanation heavily hinges on how these nanoparticles are organized at the molecular level.

The particles may affect cell division by altering the cellular environment, but they can harm the cell wall and plasma membrane directly, making them weaker places where damage is suspected. According to other investigations, extremely reactive metal oxide nanoparticles were used to treat *Escherichia coli* germs. The permeability of a bacterial cell membrane with this shape increases noticeably, rendering the bacterial cells unable to control transportation through the plasma membrane and

 ISSN (print) 1813-2065, (online) 2309-1673

ultimately leading to cell death [60,61]. At the moment when TiO_2 comes into contact with a cell, oxidative damage to the cell wall occurs first. Previous antimicrobial studies have found that irradiated TiO_2 possesses bactericidal activity and that the effectiveness of this disinfectant is proportionally connected with the TiO_2 dose and the duration of exposure [62,63].

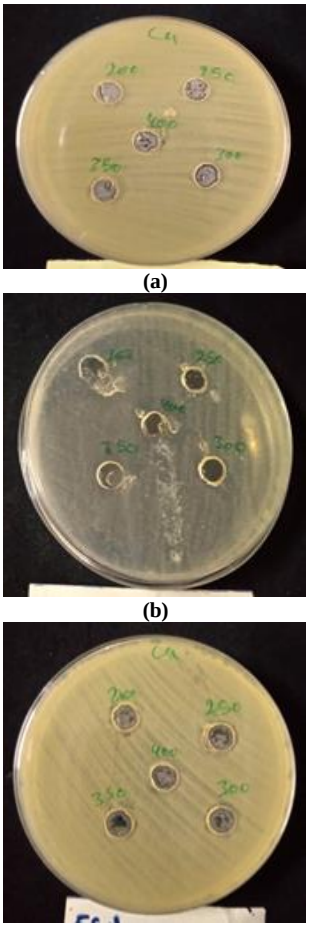

(a)

(b)

(c)

Fig. (8) Antibacterial activity of the prepared TiO_2 nanoparticles against (a) *Streptococcus mutans*, (b) *Candida albicans*, (c) *Escherichia coli*

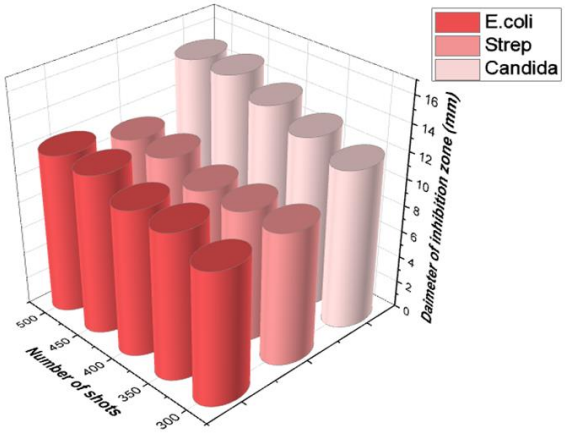

Fig. (9) Histogram of antibacterial activity of the prepared TiO_2 nanoparticles against the bacteria and fungus

Because of the diversity of microorganisms found in the oral cavity – not all of which are potential human pathogens given the length of the list of bacteria linked to mouth infections – antibiotics are referred to as broad-spectrum. Beta-lactam antibiotics are frequently used because they are effective against *Streptococci* and *Staphylococci*, as well as some Gram-negative bacteria [64], so they are frequently given to patients after enquiring about their lack of sensitivity to their types. However, long-term use of antibiotics can result in the emergence of resuscitation-resistant organisms [65]. Figure (10) depicts the results of an antibiotic sensitivity test for the two bacterial species that were the subject of the study – *Streptococcus mutans*, *Escherichia coli*, and *Candida albicans*, respectively. It is possible to see the differences in the sensitivity and resistance of bacterial species used for antibiotics in Fig. (11), which shows the histogram of antibiotic activity according to the width of inhibition zones. The development of metal oxide nanoparticles as an antibiotic alternative is driven in part by the resistance of bacterial species and their variable sensitivity to antibiotics.

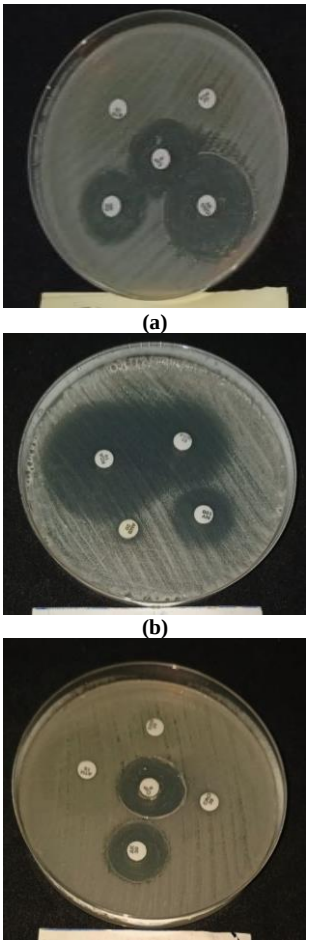

(a)

(b)

(c)

Fig (10) Antibiotic sensitivity test of (a) *Streptococcus mutans*, (b) *Candida albicans*, and (c) *Escherichia coli*

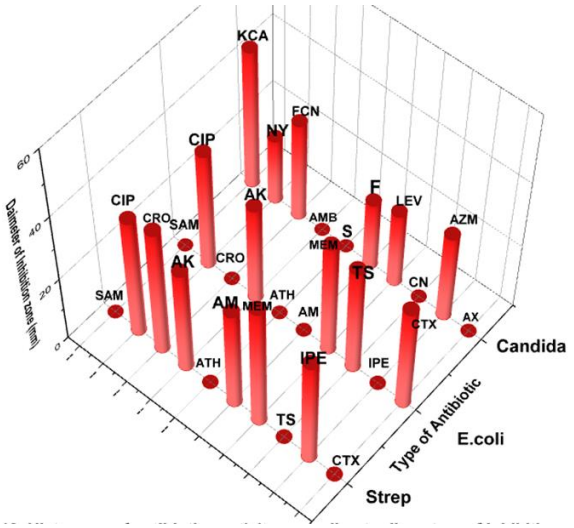

Fig. (11) Histogram of antibiotic activity according to dimeters of inhibition zones

1. Conclusions

In concluding remarks, TiO_2 nanoparticles can be successfully prepared by PLAL technique by irradiation of titanium target immersed in ethanol. The number of laser pulses used for PLAL has an effect on the sizes and shapes of the prepared nanoparticles. Due to their small size (24.5nm) and high concentration, TiO_2 nanoparticles have shown reasonable effectiveness to inhibit the growth of a variety of microorganisms in antibacterial activity assays.

References

[1] M. Yin et al., "Copper oxide nanocrystals", *J. Am. Chem. Soc.*, 127 (2005) 9506-9511.

[2] Y. Lee et al., "Large-scale synthesis of copper nanoparticles by chemically controlled reduction for applications of inkjet-printed electronics", *Nanotechnol*., 19(41) (2008) 415604.

[3] A.M. Hameed and M.A. Hameed, "Spectroscopic characteristics of highly pure metal oxide nanostructures prepared by DC reactive magnetron sputtering technique", *Emer. Mater*., 6 (2022) 627-633.

[4] A.M. Hameed and M.A. Hameed, "Highly-Pure Nanostructured Metal Oxide Multilayer Structure Prepared by DC Reactive Magnetron Sputtering Technique", *Iraqi J. Appl. Phys.*, 18(4) (2022) 9-14.

[5] O.A. Hammadi, M.K. Khalaf and F.J. Kadhim, "Fabrication of UV Photodetector from Nickel Oxide Nanoparticles Deposited on Silicon Substrate by Closed-Field Unbalanced Dual Magnetron Sputtering Techniques", *Opt. Quantum Electron.*, 47(12) (2015) 3805-3813.

[6] S. Anwaar et al., "The effect of green synthesized CuO nanoparticles on callogenesis and regeneration of Oryza sativa L", *Front. Plant Sci.*, 7 (2016) 1330.

[7] M.A. Hameed and Z.M. Jabbar, "Preparation and Characterization of Silicon Dioxide Nanostructures by DC Reactive Closed-Field Unbalanced Magnetron Sputtering", *Iraqi J. Appl. Phys.*, 12(4) (2016) 13-18.

[8] O.A. Hammadi, M.K. Khalaf and F.J. Kadhim, "Fabrication and Characterization of UV Photodetectors Based on Silicon Nitride Nanostructures Prepared by Magnetron Sputtering", *Proc. IMechE, Part N, J. Nanomater. Nanoeng. Nanosys.*, 230(1) (2016) 32-36.

[9] F.J. Kadhim and A.A. Anber, "Fabrication of Nanostructured Silicon Nitride Thin Film Gas Sensors by Reactive DC Magnetron Sputtering", *Proc. IMechE, Part N, J. Nanomater. Nanoeng. Nanosys.*, 231(4) (2017) 173-178.

[10] O.A. Hammadi and N.E. Naji, "Fabrication and Characterization of Polycrystalline Nickel Cobaltite Nanostructures Prepared by Plasma Sputtering as Gas Sensor", *Phot. Sen.*, 8(1) (2018) 43-47.

[11] A.A. Anber and F.J. Kadhim, "Preparation of Nanostructured Si_xN_{1-x} Thin Films by DC Reactive Magnetron Sputtering for Tribology Applications", *Silicon*, 10 (2018) 821-824.

[12] M.A. Hameed and Z.M. Jabbar, "Optimization of Preparation Conditions to Control Structural Characteristics of Silicon Dioxide Nanostructures Prepared by Magnetron Plasma Sputtering", *Silicon*, 10(4) (2018) 1411-1418.

[13] J.S. Ali et al., "Antimicrobial, antioxidative, and cytotoxic properties of *Monotheca buxifolia* assisted synthesized metal and metal oxide nanoparticles", *Inorg. Nano-Metal Chem.*, 50 (2020) 770-782.

[14] B.K. Nasser and M.A. Hameed, "Narrow Emission Linewidth of Highly-Pure Silicon Nitride Nanoparticles in Different Dye Solutions as Random Gain Media", *Nonl. Opt. Quantum. Opt.*, 53(1-2) (2019) 99-105.

[15] H.G. Fahad and O.A. Hammadi, "Characterization of Highly-Pure Silicon Dioxide Nanoparticles as Scattering Centers for Random Gain Media", *Iraqi J. Appl. Phys.*, 16(2) (2020) 37-42.

[16] N.H. Mutesher and F.J. Kadhim, "Comparative Study of Structural and Optical Properties of Silicon Dioxide Nanoparticles Prepared by DC Reactive Sputtering and Sol-Gel Route", *Iraqi J. Appl. Phys.*, 17(1) (2021) 17-20.

[17] K.J. Klabunde and R.S. Mulukutla, "Chemical and catalytic aspects of nanocrystals", Ch. 7, in **Nanoscale Materials in Chemistry**, ed. K.J. Klabunde, Wiley (2001) 223-259.

[18] Y.Yamamoto et al., "Magnetic properties of the noble metal nanoparticles protected by polymer", *Physica B: Cond. Matter*, 329 (2003) 1183-1184.

 ISSN (print) 1813-2065, (online) 2309-1673 PRINTED IN IRAQ

[19] S. Jang et al., "Sintering of inkjet printed copper nanoparticles for flexible electronics", *Scripta Materialia*, 62(5) (2010) 258-261.
[20] M.A. Hameed, S.H. Faisal and R.H. Turki, "Characterization of Multilayer Highly-Pure Metal Oxide Structures Prepared by DC Reactive Magnetron Sputtering Technique", *Iraqi J. Appl. Phys.*, 16(4) (2020) 25-30
[21] E.A. Al-Oubidy and F.J. Al-Maliki, "Effect of Gas Mixing Ratio on Energy Band Gap of Mixed-Phase Titanium Dioxide Nanostructures Prepared by Reactive Magnetron Sputtering Technique", *Iraqi J. Appl. Phys.*, 14(4) (2018) 19-23.
[22] F.J. Al-Maliki, O.A. Hammadi and E.A. Al-Oubidy, "Optimization of Rutile/Anatase Ratio in Titanium Dioxide Nanostructures prepared by DC Magnetron Sputtering Technique", *Iraqi J. Sci.*, 60(special issue) (2019) 91-98.
[23] F.J. Al-Maliki and E.A. Al-Oubidy, "Effect of gas mixing ratio on structural characteristics of titanium dioxide nanostructures synthesized by DC reactive magnetron sputtering", *Physica B: Cond. Matter*, 555 (2019) 18-20
[24] Z.H. Zaidan, Q.H. Mahmood and O.A. Hammadi, "Using Banana Peels for Green Synthesis of Mixed-Phase Titanium Dioxide Nanopowders", *Iraqi J. Appl. Phys.*, 18(4) (2022) 27-30.
[25] M.K. Ali and F.J. Kadhim, "Structural Characteristics of TiO_2/TiN Nanocomposites Synthesized by DC Reactive Magnetron Sputtering Technique", *Iraqi J. Appl. Phys.*, 19(3A) (2023) 49-54.
[26] J. Blanco-Galvez, P. Fernández-Ibáñez and S. Malato-Rodríguez, "Solar photocatalytic detoxification and disinfection of water: recent overview", *J. Sol. Energy Eng.*, 129(1) (2007) 4-15.
[27] O.A. Hammadi, F.J. Kadhim and E.A. Al-Oubidy, "Photocatalytic Activity of Nitrogen-Doped Titanium Dioxide Nanostructures Synthesized by DC Reactive Magnetron Sputtering Technique", *Nonl. Opt. Quantum Opt.*, 51(1-2) (2019) 67-78.
[28] E.A. Al-Oubidy and F.J. Al-Maliki, "Photocatalytic activity of anatase titanium dioxide nanostructures prepared by reactive magnetron sputtering technique", *Opt. Quantum Electron.*, 51(1-2) (2019) 23.
[29] F.J. Al-Maliki, O.A. Hammadi, B.T. Chiad and E.A. Al-Oubidy, "Enhanced photocatalytic activity of Ag-doped TiO_2 nanoparticles synthesized by DC Reactive Magnetron Co-Sputtering Technique", *Opt. Quantum Electron.*, 52 (2020) 188.
[30] R.A.H. Hassan and F.T. Ibrahim, "Preparation and Characterization of Anatase Titanium Dioxide Nanostructures as Smart and Self-Cleaned Surfaces", *Iraqi J. Appl. Phys.*, 16(4) (2020) 13-18.
[31] S.H. Faisal and M.A. Hameed, "Heterojunction Solar Cell Based on Highly-Pure Nanopowders Prepared by DC Reactive Magnetron Sputtering", *Iraqi J. Appl. Phys.*, 16(3) (2020) 27-32.
[32] R.A.H. Hassan and F.T. Ibrahim, "Preparation and Characterization of Ni-doped TiO_2 Nanostructures for Surface Cleaning Applications", *Iraqi J. Appl. Phys.*, 17(1) (2021) 3-8.
[33] F.J. Kadhim, O.A. Hammadi and N.H. Mutesher, "Photocatalytic activity of TiO_2/SiO_2 nanocomposites synthesized by reactive magnetron sputtering technique", *J. Nanophot.*, 16(2) (2022) 026005.
[34] F.J. Al-Maliki and M.A. Al-Rubaiy, "Synthesis and study the concentration effect on the photocatalytic activity of titania nanoparticles as anti-bactria using reactive magnetron sputtering technique", *Opt. Quantum. Electron.*, 54 (2022) 377.
[35] Z.H. Zaidan, O.A. Hammadi and K.H. Mahmood, "Effect of Structural Phase on Photocatalytic Activity of Titanium Dioxide Nanoparticles", *Iraqi J. Appl. Phys.*, 19(3A) (2023) 55-58.
[36] A.M. Hameed and M.A. Hameed, "Optical Microscopy of Highly-Pure Metal Oxide Nanoparticles Irradiated with Electromagnetic Radiation in Nonmetallic Hosts", *Iraqi J. Appl. Phys. Lett.*, 6(1) (2023) 7-10.
[37] K. Sugioka, **"Handbook of Laser Micro-and Nano-Engineering"**, Springer International Publishing (2020).
[38] D.B. Geohegan et al., *"Laser Interactions in Nanomaterials Synthesis"*, in **Laser-surface interactions for new materials production**, vol. 130, ed. A. Miotello, P.M. Ossi, Springer-Verlag (Berlin, 2010) pp. 1-17.
[39] G.W. Yang, "Laser ablation in liquids: applications in the synthesis of nanocrystals", *Prog. Mater. Sci.*, 52 (2007) 648-698.
[40] C. Sima et al., "Production of oxide nanoparticles by pulsed laser ablation", *J. Optoelectro. Adv. Mater.*, 10(10) (2008) 2631-2636.
[41] V. Amendola and M. Meneghetti, "Laser ablation synthesis in solution and size manipulation of noble metal nanoparticles", *Phys. Chem. C*, 11 (2009) 3805-3821.
[42] P.S. Liu et al., "Fabrication and characteristics of rutile TiO_2 nanoparticles induced by laser ablation", *Trans. Nonferr. Metals Soc. China*, 19 (2009) s743-s747.
[43] M. Boutinguiza et al., "Production of nanoparticles from natural hydroxylapatite by laser ablation", *Nanoscale Res. Lett.*, 6 (2011) 1-5.

[44] P. Liu et al., "Fabrication of cuprous oxide nanoparticles by laser ablation in PVP aqueous solution", *RSC Adv.*, 1 (2011) 847-851.
[45] K. Mitsuo, "Laser-induced fragmentative decomposition of fine CuO powder in acetone as highly productive pathway to Cu and Cu_2O nanoparticles", *J. Phys. Chem. C*, 115 (2011) 5165–5173.
[46] M. Boutinguiza et al., "Synthesis of titanium oxide nanoparticles by ytterbium fiber laser ablation", *Phys. Procedia*, 41,(2013) 787-793.
[47] M. Muniz-Miranda et al., "Characterization of copper nanoparticles obtained by laser ablation in liquids", *Appl. Phys. A*, 110 (2013) 829-833.
[48] N.M. Obeid, "Studying the effect of laser energy and wavelength on the change of properties of colloidal nano-solutions of Pt and Au: Ag alloy prepared by laser-scraping", MSc thesis, College of Science for Women, University of Babylon (2015).
[49] G. Marzun et al., "Role of dissolved and molecular oxygen on Cu and PtCu alloy particle structure during laser ablation synthesis in liquids", *Chem. Phys. Chem.*, 18 (2017) 1-11.
[50] W.J. Aziz, S.Q. Ali and N.Z. Jassim, "Production TiO_2 Nanoparticles Using Laser Ablation in Ethanol", *Silicon*, 10(5) (2018) 2101-2107.
[51] A.M. Mostafa, E.A. Mwafy and M.S. Hasanin, "One-pot synthesis of nanostructured CdS, CuS, and SnS by pulsed laser ablation in liquid environment and their antimicrobial activity", *Opt. Laser Technol.*, 121(9) (2019) 105824.
[52] E. Solati, Z. Aghazadeh and D. Dorranian, "Effects of liquid ablation environment on the characteristics of TiO_2 nanoparticles", *J. Cluster Sci.*, 31(5) (2020), 961-969.
[53] M. Fernández-Arias et al., "Fabrication and deposition of copper and copper oxide nanoparticles by laser ablation in open air", *Nanomaterials*, 10(2) (2020) 10020300.
[54] N.N. Greenwood and E.J.F. Ross, **"Index of Vibrational Spectra of Inorganic and Organometallic Compounds"**, vol. II, Butterworth Group (London, 1963), p. 457.
[55] N.N. Greenwood and E.J.F. Ross, **"Index of Vibrational Spectra of Inorganic and Organometallic Compounds**", vol. III, Butterworth Group (London, 1966), p. 800, 1078.
[56] FTIR: R.L. Hudson, "An IR investigation of solid amorphous ethanol - Spectra, properties, and phase changes", *Spectrochimica Acta Part A: Mol. Biomol. Spectro.*, 187 (2017) 82-86.
[57] FTIR 1925 cm^{-1} D. Li et al., "Automated Acid Content Determination in Lubricants by FTIR Spectroscopy as an Alternative to Acid Number Determination", *J. ASTM Int.*, 6(6) (2009) Paper ID JAI102110.
[58] J.M. Hajipour et al., "Antibacterial properties of nanoparticles", *Trends in Biotechnol.*, 30 (2012) 499-511.
[59] T.M. Al-Nori, "Antibacterial activity of Silver and Gold Nanoparticles against *Streptococcus, Staphylococcus aureus* and *E. coli*", *Al-Mustansiriyah J. Sci.*, 23(3) (2012) 45-54.
[60] I. Sondi and B. Salopek-Sondi, "Silver nanoparticles as antimicrobial agent: a case study on E. coli as a model for Gram-negative bacteria", *J. Colloid Interface Sci.*, 275(1) (2004) 177-182.
[61] T. Matsunaga et al., "Continuous-sterilization system that uses photosemiconductor powders", *Appl. Enviro. Microbiol.*, 54(6) (1988) 1330-1333.
[62] T.A. Mezher, A.M. Ali and A.N. Abd, "Characterization and Antimicrobial Activity of Copper Oxide Nanoparticles", *Iraqi J. Appl. Phys. Lett.*, 4(3) (2021) 19-22.
[63] A. Vohra et al., "Enhanced photocatalytic inactivation of bacterial spores on surfaces in air", *J. Ind. Microbiol. Biotechnol.*, 32(8) (2005) 364.
[64] S. Karikalan and A. Mohankumar, "Antibiogram of *Streptococcus mutans* isolated from dental caries patients", *Int. J. Med. Health Res.*, 2(3) (2016) 79-83.
[65] K.S. Khashan et al., "Antibacterial Activity of TiO_2 Nanoparticles Prepared by One-Step Laser Ablation in Liquid", *mdpi Appl. Sci.*, 11(10) (2021) 4623.

 ISSN (print) 1813-2065, (online) 2309-1673

IRAQI JOURNAL OF APPLIED PHYSICS
Vol. 19, No. 4C, December 2023, pp. 187-190

Effect of Copper Dopants on Structural and Optical Properties of Nickel Oxide Thin Films as NO_2 Gas Sensors

Bahaa M. Mohammed
Sabri J. Mohammed

Department of Physics, College of Education for Pure Sciences, University of Tikrit, Tikrit, IRAQ

Nickel oxide (NiO) thin films have been prepared and deposited on glass substrates by thermal evaporation of nickel metal powder and oxidation throughout annealing to form nickel oxide thin films. The structural and optical properties of these films annealed at 450°C were examined. The x-ray diffraction (XRD) patterns of the prepared thin films revealed cubic structure with dominant (111), (200) and (220) orientations. The results of atomic force microscopy (AFM) showed that the roughness and grain size distribution increased with increasing Cu content. The transmittance was decreasing while the absorbance was increasing with increasing Cu doping content. The energy gap was decreased from 3.65 eV (undoped NiO) to 3.52 eV (3% Cu:NiO) and 3.39 eV (5% Cu:NiO). The results of NO_2 gas sensing showed that the sensitivity increased with increasing Cu doping content.

Keywords: Thin films; Nickel dioxide; Copper dopants; Gas sensors
Received: 13 August 2023; **Revised:** 08 September 2023; **Accepted:** 15 September 2023

1. Introduction

Semiconductors are important materials, which have made significant progress, have made the extent of the last decade, inherited extensively through a range of electronic applications and devices, including electronic devices, optical guests, light-emitting, photocatalysis, and other applications [1-3]. Nickel oxide (NiO) is a semiconductor p-type; it has a cube structure, as well thin films, and good transparency. NiO has been used in many applications because of its crystal good and best permeability of a wide range of visible wavelengths, also, possessing an energy gap between 3.6 and 4 eV [4]. The thin films of NiO are used in many applications such as solar cells, gas sensors, electric minors, photovoltaic, organic-relief diodes, and UV detection devices [5]. Nitrogen dioxide (NO_2) is one of the numerous nitrogen oxides. It is a gas in its natural state, brown-red color has a sharp permeable smell [6]. NO_2 is one of the most important and most common air pollutants and causes poisoning when inhaled. Traffic emissions are the main source of nitrogen oxides while some small concentrations are produced from power stations and some other industrial sources, but emissions from power stations and industrial areas are in most cases high on the monitoring stations and their rise helps the speed of the spread of pollutants in the atmosphere [7]. Many researchers have fabricated NiO films by various methods such as spray pyrolysis, chemical vapor deposition, electrochemical deposition, pulsed laser deposition, sputtering, sol-gel, and thermal evaporation [8-11].

In this paper, we report the NiO thin films prepared by thermal evaporation method which is annealed at 450°C. Their structural and optical properties are characterized by x-ray diffraction (XRD), atomic force microscopy (AFM), and UV-visible spectrophotometry.

2. Experimental part

The films of NiO were deposited on cleaned glass substrate Nickel films under vacuum (10^{-5} mbar) by the combination of rotary and diffusion pump by evaporating high purity Nickel (Ni) powder from an electrically heated tungsten crucible. The distance between the substrate and the tungsten crucible is set as 15 cm. The ratios of Cu –doped were (0, 3 and 5) wt.%. After deposition the film was annealed at 450°C for 2 hours. The obtained NiO film was subjected to XRD, AFM and UV–Visible spectrophotometer. The structural properties of the NiO films were examined using X-ray diffractometer which was operated at 40 kV and 30 mA. Microstructure surface topography was estimated using (AFM). The Optical properties of the films were examined by SHIMADZU 1800 UV–Visible spectrophotometer in the range of 300-900 nm wavelength. The target gas was NO_2 with operating temperature (25, 100, 150 and 200°C).

3. Results and Discussion

Crystallite size and crystal structure of the NiO: Cu films with Cu-doping ratios (0, 3 and 5) wt.% on glass substrates were examined using by XRD method and annealing at 450 °C for two hours. Figure (1) shows the XRD patterns showed peaks at 37.45°, 43.51° and 63.22° corresponding to the (111), (200) and (220) planes, which describe a polycrystalline for the cubic structure phase of Cu –doped were (0, 3 and 5) wt.%, according to the JCPDS card no. 01-073-1519.

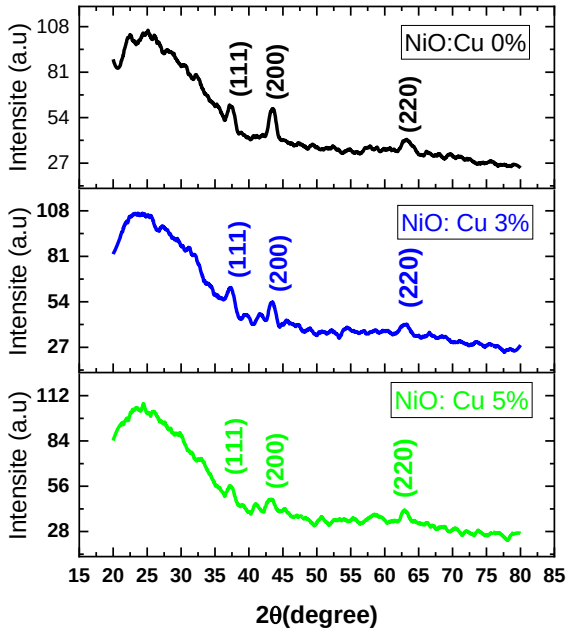

Fig. (1) The XRD patterns of the prepared samples

The crystallite size was calculated from the diffraction peaks using the well-known Debye-Scherrer's formula [12]:

$$D = \frac{0.9\,\lambda}{\beta \cos\theta_B} \quad (1)$$

where D is the crystallite size (nm), λ is the x-ray wavelength (1.54Å), β is the FWHM of the peak, and θ_B is the diffraction angle of the peak

Moreover, a dislocation density (δ), the inter-planer distance (*d*) and were measured by the equations [13]:

$$\delta = \frac{1}{D^2} \quad (2)$$

$$d = \frac{a}{\sqrt{(h^2+k^2+l^2}} \quad (3)$$

where a is the lattice constant

Table (1) summarizes the results of the XRD data analysis.

Figure (2) shows AFM images of the surface for NiO: Cu films, the scanning images of the film surfaces for all samples, and the images of the prepared films were in (3D). The grain size distribution of the surface increased with increasing the ratios of Cu-doped. Also observed that the roughness and root mean square (RMS) of the NiO sample it's increased with increased the Cu content. The reason for these increases in the value of roughness and RMS can be attributed to the increase in the Cu-doping, where the difference between Cu^{2+} and the Ni^{3+} is the latest increase in the roughness and root mean square (RMS) [14]. Table (2) summarizes the results of the AFM data analysis.

Table (2) Results of AFM analysis

NiO Sample	Average Roughness (nm)	R.M.S. Roughness (nm)	Average Grain size (nm)
0% Cu	1.56	2.09	70.1
3% Cu	2.47	3.13	68.5
5% Cu	2.47	3.36	90.7

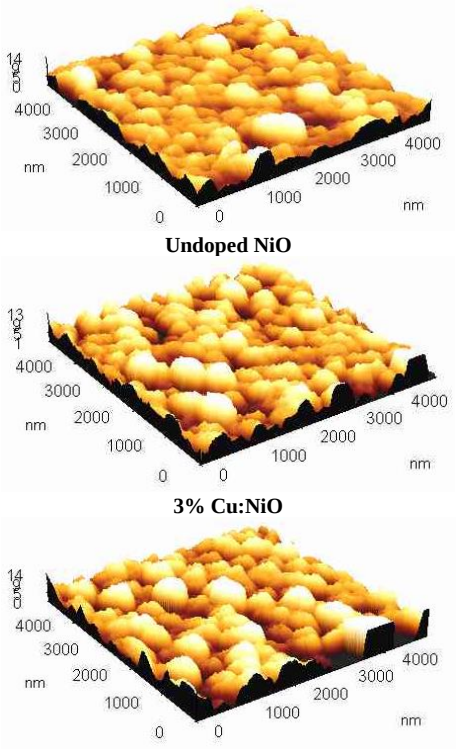

Fig. (2) AFM surface topography of the prepared samples

The optical properties of the deposited NiO:Cu thin films on glass substrate temperature 450°C by using UV-Visible spectrophotometer in the region of 300-900 nm. Figure (3) indicates the relationship between transmittance and wavelength of NiO:Cu thin films. It can notice from this figure that the transmittance decreased with increasing contain of Cu in NiO thin films, this may be attributed to the creation of levels at the energy band by increasing Cu contain [15].

Figure (4) indicates the relationship between absorption and wavelength of NiO:Cu thin films. This figure shows an exponential increase in the absorption pattern with increasing wavelength because the interaction of photons with the internal electric fields within the crystal volume of the prepared films, and the deformation that occurs to the lattice because the strain caused by the deficiency and

 ISSN (print) 1813-2065, (online) 2309-1673

inelastic scattering occurs for charge carriers by phonons [16].

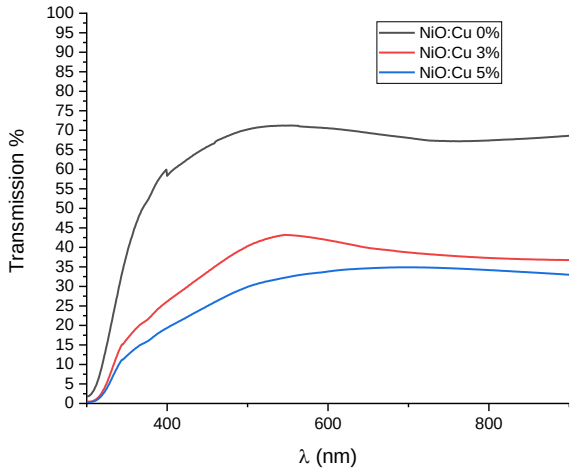

Fig. (3) Transmission spectra of the prepared samples

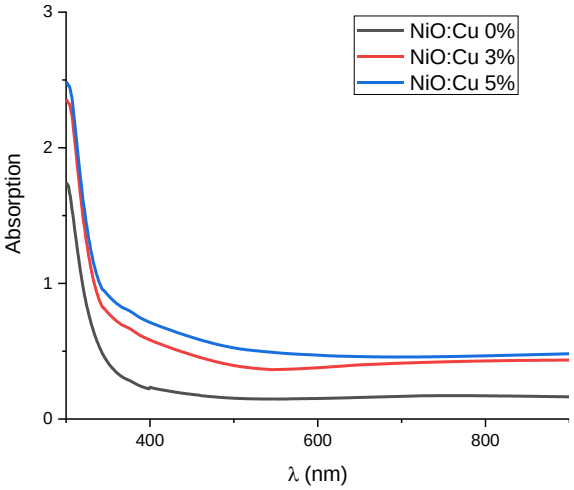

Fig. (4) Absorption spectra of the prepared samples

The optical energy gap (E_g) can be calculated from the plot made between $(\alpha h\nu)^2$ versus photon energy ($h\nu$) [17], which are shown in Fig. (5), from which, it can notice that the energy gap are decreased after added of Cu for NiO thin film ratios (3 and 5) wt.%. Table (3) summarizes the valuable of the transmittance, absorption and energy gap of NiO:Cu thin films.

Table (3) Values of transmittance, absorbance and energy gap of NiO:Cu thin films

NiO Sample	Transmittance (%)	Absorbance	Energy gap (eV)
0% Cu	73	1.74	3.65
3% Cu	52.5	2.35	3.52
5% Cu	39	2.49	3.39

The sensitivity (S) can be defined as the ratio between changing the resistance of the sensor with the presence of gas and without gas [18]. It was measured by the equation [19]:

$$S = \left|\frac{(R_g - R_a)}{R_a}\right| \times 100\% \qquad (4)$$

where R_a is the resistance of sensor in air, R_g is the resistance of sensor in presence of the tested gas

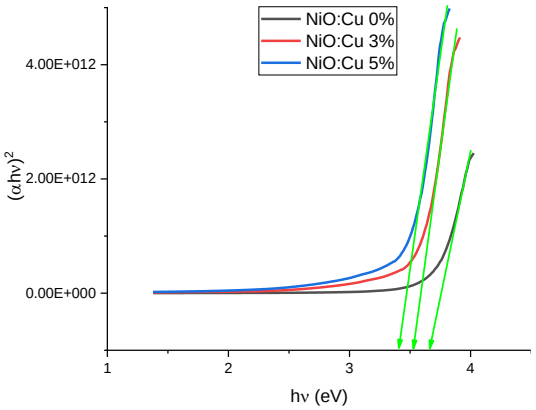

Fig. (5) Determination of energy band gap of the prepared samples

The target gas was NO_2 as an oxidized gas. Figure (6) shows the sensitivity of NiO: Cu thin films ratios (0, 3 and 5) wt.% at present NO_2 gas. The sensitivity in general increased with increasing Cu content and operator temperature, as for NiO:Cu 0% thin film, the sensitivity increased by increasing the temperature, and the reason for this is due to the nature of the semiconductor material, as its resistance is decreased by increasing the temperature and thus an increase in the sensitivity [20]. As for NiO:Cu 3% thin film, the sensitivity was also increasing with an increase in the temperature, and the reason for this positive effect of heat on-resistance of semiconductor with metal [21]. Either the sensitivity of NiO:Cu 5% thin film was also increased with an increase in the temperature because of the positive affect of heat on resistance of semiconductor with metal [22]. These results showed the doping of NiO film with Cu was suitable for gas sensing applications where the electrical conductivity of NiO was an enhancement.

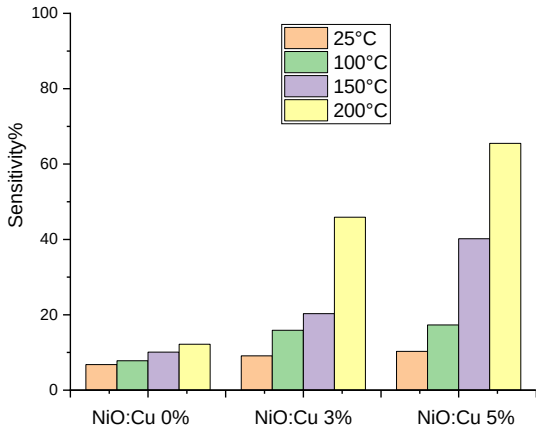

Fig. (6) Sensitivity of NiO:Cu thin films to NO_2 gas

4. Conclusions

Nickel oxide (NiO) thin films has been successfully deposited by thermal evaporation method. The structural and optical properties were investigated by (XRD), (AFM) and (UV-Visible)

studies. The XRD analysis of the prepared thin films reveals cubic structure with dominant (111), (200) and (220) orientations. The AFM showed the roughness, (RMS) and grain size distribution increased with increased the Cu content. The transmittance and energy gap are decreased with increasing Cu-doping in the prepared films, while absorption is increased with increasing Cu-doping. The results of sensing analysis showed the doping of NiO film with Cu was suitable for gas sensing applications where the electrical conductivity of NiO was an enhancement and the results indicate that the best sensitivity to NO_2 gas was 65.5 % of NiO:Cu 5% thin film at 200°C.

References

[1] M. Napari et al., "Nickel oxide thin films grown by chemical deposition techniques: Potential and challenges in next-generation rigid and flexible device applications", *Info. Mater.*, 3(5) (2021) 536-576.

[2] O.A. Hammadi, M.K. Khalaf and F.J. Kadhim, "Fabrication of UV Photodetector from Nickel Oxide Nanoparticles Deposited on Silicon Substrate by Closed-Field Unbalanced Dual Magnetron Sputtering Techniques", *Opt. Quantum Electron.*, 47(12) (2015) 3805-3813.

[3] F.J. Al-Maliki et al., "Enhanced photocatalytic activity of Ag-doped TiO_2 nanoparticles synthesized by DC Reactive Magnetron Co-Sputtering Technique", *Opt. Quantum Electron.*, 52 (2020) 188.

[4] S. Benramache, B. Benhaoua and H. Guezzoun, "Study the Effect of Cu Doping on Optical and Structural Properties of NiO Thin Films", *Annals West Univ. Timisoara Phys. Ser.*, 62 (2020) 15-22.

[5] S. Benramache, H. Guezzoun and B. Benhaoua, "Synthesis and characterizations of nanocrystalline Na and Al codoped NiO thin films", *Int. J. Integ. Eng.*, 12(1) (2020) 204-209.

[6] R.K. Sonker et al., "Low temperature sensing of NO_2 gas using SnO_2-ZnO nanocomposite sensor", *Adv. Mater. Lett.*, 4(3) (2013) 196-201.

[7] I. Hotovy et al., "Sensing characteristics of NiO thin films as NO_2 gas sensor", *Thin Solid Films*, 418(1) (2002) 9-15.

[8] S.S. Ahmed, E.K. Hassan and G.H. Mohamed, "Investigation of optical properties of $NiO_{0.99}Cu_{0.01}$ thin film by thermal evaporation", *Int. J. Adv. Res.*, 2(2) (2014) 633-638.

[9] R.H. Turki and M.A. Hameed, "Spectral and Electrical Characteristics of Nanostructured NiO/TiO_2 Heterojunction Fabricated by DC Reactive Magnetron Sputtering", *Iraqi J. Appl. Phys.*, 16(3) (2020) 39-42.

[10] M.A. Hameed, S.H. Faisal, R.H. Turki, "Characterization of Multilayer Highly-Pure Metal Oxide Structures Prepared by DC Reactive Magnetron Sputtering Technique", *Iraqi J. Appl. Phys.*, 16(4) (2020) 25-30

[11] Asraa M. Hameed and Mohammed A. Hameed, "Highly-Pure Nanostructured Metal Oxide Multilayer Structure Prepared by DC Reactive Magnetron Sputtering Technique", *Iraqi J. Appl. Phys.*, 18(4) (2022) 9-14.

[12] J.S. Blakemore, **"Solid State Physics"**, Cambridge University Press (1985).

[13] K.L. Chopra, **"Thin Film Phenomena"**, McGraw Hill Co. (NY, 1969).

[14] S. Gurakar, T. Serin and N. Serin, "Electrical and microstructural properties of (Cu,Al,In)-doped SnO_2 films deposited by spray pyrolysis", *Adv. Mater. Lett.*, 5(6) (2014) 309-314.

[15] N.N. Jandow, "Effects of Cu-doping on optical properties of NiO", *Int. Lett. Chem. Phys. Astron.*, 48 (2015) 155-162.

[16] H.T. Hashim et al., "Preparation Nanostructured of Cu-Doped NiO Thin Films Using Spin Coating Method for Gas Sensors Applications", *J. Nanostruct.*, 12(4) (2022) 882-891.

[17] X. Chen, L. Zhao and Q. Niu, "Electrical and optical properties of p-type Li, Cu-codoped NiO thin films", *J. Electron. Mater.*, 41 (2012) 3382-3386.

[18] S.G. Khalil et al., "Fabrication and characterization of gas sensor from ZrO_2:MgO nanostructure thin films by RF magnetron sputtering technique", *Baghdad Sci. J.*, 16(1) Supplement (2019) 199-208.

[19] S. Boulila et al., "Photocatalytical properties of NiO nanofilms doped with Ba", *Phil. Magaz. Lett.*, 100(6) (2020) 283-293.

[20] A. Rydosz, "The use of copper oxide thin films in gas-sensing applications", *Coatings*, 8(12) (2018) 425.

[21] A. Kılıç et al., "The effect of Ag loading on gas sensor properties of TiO_2 nanorods", *Thin Solid Films*, 726 (2021) 138662.

[22] Y. Deng, "Sensing mechanism and evaluation criteria of semiconducting metal oxides gas sensors", Semiconducting Metal Oxides for Gas Sensing, Springer Nature (Singapore, 2023) pp. 33-74.

Table (1) calculations of structural parameters according to the XRD patterns

NiO Sample	(hkl)	2θ (deg)	β (deg)	d_{hkl} (Å)	*a* (Å)	*D* (nm)	$\delta x10^{-3}$ (line/Å^2)
0% Cu	(111)	37.43	0.48	2.399	4.155	7.85	16.23
	(200)	43.46	0.62	2.078	4.156	6.42	24.26
	(220)	62.92	1	1.469	4.157	5.04	39.36
3% Cu	(111)	37.43	0.8	2.400	4.158	9.82	10.37
	(200)	43.46	1	2.091	4.183	7.71	16.82
	(220)	62.92	1.1	1.478	4.181	6.43	24.18
5% Cu	(111)	37.43	0.74	2.405	4.167	10.62	8.86
	(200)	43.46	1	2.084	4.169	9.71	12.81
	(220)	62.92	1.3	1.472	4.166	5.44	33.79

 ISSN (print) 1813-2065, (online) 2309-1673

IRAQI JOURNAL OF APPLIED PHYSICS
Vol. 19, No. 4C, December 2023, pp. 191-196

Synthesis of Copper Nanoparticles Using Liquorice Extract as Reduction Agent and Their Antibacterial Properties

Abeer H. Fezaa [1]
Abduallah M. Ali [1]
Raad M.S. Al-Haddad [2]

[1] *Department of Physics, College of Education for Pure Sciences, University of Tikrit, Tikrit, IRAQ*
[2] *Department of Physics, College of Science, University of Baghdad, Baghdad, IRAQ*

The antibacterial properties of copper nanoparticles were tested using environmentally friendly Liquorice extract (LE) for their synthesis. The unique properties of the synthesized copper nanoparticles were observed through the characteristic peak of the harmonic surface plasmon at a wavelength of 630 nm in the UV spectrum. The x-ray diffraction (XRD) patterns did not display any peaks for impure crystalline phases, which aligns with standard values for the face-centered cubic structure of metallic copper. The presence of spherical nanoparticles with a size of 128 nm was revealed. These nanoparticles displayed a negative zeta potential, which suggests higher stability. To investigate the efficacy of the prepared nanoparticles against bacteria, varying amounts of copper and liquorice extract were employed. The control sample had a zone of inhibition of 6 mm, whereas the smallest and largest zones of inhibition measured were 17 mm and 25 mm respectively. The higher concentrations of copper produced better outcomes, and it was evident that the tested bacteria were inhibited at all concentrations. Copper nanoparticles synthesized with Cu@LE demonstrated good inhibition against two types of bacteria choosing, Streptococcus mutans and Proteus mirabilis.

Keywords: Nanoparticles; Green synthesis; Antibacterial activity; Liquorice extract
Received: 24 August 2023; **Revised:** 07 September 2023; **Accepted:** 14 September 2023

1. Introduction

Nanoparticles (NPs) possess enhanced characteristics, including plasmon resonance properties [1]. Copper (Cu) nanoparticles (NPs) have gained the attention of many researchers due to their unique properties compared to bulk materials. Their distinct characteristics are a result of their size, shape, distribution, and morphology. These NPs have proven to be useful in various fields, as they possess exceptional catalytic, optical, and electrical properties. Moreover, they exhibit antifungal and antibacterial activity as well. Synthesising Cu NPs is relatively inexpensive, making them an attractive option for different applications [2]. Nanoparticles (NPs) made of noble metals, especially Cu, are among the most significant discoveries in recent years. This is due to the fact that for certain metals, the frequency of localised surface plasmon resonance [3] is in the visual range). A surface plasmon is the electron excitation in the conduction band of the NPs' surface. The metal NPs providing characteristic absorption spectra in the UV-visible region are called surface plasmon resonance NPs. Surface plasmons are characterised as oscillations of free electrons in metal [4,5]. In addition to their outstanding biological activity, Cu NPs also exhibit extraordinary physical and chemical characteristics, such as high thermal and electrical conductivity [6]. Cu is a highly toxic substance to organisms, but it is non-toxic to animal cells, making it a useful bactericidal metal. Copper nanoparticles (Cu NPs) have been utilized in various applications, such as health, food, medical, consumer, and some industrial sectors. This manuscript reports the first-ever green synthesis of Cu NPs using a novel plant extract [7]. The green synthesis of copper nanoparticles (Cu NPs) has gained significant attention in recent times for its potential applications in biomedicine, biosensors, and pharmacy. In this method, fungi, bacteria, and plant extracts are used as reducing and capping agents to produce Cu NPs [8]. The use of plant extracts is a more accessible method of synthesizing nanoparticles due to their biological origin. *Azadirachta indica* is a plant extract that has been widely used for the synthesis of Copper nanoparticles (Cu NPs) using physical, thermal, and chemical reduction methods. However, these methods are expensive, sophisticated, and may have toxic effects [7].

The green synthesis of NPs using plant extracts offers a simple, environment-friendly, and economical procedure to resolve these issues. Plant extracts are cheap and stable against harsh environmental conditions [9] .

Nanoparticles (NPs) are formed through redox reactions that reduce metal ions. This reaction is aided by metabolites such as sugar, terpenoids,

polyphenols, alkaloids, phenolic acids, and proteins. These metabolites play a crucial role in the reduction of metal ions and also ensure the stability of NPs [10,11] .Several studies have examined the potential of plant extracts, such as *Solanum Lycopersicum*, *Eclipta prostrate*, *Punica granatum*, *Plantago asiatica*, *Gnidia glauca*, *Plumbago zeylanica*, and *Moringa oleifera* [12], for the synthesis of Cu nanoparticles. Different plant extracts are associated with different NP characteristics, including antioxidant, mosquito larvacidal, antimicrobial, insecticidal [13] anti-dengue virus, cytotoxic/anticancer, and antifungal properties [14].

The aim of this research is to produce copper nanoparticles (Cu NPs) using the green method involving licorice extract (L.E.) and evaluate their properties by x-ray diffraction (XRD), zeta potential, UV-visible spectroscopy, and transmission electron spectroscopy. Microscopy (TEM). The effectiveness of copper NPs as an antibacterial agent against two strains of bacteria, *Streptococcus mutans* and *Proteus mirabilis*, was tested.

2. Experimental Part

Cu sulphate ($CuSO_4.5H_2O$), sodium hydroxide (NaOH), ascorbic acid ($C_6H_8O_6$), ethanol, cetyltrimethylammonium bromide (CTAB), L.E., and distilled water.

To prepare the liquorice plant extract, the leaves were first cleaned and washed thoroughly to get rid of any impurities. The leaves were then sun-dried for a while and crushed into a fine powder. Then, 5 g of the powder was mixed with 50 mL of deionized water to make an extract. The mixture changed its color to pale yellow. After that, the solution was centrifuged at 4000 rpm for 10 minutes. The extract was collected and stored in the refrigerator.

In order to prepare Cu NPs, we started by dissolving 2.7 g (0.1 M) of Cu sulphate in 50 mL of deionised water through continuous stirring for 35 minutes. Then, we dissolved 0.05 g of C-Tab solution in 10 mL of deionised water and added it to the Cu solution, followed by dissolving 0.5 g (0.2 M) of ascorbic acid in 15 mL of deionised water and adding it to the Cu solution. We then dissolved 0.9 g of sodium hydroxide (1 M) in 20 mL of deionised water and added it to the Cu solution. The solution was stirred at full speed for three hours. After that, we added 10 mL of the extract to the solution and stirred it continuously for two hours. Finally, a dark brown Cu solution containing the extract was obtained as shown in Fig. (1).

The Cu NPs prepared using L.E. (Cu@L.E.) were examined by ultraviolet spectrum analysis with a Shimadzu UV-16601 spectrophotometer. The shape and structure of the Cu NPs were evaluated by TEM with a Leo920 TEM (Karl Zeiss, Germany). Zeta potential is important for assessing superficial shipment, stability, and size distribution with density. The Fourier-transformed infrared (FTIR) spectroscopy and XRD (Shimadzu XRD-6000) used the infrared spectrum scale.

Fig. (1) Final output copper and plant extract (Cu@L.E.)

3. Results and Discussion

L.E. was shown to synthesise stable Cu NPs in this study using ultraviolet-to-visible spectroscopy. The formation of Cu NPs was confirmed using UV-visible spectra due to surface plasmon resonance. The UV-visible absorption spectra of synthesised Cu NPs were recorded at fixed wavelengths from 200 to 700 nm. , UV spectrum in L.E. It shows distinct and clear absorption bands the characteristic absorption peak of the Cu solution was observed at 627 nm, which shifted to the longer wavelength of 631 nm after adding L.E. (Fig. 2). The synthesised Cu NPs' stable surface plasmon band at 620–630 nm confirms the formation of Cu NPs. It also shows that NPs in the solution are monodispersed with no sign of agglomeration Due to the addition of the CTAB to a stability and more dispersal of the solution, as shown in the final form resulting from the synthesis of copper and plant extract (Fig. 1).

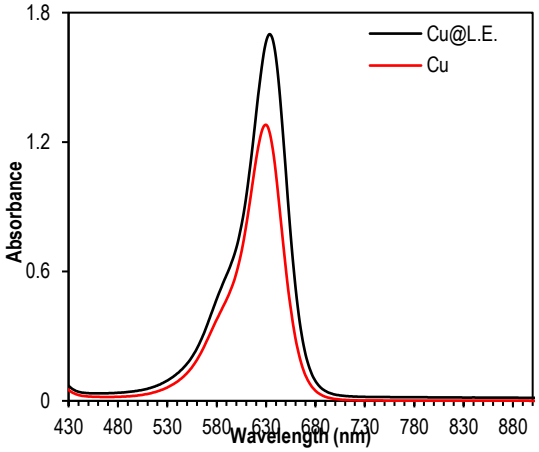

Fig. (2) UV-visible spectra of L.E. and synthesised Cu NPs (inset shows the change in colour after Cu NP formation)

The XRD patterns of L.E. synthesised Cu NPs are shown in Fig. (3). The XRD pattern of the synthesised Cu NPs contains all of the possible peaks of metallic Cu, showing the polycrystalline nature of Cu NPs. Three distinct diffraction peaks for Cu NPs are observed in the XRD pattern. XRD is one of the most

 ISSN (print) 1813-2065, (online) 2309-1673

effective and simple methods for determining a compound's crystallite properties. The XRD measurements showed that Cu NPs are crystallised. Figure (3) shows the XRD patterns of the Cu NPs, which are comparable to those seen in JCPDS Cu. 04-0836 (43.6, 50.8, and 74.4) and correspond to the metallic Cu planes (111), (200), and (220) [15]. The XRD analysis shows that the Cu peaks produced by the Cu NPs have a face-centred cubic structure, in addition to diffraction peaks that appear after the coating process. Table (1) summarizes the values of structural parameters obtained from the XRD results.

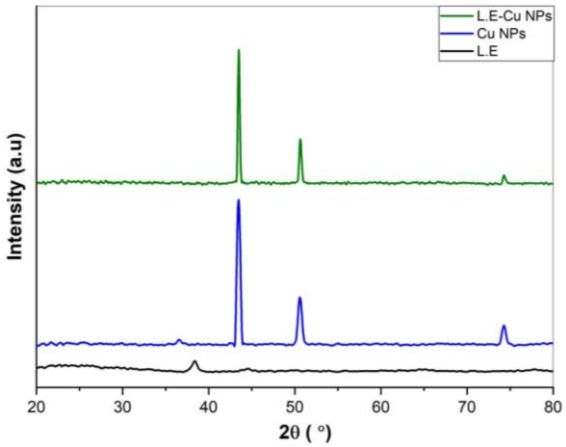

Fig. (3) XRD patterns of Cu NPs for capping L.E.

Table (1) Analysis of the XRD pattern

Sample	(2θ)	FWHM (2θ)	d-Space Standard (Å)	Grain size (nm)
Cu@L.E.	43.5007	0.1750	2.08	42.14765
	50.6481	0.2037	1.81	35.23844
	74.3042	0.2022	1.28	31.30273

FTIR was used to determine whether active phenolic components, such as flavonoids, were present in the L.E. before and after the bio-reduction procedure. The L.E. had several absorption peaks, illustrating its complexity [27]. However, the L.E.'s FTIR spectrum extract (Fig. 4, black) shows five primary peaks at 3419, 2952, 1760, 1688, and 1141 cm^{-1}, suggesting O-H stretching vibrations (alcoholic or phenolic), C-H asymmetric stretching, C=O stretching, C=C stretching, and C-OH bending, respectively. Flavonoids and phenolic acids could be adsorbed on the Cu NPs' surface, possibly through the л-electrons interaction. [14,16] The carbonyl and hydroxyl linkages in the L.E.'s components are responsible for reducing Cu ions into Cu NPs. However, the FTIR spectrum of green synthesised Cu NPs (Fig. 4, red) shows a broad peak at 3410 cm^{-1} due to O-H groups; some signals that emerged at 2949, 1783, 1615, and 1028 cm^{-1} are related to C-H asymmetric stretching, C=O of aromatic rings, C=C stretching, and C-OH bending, respectively. The Cu NPs' FTIR spectrum also indicates the possible interaction between Cu ions and L.E. during bioreduction [17] at 621 cm^{-1}. Comparing the spectra of Cu NPs and L.E. showed that some peaks obtained from the L.E. had been repeated in the FTIR spectrum of Cu NPs, with slight changes in the band positions and the absorption intensities. These results show that the as-synthesised Cu NPs are non-oxidative, pure, and coated with L.E. components.

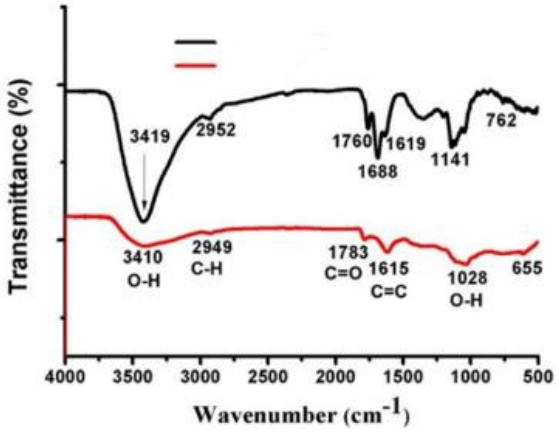

Fig. (4) FTIR spectra of L.E. and Cu NPs (red curve) in the 500-4500 cm^{-1} wave number range

TEM was used to characterise the size and shape of the Cu NPs. The Cu@L.E. NPs synthesised using the green method were imaged using TEM. They were spherical and homogeneously distributed. The particle size distribution graph for the Cu@L.E. NPs is shown in Fig. (5). The average particle size was 128 nm. The reason for the larger size of Cu NPs. Due to the addition of the CTAB to a stability and more dispersal of the solution, as well as adding the green extract.

The zeta potential is used to determine the stability of colloidal particles, and its magnitude indicates the degree of electrostatic interaction between similarly charged particles in dispersion [30]. NPs with zeta potentials of >+25 mV or <−25 mV are usually highly stable. The zeta potential of the Cu NPs was −16.1 mV (Fig. 6), confirming their stability. The negative zeta potential of biosynthesised Cu NPs may be due to bioorganic components in the L.E. as capping agents [18] . The mutual repulsion of NPs depends on having either a large negative or positive zeta potential. Zeta potential measurements of Cu NPs with L.E. show that the synthesised Cu NPs have a negative surface charge. This finding indicates the colloidal stability of the Cu NPs, which can form various chemical bonds with metal components, enhancing their stability and preventing agglomeration.

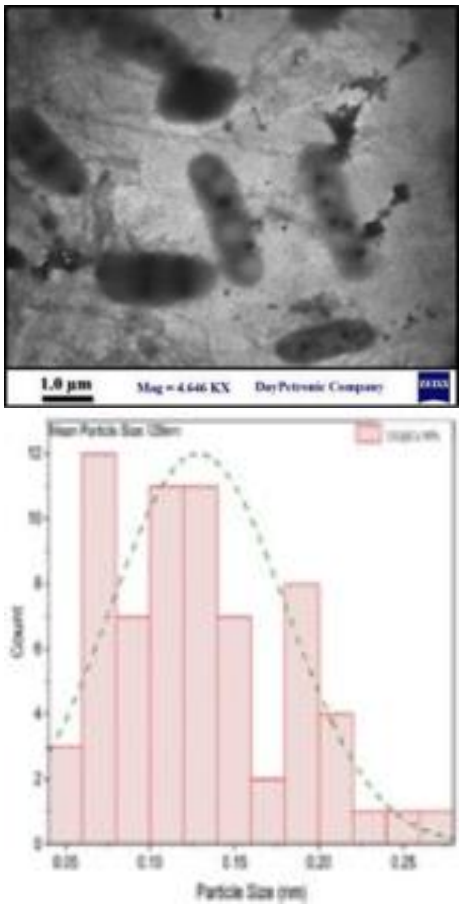

Fig. (5) TEM image of the capping L.E. around the Cu NPs

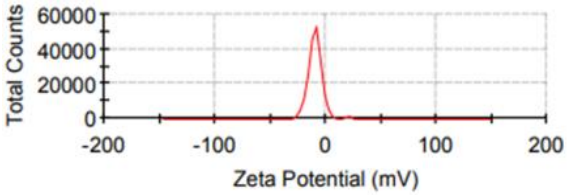

Fig. (6) The zeta potential of the cu @L.E. NPs

The antibacterial activity of various Cu concentrations against two pathogenic bacteria, Streptococcus mutans and Proteus mirabilis, is shown in figures (7-10). Cu@L.E. and L.E. were examined for their antibacterial activity, and the mean values of the inhibition zone are shown in table (2). Numerous studies have shown that NPs have strong antibacterial activity. This study shows that all harmful bacterial strains had a good inhibition zone. It also found that high metal NP concentrations resulted in a larger inhibition zone. Therefore, the relationship between the inhibition zone and Cu NP concentration was linear. The reactive oxygen species that kill bacteria comprise radical substances such as hydroxyl (-OH), superoxide radical (O_2^-), singlet oxygen (O_2), and hydrogen peroxide (H_2O_2). Therefore, the green-produced Cu NPs showed significant antibacterial efficacy against various species.

Table (2) Comparison of the antibacterial action of L.E. and Cu NPs against the two tested strains

Sample	Amm	Bmm	Cmm	Dmm	Emm
Streptococcus mutans (Cu@L.E)	6	18	19	20	21
Proteus mirabilis (L.E.)	6	18	20	23	25
Streptococcus mutans (L.E.)	6	17	18.5	21	22
Proteus mirabilis (Cu@L.E.)	6	17.5	19.5	20.5	21.5

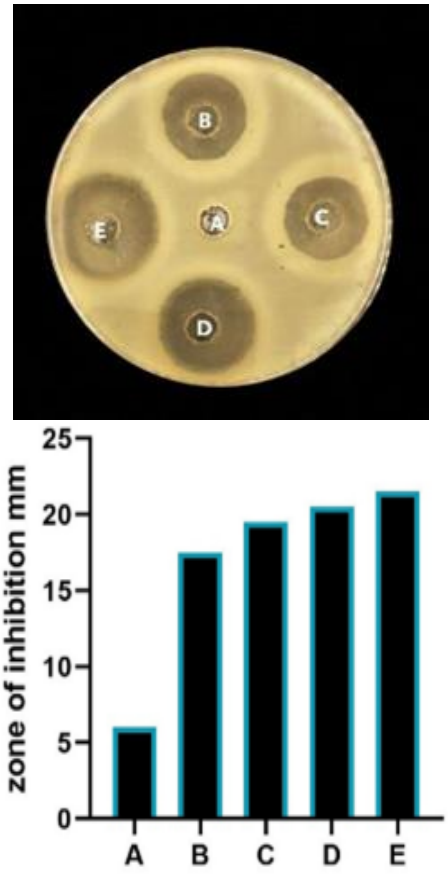

Fig. (7) Antibacterial activity of Cu@L.E. NPs against Proteus mirabilis. (A) Control. (B) 12.5 %. (C) 25 %. (D) 50%. (E) 100%

Metal NPs may adhere to the bacterial cell wall's surface and then break through the bacterial cell membrane, disrupting the cytoplasmic membrane's integrity and stability and ultimately killing the bacterium [19]. It was suggested that Cu NPs' antibacterial effectiveness depends on their form. The form, surface-adhering components, and surface charge of Cu NPs may account for their significant antibacterial activity. According to microscopic analysis and nucleic acid leakage, physical damage to bacterial cells is the primary cause of Cu NP damage potential. Negatively charged cell walls and positively charged NPs interact electrostatically, causing cell wall destruction [20]. Streptococcus mutans strains associated with hospital infections are frequently multidrug-resistant, leaving only low-efficiency antibiotics available for therapy [21] . Table 2 shows that, compared to L.E., Cu NPs had the most antibacterial action against the two tested

 ISSN (print) 1813-2065, (online) 2309-1673

strains. The antibacterial effects of different concentrations of Cu@L.E. NPs against Proteus mirabilis and Streptococcus mutans are shown in Figures 7 and 8, respectively. The antibacterial effects of different concentrations of L.E. against Proteus mirabilis and Streptococcus mutans are shown in Figures 9 and 10, respectively. The L.E. and Cu@L.E. NPs were highly effective against the two tested bacteria at all concentrations obtained with L.E. treatment of Streptococcus mutans. This activity was due to the nanoscale Cu concentration. The control had an inhibition zone of 6 mm.

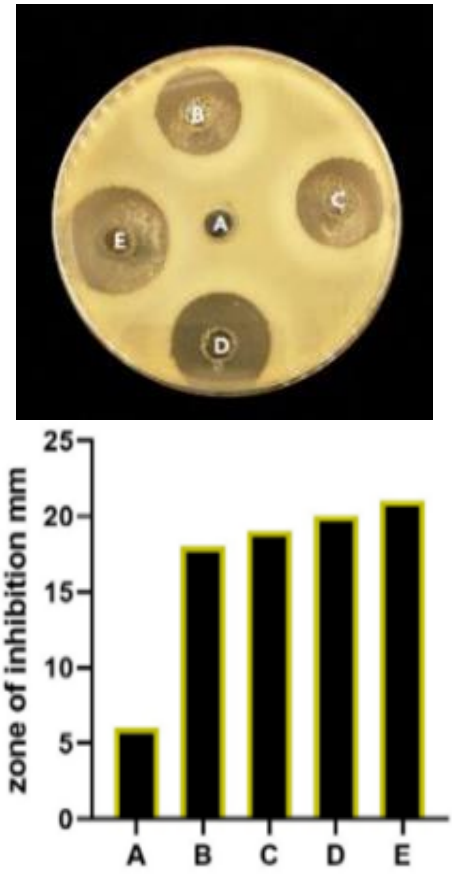

Fig. (8) Antibacterial activity of Cu@L.E. NPs against Streptococcus mutans. (A) Control. (B) 12.5%. (C) 25%. (D) 50%. (E) 100%

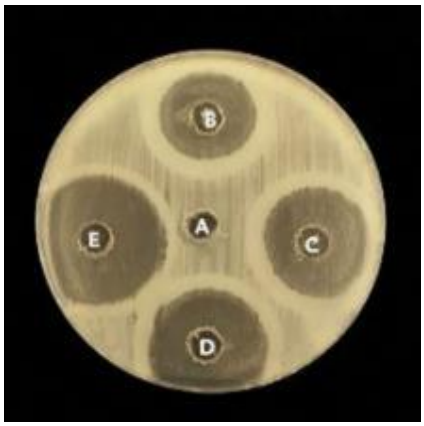

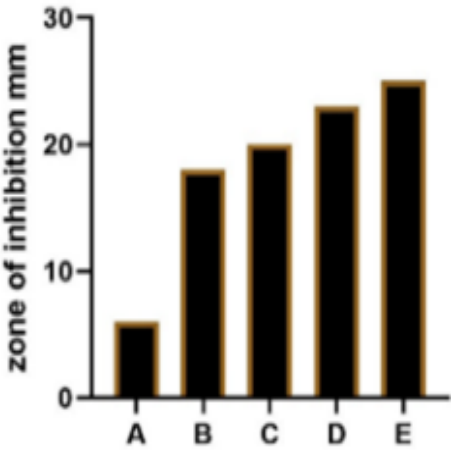

Fig. (9) Antibacterial activity of L.E against Proteus mirabilis. (A) Control. (B) 12.5%. (C) 25%. (D) 50%. (E) 100%

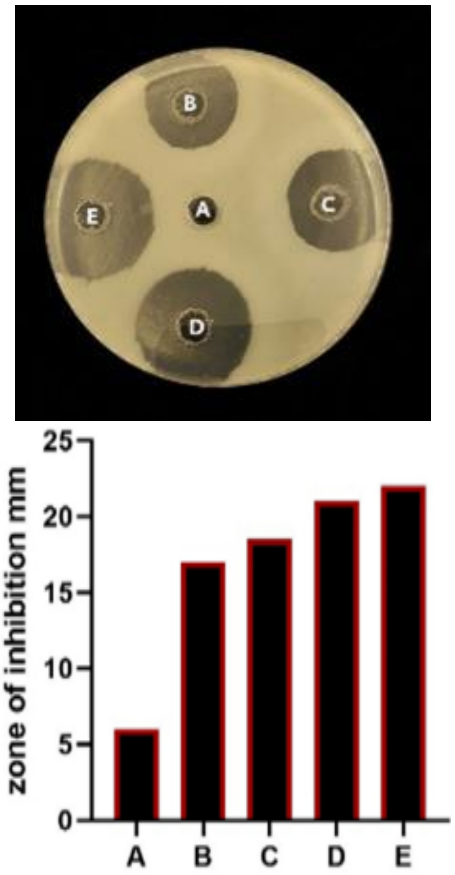

Fig. (10) Antibacterial activity of L.E. against Streptococcus mutans. (A) Control. (B) 12.5%. (C) 25%. (D) 50%. (E) 100%

4. Conclusions

In this study, Copper nanoparticles (Cu NPs) were successfully synthesized for the first time using L.E. The XRD analysis confirmed that the NPs are crystalline and mostly spherical in shape. The NPs showed high effectiveness against two bacterial species at all tested concentrations, with a higher concentration leading to a greater inhibition zone. The lowest zone of inhibition was 17mm, observed in Streptococcus mutans treated with L.E. The highest inhibition zone was 25mm, obtained with L.E. treatment of Streptococcus mutans.

References

[1] R.M. Abdallah and R.M.S. Al-Haddad, "Magnetic, Optical Properties of Magnetite Nanoparticle Synthesized in Different Parameters", *J. Nano Res.*, 74 (2022) 59-68.
[2] A. Singh *et al.*, "Green synthesis of metallic nanoparticles as effective alternatives to treat antibiotics resistant bacterial infections: A review", *Biotechnol. Rep.*, 25 (2020) e00427.
[3] Z.S. Sadeq, "Non Linear Optical Properties of Silver Nanoparticles", *Iraqi J. Sci.*, 57(3C) (2016) 2240-2244.
[4] F.J. Kadhum et al., "Theoretical Biosensor Design for Gold-PVA Surface Plasmon Resonance Layers", *Iraqi J. Sci.*, 62(11) (2021) 4232-4239.
[5] A.F.H. Al-Ajeeli, K.H. Razeg and F.T. Ibrahim, "Copper at silica core–shell nanoparticles as antibacterial agents by sol-gel chemical methods", *3c Tecnol. glosas innovación Apl. a la pyme*, 12(1) (2023) 337-352.
[6] A.M. El Shafey, "Green synthesis of metal and metal oxide nanoparticles from plant leaf extracts and their applications: A review", *Green Process. Synth.*, 9(1) (2020) 304-339.
[7] P. Sharma et al., "Green synthesis and characterization of copper nanoparticles by Tinospora cardifolia to produce nature-friendly copper nano-coated fabric and their antimicrobial evaluation", *J. Microbiol. Meth.*, 160 (2019) 107-116.
[8] M.M. Zangeneh et al., "Novel synthesis of Falcaria vulgaris leaf extract conjugated copper nanoparticles with potent cytotoxicity, antioxidant, antifungal, antibacterial, and cutaneous wound healing activities under in vitro and in vivo condition", *J. Photochem. Photobiol. B Biol.*, 197 (2019) 111556.
[9] M. Ismail et al., "Green synthesis of zerovalent copper nanoparticles for efficient reduction of toxic azo dyes congo red and methyl orange", *Green Process. Synth.*, 8(1) (2019) 135-143.
[10] M. Shah et al., "Green synthesis of metallic nanoparticles via biological entities", *Materials (Basel)*, 8(11) (2015) 7278-7308.
[11] M. Pattanayak and P.L. Nayak, "Green synthesis of gold nanoparticles using Solanum lycopersicum (tomato) aqueous extract", *World J. Nano Sci. Technol.*, 3(2) (2014) 74-80.
[12] D.A. Jamdade et al., "Gnidia glauca-and Plumbago zeylanica-mediated synthesis of novel copper nanoparticles as promising antidiabetic agents", *Adv. Pharmacol. Pharm. Sci.*, 2019 (2019) 9080279.
[13] O. Długosz, J. Chwastowski and M. Banach, "Hawthorn berries extract for the green synthesis of copper and silver nanoparticles", *Chem. Pap.*, 74 (2020) 239-252.
[14] N. Klawikkan et al., "Effect of Thai medicinal plant extracts against Dengue virus in vitro", 38(1-2) (2011) 13-18.
[15] G. Ertl, H. Knözinger and J. Weitkamp, **"Handbook of Heterogeneous Catalysis"**, vol. 2. VCH Weinheim (1997).
[16] V.P. Tolstoy, I. Chernyshova and V.A. Skryshevsky, "**Handbook of infrared spectroscopy of ultrathin films**", John Wiley & Sons (2003).
[17] M.A. Shoeib et al., "Synthesis of Cu2O nanocrystallites and their adsorption and photocatalysis behavior", *Adv. Powd. Technol.*, 23(3) (2012) 298-304.
[18] I. Jahan, F. Erci and I. Isildak, "Facile microwave-mediated green synthesis of non-toxic copper nanoparticles using Citrus sinensis aqueous fruit extract and their antibacterial potentials", *J. Drug Deliv. Sci. Technol.*, 61 (2021) 102172.
[19] N. Liu et al., "Effect of MW and concentration of chitosan on antibacterial activity of *Escherichia coli*", *Carbohydr. Polym.*, 64(1) (2006) 60-65.
[20] S. Hameed et al., "Shape-dependent significant physical mutilation and antibacterial mechanisms of gold nanoparticles against foodborne bacterial pathogens (*Escherichia coli*, *Pseudomonas aeruginosa* and *Staphylococcus aureus*) at lower concentrations", *Mater. Sci. Eng. C*, 108 (2020) 110338.
[21] M.K. Abdrabaa and R. Abd Aburesha, "Gene Expression Evaluation of Intracellular Adhesins and Regulatory Genes among Biofilm Producing MRSA Isolates", *Iraqi J. Sci.*, 64(1) (2023) 75-83.

 ISSN (print) 1813-2065, (online) 2309-1673

IRAQI JOURNAL OF APPLIED PHYSICS
Vol. 19, No. 4C, December 2023, pp. 197-204

Highly-Sensitive Room-Temperature Ammonia Gas Sensor Fabricated from Modified Copper Oxide Nanostructures

Shahed A. Dheyab
Nadim K. Hassan

Department of Physics, College of Education for Pure Sciences, University of Tikrit, Tikrit, IRAQ

Ammonia (NH_3) is a very dangerous gas. The creation of a reliable NH_3 gas sensor with high response at room temperature is crucial and is still fairly challenging. Here, using CuO crystal engineering, we created a CuO-based gas sensor for ammonia detection at room temperature. Vacuum thermal evaporation was used to create the CuO crystal-like material, and several characterization techniques such as field-emission scanning electron microscopy (FE-SEM), X-ray diffraction, and UV-visible spectroscopy respectively were used to determine the crystal structure and optical properties of the (CuO) nanocrystals grown on glass substrate. MSM with Aluminum (Al) contact electrodes (Al-CuO-Al) gas sensor exhibits a high sensitivity of 492.6 % for 17.25 ppm NH_3, fast response and recovery times about, 8.2 and 4.3s respectively at room temperature which are attributed to the morphological structure and increased grain boundary density for the sensor fabricated on CuO Nano crystals oxidized under 400 °C.

Keywords: Nanoparticles; Copper oxide; Thermal evaporation; NH_3 gas sensor
Received: 24 August 2023; **Revised:** 07 September 2023; **Accepted:** 14 September 2023

1. Introduction

Ammonia (NH_3) is a hazardous and toxic gas widely used in various industrial productions like the automobile, chemical, textile, fertilizer, paper products, and food industries [1-3]. Ammonia releases severely contaminate the environment, which leads to life-threatening situations [4]. At present, copper oxide (CuO) is one of the most common commercial sensing element materials [5-7]. The mutual advantages of CuO nanomaterials with well-defined morphological structures led to countless in-depth investigations to grow a variety of CuO nanostructures with a high surface-to-volume ratio, which are of great importance in the manufacture of gas sensors because they have high gas sensitivity and fast response and recovery times [8,9]. Among these various morphologies, the crystal-like CuO nanostructure is a p-type metal oxide semiconductor (MOS) material with a narrow indirect band gap of 1.2–1.8 eV [10-13] and exceeds a 2 eV direct band gap have received a lot of attention recently due to their distinctive shape and structure, which produce exceptional physical and electrical properties, making them the material of focus in sensing and optoelectronics [14-17]. Due to its high potential as a sensing material, CuO nanostructure has received extensive attention in such applications [18]. While the p-type metal oxide gas sensor has a few advantages over the n-type metal oxide gas sensor when the morphological configurations of both sensor materials are the same [19]. The response of a p-type oxide semiconductor gas sensor to a given gas was equal to the square root of that of an n-type oxide semiconductor gas sensor [20,21]. Various techniques have been reported in recent years for the production of CuO nanoparticles: wet chemical methods, low-temperature solid-phase processes, plasma sputtering, oxidation reactions caused by heating copper substrates in the air, or electrodeposition [22-26].

Many researchers have focused mainly on the growth of various nanostructured CuO materials using different growth methods and investigated their gas sensing properties, for example, nanowires, nanorods, nanotubes, nanoflowers, and nanoparticles [27-37]. Based on the reported structures, the limiting factor is the inability to use high-quality CuO nanostructures in practice. This limitation can be related to the weak and easily broken nature of the mentioned structures when they are thermally grown [38].

Determining how the CuO nanostructures' dimensions and shape affect their ability for ammonia gas detection gives deep insight regarding the fundamental rules influencing gas-surface interactions. This information is necessary for creating high-performance sensors and predicting how they will respond to various environmental factors. In this study, the vacuum thermal evaporation approach was used to grow different sizes and shapes of crystal-like CuO nanocrystals using varied annealing temperatures. The aim of the present study is to investigate how the morphology and surface structure of CuO affect ammonia (NH_3) gas sensing

characteristics. This study concentrated on how the annealing temperature affected the structural, optical, and morphological characteristics of CuO thin films. Studies on the (NH_3) gas sensing properties of Al/CuO NC/Al have been conducted. Gas sensing characteristics, including sensitivity, response, and recovery times, have also been suggested, along with an effective approach for gas detection.

2. Experimental Detail

Glass substrates were immersed in the mixture of boiled acetone and ethanol for 10 minutes and then washed in deionized water. After cleaning, the glass substrates were placed over the substrate holder at a distance of 20 cm from the tungsten boat, which contained high-purity copper (Cu) powder (1g, 99.999%, Sigma-Aldrich) in the vacuum thermal evaporator, and a 75-nm copper (Cu) layer was deposited on the glass surface. After 24 hours the process was repeated using the same conditions and another (Cu) layer was deposited on the first (Cu) layer. The resulting sample (Cu/Cu/glass) was removed from the evaporator system, and the produced samples was successively transferred into a thermal furnace for oxidation at 350, 400, and 450 °C under ambient gas for 120 min, and then the furnace temperature was cooled to room temperature.

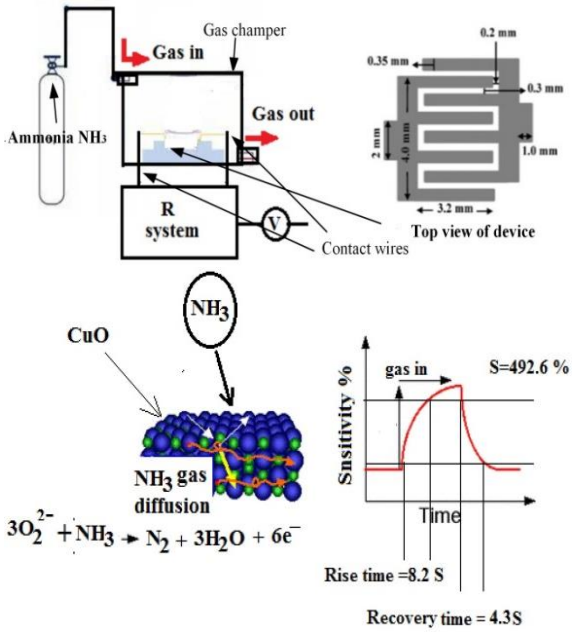

Fig. 1. Schematic illustration of measurement set-up

Field-emission scanning electron microscopy (FE-SEM, NOVA NANOSEM 450, USA) and X-ray diffraction (XRD) by an X-ray diffractometer system type (Philips PW 1710, USA) were used to figure out the shape and crystallinity of the crystalline CuO. The source of radiation was Cu (kα) and λ=1.5406Å. A Shimadzu, UV-3600 UV-Visible spectrometers were used to record the optical characteristics of the deposited films at room temperature. Two interdigitated electrodes with four fingers were used to build the MSM gas sensor. Each finger is 230 µm wide and 3.3 mm long, and the spacing between each finger is 400 µm. Aluminum (Al) contacts were deposited by vacuum thermal evaporation using a metal mask based on the pattern of the contact structure. [39]. The gas sensor performance measurement set-up is shown in Fig. (1). The CuO sensor was placed inside the chamber (Fig. 1), and later the desired gas (NH_3) with a concentration of 17.25 ppm was injected. The change in sensor resistance when exposed to NH_3 gas is measured.

3. Results and Discussion

Figures 2a, b, and c show the typical FESEM images of the crystal-like CuO grown on glass substrates. It can be seen that the grown CuO consists of well-defined crystal structures composed of regular cubic structures. Highly dense crystal shapes of CuO with an average length of 40 nm were successfully obtained. The importance of the first very thin layer of Cu, which acts as a buffer layer, in preventing the crystal mismatch usually seen when CuO is directly deposited on glass substrates

Generally, the buffer layer acts as an intermediate layer between the amorphous substrate and the thin film. The reasons why the buffer layer plays an important role are as follows: Amorphous substrates don't have well-defined crystals, which makes it hard to grow thin films and get a well-defined structure. The substrate and the new material to be deposited should have identical lattice constants to compensate for the mismatch in crystals and to start nucleation and growth. Nucleation and growth, improving adhesion and compatibility, improving surface morphology, and providing crystalline control—all of these can be obtained through a match between the substrate and the material to be deposited.

There is a Cu layer formed between the upper Cu and lower glass substrates. After the heating process, a thin layer of copper oxide forms between the Cu layer and the glass substrate, which is then followed by a second layer of CuO. Finally, both layers of Cu are oxidized to make structures that look like crystals of CuO. Mechanisms of the nanocrystal and the reasons for the differences in the crystal-like size and phases between different nanocrystals are proposed and explained as follows: For a copper-coated glass annealed at 350°C, there is nothing to diminish the downward diffusion of oxygen to the copper substrate as well as the reaction of the second layer of Cu atoms with oxygen in the air. Consequently, the surface of the Cu first layer is quickly oxidized, and CuO is formed through the second oxidation of Cu_2O as follows [38]:

$$4Cu + O_2 \rightarrow 2Cu_2O \quad (1)$$

$$2Cu_2O + O_2 \rightarrow 4CuO \quad (2)$$

From figures (2a,b,c), it can be seen that the annealing temperature can significantly influence the size and shape of CuO crystals. Annealing at different temperatures can increase the diffusion of atoms or

 ISSN (print) 1813-2065, (online) 2309-1673

molecules and enhance the growth of nanoparticles, which leads to variations in the size of these nanoparticles. Higher annealing temperatures can result in larger particle sizes. On the other hand, lower annealing temperatures may decrease diffusion, leading to smaller particle sizes. Therefore, by controlling the annealing temperature, it can help obtain a size that is effective in sensors. The annealing temperature affected the shape of the nanoparticles.

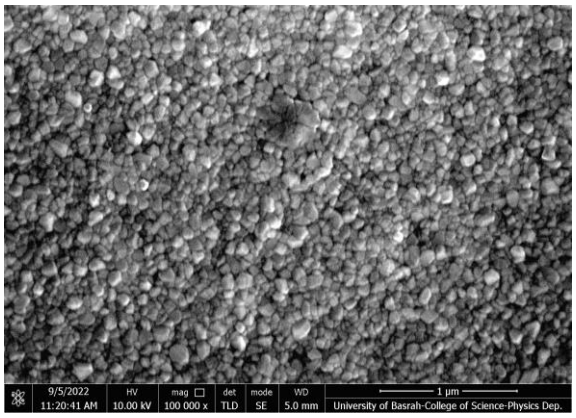

(a)

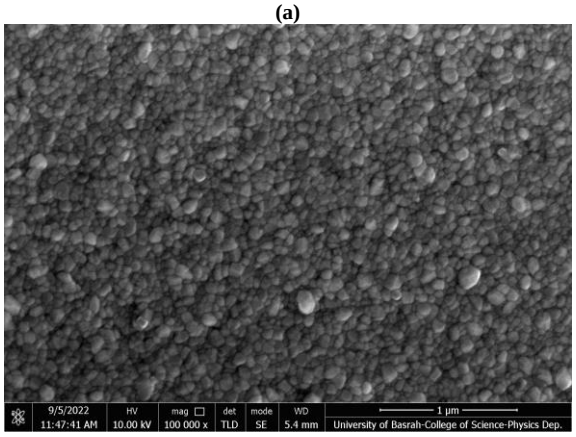

(b)

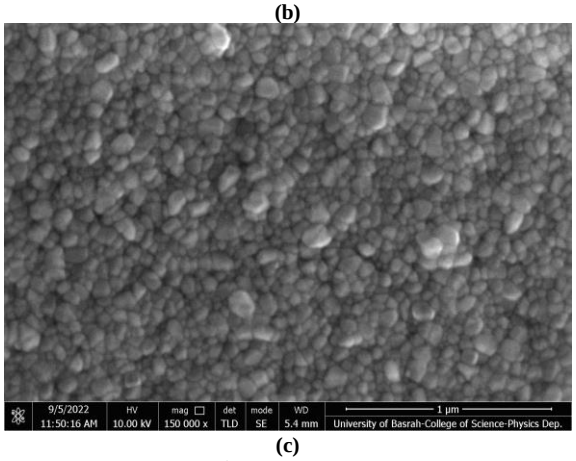

(c)

Fig. 2. FESEM images of CuO nano-crystals deposited on glass as a function of oxidation temperature; (a) 350°C, (b) 400°C, and (c) 450°C

The crystal structure of nanoparticles is greatly affected by annealing temperature. Fig. 2 b shows that at high temperature, recrystallization and the formation of more ordered crystal-like structures of CuO occurred. The annealing can influence the preferential growth directions of nanoparticles, resulting in uniform shapes and a high density of CuO crystals. Higher annealing temperature (Fig. 2c) may lead to disordered structures or inhibit crystal growth on a large scale.

In addition to the reasons listed above, the CuO layer on the surface of the substrate formed when oxygen atoms from the air moved downward and oxidized the Cu substrate. The thickness of the oxide increases along with the heating time due to the continuous diffusion of oxygen atoms to the deeper region of the substrate. In the deeper region that lacks oxygen, only the surface region of the copper oxide is transformed to CuO, while most of the copper oxide region remains as Cu2O, as shown in Fig. (3a).

Figure 3 depicts the XRD patterns of the crystal structure of CuO nanoparticles annealed at temperatures of 350, 400, and 450°C. It can be observed that the X-ray pattern confirms that the samples obtained are crystalline and have the monoclinic structure of CuO.

The decomposition of CuO crystal- like is believed to be carried out in two steps: Cu first reacts with O_2 to produce Cu_2O, followed by the phase transition of Cu_2O to CuO at higher temperature. The peak positions and relative intensities of the diffraction peaks of 32.5, 35.5, and 38.9 correspond to the lattice planes of (110), (002), and (111), respectively, in agreement with JCPDS data for CuO (JCPDS card no. 48-1548) [38-42]. Therefore, the result here confirms that the evaporated films are CuO. However, upon annealing, a low-intensity diffraction peak belonging to the Cu_2O phase (2θ = 29.628°), corresponding to (110) reflection, The appearance of weak Cu_2O peaks in the XRD pattern of CuO can be attributed to various factors, such as small amounts of Cu_2O impurities, the possibility of some Cu_2O forming along with CuO due to insufficient temperature for the reaction, surface oxidation, and other crystal defects.

It was noted from the XRD results that the main phases of the nanoscale CuO grown on pure Cu metal/glass substrates after vacuum thermal evaporation, which is followed by oxidation, were CuO and Cu_2O.

From the figure, it is noticed that the appearance of high peaks was at Fig. 3 b, and the absence of another peak of Cu_2O indicates the purity of this thin film. No peaks of Cu metal are observed in the XRD patterns, indicating that phase-pure CuO is readily obtained. It can be clearly observed that the broadness and intensities of the peaks in the XRD spectra of the sample annealed at 450°C (Fig. 3 c) revealed that the film is mainly composed of CuO and contains a small amount of Cu_2O. This means that with increasing the temperature of oxidation, crystallization decreased.

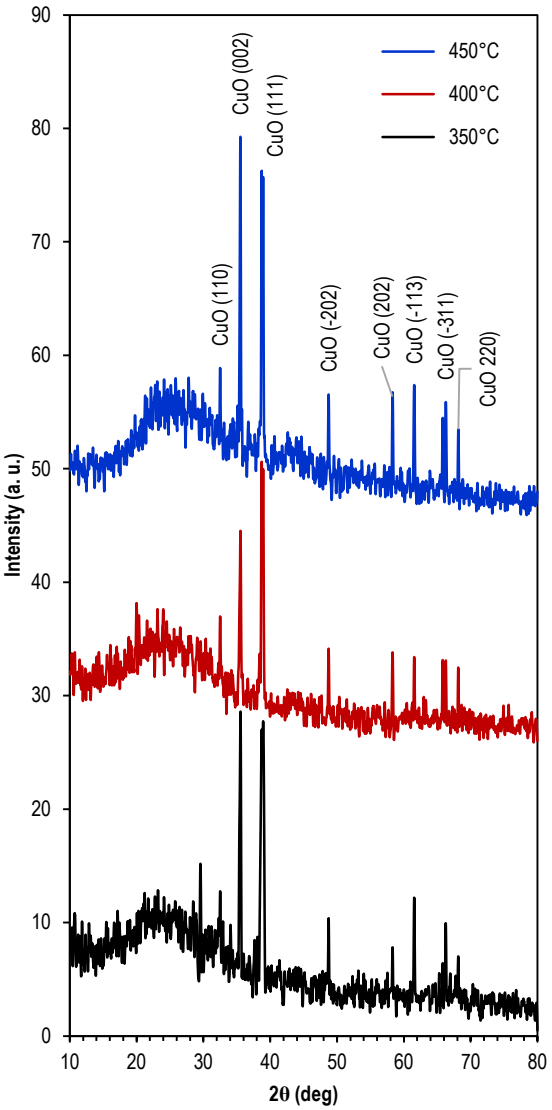

Fig. (3) XRD patterns of CuO nanocrystals deposited on glass at oxidation temperatures (a) 350°C, (b) 400°C, and (c) 450°C

Figure 4 shows the linear relationship between the $(\alpha hv)^2$ and photon energy (hv) was obtained by plotting $(\alpha hv)^2$ against (hv) to determine the value of the optical energy gap at α= 0, where α is the absorption coefficient and hv is the photon energy. The energy band gap of CuO nanocrystals is found to be 2.1, 2.17 and 2.35 eV for the CuO samples annealed at 350, 400 and 450°C, respectively; these are greater than those of the bulk CuO band gap. The observed deviation to a blue shift in the value of the energy gap occurred due to the quantum confinement effect resulting from the reduction in the size and dimensional structure of the nanoparticles and the existence of an amorphous phase in films [11,12]. The change in energy gap values is due to the formation of different sizes of CuO nanoparticles, which resulted in an increase in the value of the energy gap for the sample annealed at 400 °C (Fig. 4 b) and then a decrease in its value at an annealing temperature of 450°C (Fig. 4c). These values match the energy gaps in the direct gap of p-type CuO [43,44]. Energy gap values indicate that the absorption edge was due to a direct allowed transition [45]. It is clear that the direct band gap increases with decreasing particle size [41,42,46]. For the smallest particle size, the band gap is 2.37 eV (Fig. 4b), while its value for the larger particles is 2.17 eV (Fig. 4 a).

It is significant to note that although grain boundaries and nanocrystal size might affect the energy gap, their exact relationship is complex and depends on the particular material and size distribution.

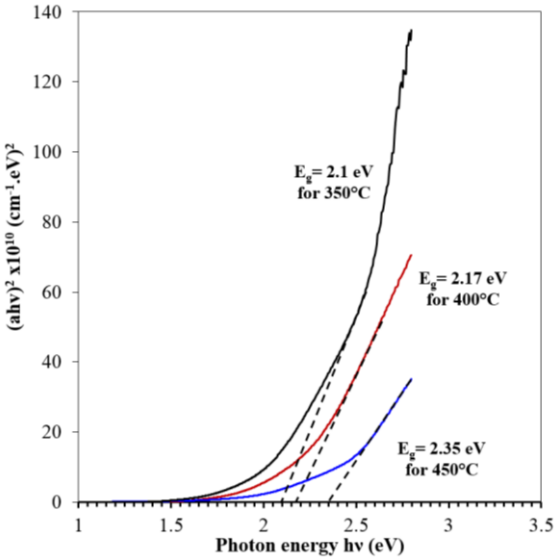

Fig. (4) Tauc plots for optical band gap of a CuO nanocrystals deposited on glass as a function of oxidation temperature (a) 350°C, (b) 400°C, and (c) 450°C

The schematic of the crystal-like CuO MSM NH_3 sensor, as well as the Al finger contacts deposited on top of the CuO nanocrystals, is shown in Fig. 1. To describe NH_3 sensor performance characteristics, electrical responses of the gas sensors fabricated from Al-crystal-like CuO-Al were investigated at room temperature and 17.25 ppm NH_3 gas.

Figure 5 shows the electrical responses of crystal-like CuO as a function of time. The enlarged parts of our recorded data have been drawn in Fig. 5 (a), (b), and (c), measured at a NH_3 concentration of 17.25 ppm in cases of gas input and gas stop. The gas response, response time, and recovery time were used to describe the gas-sensing performances. This formula was used to determine the gas response [47].

$$R_{response}\% = \left|\frac{R_{air}-R_{gas}}{R_{air}}\right| x100 \qquad (3)$$

The sensor's reaction grew linearly as the quantity of ammonia gas increased. When exposed to fresh air, the response immediately returns to the initial value; this shows that the Al-CuO-Al sensor has strong repeatability and reproducibility. The response and recovery times of a gas sensor are another crucial fundamental element. For real-time use in practical applications, a sensor with quick reaction and recovery is required. Response time was found to be

 ISSN (print) 1813-2065, (online) 2309-1673

8.2 s for 17.25 ppm ammonia gas, and recovery time is 4.3 s, as shown in table (1).

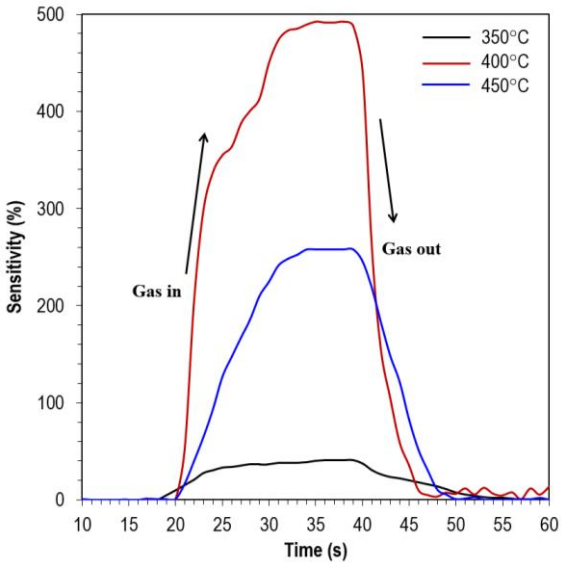

Fig. 5. NH_3 sensing responses of CuO nano-crystals deposited on glass as a function of oxidation temperature; (a) 350 ºC, (b) 400 ºC, and (c) 450 ºC

Table (1) Variation of sensitivity, response and recovery times of Al-CuO-Al gas sensor with annealing temperature of CuO

Annealing Temperature (°C)	Sensitivity (%)	Response Time (s)	Recovery Time (s)
350°C	40.7	8.6	11.8
400°C	492.6	8.2	4.3
450°C	257.6	10.4	7.2

The reactions at the CuO surface and the diffusion within the crystal –like are the basis for the basic operation of the NH_3 gas sensor. Surface polarity and enhanced oxygen adsorption at the CuO surface upon exposure to ammonia gas at room temperature. Based on the energy gap values obtained during thermal treatment, p-type CuO could be formed [48,49], which was confirmed by the behavior of the sensor, where there was a change in the resistance values of the sensor with its exposure to ammonia gas. [47].

The sensor response to 17.25 ppm NH_3 was measured, as shown in Fig. 5. The corresponding dynamic response properties of the CuO gas sensor to 17.25 ppm NH_3 at various times. The real-time on/off switching was measured by exposing the NH_3 gas. The measured current rapidly increased upon exposure to NH_3 gas and then decreased when there was no gas flow. The response and decay times for the sensor CuO were calculated.

CuO's resistance decreases as a result of the removal of electrons by surface oxygen species and the formation of holes in the material. Upon exposure to NH_3, ammonia reacts with CuO and can act as a reducing agent. A possible reduction reaction path at the CuO surface can be given as follows [47,50,51]

$$NH_3(gas) \leftrightarrow NH_3(ads) \quad (4)$$
$$3O_2^- + 4NH_3 \leftrightarrow 2N_2 + 6H_2O + 3e^- \quad (5)$$
$$3O^- + 2NH_3 \leftrightarrow N_2 + 3H_2O + 3e^- \quad (6)$$
$$3O^{2-} + 2NH_3 \leftrightarrow N_2 + 3H_2O + 6e^- \quad (7)$$

The gas sensing ability of CuO sensors as a change in sensor resistance can be explained on the basis of their adsorption, desorption, and reaction with reducing gas molecules. In the initial stages, oxygen molecules get absorbed through the CuO sensor when it is exposed to the air, and oxygen ionic species (O^{2-}, O^-, and O^{2-}) are formed by capturing one electron from the CuO surface.

Consequently, there is a decrease in electrical resistance due to an increase in hole concentration. When ionic oxygen species on the surface of CuO are exposed to reducing gases, like molecules of ammonia, they interact with these molecules. This releases a lot of electrons back into the CuO conduction band. The recombination of these electrons with the existing holes raises the electrical resistance of the CuO sensor. As a result, the electrical resistance of the sensor changes in a manner that is proportionate to the presence of ammonia gas. The CuO surface consists of a large number of grains, contacting at their boundaries. The creation of double Schottky potential barriers at the interface of adjacent grains, brought on by charge trapping at the interface, governs the electrical behavior. The conductivity is determined based on the height of this barrier. Charge trapping at the interface is what caused this process. The majority of carriers can be caught in trap states that are present at these interfaces. As a result, the band bends, creating a barrier at the interface. The conductivity of this barrier is regulated by its height [52-54]. It is evident that the relationship between the change in conductance and the change in barrier height and the temperature. When determining the sensitivity of CuO gas sensors, grain boundaries are a key factor through its effect on the value of the height of the Schottky potential barrier. Gas molecules react and adsorb on the surface of CuO particles as part of the sensing mechanism. Because the gas molecules move across the gaps between the grains and interact with the CuO surface, the sensor's electrical and chemical properties change. From the results that we obtained, it was shown that the annealing temperature has a large effect on the size of the grains and therefore on the sensor. More active areas for gas molecules to interact with CuO nanocrystals are made available as the size of the nanocrystals decreases. Due to the exposed surface atoms in nanocrystals and the shorter diffusion paths that gas molecules must take to reach the sensor's surface, response and recovery times are reduced. Gas molecules can

diffuse into and out of a material through grain boundaries. Due to the shorter diffusion paths that gas molecules have to take in order to reach the active areas of the sensor, gas response and recovery times may be reduced. Our results showed that with the wide spread of the grains on the substrate, the values of the grain boundaries decreased, thus decreasing the sensitivity of the sensor, and the values of response and recovery times decreased, as shown in table (1).

4. Conclusions

Using the vacuum thermal evaporation method, two layers of Cu that oxidized at different annealing temperatures were used to make a crystal-like CuO on a glass substrate. Al-CuO NCs -Al were used to successfully build gas sensors, and their gas-detecting ability was evaluated for ammonia. According to the gas sensing results, the sensor based on CuO that was annealed at 400 ºC demonstrated superior gas sensing performance, with a fast response (8.2 s) and quick recovery (4.3 s) time toward 17.25 ppm ammonia at ambient temperature. As a suitable substrate to form crystals, like CuO thin films, the Cu intermediate thin layer emerges. Our findings show that the high sensitivity to NH3 gas found for CuO film is based on two elements: the CuO's crystal size structure and the grain boundaries.

References

[1] M. Poloju, N. Jayababu and M.V. Ramana Reddy, "Improved gas sensing performance of Al doped ZnO/CuO nanocomposite based ammonia gas sensor", *Mater. Sci. Eng. B,* 227 (2018) 61-67.

[2] J. Yun et al., "A review of nanostructure-based gas sensors in a power consumption perspective", *Sens. Actuat. B: Chem.,* 372 (2022) 132612.

[3] C.A. Betty, S. Choudhury and A. Shah, "Nanostructured metal oxide semiconductors and composites for reliable trace gas sensing at room temperature", *Surf. Interfaces,* 36 (2023) 102560.

[4] K.G. Krishna et al., "Nanostructured metal oxide semiconductor-based gas sensors: A comprehensive review", *Sens. Actuat. A: Phys.,* 341 (2022) 113578.

[5] M.A. Hameed, S.H. Faisal, R.H. Turki, "Characterization of Multilayer Highly-Pure Metal Oxide Structures Prepared by DC Reactive Magnetron Sputtering Technique", *Iraqi J. Appl. Phys.,* 16(4) (2020) 25-30

[6] C. Gherasim et al., "Copper oxide nanostructures: Preparation, structural, dielectric and catalytic properties", *Ceram. Int.,* 48(17) (2022) 25556-25568.

[7] M. Xu et al., "Controlled oxidation of Cu particles by H_2O_2 to form Cu/CuO nanostructure with enhanced gas sensing performance", *Appl. Surf. Sci.,* 618 (2023) 156668.

[8] L. Hou et al., "CO gas sensors based on p-type CuO nanotubes and CuO nanocubes: Morphology and surface structure effects on the sensing performance", *Talanta,* 188 (2018) 41-49.

[9] A.S. Zoolfakar et al., "Nanostructured copper oxides as ethanol vapour sensors", *Sens. Actuat. B: Chem.,* 185 (2013) 620-627.

[10] D. Wu, Q. Zhang and M. Tao, "LSDA+Ustudy of cupric oxide: Electronic structure and native point defects", *Phys. Rev. B,* 73(23) (2006) 235206.

[11] N. Duc Hoa et al., "Facile synthesis of p-type semiconducting cupric oxide nanowires and their gas-sensing properties", *Physica E: Low-dimen. Syst. Nanostruct.,* 42(2) (2009) 146-149.

[12] J. Koshy et al., "Optical Properties of CuO Nanoparticles", *AIP Conf. Proc.,* 1391(1) (2011) 576-578.

[13] A.M. Hameed and M.A. Hameed, "Spectroscopic characteristics of highly pure metal oxide nanostructures prepared by DC reactive magnetron sputtering technique", *Emer. Mater.,* 6 (2022) 627-633.

[14] M. Dahrul, H. Alatas and Irzaman, "Preparation and Optical Properties Study of CuO thin Film as Applied Solar Cell on LAPAN-IPB Satellite", *Proc. Enviro. Sci.,* 33 (2016) 661-667.

[15] S. Ahmmed et al., "CuO based solar cell with V2O5 BSF layer: Theoretical validation of experimental data", *Superlat. Microstruct.,* 151 (2021) 106830.

[16] S.H. Faisal and M.A. Hameed, "Heterojunction Solar Cell Based on Highly-Pure Nanopowders Prepared by DC Reactive Magnetron Sputtering", *Iraqi J. Appl. Phys.,* 16(3) (2020) 27-32.

[17] A.M. Hameed and M.A. Hameed, "Highly-Pure Nanostructured Metal Oxide Multilayer Structure Prepared by DC Reactive Magnetron Sputtering Technique", *Iraqi J. Appl. Phys.,* 18(4) (2022) 9-14.

[18] F. Wang et al., "A highly sensitive gas sensor based on CuO nanoparticles synthetized via a sol–gel method", *RSC Adv.,* 6(83) (2016) 79343-79349.

[19] M. Solhi et al., "Synthesis and characterization of a high-performance enzyme-free glucose sensor based on mesoporous copper oxide nanoparticles", *Mater. Res. Bull.,* 164 (2023) 112240.

[20] M. Hübner et al., "Influence of humidity on CO sensing with p-type CuO thick film gas sensors," *Sens. Actuat. B: Chem.,* 153(2) (2011) 347-353.

[21] S. Biswas, P. Kumbhakar and T. Kobayashi, "Viscosity sensing by low power optical self phase modulation in two dimensional copper oxide nanostructures", *Optik,* 252 (2022) 168546.

 ISSN (print) 1813-2065, (online) 2309-1673

[22] Y. Chang and H.C. Zeng, "Controlled Synthesis and Self-Assembly of Single-Crystalline CuO Nanorods and Nanoribbons," *Cryst. Growth Des.*, 4(2) (2004) 397-402.
[23] S.H. Jun et al., "Synthesis of chrysalis-like CuO nanocrystals and their catalytic activity in the thermal decomposition of ammonium perchlorate", *J. Chem. Sci.*, 121(6) (2009) 1077–1081.
[24] X. Jiang, T. Herricks and Y. Xia, "CuO Nanowires Can Be Synthesized by Heating Copper Substrates in Air", *Nano Lett.*, 2(12) (2002) 1333-1338.
[25] P. Raksa et al., "Ethanol sensing properties of CuO nanowires prepared by an oxidation reaction", *Ceram. Int.*, 35(2) (2009) 649-652.
[26] I.C. Cancellieri et al., "Synthesis of nanostructured sphere-like copper oxide by microwave spray pyrolysis", *Mater. Lett.*, 350 (2023) 134957.
[27] J. Suganthi, J. Priyanka and S. Johnsonjeyakumar, "Study of Structural and Morphological Properties of Vacuum Coated Copper Oxide (CuO) Thin Film by Thermal Evaporation Technique", *Int. J. Curr. Res. Rev.*, 10(21) (2018) 91-93.
[28] H.-L. Chen, T.-H. Chiang and M.-C. Wu, "Evolution of Morphology of Nano-Scale CuO Grown on Copper Metal Sheets in 5 wt% NaCl Solution of Spray Fog Environment", *J. Surf. Eng. Mater. Adv. Technol.*, 2(4) (2012) 278-283.
[29] Y.H. Ko et al., "Facile preparation and optoelectronic properties of CuO nanowires for violet light sensing", *Mater. Lett.*, 117 (2014) 217-220.
[30] H. Kim et al., "H_2S gas sensing properties of bare and Pd-functionalized CuO nanorods", *Sens. Actuat. B: Chem.*, 161(1) (2012) 594-599.
[31] Y.-S. Kim et al., "CuO nanowire gas sensors for air quality control in automotive cabin", *Sens. Actuat. B: Chem.*, 135(1) (2008) 298-303.
[32] C. Wang et al., "Surface accumulation conduction controlled sensing characteristic of p-type CuO nanorods induced by oxygen adsorption", *Nanotechnol.*, 18(14) (2007) 145506.
[33] Y. Sun et al., "$Cu(OH)_2$ and CuO nanotube networks from hexaoxacyclooctadecane-like posnjakite microplates: Synthesis and electrochemical hydrogen storage", *Int. J. Hydrog. Ener.*, 37(3) (2012) 2336-2343.
[34] K. Khun, Z.H. Ibupoto and M. Willander, "Urea Assisted Synthesis of Flower Like CuO Nanostructures and Their Chemical Sensing Application for the Determination of Cadmium Ions", *Electroanal.*, 25(6) (2013) 1425-1432.
[35] A. Das et al., "Facile synthesis of nanostructured CuO for low temperature NO_2 sensing", *Physica E: Low-dimen. Syst. Nanostruct.*, 54 (2013) 40-44.
[36] G. G. Welegergs et al., "Structural and optical properties of copper oxide (CuO) nanocoatings as selective solar absorber", *Mater. Today: Proc.*, 36 (2021) 509-513.
[37] A. Taubert et al., "CuO Nanoparticles from the strongly hydrated ionic liquid precursor (ILP) tetrabutylammonium hydroxide: evaluation of the ethanol sensing activity", *ACS Appl. Mater. Interfaces*, 4(2) (2012) 791-805.
[38] R.-C. Wang and C.-H. Li, "Improved Morphologies and Enhanced Field Emissions of CuO Nanoneedle Arrays by Heating ZnO Coated Copper Foils", *Cryst. growth Des.*, 9(5) (2009) 2229-2234.
[39] N.K. Hassan, M.R. Hashim and M. Bououdina, "Optical properties and I–V characteristics of ZnO nanostructures grown by electrochemical deposition on Si (111) and Si (100)", *Superlat. Microstruct.*, 62 (2013) 182-191.
[40] H. Siddiqui et al., "Studies of structural, optical, and electrical properties associated with defects in sodium-doped copper oxide (CuO/Na) nanostructures", *J. Mater. Sci.*, 53(12) (2018) 8826-8843.
[41] F.M. Fakhree, I.F. Waheed and K.M. Mahmoud, "Synthesis and characterization of CuO nanoparticles stabilized by quercetin and its application for anti-breast cancer activity", *Egyptian J. Chem.*, 64(6) (2021) 2989-2995.
[42] H.J. Jung, Y. Yu and M.Y. Choi, "Facile Preparation of Cu_2O and CuO Nanoparticles by Pulsed Laser Ablation in NaOH Solutions of Different Concentration", *Bull. Korean Chem. Soc.*, 36(1) (2015) 3-4.
[43] S.M. Mousavi, M. Chamack and H. Fakhri, "Study of New Hybrid Material of ZnO/CuO and Metal-Organic Framework as Photocatalyst for Removal of Tetracycline from Water", *J. Nanostruct.*, 12(4) (2022) 1097-1107.
[44] R. Hussain, W. Aziz and I.A. Ibrahim, "Antibacterial Activity of CuO - Cellulose Nano rods Depends on Anew Green synthesis (cotton)", *J. Nanostruct.*, 9(4) (2019) 761-767.
[45] Y.-F. Lim, J.J. Choi and T. Hanrath, "Facile Synthesis of Colloidal CuO Nanocrystals for Light-Harvesting Applications", *J. Nanomater.*, 2012, 1-6.
[46] R. Bunea, A.K. Saikumar and K. Sundaram, "A Comparison of Optical Properties of CuO and Cu_2O Thin Films for Solar Cell Applications", *Mater. Sci. Appl.*, 12(7) (2021) 315-329.
[47] S. Rehman, A. Mumtaz and S.K. Hasanain, "Size effects on the magnetic and optical properties of CuO nanoparticles", *J. Nanopart. Res.*, 13(6) (2010) 2497-2507.
[48] V. Usha et al., "Effect of catalysts on the synthesis of CuO nanoparticles: Structural and optical properties by sol–gel method", *Superlat. Microstruct.*, 86 (2015) 203-210.

[49] G. Chaloeipote et al., "3D printed CuO semiconducting gas sensor for ammonia detection at room temperature", *Mater. Sci. Semicond. Process.*, 123 (2021) 105546.
[50] A.A. Al-Ghamdi et al., "RF sputtered CuO thin films: Structural, optical and photo-catalytic behavior", *Physica E: Low-dimen. Syst. Nanostruct.*, 81 (2016) 83-90.
[51] Y. Du et al., "Characterization of the microstructure and the optical and electrical properties of the direct-current magnetron sputtered CuO films at different substrate temperatures", *Physica B: Cond. Matter*, 546 (2018) 28-32.
[52] F. Shao et al., "Copper (II) oxide nanowires for p-type conductometric NH_3 sensing", *Appl. Surf. Sci.*, 311 (2014) 177-181.
[53] N. Sharma et al., "Heptazine based organic framework as a chemiresistive sensor for ammonia detection at room temperature", *J. Mater. Chem. A*, 6(38) (2018) 18389-18395.
[54] P.L. Rajeev K. Srivastava, R. Dwivedi, SK. Srivastava, "Sensing mechanism in tin oxide-based thick-film gas sensors", *Sens. Actuat. B: Chem.*, 21 (1994) 213-218.

 ISSN (print) 1813-2065, (online) 2309-1673

IRAQI JOURNAL OF APPLIED PHYSICS
Vol. 19, No. 4C, December 2023, pp. 205-210

Design and Development of Atmospheric Pressure DBD Ar Plasma Jet for Investigating Cotton Fabric Hydrophilicity

Thikra K. Al-Khafaji

First Al-Karkh Education, Ministry of Education, Baghdad, IRAQ

Atmospheric pressure DBD Ar plasma jet is a new technology applied treatment on cotton fabric to improve its hydrophilicity. In the current study, employed argon as the working gas and investigated various plasma properties using an AC power supply operating at 8kV peak to peak with a frequency of 28 kHz. Additionally, The water contact angle as wettability measurements reveals the hydrophilic properties of the cotton surface after plasma treatment at the study conditions. The plasma treatment caused a reduction in the water contact angle, indicating enhanced hydrophilic properties of the cotton fabric surface. with noticeable effects starting to appear after only 5 seconds of treatment. This work demonstrates the enhancement of hydrophilic surfaces on cotton fabrics using atmospheric pressure DBD as effective and environmentally safe method.

Keywords: Cotton; DBD Ar plasma jet; surface modification; hydrophilicity
Received: 13 August 2023; **Revised:** 10 September 2023; **Accepted:** 17 September 2023

1. Introduction

Textiles hold considerable importance within society, given their multifarious applications and consequential societal significance. Examples include interior textiles, wearable electronics, and medical implants [1]. Through innovation in numerous economic sectors, textile uses are growing and developing continuously. The demand for a higher quality of life, access to better facilities, modern lifestyle choices with an increased awareness of hygiene, and population expansion are the primary market drivers for the development of textiles. Here, enhanced textiles are essential to achieving the goal of offering a healthy lifestyle that is affordable and of high quality in both private and public spaces [2].

Due to its softness, porous, flexible, comfortable and breathable qualities, cotton is one of the most widely used fibers in the textile industry and is therefore ideal for use in clothing, pillowcases, bed sheets, draperies, towels, tents, underwear, hospital healthcare textiles, military garments, gauze and other items [3,4]. Cotton textiles are used frequently where a cellulose is the primary chemical constituent of cotton. the cuticle, which is the cotton fiber's outermost layer. includes waxes, lipids, and pectins that give the fibers adhesive qualities [5]. Cotton, on the other hand, is naturally hydrophobic because it has waxes and oils that stop it from absorbing water and/or moisture. Natural oils and waxes are partially removed from cotton during the purification process, which removes impurities from the growing and ginning processes [6]. Currently available softening agents have a specific chemical composition that includes two lengthy hydrophobic alkyls chains. The drawbacks with these softeners, such as a result, yarns and fabrics treated with softeners easily develop hydrophobic surfaces, which prevent water from being efficiently absorbed between the fibers. This explains why cotton materials' ability to absorb water quickly degrades, in addition to environmental safety issues such as low biodegradability [7]. Over the previous years, several traditional chemical procedures have been used to increase the hydrophilicity of cotton fabrics. These traditional methods are fundamentally expensive and harmful to the environment. Additionally, the performance of the final product may be negatively impacted by the usual method that handles the fabric bulk [8]. There is an increasing amount of attention being paid to developing new technology that can vary the mechanical and surface qualities of natural and synthetic fabrics while preserving the useful attributes of cotton fibers [9].

Cold plasma technique has a variety of advantages over conventional chemical techniques, including the ability to modify surfaces without the utilization of water or chemical compounds, making it both affordable and environmentally friendly [10]. It was discovered that the non-thermal plasma treatment is a useful technique for enhancing surface qualities without changing the bulk of the fabric [8]. This technology has mostly been utilized to enhance various aspects and characteristics of cotton textiles, such as the fibers' hydrophilicity [11]. Free electrons receive greater energy during a plasma atmosphere discharge from an applied electric field besides losing energy when they collide with neutral molecules. Depending on the plasma feeding gas (helium, argon and oxygen), the energy transmission to the molecules causes the production of new species, including free radicals, ultraviolet radiation, photons, electrons, ions, atoms, and different excited particles

[12] enhances cotton fiber's ability to absorb water by surface oxidation and etching caused by plasma active species. High concentration of neutral reactive species plasma cause grooves and cracks of the fiber surface [13]. The surface of the substrate reacts with all of the active species, creating chemical functionality [14]. As a result, the treatment of fabric surface creates channels facilitate water penetration and hydrophilic groups formation. These chemical and physical changes after plasma treatment lead to prompt increase in the water absorbance of cotton materials [8,13].

When a solid intersects gas and liquid at the three-phase boundary, a liquid creates an angle known as the water contact angle. Water contact angle gives a direct indication of the wettability of the solid surfaces. If the water contact angle exceeds 90°, it means the surface has a poor wetting, which have minor inclination to interact with water. If the contact angle falls below 90°, indicates water molecules have a high binding affinity to the substrate. The presence of active polar groups leads to hydrophilic substances features that readily absorbs water [15].

Dielectric Barrier Discharge (DBD) plasma jet was used in the current study that is generated by a single electrode arrangement and operated with noble gases. This type of plasma is operated at atmospheric pressure and room temperature that allows treatment of irregular surfaces with small penetration depth. Human skin can be exposed to Ar glow discharge without suffering any negative effects. This is such that the multiple kilovolt pulsed power that was applied to operating gas only excited the light electrons and had no effect on the heavy neutral particles. As a result, even materials that are sensitive to heat are more appropriate for plasma-mediated treatment [16-18].

In this study, we used calculations contact angle to examine the effect of plasma treatment on the wettability of the cotton fabrics.

2. Material and methods

Weave cotton fabric without additional purification, the cotton fabrics used in this research were from the Kut Factory for Cotton Textiles in Kut City (Iraq).

To generate DBD plasma jet has cross-field configuration, it requiers a constraction of high voltage power supply. The electric circuit used to drive the high voltage power supply was shown in Fig. (1). The transistor (MOSFET) IRF 540A conducts the current transmission through resistors R1 and R2 to the flyback primary when power is applied, leading to current induction on the secondary and on the feedback winding. As the magnetic field in the ferrite core collapses, this feedback current will cause the transistor to stop conducting, causing a sizable high voltage spike to appear on the secondary winding. However, since there is no longer any feedback current to keep the transistor shut off, it will restart conducting, and the cycle will repeat at a natural frequency that causes the transformer to enter into resonance. The circuit becomes dynamic when there is a feedback winding, which is one of its benefits. The operational frequencies are automatically tuned to resonance.

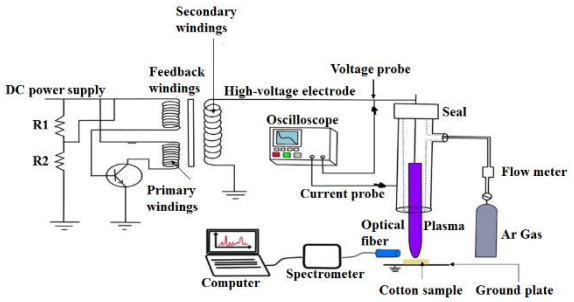

Fig. (1) Detailed schematic of the DBD plasma jet source

A high-voltage copper electrode wire with diameter of 10 mm with a length of 100 mm is inserted into the center of the quartz tube. The tube thickness is about 1 mm, and its length is 180 mm which represents the dielectric layer, the Ar with High-purity (99.999%) and a flow rate of 2 L/min is considered as the operating gas and is supplied into a quartz tube. The flow rate was measured and regulated by a mass flow controller. The tissue cotton sample is placed on an aluminum stage which represents the ground electrode. The plasma jet occurs between the bottom surface of the quartz tube and the top surface of the sample, where 5 mm is the distance between them. A 28 kHz ac sinusoidal HV power supply with a peak voltage that can be adjusted between 0 and 8 kV powers the DBD plasma jet, this produces an energetic plasma that is stable. The voltage waveform was assessed through the utilization of an internally crafted high-voltage probe featuring a substantial attenuation factor of 1000-fold. Simultaneously, an oscilloscope (Gos-652G 50MHz) was employed for visualization. Concurrently, the measurement of current was conducted using a Tektronix A6302 current probe, augmented by an Am503 current probe amplifier, and the resultant data was displayed on the oscilloscope. Furthermore, it is viable to ascertain the plasma's distinct characteristics by engaging in electrical characterization, a process that involves the precise measurement of both current and voltage. Measurements are made of the jet plasma's optical emission spectrum by Spectrometer model (SpectraPro S3000). The spectrometer has a high resolution depending on grating used and responds to a wavelength between 320 and 750nm. Optical emission spectroscopy (OES) was applied in order to calculate plasma parameters including plasma frequency, electron density, and Debye length. The plasma electron temperature was counted using Boltzmann plot method [19].

$$ln\left[\frac{\lambda_{ji} I_{ji}}{hcA_{jig_j}}\right] = -\frac{1}{k_B T}(E_j) + ln\left|\frac{N}{U(T)}\right| \qquad (1)$$

 ISSN (print) 1813-2065, (online) 2309-1673

Where g_i is statistical weight, while I_{ji} is the relative emission line density between energy levels i and j, λ_{ij} is the wavelength (in nm), k_B is Boltzmann constant, A_{ji} is the potential for radiation to be automatically transmitted from level i to the lower level j, E_j is the excitation energy (in eV) for level i, N refers to the densities of the population of the state, $U(T)$ partition function, h is the Planck's constant, and c is the speed of light. Debye's length (λ_D) is calculated using the formula shown below [20]

$$\lambda_D = \left(\frac{\varepsilon_0 k_B T_e}{n_e e^2}\right)^{1/2} \quad (2)$$

where n_e is the density of the electrons, ε_0 is the permittivity of free space, k_B the Boltzmann constant, T_e is the electron temperature and e the electron charge

Plasma frequency (ω_p) can be given as [21,22]

$$\omega_p = \left(\frac{n_e e^2}{\varepsilon_0 m_e}\right)^{1/2} \quad (3)$$

where m_e is the mass of the electron, and the rest of the parameters were defined before

DBD plasma jet activation of a textile surface as can be seen in Fig. (2). Cotton samples underwent air atmospheric DBD plasma treatment. Apply a 50 µL water drop to the fabric sample before applying a plasma torch, and then use a camera phone to take a photo of the droplet to determine the tangent angle. Place a drop of water on the plasma-treated tissue once more, and then display a plasma torch for 5, 15, 30, and 60 s to compute the tangent angle.

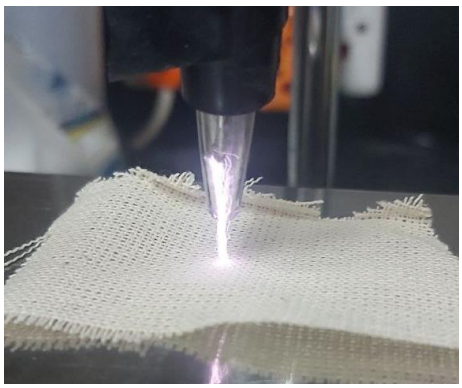

Fig. (2) Photograph of cotton sample during exposure to DBD plasma treatment

The most used technique for measuring contact angles is the sessile drop method. A contact angle can be simply determined from a few drop boundary points, by knowing the base diameter and height of the sessile drop, as shown in Fig. (3). The contact angles were calculated using Eq. (4) [5,23], the droplet height and width were measured using the ImageJ software

$$\theta = 2\tan^{-1}\left(\frac{2h}{D}\right) \quad (4)$$

where θ is contact angles, h is droplet height, D is width of the droplet touching the surface of the fabric

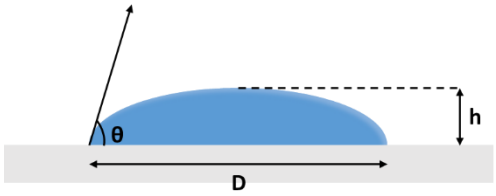

Fig. (3) A drop's dimensions on a flat surface

3. Results and Discussion

The waveforms of voltage and current are shown in Fig. (4). The flyback transformer's secondary coil's ends were where the voltage was measured, and the voltage exhibited a sinusoidal wave pattern with a 28 kHz frequency, as shown in Fig. (4a).This frequency are close to the flyback transformer's secondary circuit's resonant frequency, which was determined using the secondary coil's RLC values. The voltage seen at the ends of the secondary coil is around 8 kV peak to peak. Figure (4b) shows four damped oscillations of the applied voltage with a 35µs cycle are present in the current waveform. The capacitive coupling of the circuits with the discharged gas may be the cause of this behavior. It can be seen from Fig. (4) that the voltage and current are not in phase, as well as the absence of spiky lines in the voltage and current suggests that the discharges are homogenous glows [24]. Additionally, this figure shows that the voltage lags behind the current, illustrating the discharge's capacitive character [25].

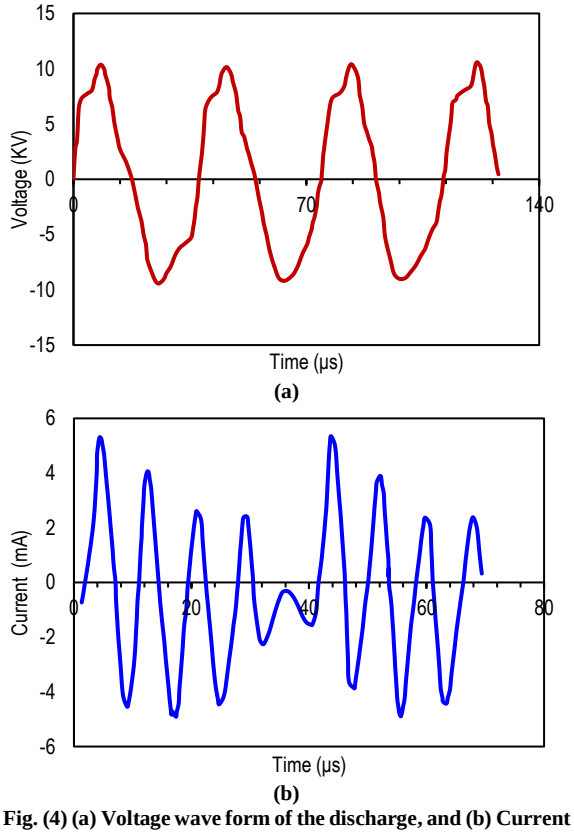

Fig. (4) (a) Voltage wave form of the discharge, and (b) Current waveform of the discharge

OES has been implicated to the detection of plasma composition via monitoring the species that are electrically stimulated and the intensity of the discharges produced by an Ar plasma torch. Figure (5) shows the optical spectrum has various peaks, most of it belong to the ArI which agrees with NIST data [26] and Ar plasma's spectrum shows emission lines that match to the group of N_2 emissions in the range 300-400nm. They fall into the first-negative and second-positive bands, respectively, and also we can see OH (at 306nm) [27]. Given that the DBD plasma jet runs on Ar gas, this is to be expected. Normally, the plasma jet is generated in surrounding air, due to the air diffusion, associated with nitrogen emission. Thus, the nitrogen, oxygen, and hydroxyl radicals can be caused by the interaction of plasma-produced particles with the surrounding atmosphere's N_2, O_2, and H_2O. The existed emissions of OH and nitrogen generally could be recognized to the existence of water vapor from air atmosphere [28,29].

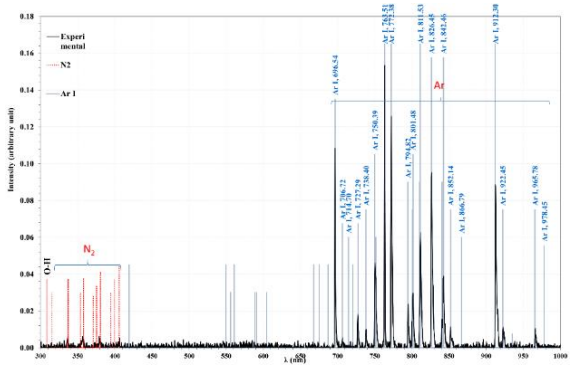

Fig. (5) The DBD jet system's optical emission spectra at atmospheric pressure

Highest peak appears at 763.51nm (as show of Lorentzian fit in Fig. 6) which reveals the active species created in the Ar plasma represented by ArI. All peaks are found in the visible range of wavelengths (650-800nm). This result which agrees with [30] and [31].

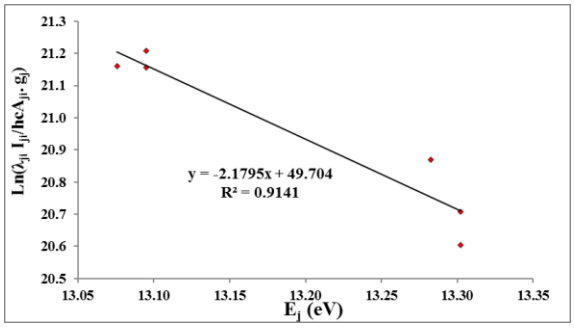

Fig. (6) The Lorentzian fitting of intensity and wavelength at highest peak

The Boltzmann plot technique was used to assess the discharge and determine the electron temperature (T_e). In this technique, five suitable lines of Ar I were taken from the spectral lines of argon plasma discharge (696.54, 706.72, 763.54, 801.47, 811.53nm). The T_e values were calculated by Eq. (1), using the relation between $(\ln\frac{\varepsilon_{ji}\lambda_{ij}}{A_{ji}g_j})$ versus upper energy level (E_j) were shown in Fig. (7). The electron temperature was found to be of the order of 0.459 eV.

The figures include the equations of fitting lines and the R2, which is a statistical coefficient, the value was 0.9141, demonstrating the accuracy of the linear fit which takes a value between (0,1), where the values closer to1 is the best one.

While the results of plasma parameters such as plasma frequency (f_p) 6.602x10^{12} Hz, Debye length (λ_D) 6.845x10^{-6} cm, electron density (n_e) 5.405x10^{17} cm^{-3} and full-width at half maximum (FWHM) 0.800 nm that were calculated for the DBD plasma jet produced at flow rate of argon gas 2 L/min was maintained.

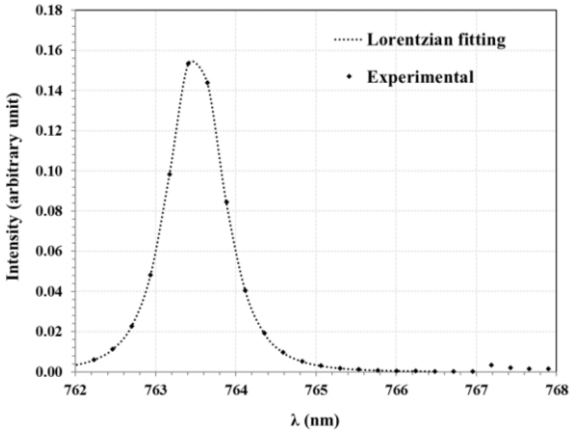

Fig. (7) Boltzmann plot for ArI peaks utilizing the DBD plasma jet technique

The modification of the textile surface through atmospheric pressure DBD plasmas is influenced by variables such as exposure duration and the type of gas involved research in the field highlights that subjecting cotton surfaces to atmospheric plasma treatment with air leads to heightened surface wettability, prominently displaying enhanced hydrophilic behavior. Following the application of plasma treatment to cotton fabric, water droplets of 50 µL at room temperature were placed onto the fabric surface, with variations in exposure time ranging from 5 to 60 s. This meticulous process was meticulously repeated thrice to ensure measurement accuracy. The calculation of contact angles for both untreated and treated samples was performed as per Eq. (4), involving the measurement of drop diameter and height at distinct time intervals (as detailed in table 1). The process utilized an image analyzer, as depicted in Fig. (8). Notably, with prolonged plasma exposure, a noticeable decrease in contact angle becomes apparent.

 ISSN (print) 1813-2065, (online) 2309-1673

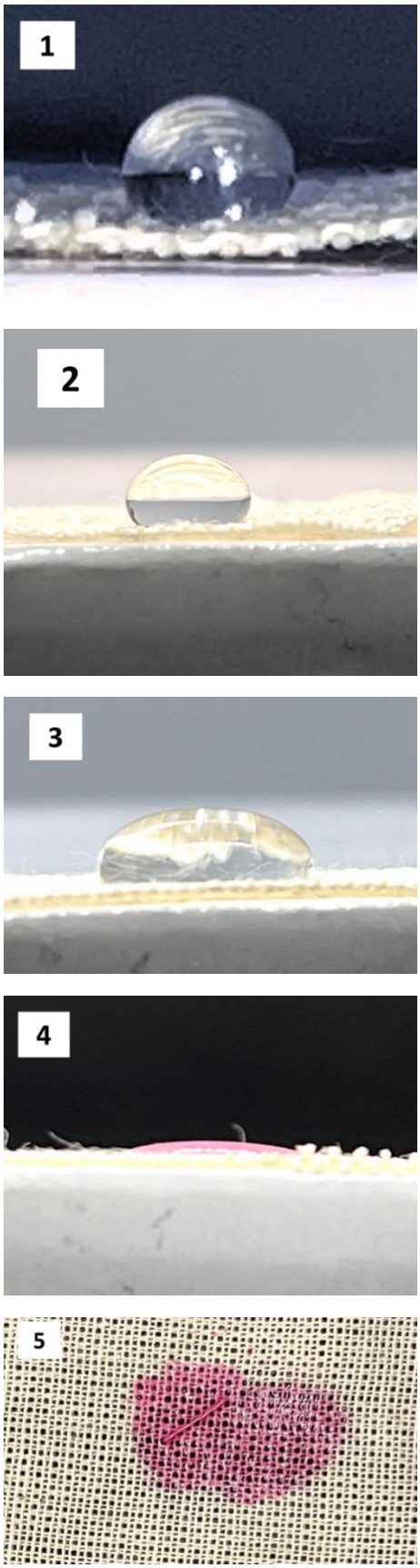

Fig. (8) Digitized images of cotton samples (1) untreated, and (2,3,4,5) being exposed to a plasma jet during 5, 15, 30, and 60s, respectively

The initial contact angle for untreated samples measured at 132°, a value that decreased to zero upon 60 s of plasma treatment. The fabric's hydrophobic nature prior to treatment was attributed to the presence of cellulosic impurities is covered with a layer of wax, and the smooth textile surface. This impurity layer was identified as the driving factor behind fabric hydrophobicity [8]. The findings underscored that DBD plasma-treated samples exhibit the removal of organic materials from the surface, possibly attributed to two main factors.

Table (1) Effect of plasma treatment on the contact angle of against in various time intervals on cotton textiles

Plasma-treated Samples	Droplet Height (pixels)	Droplet Width (pixels)	Contact Angle (°)
untreated samples	372	332	132
5 s	302	424	110
15 s	252	648	76
30 s	114	1248	21
60 s	0	0	0

Firstly, the influence of plasma species, including reactive species and free electrons, brings about physical changes due to an etching effect on cotton fabrics. The concentration of active plasma species on the substrate notably impacts the efficacy of plasma modification, leading to the incorporation of polar groups and surface roughness, ultimately resulting in heightened water absorbency [13]. The treatment's impact on cotton textile pores is further evidenced by an increase in effective pore size, brought about by the etching action of atomic Ar, reactive nitrogen species (RNS), and reactive oxygen species (ROS).

Secondly, the surface chemistry and morphology alteration induced by the plasma treatment lead to the formation of free radicals and polar groups, exemplified by the introduction of OH bonds [13,32]. Consequently, the hydrophobic layer on the textile surface undergoes a transformation, resulting in a shift towards hydrophilicity [33].

4. Conclusion

Atmospheric pressure argon DBD plasma jet treatment is a favorable procedure for surface treatment of cotton fabric. our study delved into the utilization of plasma treatment to enhance the hydrophilicity of cotton fabric. Through meticulous experimentation, we established a definitive connection between the contact angle, exposure time, and the choice of gas. The findings revealed a noteworthy transformation of the cotton fabric's hydrophilic properties, with a remarkable impact discernible within a mere 5 s of exposure. Additionally, the environmentally friendly aspect of this approach is underscored by its dry process nature, eliminating the necessity for traditional wet chemical methods. plasma treatment showcases its potential as a sustainable technique within the textile industry. In summary, our study underscores the effectiveness of

plasma treatment in converting cotton fabric into a more hydrophilic material. The intricate interplay between contact angle, exposure time, and gas selection, combined with the rapid response observed in short timeframes, presents a promising avenue for fabric enhancement in scientific and industrial realms.

References

[1] S. Black, **"Trends in Smart Medical Textiles"**, Woodhead (Cambridge, 2007) pp. 3-26.
[2] Y. Qin, **"Medical Textile Materials"**, Elsevier, Woodhead (2016).
[3] A. Soleimani-Gorgani and Z. Karami, "The effect of biodegradable organic acids on the improvement of cotton ink-jet printing and antibacterial activity", *Fibers Polym.*, 17(4) (2016) 512–520.
[4] D. Zhang et al., "Flame retardant and hydrophobic coatings on cotton fabrics via sol-gel and self-assembly techniques", *J. Colloid Interface Sci.*, 505 (2017) 892–899.
[5] I. Belhaj Khalifa and N. Ladhari, "Hydrophobic behavior of cotton fabric activated with air atmospheric-pressure plasma", *The J. Textile Inst.*, 111(8) (2020) 1191-1197.
[6] T. Makowski, "Hydrophobization of cotton fabric with silanes with different substituents", *Cellulose*, 27(1) (2020) 1-9.
[7] T. Igarashi and K. Nakamura, "Improvement of the Water Absorbency of Softener-treated Fabric: Addition of a New Hydrophilic Surface", *J. Oleo Sci.*, 70(4) (2021) 509-519.
[8] K.N. Pandiyaraj and V. Selvarajan, "Non-thermal plasma treatment for hydrophilicity improvement of grey cotton fabrics", *J. Mater. Process. Technol.*, 199(1-3) (2008) 130-139.
[9] S. Sfameni et al., "Functional Silane-Based Nanohybrid Materials for the Development of Hydrophobic and Water-Based Stain Resistant Cotton Fabrics Coatings", *Nanomater.*, 12(19) (2022) 3404.
[10] A.I. Susan, M. Widodo and M. Nur, "Corona Glow Discharge Plasma Treatment for Hidrophylicity Improvement of Polyester and Cotton Fabrics", *IOP Conf. Ser. Mater. Sci. Eng.*, 214 (2017) 012031.
[11] S. Ražić et al., "Hydrophilicity Improvement of Cellulose Based Materials by Plasma", 41th Int. Symp. on Novelties in Textiles, Ljubljana, Slovenia (August 2010).
[12] M. Prabaharan and N. Carneiro, "Effect of low-temperature plasma on cotton fabric and its application to bleaching and dyeing", *Indian J. Fiber Text. Res.*, 30 (2005) 68-74.
[13] W.S. Man, C.W. Kan and S.P. Ng, "The use of atmospheric pressure plasma treatment on enhancing the pigment application to cotton fabric", *Vacuum*, 99 (2014) 7-11.
[14] H. Nguyen Thi et al., "Application of Plasma Activation in Flame-Retardant Treatment for Cotton Fabric", *Polymers (Basel)*, 12(7) (2020) 1575.
[15] R.S. Hebbar, A.M. Isloor and A.F. Ismail, "Contact Angle Measurements", in **Membrane Characterization** (Elsevier, 2017), pp. 219-255.
[16] E. Stoffels et al., "Plasma needle: a non-destructive atmospheric plasma source for fine surface treatment of (bio)materials", *Plasma Sourc. Sci. Technol.*, 11(4) (2002) 383-388.
[17] M. Laroussi and F. Leipold, "Evaluation of the roles of reactive species, heat, and UV radiation in the inactivation of bacterial cells by air plasmas at atmospheric pressure", *Int. J. Mass Spectrum*, 233(1-3) (2004) 81-86.
[18] H.Y. Erbil, "The debate on the dependence of apparent contact angles on drop contact area or three-phase contact line: A review", *Surf. Sci. Rep.*, 69(4) (2014) 325-365.
[19] Y.K. Jabur, M.Gh. Hammed and M.K. Khalaf, "DC Glow Discharge Plasma Characteristics in Ar/O_2 Gas Mixture", *Iraqi J. Sci.*, 62(2) (2021) 475-482.
[20] P.M. Bellan, **"Fundamentals of Plasma Physics"**, Cambridge University Press (2006).
[21] F.F. Chen, **"Introduction to Plasma Physics and Controlled Fusion"**, Cham: Springer International Pub. (2016), pp. 183-202.
[22] T.A. Hameed and S.J. Kadhem, "Plasma diagnostic of gliding arc discharge at atmospheric pressure", *Iraqi J. Sci.*, 60(12) (2019) 2649–2655.
[23] D. Williams et al., "Computerised Measurement of Contact Angles", *Galvanotechnik*, 101(11) (2010) 2502-2512.
[24] B. Onyenucheya et al., "Characterization of a nonthermal plasma torch", *IEEE Pulsed Power Conference* (2009), pp. 1022-1024.
[25] S.D. Anghel et al., "A very low temperature atmospheric-pressure plasma jet in a single electrode configuration", *Romanian J. Phys.*, 56 (2011) 90-94.
[26] J.E. Sansonetti and W.C. Martin, "Handbook of basic atomic spectroscopic data", *J. Phys. Chem. Ref. Data*, 34(4) (2005) 1559-2259.
[27] T. Shimizu et al., "Characterization of Microwave Plasma Torch for Decontamination", *Plasma Process. Polym.*, 5(6) (2008) 577-582.
[28] X. Fei, "Characterization, comparison and application of two types of atmospheric pressure cold argon plasma jets", Ph.D. thesis, Gunma University (2011).
[29] N. Şahin and M. Tanışlı, "Electron temperature estimation of helium plasma via line intensity ratio at atmospheric pressure", *The Euro. Phys. J. Plus*, 135(8) (2020) 653.
[30] H.Q. Farag and S.J. Kadhem, "Study the Effect of Dielectric Barrier Discharge (DBD) Plasma on the Decomposition of Volatile Organic Compounds", *Iraqi J. Phys.*, 20(4) (2022) 45-53.
[31] H.B. Baniya et al., "Cold Atmospheric Pressure Plasma Jet for the Improvement of Wettability of Polypropylene", *Int. J. Polym. Sci.*, 2020 (2020) 1-9.
[32] E. Nithya et al., "Synergetic effect of DC air plasma and cellulase enzyme treatment on the hydrophilicity of cotton fabric", *Carbohydr. Polym.*, 83(4) (2011) 1652-1658.
[33] B. Ghimire, D.P. Subedi and R. Khanal, "Improvement of wettability and absorbancy of textile using atmospheric pressure dielectric barrier discharge", *AIP Adv.*, 7(8) (2017) 085213.

 ISSN (print) 1813-2065, (online) 2309-1673

IRAQI JOURNAL OF APPLIED PHYSICS
Vol. 19, No. 4C, December 2023, pp. 211-216

Enhanced Fatigue Characteristics of Aluminum Alloy 6082 Reinforced with SiC Nanoparticles

Maha N. Abdulridah

Department of Electrical Engineering, University of Technology, Baghdad, IRAQ

This study investigates the fatigue characteristics of nanocomposites comprising an aluminum alloy 6082 matrix reinforced with 3 wt.% SiC particles. The investigation focused on assessing the constant fatigue strength and fatigue life of these nanocomposites under two distinct testing conditions. At room temperature, the fatigue strength improvement factor exhibited a remarkable improvement, rising from 3.5% to 5.4% for low cycles (10^3) and high cycles (10^5), respectively. Under elevated temperature conditions, the nanocomposite displayed an even greater enhancement, with fatigue strength improvement factor (FSIF) values of 0.69% and 11.37% for 10^3 and 10^5 cycles, respectively. These results indicate that the incorporation of nanoreinforced materials significantly bolstered fatigue endurance, with the nanocomposite exhibiting increased fatigue strength from 33.3 to 35.8 MPa at RT and from 27.4 to 33.7 MPa at 500°C for high cycles (10^7) tests. This improvement in fatigue behavior is attributed to the unique combination of the aluminum alloy 6082 matrix and the dispersed particles, which were effectively, synthesized using the stir casting technique.

Keywords: Nanocomposites; Thermal Fatigue; Endurance Fatigue Limit; FSIF
Received: 24 August 2023; **Revised:** 13 September 2023; **Accepted:** 20 September 2023

1. Introduction

Aluminum alloys are renowned for their exceptional properties, encompassing high resistance to corrosion, efficient thermal conductivity, satisfactory strength characteristics, recyclability, ductility, durability, and notably, low density. These attributes render aluminum highly versatile and extensively employed in various industrial domains, including aerospace, architectural construction, marine industries, and notably, automotive applications [1].

Industries seek substitute engineered materials, including composites made from matrix and reinforcement materials. Metal matrix composites (MMCs) have gained attention, with aluminum and its alloys being key focal points [2].

Mege-Revil et al the study demonstrates the use of a hybrid vapour deposition process to create TiSiAlN and TiSiN coatings on M2 steel. The process involves SiH4 precursors and metals via arc evaporation, resulting in a multilayered structure with a 700 nm period. The coatings show improved mechanical properties and oxidation resistance under various conditions. The addition of aluminum enhances oxidation resistance by forming an outer refractory alumina layer [3].

Zhang et al, examined the thermomechanical characteristics of coatings made of TiSin and TiSinAlN nanocomposites and compared these characteristics to thermal fatigue. Under isothermal, dynamic, and cycling (10 cycles rms 25-800-25°C) conditions, the fatigue resistance was examined. Thermal cycling revealed that nanocomposites had high fatigue resistance while base metals without nanoparticles had decreased resistance [4].

Divaga et al. investigated the impact of nano-sized particles reinforcement on the fatigue life of AA7075-T651 grade aluminum alloy-based metal matrix nanocomposites (MMNCs) produced through an emerging stir casting process. The mechanical properties of the metal matrix composites were effectively enhanced by the addition of Nano particles compared to micron-level particles, owing to their bonding nature. SiC nanoparticles were incorporated into the parent metal at three different volume fractions, namely 5%, 10%, and 15%, along with a constant nano Al_2O_3 fraction of 5%, resulting in the formation of nanocomposites. The findings of this study offer valuable perspectives on how dual nano-sized particles reinforcement impacts the fatigue performance of aluminum alloy-based MMNCs, holding significant potential for enhancing the mechanical properties and performance of advanced engineering applications [5].

In the current work, the constant fatigue behavior of Al6082 alloy 3wt.% SiC nanocomposite reinforced was investigated. A comparison between the fatigue strength and life for the above composite with the base metal (matrix) was made.

2. Experimental Investigation

2.1 Material selection

Aluminum alloy 6082 is commonly used due to its favorable mechanical properties and lightweight

nature. This alloy is commonly employed in aerospace applications highly stressed structural applications, and other areas where extremely high strength is needed [6,7]. Table (1) shows chemical composition of 6082 aluminum alloy and table (2) shows the mechanical properties for base metal.

Table (1) Chemical composition of base metal 6082Al alloy

Element	6082 Standard Ref. [7]	6082 Experimental
Zn	0.2%	0.17
Mg	0.6-1.2%	0.98
Cu	0.1	0.087
Si	0.7-1.3%	1.07
Fe	0.5%	0.45
Mn	0.4-1%	0.7
Cr	0.25%	0.23
Ti	0.1	0.08
Al.	Bal.	Bal.

Table (2) Mechanical properties of Al 6082 alloy [7]

Conditions	σ_u (Mpa)	σ_y (Mpa)	Hardness BHN	Modulus of Elasticity (GPa)
AA 6082 /0 wt.%	140	85	40	69

2.2 Composites Preparation

The nanocomposite was fabricated using the stir casting method, a well-established technique for incorporating nanoparticles into a metal matrix. Before being included into the melting aluminum alloys, the SiC reinforced particles were heated to a temperature of 200°C. 450 revolutions per minute and 850°C were the stirrer velocity and temperature predictions, respectively. The manufacturing process involved the following several steps, each meticulously performed to ensure the quality and homogeneity of the resulting material. More information regarding the development of the composites rig used to create the composite can be found in Ref. [8].

2.3 Fatigue Test

The specimens of the fatigue test were prepared according to the Machines manual as shown in Fig. The specimens were manufactured and tested to generate the S-N curve by an alternating bending specification of fatigue test machine (rotating bending fatigue testing machine).

The application stress is calculated from the applied moment according to the simple theory of a cantilever beam as:

$$\sigma = 1281 \frac{P}{d^3} \quad (1)$$

where σ is the bending stress in (MPa), P is the force in (N), and d is the minimum diameter of the specimen (mm)

In this research, constant fatigue tests were conducted in a laboratory setting using a rotary fatigue bending rig, subjecting the specimens to a stress ratio of R=-1. Failure was determined by the fracturing of the fatigue specimen into two separate pieces, at which point the fatigue testing process automatically ceased. The number of stress cycles endured by the specimens until failure was meticulously recorded using a mechanical counter, which directly interfaced with the drive shaft of the dc motor responsible for conducting the fatigue tests. The experimental setup for these fatigue tests was specifically designed and carried out at the Department of Electromechanical Engineering, University of Technology, Baghdad. The laboratory facilities provided a controlled environment for accurate data collection and analysis.

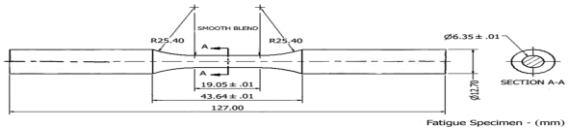

Fig. (1) Rotating bending fatigue specimen (cantilever beam)

The rigorous experimental setup and the utilization of specialized equipment, such as the rotary fatigue bending rig and the mechanical counter, contributed to the accuracy and reproducibility of the results. This approach ensures that the fatigue behavior of the specimens was thoroughly investigated, providing valuable insights for understanding material performance and design considerations in various engineering applications.

2.4 Thermal Device

To investigate fatigue behavior at elevated temperatures, a specialized thermal device was employed to precisely control the environmental temperature surrounding the test specimens. For this purpose, an electric furnace was custom-manufactured, featuring dimensions of 100×120×140mm, tailored to accommodate the specimens within its controlled heating environment. The furnace was thoughtfully designed to seamlessly integrate with the testing machine, and a digital thermal control unit board facilitated accurate temperature regulation the performance of a temperature control system is affected by a number of components. To ensure effective insulation and uniform heating, the furnace was constructed with two layers of steel plate, each with a thickness of 3 mm. This design choice minimized heat loss and provided a stable thermal environment for the specimens. An electric heater with a power rating of 2000W was securely installed inside the furnace, serving as the primary heating element. To monitor and control the internal heating temperature, a K-type thermocouple was strategically positioned within the furnace [9].

The integrated thermal control system enabled precise adjustment of the furnace temperature, allowing the researchers to subject the specimens to targeted elevated temperatures during the fatigue tests. The capability to conduct fatigue tests at elevated temperatures is particularly essential for

 ISSN (print) 1813-2065, (online) 2309-1673

evaluating materials' performance under high-temperature operating conditions, as experienced in various industrial applications. Fig.) showcases the furnace and digital thermal control unit board, visually depicting the setup utilized for the elevated temperature fatigue tests. This illustration provides a comprehensive view of the sophisticated equipment employed to ensure the accuracy and reliability of the experimental data.

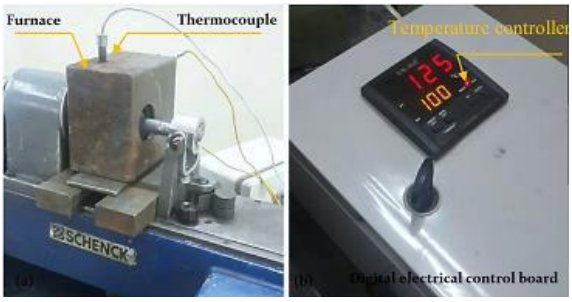

Fig. (2) Furnace attached to fatigue machine with control board

By employing this advanced thermal device and controlling the testing conditions with great precision, the researchers were able to assess the fatigue behavior of the specimens under elevated temperatures, shedding light on material performance at high operating conditions. The detailed design and construction of the electric furnace, combined with the sophisticated thermal control system, enhance the experimental setup's validity and the reliability of the findings obtained in this study.

3. Results and Discussions

3.1. Constant Amplitude Fatigue Results

The specimens were tested under constant amplitude fatigue stress rotating bending with a stress ratio R=-1 at room temperature and for high temperatures 500°C, to estimate the S-N curves. The results of aluminum alloy 6082 are given in table (3). Basquin equations were obtained from best fitting using interpolation in Excel. Figure (3) shows applied stress changes with number of cycles. According to Basquin equation

$$\sigma_f = M\,(N_f)^n \qquad (2)$$

where M and n are material constants.

The obtained results indicate a notable degree of correlation between the above equation and the experimental data, as evident from the high value of the coefficient of determination (R2). This high correlation coefficient provides substantial evidence supporting the suitability of the Basquin equation in accurately describing and explaining the recorded experimental data.

The successful correlation of the experimental data with the Basquin equation underscores the efficacy of this model in characterizing fatigue behavior under the specific testing conditions. Such validation is vital in ensuring the accuracy and reliability of the fatigue analysis, which, in turn, facilitates the understanding of material responses and the prediction of fatigue life. The data presented in Fig. (3) elucidates the advantageous effects of nanomaterial reinforcement on the fatigue strength of the tested specimens over different cycles. These enhancements in fatigue performance may be attributed to the unique strengthening mechanisms induced by the nanomaterials, including grain refinement, dislocation pinning, and interfacial strengthening. Such improvements hold significant promise in optimizing material performance in critical engineering applications, where fatigue resistance is of paramount importance.

Table (3) S-N curve results of Al6082 at four cases

Al6082 Best Zero			
Applied Stress (σ_f) MPa	No. of average cycle to Failure, Nf_{av}	Basquin equation	R^2
60	120300	$\sigma_f = 307.96\,(N_f)^{-0.138}$	0.97
70	40320		
80	24500		
100	3010		
Al6082 Best Nano 3% SiC at R.T.			
Applied Stress (σ_f) MPa	No. of average cycle to Failure, Nf_{av}	Basquin equation	R^2
60	210540	$\sigma_f = 310.13\,(N_f)^{-0.134}$	0.99
70	58250		
80	25540		
100	4523		
Al6082 Zero Nano at 500°C			
Applied Stress (σ_f) MPa	No. of average cycle to Failure, Nf_{av}	Basquin equation	R^2
60	80250	$\sigma_f = 338.11\,(N_f)^{-0.156}$	0.93
70	21030		
80	7050		
100	3730		
Al6082 Best Nano 3% SiC at 500°C			
Applied Stress (σ_f) MPa	No. of average cycle to Failure, Nf_{av}	Basquin equation	R^2
60	126300	$\sigma_f = 292.27\,(N_f)^{-0.134}$	0.98
70	55000		
80	14000		
100	3200		

Overall, the successful utilization of the Basquin equation and the clear demonstration of fatigue strength improvements resulting from nanomaterial reinforcement contribute to the advancement of knowledge in fatigue mechanics and the design of fatigue-resistant materials. These findings have implications in diverse industries, ranging from aerospace and automotive to structural engineering, where fatigue failure prevention is a crucial concern. The influence of incorporating 3 wt.% SiC nanoparticles on fatigue performance becomes clear when assessing the enhancement in fatigue strength. This improvement in fatigue strength can be calculated by the equation below [10]

$$\text{FSIF} = \frac{\sigma_{nano} - \sigma_{unreinforced}}{\sigma_{unreinforced}} * 100\% \qquad (3)$$

Tables (4) and (5) present a comprehensive summary of the improvements in fatigue strength observed at both 10^3 and 10^5 cycles, attributed to the incorporation of nanomaterial reinforcements. The tables showcase the quantitative enhancements in fatigue performance achieved through the addition of these nanomaterials.

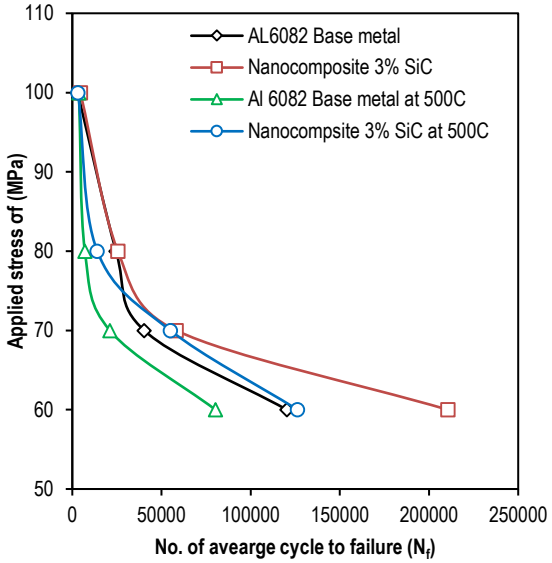

Fig. (3) S-N curves behaviors for four cases of testing

Table (4) Dry Fatigue without and with 3 wt.% SiC at 10^3 and 10^5 cycles

Cycles	10^3 cycles	10^5 cycles
Without nano (MPa)	118.7	62.88
With nano (MPa)	122.9	66.3
Fatigue Strength Improvement Factor (FSIF)	3.5%	5.4%

Table (5) Thermal fatigue without and with 3 wt.% SiC at 10^3 and 10^5 cycles

Cycles	10^3 cycles	10^5 cycles
Without nano (MPa)	115	56.1
With nano (MPa)	115.8	62.48
Fatigue Strength Improvement Factor (FSIF)	0.69%	11.37%

Based on the data presented in tables (4) and (5) and Fig. (4), a notable increase in fatigue life, from 10^3 to 10^5 cycles, correspondingly led to a significant rise in the FSIF, ascending from 3.5% to 5.4%. This observation demonstrates a direct correlation between fatigue life extension and FSIF enhancement. Notably, the influence of low cycle fatigue on FSIF appeared comparatively limited. This disparity can be attributed to the distinctive fatigue mechanisms at play under low cycle conditions, which may not exhibit the same magnitude of impact on the overall FSIF. In the context of thermal fatigue, a considerable improvement in fatigue strength was observed, increasing from 0.69% to 11.37%. This improvement was made possible by lowering the applied fatigue stress, which also led to higher FSIF values in both dry and thermal fatigue scenarios. These results demonstrate the importance of stress reduction in promoting enhanced fatigue performance, particularly in the setting of thermal fatigue conditions.

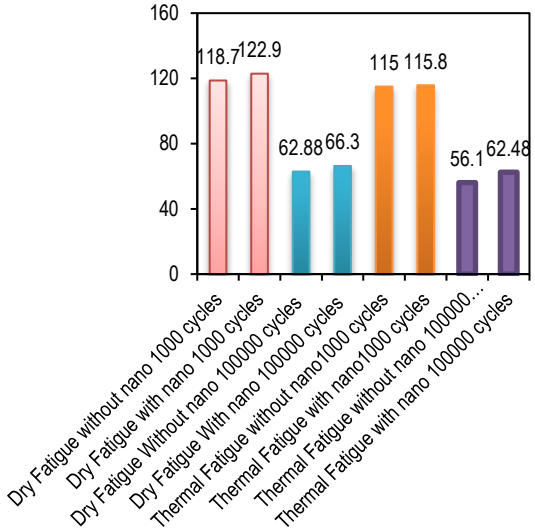

Fig. (4) S-N fatigue behaviors at 10^3 and 10^5 cycles

According to the experimental results, the fatigue strength improvement factor is an important statistic to evaluate the influence of many variables on fatigue behavior. It provides useful information about the material's ability to be cyclically loaded under different conditions and is an important factor in fatigue life prediction and material selection for difficult engineering applications. Furthermore, the outcomes underscore the effectiveness of incorporating nanocomposite reinforcement, as discussed in the previous sections, in enhancing fatigue properties, thus accentuating the potential of these advanced materials in fatigue-critical applications across various industries. Additionally, the exploration of thermal fatigue behavior demonstrates the importance of considering operating conditions, as they can significantly impact the fatigue performance of materials in real-world applications subject to varying thermal environments.

3.2. Endurance fatigue limit at 10^7 cycles

The improvements in fatigue performance achieved through the addition of SiC nano-reinforcements are particularly prominent when the material is subjected to low applied stress levels, typical of high cycle fatigue conditions. Under such circumstances, the smaller grain size induced by the nano-reinforcements acts as a barrier to fatigue crack initiation and propagation, effectively retarding the onset of failure and prolonging the material's fatigue life. In contrast, the impact of the nanoreinforcements is less pronounced under high applied stress conditions, characteristic of low-cycle fatigue.

 ISSN (print) 1813-2065, (online) 2309-1673

Table (6) and figure (5) offer endurance fatigue limit at 10^7 cycles and an improvement factor of material Al6082 reinforced with 3 wt.% SiC. By leveraging the advantages of nanoreinforcements, researchers and engineers can advance the development of advanced materials tailored to meet the stringent demands of fatigue-critical applications in industries such as aerospace, automotive, and structural engineering. Additionally, the study of the endurance fatigue limit at 10^7 cycles provides a useful guide for material selection and design considerations, assuring long-term performance and reliability in high-stress conditions. Elevated temperatures have been observed to detrimentally affect on the fatigue properties of composites, leading to a considerable degradation in endurance fatigue and a reduction in fatigue life [11].

Table (6) Endurance fatigue limit at room temperature and at 500°C

Conditions	Endurance Fatigue at 10^7 cycles	Improvement Factor
Al 6082 Best Zero at R.T	33.3 MPa	7.4%
Al 6082 Best Nano 3% SiC at R.T	35.8MPa	
Al 6082 Zero nano at 500°C	27.4 MPa	23.2%
Al6082 Best Nano 3% SiC at 500°C	33.7 MPa	

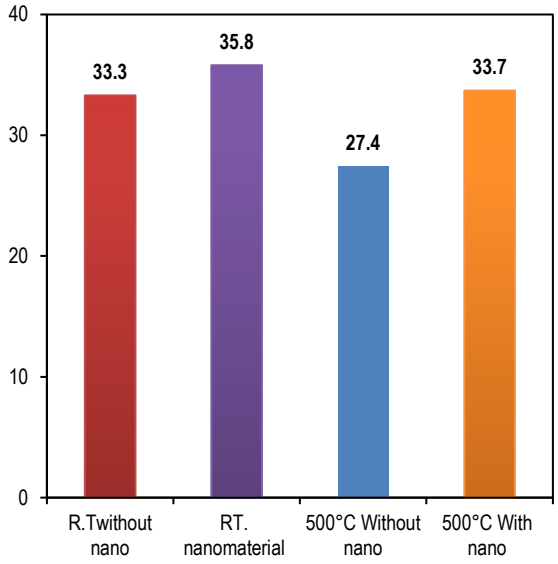

Fig. (5) Comparison between endurance fatigue

The experimental results presented in table (6) corroborate the findings of numerous studies, which consistently report a decrease in fatigue life with increasing testing temperature [12]. The data in table (6) clearly highlight the remarkable influence of temperature on the endurance fatigue limit of the composite.

The addition of nanoreinforcements in the form of SiC has proven to be effective, significantly improving the fatigue strength of the composite at 10^7 cycles. At room temperature, the fatigue strength increases from 33.3 to 35.8 MPa with an improvement ratio of 7.4%, whereas at 500°C, the fatigue strength increases from 27.4 to 33.7 MPa with an improvement factor of 23.2%. This improvement in fatigue endurance can be related to the unique qualities of nanoreinforcement, especially its high hardness and excellent mechanical properties [13]. The addition of nanosized SiC particles to the composite improves its resistance to fatigue crack initiation and propagation, resulting in better endurance fatigue and fatigue life. The outcomes of the present research highlight the importance of taking temperature effects into consideration when evaluating the fatigue performance of composites. Moreover, the incorporation of nanoreinforcements, such as Silicon carbide particles, offers a promising avenue for enhancing the fatigue resistance and endurance of composites, making them more suitable for demanding engineering applications subjected to cyclic loading and elevated temperatures.

These insights contribute to advancing the understanding of fatigue behavior in composite materials, enabling the development of novel and durable materials tailored to meet the challenges of fatigue-critical applications in diverse industries. By comprehending the mechanisms governing fatigue strength and endurance, researchers and engineers can optimize material design and selection, ensuring reliable and high-performance components in aerospace, automotive, and structural engineering, among other fields.

4. Conclusion

The present study focused on investigating the constant S-N curves fatigue strength and life of 6082Al alloy reinforced with 3 wt.% SiC under rotating bending loading conditions. From the comprehensive analysis, several key conclusions can be drawn. The addition of 3 wt.% SiC nanoreinforced material significantly improved the fatigue strength improvement factor (FSIF) of a composite, with values at room temperature and 500°C reaching 3.5% and 11.37% respectively. This highlights the nanoreinforced material's beneficial influence on composite fatigue behavior. The endurance fatigue limit of the nanocomposite showed significant improvements at both room and elevated temperatures, with a 7.4% increase at room temperature and 23.2% increase at 500°C, These significant enhancements underscore the advantageous effects of the 3 wt.% SiC nanoreinforcements in elevating the fatigue performance of the composite at both room and elevated temperatures. The outcomes of this study provide valuable insights into the fatigue behavior of 6082Al alloy reinforced with SiC nanoreinforcements, with implications for the design and optimization of high-performance materials in engineering applications. The observed improvements in fatigue strength and endurance fatigue limit emphasize the potential of nanocomposite materials for enhancing fatigue

resistance and durability, particularly in demanding environments subject to cyclic loading and varying temperatures. These findings contribute to the growing body of knowledge in the field of composite materials and pave the way for further advancements in fatigue-resistant materials for aerospace, automotive, and structural applications, among others.

References

[1] B. Stojanovic, M. Bukvic and I. Epler, "Application of aluminum and aluminum alloys in engineering", *Appl. Eng. Lett. J. Eng. Appl. Sci.*, 3(2) (2018) 52-62.
[2] M.A.A. Al-Jaafari, "Study the effects of titanium dioxide nano particles reinforcement on the mechanical properties of aluminum alloys composite", *IOP Conf. Ser.: Mater. Sci. Eng.*, 1105(1) (2021) 012062.
[3] A. Mège-Revil et al., "Correlation between thermal fatigue and thermomechanical properties during the oxidation of multilayered TiSiN nanocomposite coatings synthesized by a hybrid physical/chemical vapour deposition process", *Thin Solid Films*, 518(21) (2010) 5932-5937.
[4] X.P. Zhang et al., "Thermal Fatigue and Creep Fracture Behaviors of a Nanocomposite Solder in Microelectronic/optoelectronic Packaging", *Key Eng. Mater.*, 312 (2006) 237-242.
[5] S. Divagar, M. Vigneshwar and S.T. Selvamani, "Impacts of nanoparticles on fatigue strength of aluminum based metal matrix composites for aerospace", *Mater. Today: Proc.*, 3(10) (2016) 3734-3739.
[6] R.K. Sahu et al., "Effect on Mechanical and Structural Properties of Rolled Aluminum Alloy 6082 by Using Friction Stir Processing with Silicon Carbide as Particulate Matter", *Int. J. Appl. Eng. Res.*, 14(14) (2019) 3301-3303.
[7] "International Alloy Designations and Chemical Composition Limits for Wrought Aluminum and Wrought Aluminum Alloys", The Aluminum Association (January 2015).
[8] M.N. Abdulridah, A.D. Assi and H.J. Al-Alkawi, "Influence of cryogenic temperature (CT) on tensile properties and fatigue behavior of 2024-Al_2O_3 nanocomposites", *IOP Conf. Ser.: Mater. Sci. Eng.*, 765(1) (2020) 012052.
[9] A.A. Mohammed, H.J. Al-Alkawi and F.A.F. Al-Bayati, "Prediction of Fatigue-Creep Interaction Life of Aluminum and Copper Alloys Using Electromechanical Devices", M.Sc. thesis, University of Technology (2014).
[10] H.J.M. Alalkawi, A.Y.K. Khenyab and A.H. Ali, "Improvement of Mechanical and Fatigue Properties for Aluminum Alloy 7049 By Using Nano Composites Technique", *Al-Khwarizmi Eng. J.*, 15(1) (2019) 1-9.
[11] W.V. Mars and A. Fatime, "Factors that Affect the Fatigue Life of Rubber. A Literature Survey", *J. Rubb. Chem. Technol.*, 77(3) (2004) 391-412.
[12] H.J. Al-Alkawi, F.A. Kareem and A.A.M. Ali, "Prediction of Fatigue-Creep Interaction Life of Aluminum Alloy AA7349 Using Electromechanical Devices", *Eng. Technol. J.*, 33(3A) Eng.,(2015) 535-547.
[13] R. Thimmarayan and G. Thanigaiyarasu, "Effect of particle size, forging and ageing on the mechanical fatigue characteristics of Al6082/SiC p metal matrix composites", *The Int. J. Adv. Manufact. Technol.*, 48 (2010) 625-632.

 ISSN (print) 1813-2065, (online) 2309-1673

IRAQI JOURNAL OF APPLIED PHYSICS
Vol. 19, No. 4C, December 2023, pp. 217-222

Comprehensive Investigation of Morphological, Structural, and Optical Properties of NiO:Al Films Prepared by Thermal Evaporation

Nariman M. Ibraheem
Sabri J. Mohammed

Department of Physics, College of Education for Pure Sciences, University of Tikrit, Tikrit, IRAQ

In this study, aluminum-doped nickel oxide (NiO) thin films were prepared by vacuum thermal evaporation technique on glass substrates. The structural and spectroscopic characteristics of these films were determined and analyzed. Adding 6 wt.% of aluminum has transformed the crystalline structure of nickel oxide layer into a polycrystalline phase. Uniform grains were produced in the undoped NiO films while the doping with aluminum has reduced the particle size by 6%. Surface topography changes were also observed. The spectroscopic properties have revealed a 65% visible image transmission rate, tied to an adjustable energy gap from 3.81 to 3.89 eV with increasing doping ratio. This study unveils the interplay between composition, morphology, and optics, promising versatile applications of NiO thin films doped with metal like aluminum.

Keywords: Nickel oxide; Thin films; Vacuum thermal evaporation; Optical properties
Received: 31 July 2023; **Revised:** 14 September 2023; **Accepted:** 21 September 2023

1. Introduction

Metal oxide thin films have become the focus of many studies in recent years in view of their electrical properties, stability at high temperature and durability. Many researchers have studied metal oxide thin films as electronic materials due to their structural simplicity and low cost [1-5]. However, in order to improve such devices the surface defects and the characteristics of thin films prevailing in film fabrication processes need to be carefully understood [6,7]. Transparent conducting oxides (TCOs) denote a class of oxide materials that simultaneously exhibit high electrical conductivity and optical transparency to visible light [8,9]. TCOs are critical to numerous state-of-the-art technological applications, ranging from touchscreen screens, flat panel displays, and photovoltaic cells to light emitting diodes and transparent electronics [10-12]. However, the properties of electrical conductivity and optical transparency are mutually exclusive and there is a challenge to combine them. Nickel oxide is p-type semiconductor material and is widely used in different applications such as transparent conductive films and electrochromic devices, as a potential candidate in the chemical sensors [13,14]. NiO exhibits a wide bandgap of 3.6–4.0 eV at room temperature; thus, NiO is considered transparent in the visible light region [15,16]. Moreover, NiO is largely used as a cocatalyst with different n-type semiconductors due its high p-type concentration, high hole mobility and low cost. The existence of NiO enhances the separation of electron and hole pairs via electric junction field and also promotes the interfacial charge transfer [17,18]. Nanoscale NiO structures NiO thin films can be made using a variety of techniques, such as spraying, spray pyrolysis, the sol-gel process, chemical vapor deposition, electron beam evaporation, molecular beam inflation, and electroposition [19-22]. We will primarily focus on thermal evaporation under vacuum among these technologies in this work because of its several advantages, including its ability to produce extremely clean films, excellent surface areas, and great crystalline regularity [23-26].

In this paper, the nickel oxide thin films were fabricated by vacuum thermal evaporation on glass substrate. The effect of the aluminum doping ratio on the structural, surface morphology and optical properties has been investigated.

2. Experimental procedures

Powders of nickel and aluminum with 99.9% purity were used in this work. Aluminum was employed as an additive at a ratio of x=6 wt.% with respect to nickel, which served as the basis material (1-x). After adding the aluminum to the nickel, the components are blended in an agate mill for 30 minutes. The mixture is then put into a steel mold and pressed for 5 minutes at a pressure of 5 tons/cm^2, then dried in an oven.

Deionized water (DI), methanol, acetone, and isopropyl alcohol were used to clean the glass

substrates. Pure aluminized nickel powder was applied in weight ratios (0.6 wt.%) to the substrates on the sample holder and evaporation chamber. It was heated in a tungsten boat under a pressure of about $3.2x10^{-5}$ Torr and the films were extracted first from the device after deposition and then placed in a thermal oxidation furnace at a temperature of 400 °C for two hours to obtain pure Al-doped NiO films.

The prepared samples were characterized using Shimadzu XRD-6000 X-ray Diffractometer, Inspect TM F50 field-emission scanning electron microscope (FE-SEM), Nanosurf NaioAFM 2022 atmic force microscope, and Shimadzu UV-1800 UV/Visible Spectrophotometer.

3. Results and discussion

The undoped NiO thin films that were doped with aluminum were examined using the XRD analysis using an x-ray source with wavelength of 0.15406 nm. The range of diffraction angle (2θ) from 20° to 80° was considered for the XRD measurements. Additionally, Scherrer's formula was applied to the XRD pattern to determine the crystallite size (*D*) within the thin film structure as:

$$D(nm) = \frac{0.9\lambda}{\beta cos\theta} \quad (1)$$

where λ is the x-ray wavelength (0.154nm), β is the full-width at half maximum (FWHM), which is determined from the XRD pattern, and θ is the diffraction angle (peak position)

Figure (1) shows the XRD patterns of pure nickel oxide films doped with aluminum (6 wt.%). It is clear that all films were polycrystalline, and that the crystal system was of the cubic type. The peaks identifying nickel oxide appeared with crystalline directions (111), (200), (220), and (311), with average crystallite size of 62.18nm.

The addition of (6 wt%) Al, this percentage, increased the randomness of the composition, as this percentage of the addition overwhelmed and separated from the dominant substance. The atoms of the added substance have created their atomic levels within the crystal lattice of the base material, so the scattering of the X-rays falling at the atomic levels of each atom of the substance that has been added, and the base material will not be in the same phase, and this causes destructive partial interference, and thus the amplitude or peak intensity [27].

Figure (2) displays an FE-SEM picture of the NiO thin films, an EDS histogram, and a histogram of the crystal diameter distribution. According to the morphology study, the material's sedimentation coefficients allowed it to have a structure similar to sand crystals, and the average nanocrystal diameter was 20.27 nanometers. According to EDS, the film had a uniform distribution and was smooth. The proportions of oxygen and nickel were around 60% and 40%, respectively [28].

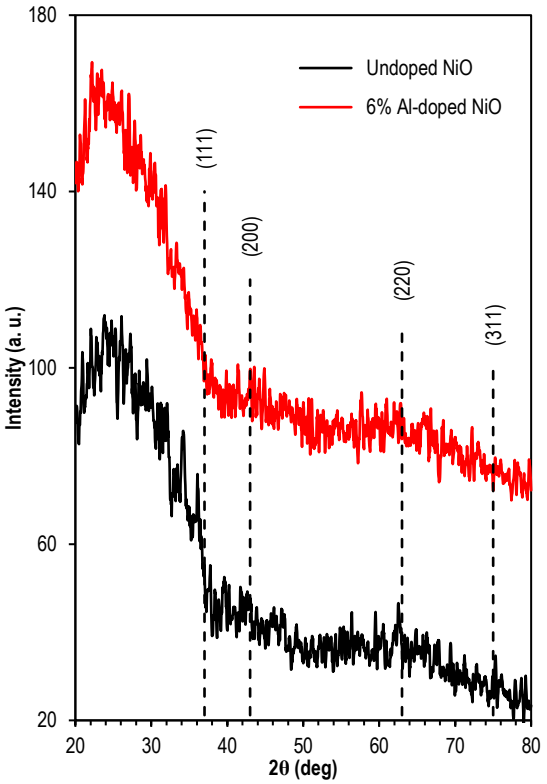

Fig. (1) XRD pattern of pure nickel oxide (NiO) films and doped aluminum by ratio (6%)

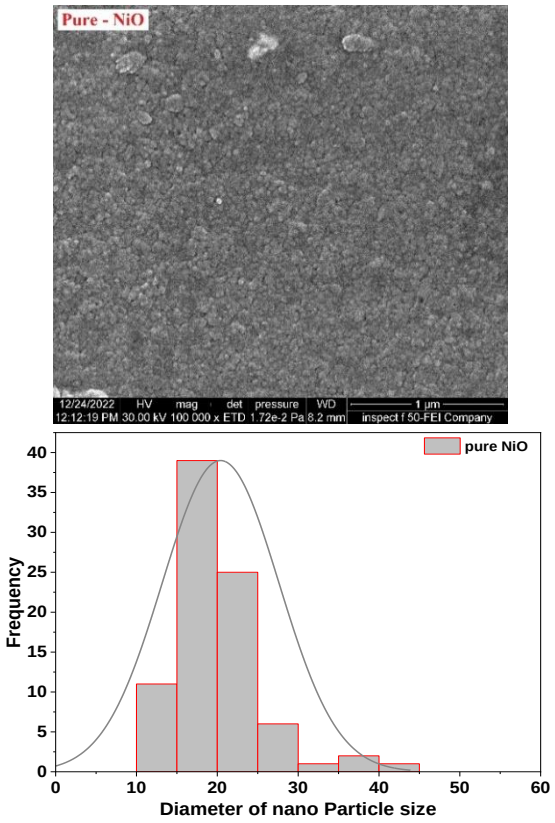

 ISSN (print) 1813-2065, (online) 2309-1673

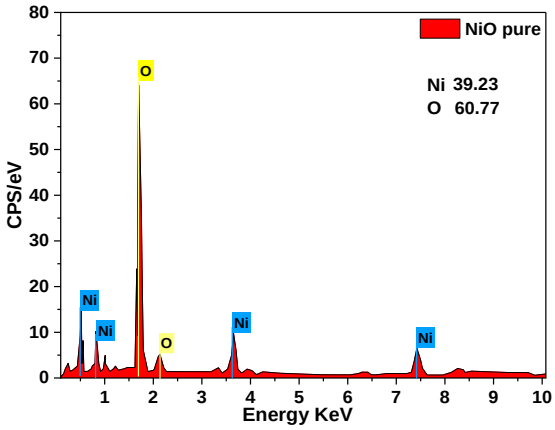

Fig. (2) FE-SEM images and EDS spectrum of NiO with histograms of diameters with Gaussian distribution

The results of the scanning electron microscopy of the neo-doping reaction with Al are shown in Fig. (3). Film analysis revealed that the doping had already occurred, as evidenced by the crystallization and agglomeration of nickel oxide, grain size reduction, and membrane surface cracking. An electron microscope magnification at a distance of 1 µm was used to obtain these results. For EDX, the doping ratios were very close to the ratios taken with a few drops, and the average grain size was between (15-17) nm [29].

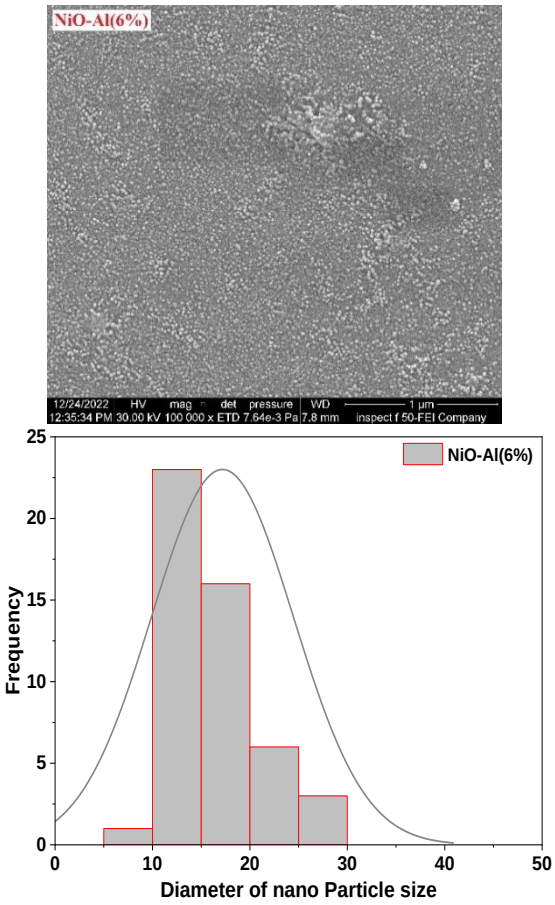

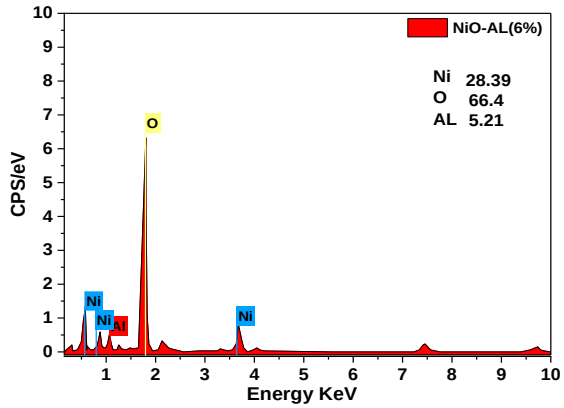

Fig. (3) FE-SEM images and EDS spectrum of NiO-Al(6%) with histograms of diameters with Gaussian distribution

After (AFM) analysis was used to examine the samples' surface morphologies, it became clear that NiO had a polycrystalline granular morphology with an average pore diameter depth and surface roughness. AFM analysis of pure and doped thin films is depicted in Fig. (4) as the results that were obtained.The 3D scans show that the nickel oxide surface layer is entirely coated with particles almost uniformly distributed over the surface.

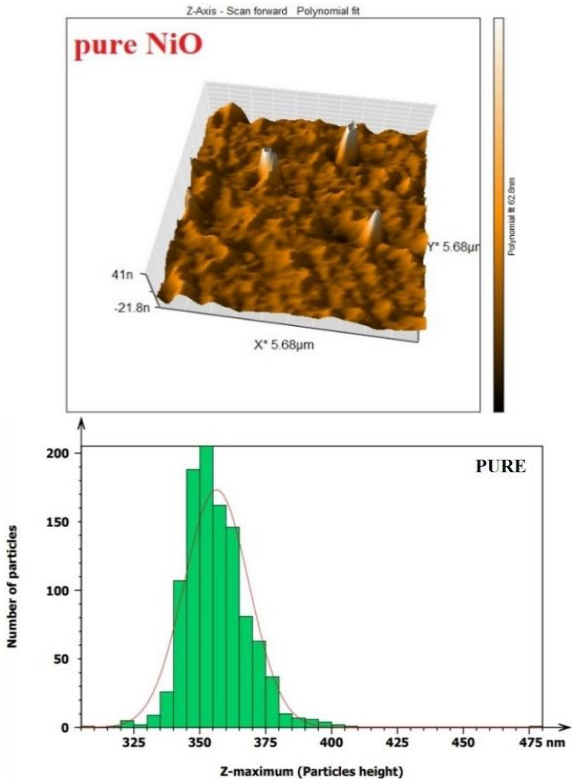

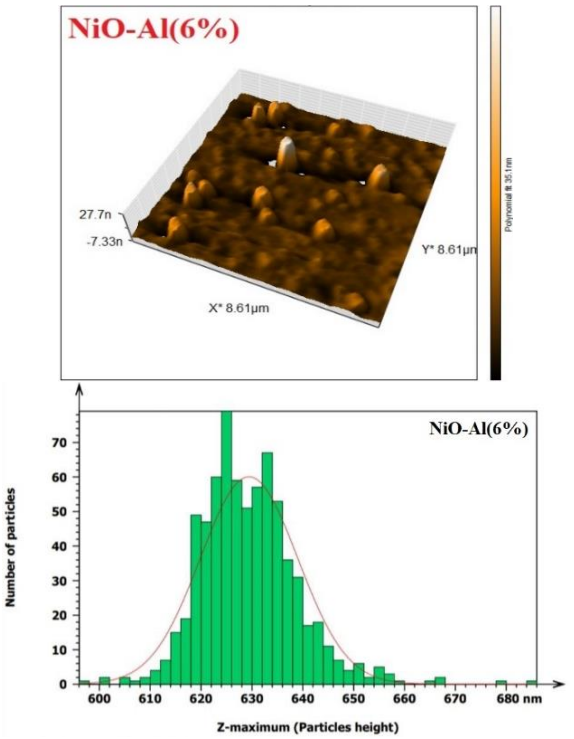

Fig. (4) 3D AFM images of pure NiO and NiO doped with 6 wt.% Al

The thin films in the 3D pictures show distinct vertical cone particles. It is noticeable that the NiO film has a modest surface roughness (5.46 nm), which can be due to minimal buildup in the material. The average surface roughness decreases by 3.37 nm, and the average peak size decreases from 41-26 nm when aluminum is added. An earlier study found that the presence of aluminum could reduce the surface's grain size and roughness [30].

Thin coatings on glass substrates were evaluated for their optical properties using the Shimadzu 1800-Japan spectrophotometer, which measures transmittance and absorption at wavelengths between 300 and 1100 nm. Equation (2) was used to determine the absorption coefficient as:

$$\alpha=2.303\left(\frac{A}{t}\right) \quad (2)$$

where A is absorption and t is the thin film thickness. Furthermore, equation (3) is used to determine the energy gap (E_g), as shown in Fig. (6)

$$(\alpha h\upsilon)^n = A\,(h\upsilon - E_g) \quad (3)$$

where $h\upsilon$ is the photon energy, A is a constant, and n is the index used to determine the type of spectral transition, which takes the value of 2 for the allowed direct transition

Figure (5) shows the UV-visible absorption spectra of undoped and Al-doped NiO (6 wt.%) thin films. It can be observed that the maximum absorbance is recorded at the wavelength of 404nm for undoped sample, while the absorbance of the films doped with 6 wt.% Al decreases due to the low absorption energies of the incident photons and their inability to excite the electrons from the valence band to the conduction band, as the relationship between wavelength and photon energy is inverse.

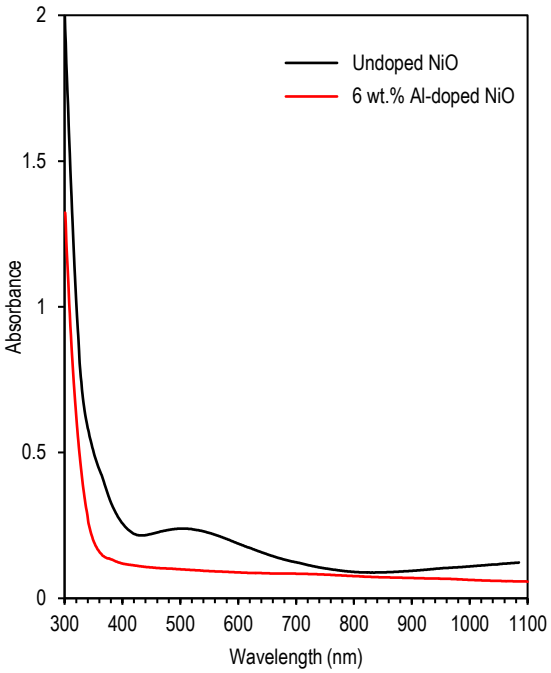

Fig. (5) Absorption spectra of undoped and 6 wt.% Al-doped NiO thin films

By plotting the $(\alpha h\upsilon)^2$ vs. photon energy ($h\upsilon$) and extrapolating the most linear part, the values and type of optical transition can be determind [31]. As shown in Fig. (6), the energy band gap (E_g) increases from 3.81 to 3.89 eV as the amount of Al dopants increases to 6 wt.%. Doping causes a decrease in the localized near-valence band (a drop in the optical energy gap due to crystallinity enhancement produced by an increase in the optical band gap) and an increase in the optical energy gap [32].

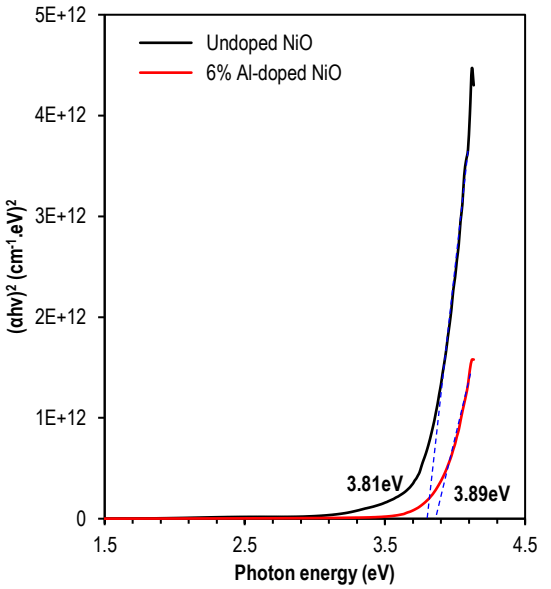

Fig. (6) determination of optical energy gap for undoped and 6 wt.% Al-doped NiO thin films

 ISSN (print) 1813-2065, (online) 2309-1673

4. Conclusions

In summary, this study provides valuable insights into Al-doped NiO thin films for photodetector applications. It was observed that increasing the aluminum doping ratio enhances substrate coverage, which serves thin film applications. The introduction of doping results in a 6% increase in the band gap, enabling tailored sensitivity to different light wavelengths. Additionally, while doping introduces disorder and defects, this may be leveraged to enhance specific photodetector characteristics. These findings suggest that Al-doped NiO films have the potential to advance photodetector technologies, offering versatility and tunable properties that can improve the efficiency and sensitivity of various photodetector devices, including diodes, transistors, and solar cells.

References

[1] S. Morphology, "Surface Morphology and Sensing Property of NiO-WO 3 Thin Films Prepared by Thermal Evaporation," pp. 519–528, 2005.
[2] M.A. Hameed, S.H. Faisal, R.H. Turki, "Characterization of Multilayer Highly-Pure Metal Oxide Structures Prepared by DC Reactive Magnetron Sputtering Technique", Iraqi J. Appl. Phys., 16(4) (2020) 25-30
[3] R.H. Turki and M.A. Hameed, "Spectral and Electrical Characteristics of Nanostructured NiO/TiO_2 Heterojunction Fabricated by DC Reactive Magnetron Sputtering", Iraqi J. Appl. Phys., 16(3) (2020) 39-42.
[4] A.M. Hameed and M.A. Hameed, "Highly-Pure Nanostructured Metal Oxide Multilayer Structure Prepared by DC Reactive Magnetron Sputtering Technique", Iraqi J. Appl. Phys., 18(4) (2022) 9-14.
[5] A.M. Hameed and M.A. Hameed, "Spectroscopic characteristics of highly pure metal oxide nanostructures prepared by DC reactive magnetron sputtering technique", Emergent Materials, 6 (2022) 627-633.
[6] P. Tan et al., "Growth of Al and Co co-doped NiO nanosheets on carbon cloth as the air electrode for Zn-air batteries with high cycling stability", Electrochimica Acta, 290 (2018) 21-29.
[7] V. Kampitakis et al., "Highly sensitive and selective NO_2 chemical sensors based on Al doped NiO thin films", Mater. Sci. Semicond. Process., 115 (2020) 105149.
[8] P. Baraskar et al., "Dispersive optical nonlinearities and optical path length compensation in NiO/Al doped NiO bilayer thin film", Opt. Mater., 96 (2019) 109278.
[9] L. Guo et al., "Al and W co-doped NiO nanoflowers with low crystallinity and rich oxygen vacancies for high stability and selective triethylamine detection", Sens. Actuat. B: Chem., 395 (2023) 134476.
[10] E. Fortunato, D. Ginley, H. Hosono, and D. C. Paine, "Transparent conducting oxides for photovoltaics," *MRS Bull.*, vol. 32, no. 3, pp. 242–247, 2007.
[11] T. Minami, "Transparent conducting oxide semiconductors for transparent electrodes," *Semicond. Sci. Technol.*, vol. 20, no. 4, p. S35, 2005.
[12] C. G. Granqvist, "Transparent conductors as solar energy materials: A panoramic review," *Sol. energy Mater. Sol. cells*, vol. 91, no. 17, pp. 1529–1598, 2007.
[13] O.A. Hammadi, M.K. Khalaf and F.J. Kadhim, "Fabrication of UV Photodetector from Nickel Oxide Nanoparticles Deposited on Silicon Substrate by Closed-Field Unbalanced Dual Magnetron Sputtering Techniques", Opt. Quantum Electron., 47(12) (2015) 3805-3813.
[14] M. Caglar et al., "Improving the electrical performance of NiO based photodiode fabricated by sol-gel process with Al doping", Sens. Actuat. A: Phys., 350 (20230 114099.
[15] Z.-W. Shang, H.-H. Hsu, Z.-W. Zheng, and C.-H. Cheng, "Progress and challenges in p-type oxide-based thin film transistors," *Nanotechnol. Rev.*, vol. 8, no. 1, pp. 422–443, 2019.
[16] N. Mironova-Ulmane, A. Kuzmin, I. Sildos, L. Puust, and J. Grabis, "Magnon and phonon excitations in nanosized NiO," *Latv. J. Phys. Tech. Sci.*, vol. 56, no. 2, pp. 61–72, 2019.
[17] F. J. Garc\'\ia-Garc\'\ia, P. Salazar, F. Yubero, and A. R. González-Elipe, "Non-enzymatic glucose electrochemical sensor made of porous NiO thin films prepared by reactive magnetron sputtering at oblique angles," *Electrochim. Acta*, vol. 201, pp. 38–44, 2016.
[18] G. S. Gund, C. D. Lokhande, and H. S. Park, "Controlled synthesis of hierarchical nanoflake structure of NiO thin film for supercapacitor application," *J. Alloys Compd.*, vol. 741, pp. 549–556, 2018.
[19] I. Manouchehri, D. Mehrparvar, R. Moradian, K. Gholami, and T. Osati, "Investigation of structural and optical properties of copper doped NiO thin films deposited by RF magnetron reactive sputtering," *Optik (Stuttg).*, vol. 127, no. 19, pp. 8124–8129, 2016.
[20] M. Karyaoui *et al.*, "Characterization of Ag-doped ZnO thin films by spray pyrolysis and its using in enhanced photoelectrochemical performances," *Inorg. Chem. Commun.*, vol. 119, p. 108114, 2020.
[21] X. Lou et al., "Electrochromic properties of Al doped B-subsituted NiO films prepared by sol–gel", Prog. Org. Coat., 64(2-3) (2009) 300-303.
[22] S. Tangwancharoen et al., "Dielectric and electrical properties of giant dielectric (Li, Al)-doped NiO ceramics", Mater. Chem. Phys., 115(2-3) (2009) 585-589.
[23] Y. M. Abdul-Hussein, H. J. Ali, L. A. Latif, M. A. Abdulsattar, and H. M. Fadhel, "Preparation of Al-doped NiO thin films by spray pyrolysis technique for CO gas sensing," *J. Adv. Pharm. Educ. \& Res. Jul-Sep*, vol. 9, no. 3, 2019.
[24] F. A. Garcés, N. Budini, J. A. Schmidt, and R. D.

Arce, "Highly doped ZnO films deposited by spray-pyrolysis. Design parameters for optoelectronic applications," *Thin Solid Films*, vol. 605, pp. 149–156, 2016.
[25] N.M. Khusayfan, "Electrical and photoresponse properties of Al/graphene oxide doped NiO nanocomposite/p-Si/Al photodiodes", J. Alloys Comp., 666 (2016) 501-506.
[26] M.N. Siddique, A. Ahmed and P. Tripathi, "Electric transport and enhanced dielectric permittivity in pure and Al doped NiO nanostructures", J. Alloys Comp., 735 (2018) 516-529.
[27] C. Wang *et al.*, "Design of superior ethanol gas sensor based on Al-doped NiO nanorod-flowers," *Acs Sensors*, vol. 1, no. 2, pp. 131–136, 2016.
[28] A. Paralikis, E. Gagaoudakis, V. Kampitakis, E. Aperathitis, G. Kiriakidis, and V. Binas, "Study on the ozone gas sensing properties of rf-sputtered Al-doped NiO films," *Appl. Sci.*, vol. 11, no. 7, p. 3104, 2021.
[29] M. Ul Haq *et al.*, "Humidity sensor based on mesoporous Al-doped NiO ultralong nanowires with enhanced ethanol sensing performance," *J. Mater. Sci. Mater. Electron.*, vol. 30, pp. 7121–7134, 2019.
[30] K. O. Ukoba, A. C. Eloka-Eboka, and F. L. Inambao, "Review of nanostructured NiO thin film deposition using the spray pyrolysis technique," *Renew. Sustain. Energy Rev.*, vol. 82, pp. 2900–2915, 2018.
[31] M. Arif, A. Sanger, P. M. Vilarinho, and A. Singh, "Effect of annealing temperature on structural and optical properties of sol--gel-derived ZnO thin films," *J. Electron. Mater.*, vol. 47, pp. 3678–3684, 2018.
[32] M. D. Devi *et al.*, "Improved UV Photodetection of Terbium-doped NiO thin films prepared by cost-effective nebulizer spray technique," *Mater. Sci. Semicond. Process.*, vol. 127, p. 105673, 2021.

 ISSN (print) 1813-2065, (online) 2309-1673

IRAQI JOURNAL OF APPLIED PHYSICS
Vol. 19, No. 4C, December 2023, pp. 223-228

Ghuzlan S. Ahmed
Bushra H. Hussein
Hanan K. Hassun
Ebtisam M-T. Salman
Rana Hameed Athab

Department of Physics, College of Education for Pure Sciences / Ibn Al-Haitham, University of Baghdad, Baghdad, IRAQ

Fabrication and Improvement of Optoelectronic Properties of Copper Chalcogenide Thin Films

Thin films from copper compound (Cu_2S) and Cu_2S doped with 5% Cd prepared by thermal evaporation have potential applications. High-quality Cu_2S thin films with thickness of 100 nm were deposited on glass and silicon substrates. They were engaged in evaluating the characteristics of films and their potential use as optoelectronic devices, specifically for solar cell applications. This study examines the structural, electrical, and optical properties of Cu_2S and Cu_2S:Cd 5% thin films. The x-ray diffraction analysis revealed that both films had a polycrystalline cubic structure with a lattice constant of 5.56Å as four sharp peaks were observed corresponding to the (220) planes. Both types of films have direct energy gap and the optical absorbance in the visible region was increasing for Cu_2S:Cd 5%. The mobility of the Cu_2S:Cd 5% films was higher than that of Cu_2S films. The results obtained from this study demonstrate that thermally evaporated Cu_2Se and Cu_2S:Cd 5% thin films can be utilized as potential materials for optoelectronic applications. The highest efficiency (1.56%) was obtained for heterojunction made from p-Cu_2S:Cd 5%/n-Si with thickness of 100nm at room temperature.

Keywords: Thin films; Cu_2S Solar cells; Conversion efficiency; Thermal evaporation
Received: 04 September 2023; **Revised:** 16 September 2023; **Accepted:** 23 September 2023

1. Introduction

Cu_2S is a semiconductor material among the important copper chalcogenides that have gained significant attention due to their unique optical, electrical, and thermoelectric properties [1,2]. These materials have a layered structure consisting of alternating layers of copper and chalcogen atoms (selenium or sulfur), and their properties are determined by the arrangement of the atoms in these layers and the interlayer bonding. Cu_2Se is a semiconductor with direct bandgap ranging from 2 to 3 eV, classified as a wide bandgap semiconductor, has high absorption coefficient, and strong light absorption [3]. In contrast, Cu_2S exhibits a narrow bandgap semiconductor behavior characterized by a direct bandgap ranging from 1.2-2.5 eV unlike Cu_2Se [4,5]. Cu_2Se has a high electron mobility and a low thermal conductivity which make it an attractive material for thermoelectric applications. It has a high thermal stability, making it suitable for high temperature applications [6]. It also has a low electron mobility and high thermal conductivity, making it less suitable for thermoelectric applications [7]. It is non-toxic and low-cost p-type semiconductor and good material for solar energy absorber [8,9]. The structure of Cu_2S thin films has a lattice parameter of a=5.564Å and a cubic crystalline structure [10]. The effect of different doping materials on characterization of Cu_2S were investigated by various researches such as the influence of zinc (Zn) doping [11] and aluminum (Al) doping on structural and optical properties of Cu_2S [12] by controlling the concentrations of copper by chemical bath deposition [13]. The properties of these materials can be controlled and optimized throughout Cu_2S various synthesis methods such as chemical bath deposition [14,15], modified chemical method [16], pulsed-laser deposition [17], reactive magnetron sputtering [18], consecutive ionic stratum adsorption and reaction [19], and chemical vapor deposition [20]. The main objective of this study is to focus on the effect of cadmium (Cd) dopants on the structural, optical and optoelectronic properties of Cu_2S films, as well as the influences associated with copper chalcogenide thin film materials, with a focus on the revision aspect.

2. Experimental Part

Copper(II) sulfide (Cu_2S) alloy and thin films have been prepared. The use of alloy in semiconductor applications has become increasingly popular due to their unique properties, such as improved electrical conductivity, enhanced optical properties, and improved mechanical strength. The preparation of alloys through thermal vacuum entails heating a vacuum chamber containing a high purity (99.99%) elemental copper, and sulfur material with a weight percentage ratio of 2:1. The heating process is carried out until the material reaches a temperature of 927°C for 8 hours. After that, it is cooled to room temperature (RT), evaporated and subsequently deposited onto a substrate to form a thin film.

The x-ray diffraction (XRD) is a powerful tool for characterizing the crystalline structure of thin films, and it has been widely used to study the structure of

 ISSN (print) 1813-2065, (online) 2309-1673

Cu_2S thin films by using Scherrer's formula and Bragg's law to calculate the crystallite size of such films [21,22]. Absorption spectroscopy is used for characterizing the optical properties of thin films, from 400 to1000 nm. Absorption spectra of Cu_2S and Cu_2S:Cd 5 wt.% thin films on glass substrates were used to determine the energy gap using the Tauc's equation [23,24]. The electrical conductivity of Cu_2S thin films was measured, and the carrier concentration, mobility, and conductivity type (n or p) of these films were determined using the Hall effect measurements throughout van der Pauw (Ecopia HMS 3000) technique. The conversion efficiency of a solar cell, which represents the ratio between the solar cell maximum power and incident light power (P_{in}), was calculated [25,26]. The formation of heterojunctions involved the synthesis of composite thin films, namely Cu_2S, deposited onto (111) single-crystalline (n-type) silicon to form two distinct interfaces (p-Cu_2S/n-Si).

3. Results and Discussion

In Fig. (1), we can observe the XRD patterns of Cu_2S alloy. The patterns exhibit four polycrystalline peaks corresponding to the reflections from (111), (200), (220), and (311) planes of the cubic phase, as confirmed by the ICDD card (00-053-0522) of Cu_2S. By examining the FWHM values of the (220) peak in the thin films depicted in Fig. (2), we can employ Scherrer's formula to estimate the crystallite size. The data presented in table (2) reveal that when copper sulfur is doped with cadmium, there is an increase in the crystallite size, suggesting a higher likelihood of material crystallization in the films, and the value of lattice constant is very close to what previously published [8,10]. The high degree of crystallinity in Cu_2S and Cu_2S:Cd 5 wt.% thin films is important for their optical, electrical, and thermoelectric properties. The smooth and homogeneous surfaces of the prepared films are also important for their application in various devices, such as solar cells and thermoelectric generators.

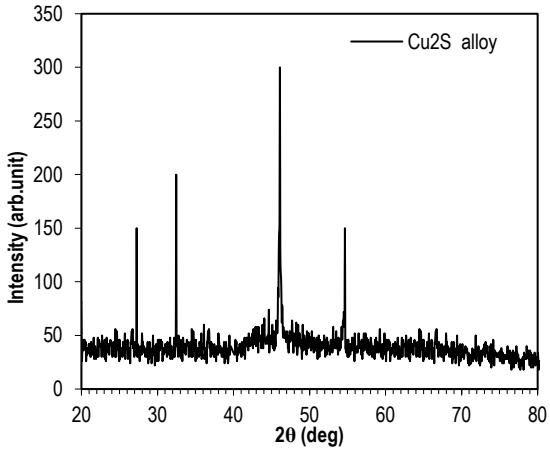

Fig. (1) The XRD pattern for Cu_2S alloy

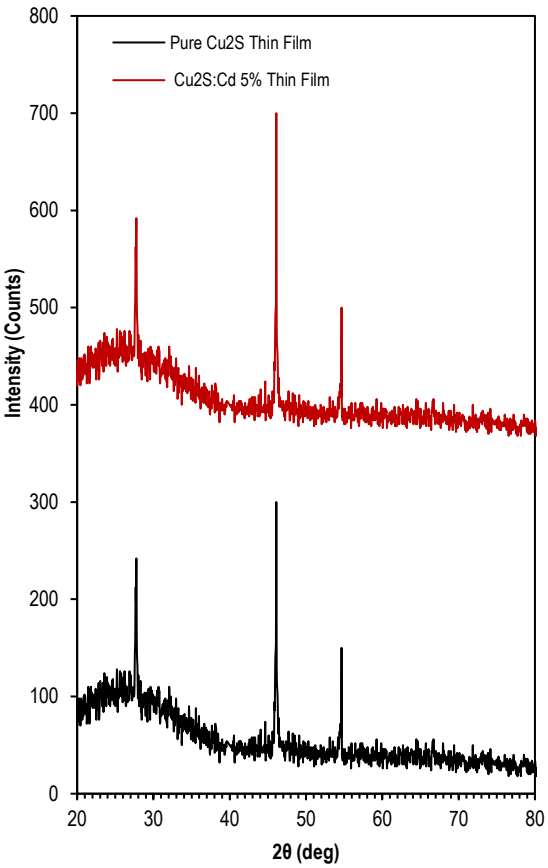

Fig. (2) XRD patterns of Cu_2S and Cu_2S:Cd 5 wt.% thin films

Figure (3) illustrates the influence of doping on Cu_2S. This was accomplished by conducting surface topography calculations for pure Cu_2S with a 5 wt.% doping level. The results from XRD corroborate the findings regarding crystallite size. Table (3) provides a comprehensive overview of the grain size, surface roughness, and root mean square roughness values for all prepared thin films.

The optical properties of the prepared thin films can be effectively characterized throughout the use of absorption spectroscopy, which is a powerful analytical tool, and it has been widely used to study the absorption properties of Cu_2S and Cu_2S:Cd 5 wt.% thin films. Absorption and transmission spectra of Cu_2S and Cu_2S:Cd 5 wt.% thin films in the range 400-1000nm are shown in Fig. (4). They have revealed that these materials have a strong absorption edge in the visible and ultraviolet regions of the electromagnetic spectrum. The absorption edge can be controlled by the preparation method and growth conditions, and it is an important factor for the optimization of the optical properties of these materials.

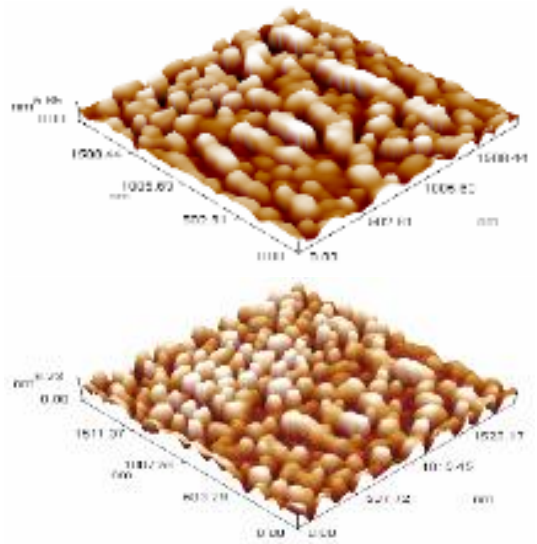

Fig. (3) 3D AFM images of thin Cu_2S and Cu_2S:Cd 5 wt.% thin films

Table (3) AFM parameters for Cu_2S and Cu_2S:Cd 5 wt.% thin films

Thin Films	Grain Size (nm)	Roughness (nm)	R.M.S. Roughness (nm)
Cu_2S	83.86	1.19	1.41
Cu_2S:Cd 5 wt.%	90.33	1.42	1.65

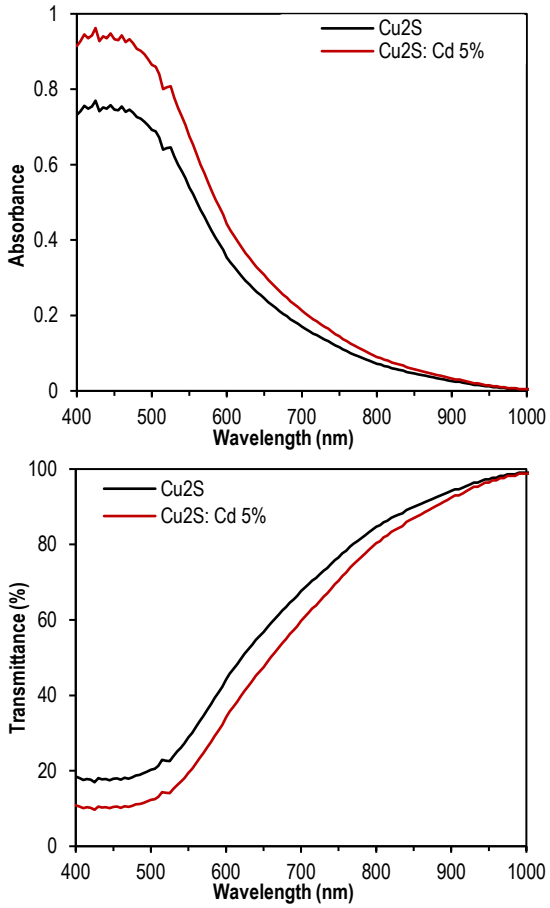

Fig. (4) Absorption and transmission spectra of Cu_2S and Cu_2S:Cd 5 wt.% thin films

The ability of the material to absorb light is determined by the absorption coefficient, which depends on both the energy of the incident photons (hυ) and the energy gap (E_g) [22,23]. In a comparable manner, it can be stated that figure (5) illustrates the variation of absorption coefficient (α) with photon energy (hυ), indicating high values above 10^4 cm^{-1}. The value of α for Cu_2S and Cu_2S:Cd 5 wt.% thin films increases from 3.18 to 4.4×10^4 cm^{-1}, which leads to an increase in absorbance of Cu_2S:Cd 5 wt.% films. Furthermore, the value of direct band gap decrease from 1.85eV for Cu_2S (wide bandgap semiconductor) to 1.5 eV for Cu_2S:Cd 5 wt.% (narrow bandgap semiconductor). This decrease in band gap (E_{gopt}) can be attributed to the increase in the absorption coefficient, which is consistent with previous studies [3,4]. The energy gap value experiences a blue shift with grain sizes ranging from 31.31 to 34.83 nm, which is explained by the energy-dependent weak quantum confinement against the grain size. The reasons for this weak correlation between the grain size and band gap value could be attributed to a variety of factors as follows: (1) the grain size being larger than the Bohr radius, (2) Coulomb interaction between the charge carriers, and (3) agglomeration of the nanomaterials. The decrease in the band gap may be ascribed to the moderate or limited impact of quantum confinement on the energy with respect to the size of the crystallites [27].

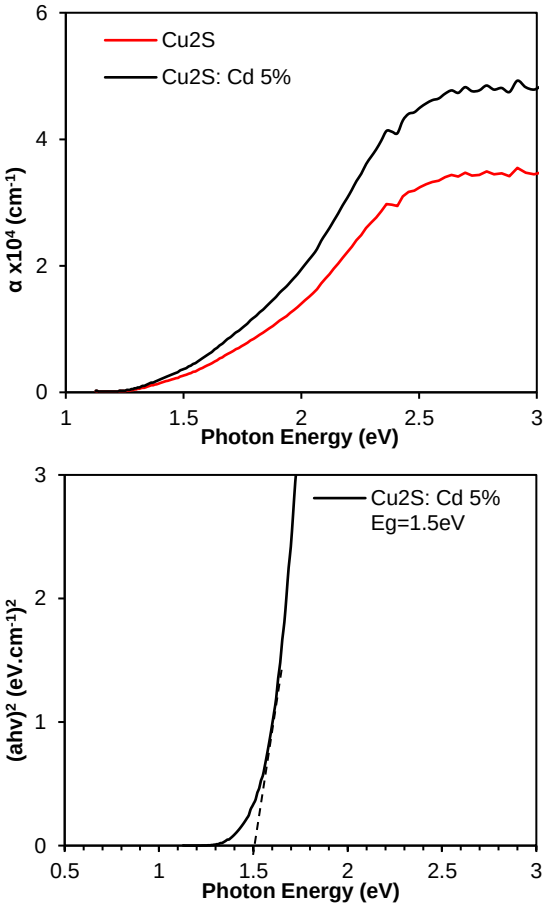

 ISSN (print) 1813-2065, (online) 2309-1673

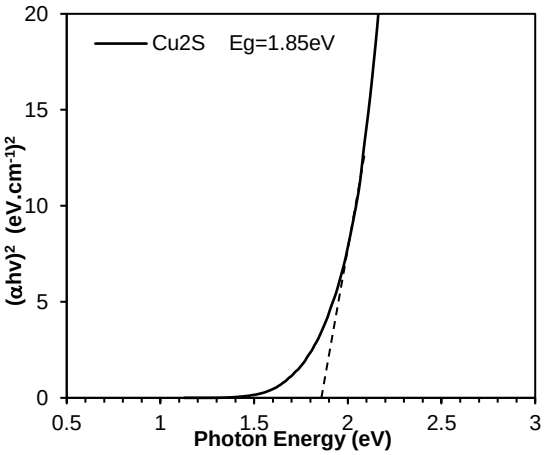

Fig. (5) Absorption coefficient and direct optical band gap for Cu_2S and Cu_2S:Cd 5 wt.% thin films

Table (4) Values of direct optical band gap and absorption coefficient for Cu_2S and Cu_2S:Cd 5 wt.% thin films

Sample	Cu_2S	Cu_2S:Cd 5 wt.%
E_g^{opt} (eV)	1.8	1.5
α x10^4 cm^{-1}	3.18	4.4

Table (5) lists the results of Hall effect measurements (R_H) that was utilized to determine the majority carriers and mobility of Cu_2S and Cu_2S:Cd 5 wt.% thin films. The results indicate that all thin films had a positive R_H value, confirming that the conducting carriers were of p-type, specifically holes. These findings are in agreement with the previous studies [14,28]. It is noteworthy that a decrease in carrier concentration for both Cu_2S and Cu_2S:Cd 5 wt.% thin films resulted in an increase in the Hall coefficient (R_H) due to an increase in voltages applied on and current passing through the films. However, this increased probability of collisions between the carriers led to a decrease in the values of mobility (μH). The Cu_2S films had the highest percentage of charge carriers.

Table (5) Results of Hall effect measurements for p-type Cu_2S and Cu_2S:Cd 5 wt.% thin films

Sample	σ $(\Omega.cm)^{-1}$	μ_H $(cm^2/V.S)$	N_A x10^{17} (cm^{-3})	$R_{(H)}$ $(cm^3.C^{-1})$
Cu_2S	0.033333	0.231739	8.99	6.952169
Cu_2S: Cd 5 wt.%	0.025	2.414992	0.647	96.59969

Table (6) lists the photovoltaic parameters variations of Cu_2S and Cu_2S:Cd 5 wt.% films obtained from current-voltage measurements. The current-voltage (I-V) curves for three Cu_2S and Cu_2S:Cd/Si heterojunction devices under illumination are displayed in Fig. (6). The efficiency of Cu_2S:Cd/Si increases with incident power of 80mW/cm^2 due to the reduction in energy gap value, as reported in the study of optical properties. Additionally, the J_{SC} values also increase. The open circuit voltages (V_{OC}) increase with crystallite size, absorption coefficient, and mobility of carrier concentration [29].

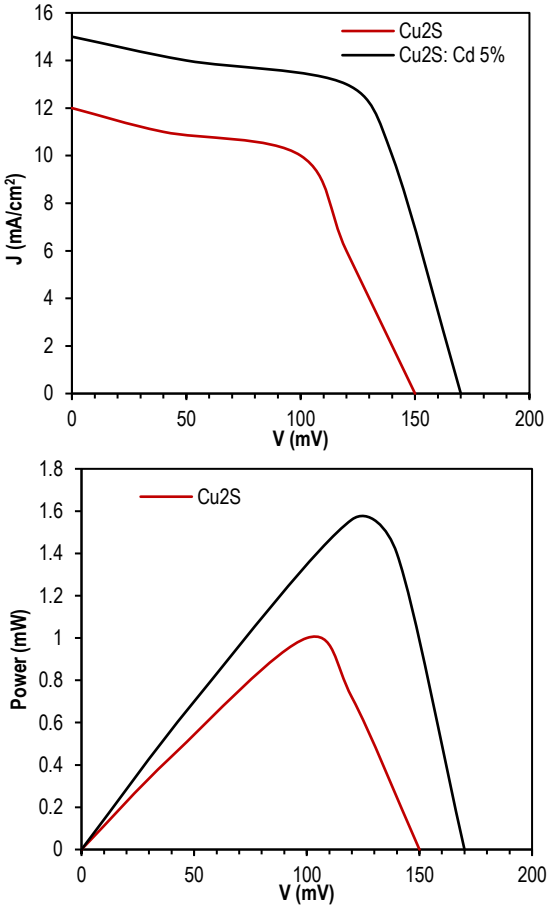

Fig. (6) Electrical characteristics under illumination for Cu_2S and Cu_2S:Cd 5 wt.% thin film heterojunction solar cells

Table (6) The I-V characteristics of solar cells fabricated from Cu_2S and Cu_2S:Cd 5 wt.% thin films

Parameter	Cu_2S/Si	Cu_2S:Cd/Si
V_{oc} (mV)	150	170
J_{sc} (mA/cm^2)	12	15
V_{max} (mV)	100	120
J_{max} (mA/cm^2)	10	13
Fill Factor	0.55	0.61
Efficiency (%)	1	1.56

4. Conclusions

Copper compound (Cu_2S and Cu_2S:Cd 5 wt.%) thin films were prepared by vacuum thermal evaporation. The prepared films showed the polycrystalline structure cubic for two compound semiconductors. Compared to the previously reported works, the p-Cu_2S:Cd 5wt. %/n-Si solar cell exhibits superior structural, optical, and electrical properties. Additionally, the decrease in resistivity values contributes to the enhancement of its optoelectronic properties, as evidenced by the fill factor values and efficiency, which were 0.61 and 1.56%, respectively.

References

[1] P. Sateesh, and P. Madhusudhanarao, "Structural, optical and electrical properties of Cu_2S thin films deposited by CBD method", *Int. J. Adv. Res. Phys. Sci.*, 2(11) (2015) 11-16.

[2] J. Choi et al., "Colloidal synthesis of cubic-phase copper selenide nanodiscs and their optoelectronic properties", *Chem. Mater*., 22(12) (2010) 3586-3588.
[3] M. Petrović et al., "Optical properties of CuSe thin films-band gap determination", *Sci. Sinter*., 49(2) (2017) 167-174.
[4] R.O. Okor et al., "Band gap determination of chemically deposited Cu_2S/Fe_2O_3 quaternary thin films", *Chalcogen. Lett*., 19(5) (2022) 353-361.
[5] K.M. Qader and E.M. Salman, "Threshold Current Density of $Al_{0.1}Ga_{0.9}N/GaN$ Triple Quantum Well Laser", *Energy Procedia*, 157 (2019) 75-83.
[6] L. Xue et al., "Thermoelectric performance of Cu2Se bulk materials by high-temperature and high-pressure synthesis", *J. Materiomics*, 5(1) (2019) 103-10.
[7] P. Nieroda et al., "Thermoelectric properties of Cu_2S obtained by high temperature synthesis and sintered by IHP method", *Ceram. Int*., 46(16) (2020) 25460-6.
[8] M. Patil et al., "Synthesis and characterization of Cu_2S thin film deposited by chemical bath deposition method", *Procedia Manuf*., 20 (2018) 505-508.
[9] H.K. Kaplan et al., "p-Type transparent Cu_2S thin film grown by Thermionic Vacuum Arc for optoelectronic applications", *Mater. Sci. Eng. B*, 263 (2021) 114872.
[10] B. Bharathi, S. Thanikaikarasan, and K. Ramesh, "Structural, compositional, and optical properties of electrochemically deposited Cu_2S thin films", *Int. J. Chemtech Res*., 6(3) (2014) 1907-1909.
[11] S. Hemathangam, G. Thanapathy and S. Muthukumaran, "Tuning of band gap and photoluminescence properties of Zn doped Cu_2S thin films by CBD method", *J. Mater. Sci. Mater. Electron*., 27 (2016) 2042–2048.
[12] A.A. Hamida and B.K.H. Al-Maiyaly, "Synthesis and characterization of Cu_2S: Al thin films for solar cell applications", *Chalcogen. Lett*., 19(9) (2022) 579-590.
[13] A.H. Omran and M.D. Jaafer, "Annealing effect on the structural and optical properties of CuS thin film prepared by Chemical Bath Deposition (CBD)", *J. Kufa phys*., 5(1) (2013).
[14] H.S. Ahmed and R.Y. Mohammed, "The effect of deposition parameters on morphological and optical properties of Cu_2S thin films grown by chemical bath deposition technique", *Photonics*, 9(3) (2022) 161.
[15] S. Bini et al., "Preparation of $CuInS_2$ thin films using CBD Cu_xS films", *Renew. Ener*., 20 (2000).
[16] H.M. Pathan, J.D. Desai and C.D. Lokhande, "Modified chemical deposition and physico-chemical properties of copper sulphide (Cu_2S) thin films", *Appl. Surf. Sci.*, 202(1-2) (2002) 47-56.
[17] I.S. Najm, A. Alwahib and S.M. Kadhim, "Study of CuS thin films deposited by PLD simulated for prism based SPR sensor", *Eng. Technol. J.*, 39(6) (2021) 936-945.
[18] Y.J. Wang, A.T. Tsai and C.S. Yang, "Synthesis of hierarchical self-supported micropatterns of Cu_2S crystals", *Mater. Lett*., 63(11) (2009) 847-849.
[19] Y.B. He et al., "Hall effect and surface characterization of Cu_2S and CuS films deposited by RF reactive sputtering", *Phys. B: Cond. Matter*, 308 (2001) 1069-1073.
[20] S. Schneider et al., "Copper (I) tert-butylthiolato clusters as single-source precursors for high-quality chalcocite thin films: film growth and microstructure control", *Chem. Mater*., 19(11) (2007) 2780-2785.
[21] B.H. AlMaiyaly, B.H. Hussein and A.H. Shaban, "Fabrication and characterization study of ZnTe/n-Si heterojunction solar cell application", *J. Phys. Conf. Ser*., 1003(1) (2018) 012084.
[22] B.H. Hussein et al., "Effect of copper on physical properties of CdO thin films and n-CdO: Cu/p-Si heterojunction" *J. Ovonic Res*., 18 (2022) 37-42.
[23] R.H. Athab and B.H. Hussein, "Growth and Characterization of Vacuum Annealing $AgCuInSe_2$ Thin Film", *Ibn al-Haitham J. Pure Appl. Sci*., 35(4) (2022) 45-54.
[24] R.H. Athab and B.H. Hussein, Preparation and study effect of vacuum annealing on structure and optical properties of $AgCuInSe_2$ thin film. *Dig. J. Nanomater. Biostructures*., 17(4) (2022).
[25] R.F. Hasan, and R.A. Rassol, "Analysis of Performance of ZnO/CdS/SnS Solar Cell Using Software Program SCAPS-1D", *Iraqi J. Appl. Phys*., 19(2) (2023) 9-14.
[26] B.H. Hussein et al., "Effect of V, In and Cu doping on properties of p-type ZnSe/Si heterojunction solar cell", *Prog. Ind. Ecol*., 13(2) (2019) 173-186.
[27] A.A. Aboud et al., "The effect of Cu-doping on CdS thin films deposited by the spray pyrolysis technique", *J. Mater. Res. Technol*., 8(2) (2019) 2021-2030.
[28] B.K.H. Al-Maiyaly, B.H. Hussein and H.K. Hassun, "Growth and optoelectronic properties", *J. Ovonic Res*., 16(5) (2020) 267-271.
[29] R.H. Athab, and B.H. Hussein, "Studying the effect of copper on the p-ZnTe/n-$AgCuInSe_2$/p-Si for thin films solar cell applications", *Chalcogen. Lett*., 20(2) (2023) 91-100.

 ISSN (print) 1813-2065, (online) 2309-1673

Table (1) Structural parameters for Cu_2S alloys

alloy	2θ (Std.) (Deg.)	2θ (Exp.) (Deg.)	d(Std.) (Å)	d(Exp.) (Å)	hkl	FWHM (deg.)	C.S (nm)	a exp. (Å)	a stand. (Å)
Cu_2S	27.7660	27.2672	3.210300	3.26797	111	0.2560	35.21	5.56	5.564
	32.1114	32.4604	2.785100	2.75602	(200)				
	36.1076	36.3375	2.485500	2.47036	(210)				
	39.6449	39.2477	2.271500	2.29363	(211)				
	46.1034	**45.9980**	**1.967200**	**1.97151**	**(220)**				
	51.9251	51.8274	1.759500	1.76263	(310)				
	54.6724	54.4014	1.677400	1.68516	(311)				

Table (2) Structural parameters for Cu_2S and Cu_2S:Cd 5 wt.% thin films

Thin Films	2θ (Std.) (Deg.)	2θ (Exp.) (Deg.)	d(Std.) (Å)	d(Exp.) (Å)	hkl	FWHM (deg.)	C.S (nm)	a exp. (Å)	a stand. (Å)
Cu_2S	46.1034	45.9980	1.967200	1.931	220)(	0.289	31.310	5.65	5.564
Cu_2S:Cd 5 wt.%	46.1034	46.2001	1.967200	1.962	220)(	0.259	34.83	5.66	5.564

IRAQI JOURNAL OF APPLIED PHYSICS
Vol. 19, No. 4C, December 2023, pp. 229-234

Structural and Optical Properties of TiN and TiO_2:TiN Nanostructures via DC Reactive Magnetron Sputtering Technique

Mays K. Ali
Firas J. Kadhim

Department of Physics, College of Science, University of Baghdad, Baghdad, IRAQ

A pure titanium nitride phase (TiN) and Titanium dioxide: Titanium nitride (TiO_2:TiN) nanocomposite thin film samples were deposited by dc reactive magnetron sputtering technique from a titanium target in a mixture of 60:40 Ar:N_2 and 40:20:20 Ar:O_2:N_2, respectively. The structural, morphological, and optical properties of the deposited films were examined. The X-ray diffraction (XRD) analysis reveals the presence of a pure TiN phase in samples prepared without oxygen, as well as mixed phases comprising anatase TiO2, rutile TiO2. Furthermore, an additional phase characterized by a cubic TiN structure is observed when samples are exposed to both reactive gases, oxygen and nitrogen. The FE-SEM test reveals a reduction in the nanostructure size and an increase in porosity in the TiN sample when compared to the composite sample. The FTIR pattern shows the bands corresponding to the Ti-N without any oxide phase, while the composite sample showed further vibrations corresponding to TiO_2, in addition to the hydroxyl band corresponding to the adsorbed water vapour on the surface of both samples. The Plasmon resonance absorbance band widened for the TiN sample to cover the entire range of the visible region. These properties make the TiN sample candidate for use in a photocatalytic application.

Keywords: Nanostructures; Reactive sputtering; Titanium nitride; Nanocomposites
Received: 09 August 2023; **Revised:** 19 September 2023; **Accepted:** 26 September 2023

1. Introduction

Pure TiO_2 thin films possess a wide bandgap, confining their utility in photocatalysis to the UV range [1]. In order to enhance the photosensitivity of TiO_2 nanocrystalline, different techniques were used such as by doping or composing with other substances [2,3]. The common technique to expand the photoresponse of TiO_2 thin films toward visible radiation by doping such as with Ag [4], N_2 [5], etc. Doping TiO_2 with N_2 aid to narrowing the bandgap of TiO_2, substitutional doping of N [6] or by plasmonic band within the visible range [7,8].

Titanium nitride (TiN), a renowned member of the refractory transition metal nitride family, boasts an array of valuable properties encompassing mechanical strength, tribological characteristics, and chemical stability [9]. Its versatility finds expression in a wide spectrum of applications, including serving as crucibles for metal casting [10], specialized refractories [11], decorative coatings akin to gold [12], and protective layers against corrosion [13]. Research investigations have illuminated the crucial role of nitrogen diffusion in the formation of TiN composites when titanium powder is heated in nitrogen-rich atmospheres [14]. Beyond these applications, TiN also exhibits inherent biocompatibility and exceptional hemocompatibility, making it suitable for use in medical contexts such as dental implants and joint prosthetics [15]. Consequently, various methods are employed to deposit TiN coatings on implants made from diverse materials, enhancing their corrosion resistance and biocompatibility [16].

Diverse techniques such as reactive evaporation [17] and radio frequency magnetron sputtering are employed for TiN thin film deposition. Plasma-enhanced methods have exhibited deep nitrogen penetration, yielding highly corrosion-resistant coatings [18]. Despite the expense of high-vacuum sputtering, it remains vital for implant coatings due to film purity, homogeneity, and nanostructural precipitation tendencies [19]. Researchers seek to control TiN stoichiometry and component ratios for specific applications using varied techniques.

Numerous studies have addressed the preparation of stoichiometric TiN thin films or TiN:TiO_2 composites through diverse methods. Ajenifuja et al. [20] employed DC reactive magnetron deposition to create TiNx thin films on carbon steel, revealing crystal orientation changes and increased nitrogen content. Wu et al. [21] compared sputtering techniques for bio-coatings, finding that higher N/Ti ratios improved corrosion resistance. Zhang et al. [22] demonstrated that increasing the Ar ratio in RF magnetron sputtering yields stoichiometric TiN and reduces surface roughness, friction, and wear. Mascaretti et al. [23] associated near-stoichiometric TiN structures with optimal plasmonic properties and

low resistivity. Jithin et al. [24] linked the Ar:N_2 ratio in plasma to microstructural, surface, and electrical characteristics of TiN films.

This study compares the structural, surface morphological, and optical properties of TiN thin films and TiO_2:TiN nanocomposite produced via dc reactive magnetron sputtering. The investigation aims to study the variation in these properties, shedding light on their potential applications in diverse technological fields.

2. Experimental Part

Pure titanium nitride (TiN) and TiN:TiO_2 composite thin films were synthesized using the dc reactive magnetron sputtering technique. A 5 cm diameter titanium target was employed for sputtering inside a stainless steel vacuum chamber. The chamber included a gas mixer system equipped with a gas mixer before the gas inlet controlled by a fine-tuned needle valve. Vacuum levels were monitored using a digital Pirani gauge. The magnetron comprised two concentric permanent magnets ring. The inter-electrode distance was fixed at 4 cm and the deposition time of 3-hours at a substrate temperature of 350°C and a working pressure of 8.5×10^{-2} mbar for all samples. Argon was used as the sputtering gas, while the nitrogen and oxygen were used as reactive gases. The gas mixture used as 60:40 Ar:N_2 for TiN sample and 40:20:20 Ar:O_2:N_2 for the TiN:TiO_2 thin film.

To assess the structural properties, surface morphology, and optical characteristics of the prepared samples, a Shimadzu XRD 6000 diffractometer, an Inspect F-50 SEM scanning electron microscope, a Shimadzu 16442 Fourier-transform infrared spectrometer, and a SP-8001 UV-visible spectrophotometer were employed.

3. Results and Discussions

Figure (1) presents the X-ray diffraction (XRD) patterns of the TiO_2:TiN composite and TiN films, offering a profound insight into their respective crystallographic structures. Both patterns exhibit a characteristic polycrystalline nature, indicative of the arrangement of atoms in multiple crystalline domains within the samples. In the case of the TiO_2:TiN composite sample, the XRD analysis unveils a complex composition. The composite is comprised of a mixture of two distinct TiO_2 phases: Anatase and Rutile, alongside a minor presence of the rock salt structured TiN. These constituents are clearly identified by their corresponding card numbers: 96-900-9087 for Anatase, 96-900-7532 for Rutile, and 96-101-1100 for TiN. Notably, the dominant Anatase phase exhibits a preferred orientation, with a discernible peak situated along the (101) crystal planes at a Bragg angle of 25.3983°. This orientation signifies a specific alignment of the crystalline domains, possibly resulting from growth conditions or the material's inherent properties. The intensity of the diffraction line along the (111) direction further emphasizes the presence of Anatase and the interplay between its crystallographic facets. The comparative intensity of the diffraction lines is also informative. In the TiO_2:TiN composite, the diffraction peaks corresponding to TiO_2 phases are notably more intense than those associated with TiN, underscoring the predominant presence of TiO_2 in the composite material. This observation aligns with the compositional information provided earlier and highlights the composite's rich TiO_2 content.

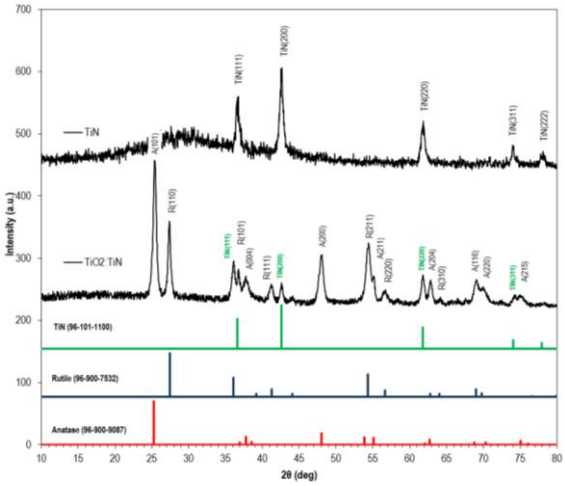

Fig. (1) XRD patterns of TiO_2:TiN and TiN films prepared by reactive dc sputtering

On the other hand, the XRD pattern corresponding to the TiN film showcases a pure cubic TiN phase. This crystalline arrangement is evident from the distinct diffraction peaks observed at Bragg angles of 36.6140°, 42.5571°, 61.7680°, 73.9800°, and 78.2400°, coinciding with the (111), (200), (220), (311), and (222) crystal planes, respectively. The presence of these peaks underscores the highly crystalline nature of the TiN film, indicating the well-defined arrangement of atoms in the cubic lattice. Notably, a preferred orientation is observed along the (200) direction, suggesting an alignment of crystal domains that contributes to the overall texture of the film.

A compelling outcome of the refinement process is the striking agreement between the calculated stoichiometric pattern and the experimental pattern of a sample. This congruence between theoretical and observed patterns validates the accuracy of the refinement technique and accentuates the reliability of the results. This alignment enhances our confidence in the structural assessment of sample. Figure (2) shows the retrieve refinement fitting for the TiO_2:TiN composite and TiN patterns with their standard cards. The contribution of anatase, rutile, and titanium nitride to the crystalline structure of the composite sample appears in the percentage of 32.6%, 45.6%, and 11.3%, respectively. From the other hand, a good fitting appeared between the

 ISSN (print) 1813-2065, (online) 2309-1673

calculated stoichiometry pattern with the experimental pattern for the pure TiN sample. This alignment is a result of the absence of oxygen atoms in the sputtering process, which, in turn, prevents the formation of oxidized phases in the sample.

The inert-planer distances (d_{hkl}) were calculated according to Bragg's law [25], while the crystallite size was calculated using Scherrer's formula [26]. The calculation of inter-planer distances (d_{hkl}) and the determination of crystallite size provide crucial insights into the materials' internal structure. Notably, the calculated crystallite size experiences a reduction from 14.7 nm in the composite sample to 11.3 nm in the TiN sample, for the preferred orientation along (101) and (200) planes, respectively, as tabulated in table (1). This reduction in crystallite size suggests a refinement in the crystal domains within the TiN sample, possibly attributed to various factors such as synthesis conditions or the intrinsic properties of the material. This change in crystallite size can impact material properties and performance, potentially influencing phenomena like catalytic activity or electronic behavior.

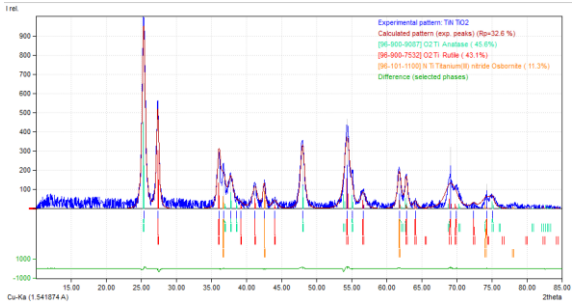

TiO_2:TiN

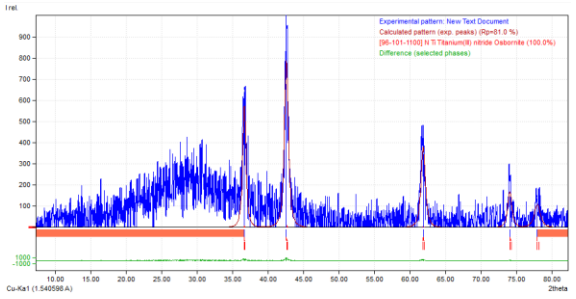

TiN

Fig. (2) XRD patterns of TiO_2: TiN and TiN films prepared by reactive dc sputtering

The field-emission scanning electron microscopy (FE-SEM) images presented in Fig. (3), at two distinct magnification levels, provide detailed information about the surface morphology of both the TiN:TiO_2 nanocomposite and the TiN thin films. These images reveal insights that highlight their potential applications in scientific fields such as catalytic processes or gas sensing. The FE-SEM images offer an intricate portrayal of the surface morphologies of the materials.

Both the nanocomposite and thin film samples exhibit nearly identical features, consisting of nearly spherical nanoparticles but with different size. The nanocomposite sample compose of consistent particle size range of 20 to 40 nm. This uniformity in particle size is a crucial aspect as it promotes consistent and predictable catalytic behavior, ensuring reproducibility in photocatalytic reactions.

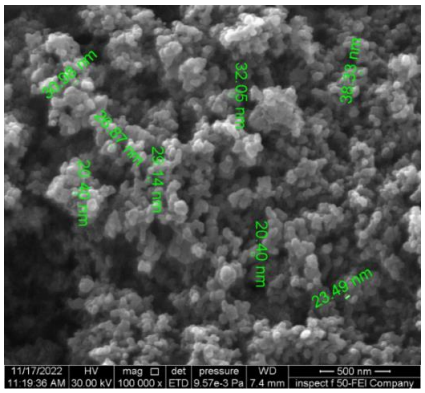

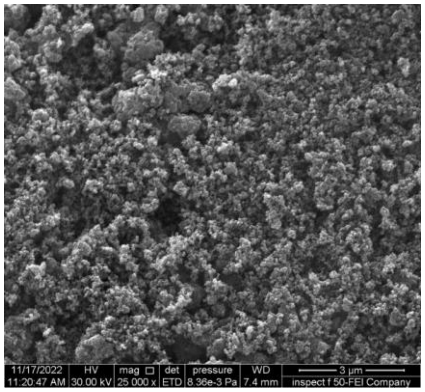

TiO_2:TiN

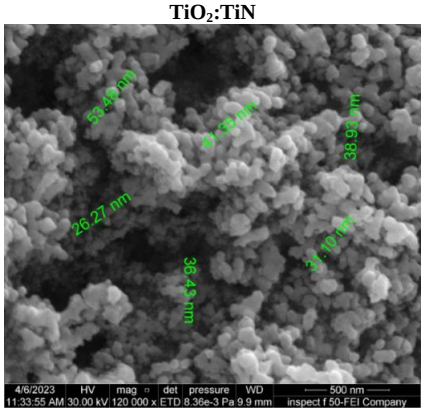

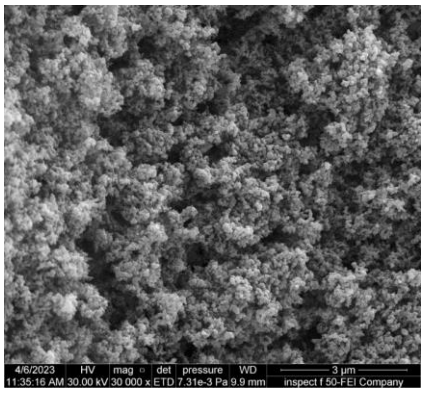

TiN

Fig. (3) FE-SEM images of TiO_2:TiN and TiN thin films deposited on glass substrates

A noteworthy observation from the images is the interconnected nature of these nanoparticles, culminating in the formation of an intricate porous structure. This porous architecture carries significant implications for photocatalysis, as it provides an amplified surface area available for interactions between the catalytic material and the target reactants. The pores serve as conduits for reactant diffusion and product desorption, enhancing the efficiency of the catalytic process by facilitating unhindered molecular movement and optimized contact between the catalyst and the reactants.

The TiN thin film exhibits reducing particle size and enhancing the degree of porosity in comparison to the composite sample. This distinction could be attributed to the presence of TiO_2 nanoparticles in the composite material. The inclusion of TiO_2 nanoparticles may influence the pore distribution and size, thereby affecting the overall porosity of the material. Small particle size increases the surface-to-volume ratio, facilitating greater interaction between surface atoms and light, thereby enhancing the material's photocatalytic activity. Surface atoms, possessing active sites, are exposed to the surrounding environment, including the light source, resulting in a range of chemical reactions. These reactions may encompass the degradation of pollutants, the generation of hydrogen from water, or other photochemical processes. Also, the variation in porosity between the two samples opens up avenues for tailored photocatalytic applications, where the choice between the nanocomposite and thin film can be made based on specific process requirements and desired outcomes.

Figure (4) displays the results of energy-dispersive x-ray spectroscopy (EDS) of the TiO_2:TiN composite and TiN samples. These results show emission lines corresponding to titanium (Ti), and nitrogen (N) in both samples, in addition to oxygen (O) in the composite sample. The absence of oxygen atoms or any other foreign atoms in the EDS analysis of TiN thin film sample indicates a high level of structural purity and suggests that the sample has not undergone oxidation. This result is consistent with the expected composition of TiN, which is composed of titanium (Ti) and nitrogen (N) atoms and does not contain oxygen (O) in its ideal form.

Elemental mapping leverages the compositional precision inherent in techniques such as EDS microanalysis and combines it with high resolution imaging to present complex data in an accessible, visually striking format. It is based on compiling extremely specific elemental composition data across an area of a sample. This is typically done in an SEM or TEM using EDS analysis.

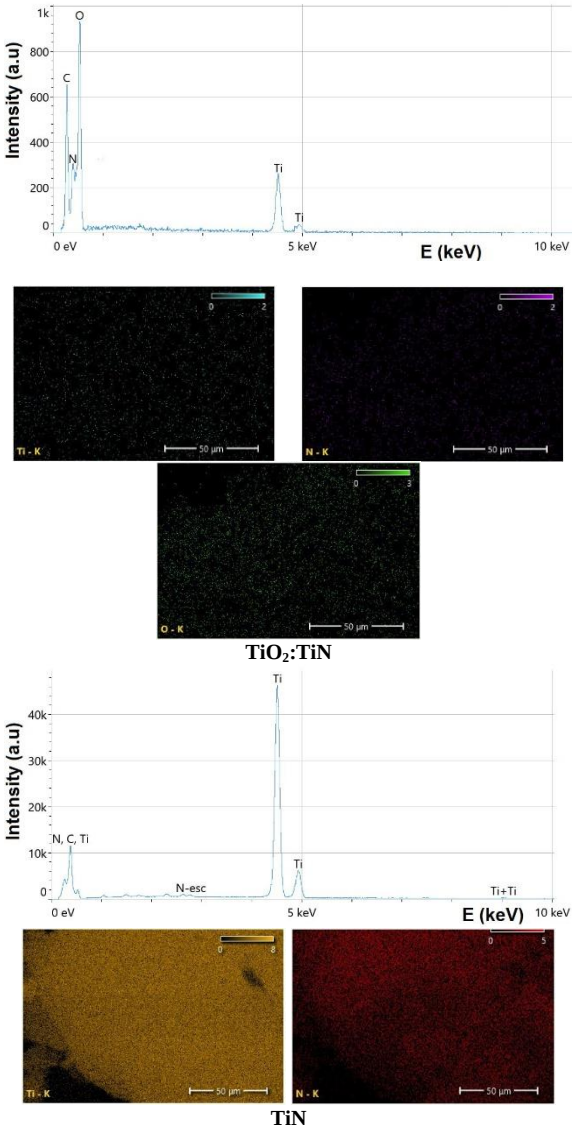

Fig. (4) EDS analysis and EDS mapping of TiO_2:TiN and TiN thin films

A high resolution image of the area of interest is collected along with the EDS data, and the two are correlated. For every pixel in the digital image collected, a complete elemental spectrum is also collected. By processing these spectra, the relative intensity of spectral features associated with a number of elements of interest can be translated into computed colorization layers, which color codes the electron photomicrograph signifying layers and sites of elemental compositional information in the prepared sample. The EDS mapping shown below the spectra specifies the uniformity of deposition. This map provides spatial information about the distribution of titanium and nitrogen within the TiN thin film, confirming that the Ti and N elements are evenly distributed, further indicating the uniformity and quality of the deposition process.

The FTIR for TiO_2:TiN nanocomposite and TiN samples were presented in Fig. (5). For the composite sample, the broad band at around 3450 cm^{-1} is

 ISSN (print) 1813-2065, (online) 2309-1673

recognized as the hydroxyl group that comes from the adsorbed water vapor on the surface of the nanoparticles. The CH_2 stretching vibration appeared at 2980 and 2920 cm^{-1} indicating the existence of some carbonyl group on the sample surface. The band at 1580 cm^{-1} for the Ti-OH, 1420 cm^{-1} for N-H. The triple bands at 1130, 1040, and 1008 cm^{-1} for Ti-N, and the band at 920 cm^{-1} for N-O. The two broad bands appeared at 640, and 540 cm^{-1} corresponding to Ti-O, Ti-O-Ti in the TiO_2 [27], while the weak band 420 cm^{-1} corresponded to Ti-O in rutile structure [28]. The pure TiN sample appeared with bands located at 3436 cm^{-1} for O-H, 1635 cm^{-1} for O-H bending, 1370 cm^{-1} for N-H, 1135, 1055 cm^{-1} for Ti-N, and 920 cm^{-1} N-O [29]. There are no bands corresponding to titanium oxide were appeared in the TiN sample.

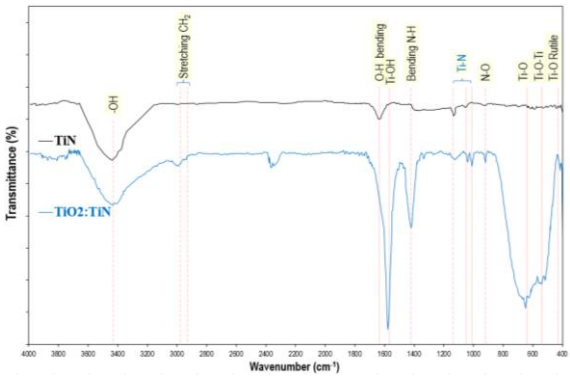

Fig. (5) FTIR spectra for TiO_2:TiN composite and TiN samples prepared by reactive dc sputtering

Figure (6) displays the absorption curves for the TiO_2:TiN and TiN thin films deposited on glass slides. The absorption edge appeared at about 370 and 350 nm for TiO_2:TiN and TiN samples, respectively. A plasmonic band appeared around 450 nm wavelength for the composite sample corresponding to plasmon resonance in the TiN structure [30]. This band appeared at a broad range covering nearly the entire visible region and redshift compared to the composite sample due to the presence of the TiO_2. This result is in line with the literature [31]. This behaviour can be applied in different applications such as in the photocatalytic technique [32].

4. Conclusions

The presented study demonstrates the efficient fabrication of TiO_2:TiN nanocomposite and high-purity TiN nanostructure using a straightforward dc reactive magnetron sputtering configuration. The thorough evaluation of their structural, morphological, and optical characteristics has unveiled significant distinctions between the two systems. Remarkably, the exceptional phase purity of these materials, covering a broad spectrum, highlights the potential versatility of TiN for various technological applications, affirming its suitability for a range of practical uses.

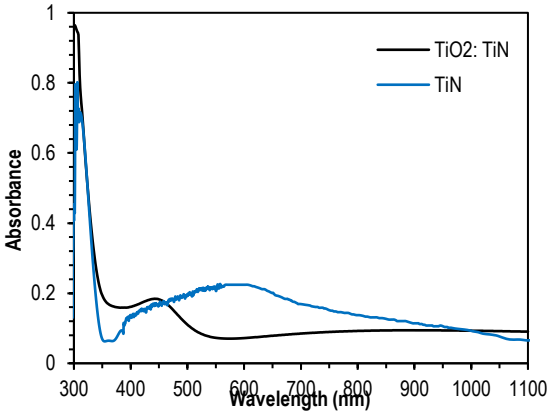

Fig. (6) Absorption spectra of TiO_2:TiN and TiN thin films deposited on glass substrates

References

[1] H. Mamane et al., "The role of physical and operational parameters in photocatalysis by N-doped TiO_2 sol–gel thin films", *Chem. Eng. J.*, 257 (2014) 159-169.

[2] B. Huber et al., "Nanocrystalline anatase TiO_2 thin films: preparation and crystallite size-dependent properties", *Thin Solid Films*, 472 (2005) 114-124.

[3] W. Naffouti et al., "Structural, morphological and optical properties of TiO_2:Mn thin films prepared by spray pyrolysis technique", *J. Mater. Sci. Mater. Electron.*, 27 (2016) 4622-4630.

[4] E.A. Al-Oubidy and F.J. Kadhim, "Photocatalytic activity of anatase titanium dioxide nanostructures prepared by reactive magnetron sputtering technique", *Opt. Quantum Electron.*, 51 (2019).

[5] C. Thambiliyagodage, "Activity enhanced TiO_2 nanomaterials for photodegradation of dyes - A review", *Enviro. Nanotechnol., Monit. Manag.* 16 (2021) 100592.

[6] B. Liu, L. Wen and X. Zhao, "The structure and photocatalytic studies of N-doped TiO_2 films prepared by radio frequency reactive magnetron sputtering", *Sol. Energy Mater. Sol. Cells.*, 92 (2008) 1-10.

[7] A.A. Hussain et al., "Self-Powered Broadband Photodetector using Plasmonic Titanium Nitride", *ACS Appl. Mater. Interfaces*, 8 (2016) 4258-4265.

[8] G.V. Naik et al., "Titanium nitride as a plasmonic material for visible and near-infrared wavelengths", *Opt. Mater. Exp.*, 2 (2012) 478.

[9] J.A. Briggs et al., "Temperature-dependent optical properties of titanium nitride", *Appl. Phys. Lett.*, 110 (2017) 101901.

[10] N.L. Erb-Satullo, B.J.J. Gilmour and N. Khakhutaishvili, "Crucible technologies in the Late Bronze–Early Iron Age South Caucasus: copper processing, tin bronze production, and the possibility of local tin ores", *J. Archaeol. Sci.*, 61 (2015) 260-276.

[11] B.T. Diroll et al., "Broadband Ultrafast Dynamics of Refractory Metals: TiN and ZrN", *Adv. Opt. Mater.*, 8 (2020) 2000652.

[12] Q. Yu et al., "Influence of Alloy Substrate Treatment on Microstructure and Surface Performances of Arc-Ion Plated Gold-Like Film", *Materials (Basel)*, 12 (2019) 180.

[13] M. Forouzanmehr et al., "Detection and Analysis of Corrosion and Contact Resistance Faults of TiN and

CrN Coatings on 410 Stainless Steel as Bipolar Plates in PEM Fuel Cells", *Sensors*, 22 (2022) 750.
[14] V.K. Prokudina, "Titanium Nitride", in: Concise Encycl. Self-Propagating High-Temperature Synth., Elsevier (2017) pp. 398–401.
[15] G.S. Kaliaraj, T. Siva and A. Ramadoss, "Surface functionalized bioceramics coated on metallic implants for biomedical and anticorrosion performance – a review", *J. Mater. Chem. B*, 9 (2021) 9433–9460.
[16] S.C. Jambagi and V.R. Malik, "A Review on Surface Engineering Perspective of Metallic Implants for Orthopaedic Applications", *J. Optoekectron. Mater.*, 73 (2021) 4349-4364.
[17] D.E. Peebles and L.E. Pope, "Reactive evaporation of thin titanium nitride films in ultrahigh vacuum and their friction and wear behavior as a function of contact stress", *Thin Solid Films*, 173 (1989) 19–37.
[18] D.V. Shtansky, E.A. Levashov and I.V. Sukhorukova, "Multifunctional bioactive nanostructured films", in: Hydroxyapatite Biomed. Appl., Elsevier (2015) pp. 159-188.
[19] Deposition Technologies, in: Handb. Depos. Technol. Film. Coatings, Elsevier (2010) pp. 1-31.
[20] E. Ajenifuja, A.P.I. Popoola and O.M. Popoola, "Thickness dependent chemical and microstructural properties of DC reactive magnetron sputtered titanium nitride thin films on low carbon steel cross-section", *J. Mater. Res. Technol.*, 8 (2019) 377-384.
[21] W.Y. Wu et al., "Bioapplication of TiN thin films deposited using high power impulse magnetron sputtering", *Surf. Coat. Technol.*, 362 (2019) 167-175.
[22] S. Zhang et al., "Effects of sputtering gas on microstructure and tribological properties of titanium nitride films", *Appl. Surf. Sci.*, 488 (2019) 61-69.
[23] L. Mascaretti et al., "Controlling the plasmonic properties of titanium nitride thin films by radiofrequency substrate biasing in magnetron sputtering", *Appl. Surf. Sci.*, 554 (2021).
[24] M.A. Jithin et al., "Development of titanium nitride thin film microheaters using laser micromachining", *Vacuum*, 197 (2022) 110795.
[25] W.H. Bragg and W.L. Bragg, "X-Rays and Crystal Structure", G. Bell and Sons, Ltd. (London, 1918).
[26] F. Li et al., "Coaxial electrospinning heterojunction SnO_2/Au-doped In_2O_3 core-shell nanofibers for acetone gas sensor", *Sens. Actuat. B: Chem.*, 252 (2017) 822–830.
[27] C. Afonso et al., "Optical, structural, morphological and chemical properties of doped TiO 2 nanoparticles with $FeCl_3$", *J. Phys. Conf. Ser.*, 2407 (2022) 012001.
[28] P. Kumar et al., "Noble Metal Free, Visible Light Driven Photocatalysis Using TiO_2 Nanotube Arrays Sensitized by P-Doped C_3N_4 Quantum Dots", *Adv. Opt. Mater.*, 8 (2020) 1901275.
[29] B. Čolović et al., "Wetting properties of titanium oxides, oxynitrides and nitrides obtained by DC and pulsed magnetron sputtering and cathodic arc evaporation", *Mater. Sci.*, 37 (2019) 173-181.
[30] U. Guler et al., "Colloidal Plasmonic Titanium Nitride Nanoparticles: Properties and Applications", *Nanophot.*, 4 (2015) 269–276.
[31] C. Li et al., "*in situ* growth of TiO_2 on TiN nanoparticles for non-noble-metal plasmonic photocatalysis", *RSC Adv.*, 6 (2016) 72659-72669.
[32] E.B. Clatworthy et al., "Enhanced Photocatalytic Hydrogen Evolution with TiO_2–TiN Nanoparticle Composites", *J. Phys. Chem. C*, 123 (2019) 3740–3749.

Table (1) XRD parameters for TiO_2 and TiO_2:TiN composite thin films prepared by reactive dc sputtering

Sample	2θ (Deg.)	FWHM (Deg.)	d_{hkl} (Å)	C.S (nm)	hkl	Phase
TiO_2:TiN	25.3983	0.5541	3.5040	14.7	(101)	Anatase
	27.4171	0.5146	3.2504	15.9	(110)	Rutile
	36.0861	0.5146	2.4870	16.2	(101)	Rutile
	37.8278	0.7126	2.3764	11.8	(004)	Anatase
	41.2716	0.5937	2.1857	14.3	(111)	Rutile
	42.7363	0.7521	2.1141	11.3	(200)	TiN
	48.0010	0.5542	1.8938	15.7	(200)	Anatase
	54.3741	0.7125	1.6859	12.5	(105)	Anatase
	55.0866	0.5542	1.6658	16.2	(211)	Anatase
	56.6700	0.5938	1.6230	15.2	(220)	Rutile
	62.0139	0.7125	1.4953	13.0	(220)	TiN
	62.8055	0.5937	1.4784	15.7	(204)	Anatase
	64.1118	0.6729	1.4514	13.9	(310)	Rutile
	69.0203	0.5542	1.3596	17.4	(116)	Anatase
	69.9703	0.7521	1.3435	12.9	(220)	Anatase
	75.0371	0.8313	1.2648	12.1	(215)	Anatase
	82.6769	0.9500	1.1662	11.1	(224)	Anatase
TiN	36.6140	0.4920	1.2769	18.3	(111)	TiN
	42.5571	0.5315	2.1141	11.3	(200)	TiN
	61.7680	0.6240	1.4953	13.0	(220)	TiN
	73.9800	0.4873	1.2769	18.3	(311)	TiN
	78.2400	0.6266	1.2769	18.3	(222)	TiN

 ISSN (print) 1813-2065, (online) 2309-1673

IRAQI JOURNAL OF APPLIED PHYSICS
Vol. 19, No. 4C, December 2023, pp. 235-242

Effects of Magnetic Field on Growth and Electrical Characteristics of Tornado Gliding Arc Discharge

Nada A. Abdullah
Saba J. Kadhem

Department of Physics, College of Science, University of Baghdad, Baghdad, IRAQ

This study investigates the characterization and growth dynamics of a Magnetically Stabilized Gliding Arc Discharge (MSGAD) system, generating non-thermal plasma with argon gas under atmospheric pressure and flow rates of 1-5 L/min. The electrical properties and growth patterns concerning gas flow rates and applied voltages were examined utilizing a magnetic field for stability. Using a digital oscilloscope, a correlation between voltage reduction and increased current was uncovered. An algorithm analyzes digital images to compute arc length, area, and volume. Results reveal how gas flow rate and applied voltage directly impact arc growth. Furthermore, the magnetic field's role in guiding and stabilizing the plasma discharge was explored. This research elucidates the interplay between electrical behavior and geometric characteristics in MSGAD, offering insights into potential applications.

Keywords: Arc discharge; Tornado gliding discharge; Plasma; Electrical characteristics
Received: 13 August 2023; **Revised:** 17 September 2023; **Accepted:** 24 September 2023

1. Introduction

In the pursuit of innovative technologies for various applications, the study of non-thermal plasma systems has garnered significant attention [1-4]. Among these systems, the Magnetically Stabilized Gliding Arc Discharge (MSGAD) stands out as a remarkable candidate, offering the potential to generate non-thermal plasmas under atmospheric pressure conditions [5-7]. This research endeavors to delve into the intricacies of the MSGAD system, focusing on its electrical characteristics and growth dynamics, with particular emphasis on the influence of gas flow rates, applied voltages, and the application of an external magnetic field [8,9]. The MSGAD system represents a fusion of advanced plasma science and engineering, where a gliding arc discharge is harnessed and stabilized by a transversal magnetic field, resulting in a striking "plasma disk" configuration [10-12]. This unique plasma configuration has the potential to revolutionize various fields, including environmental protection, chemical processes, and beyond [13-15].

The study's objectives are multifaceted, encompassing the investigation of the electrical properties of the generated discharge, the exploration of its growth patterns under varying operational parameters, and the assessment of the impact of magnetic field application on plasma behavior [16,17]. A sophisticated plasma pixel isolation algorithm is employed to precisely quantify arc length, area, and volume for different argon gas flow rates and applied voltages [18]. Through meticulous experimentation and data analysis, this research seeks to unravel the complex interplay between electrical behavior, geometric characteristics, and external magnetic fields in the context of the MSGAD system [19]. The findings hold the potential to provide valuable insights into the controlled manipulation of non-thermal plasma systems, ultimately opening new avenues for enhanced efficiency and novel applications [20-23].

In this comprehensive exploration of the MSGAD system, we aim to shed light on the fundamental aspects of its operation, paving the way for advancements in plasma technology with implications for a broad spectrum of scientific and industrial domains [24,25].

2. Experimental Setup

The experimental setup is shown schematically in Fig. (1). A gliding arc discharge at atmospheric pressure is generated between two diverging stainless steel electrodes. The GAD plasma system consists of argon gas to produce plasma in the gliding arc, gas flowmeter (K Weld Corporation, India), which was used to measure the amount of gas entering the hollow metal tube. The gas flow1rates used in this work were 1, 2, 3, 4 and 5 L/min. The system also contains of magnetic coil of 350 and 500 turns to rotate and confine plasma, and two electrodes, one of them high-voltage electrode, which is the central spiral wire, while the other is the container wall which is the grounded electrode. Also, the system contains an A.C. power supply, which was used to ensure that the electrodes are switched continuously to prevent their damage due to high temperature. The power supply operates in a range of frequencies from 0 to 150 kHz and a high voltage of 20 kV. A D.C. power supply (Pro'sKit, China) was connected to the poles

of the magnetic coil, this is to prepare the coil with electric current to obtain an electromagnet.

The total height of the system is 13 cm. The base has a width of 8 cm and a total diameter of 6.4 cm. The distance between the wire and the container wall is 1cm, is shown in figures (2) and (3).

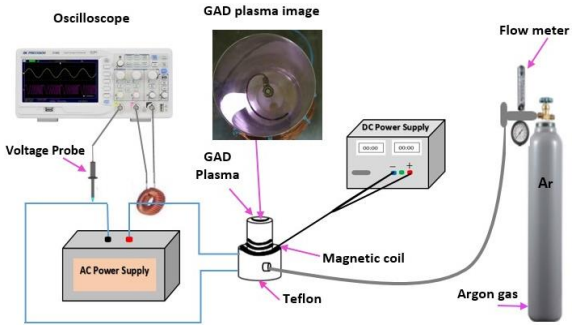

Fig. (1) Schematic1diagram of1the gliding arc discharge (GAD) system

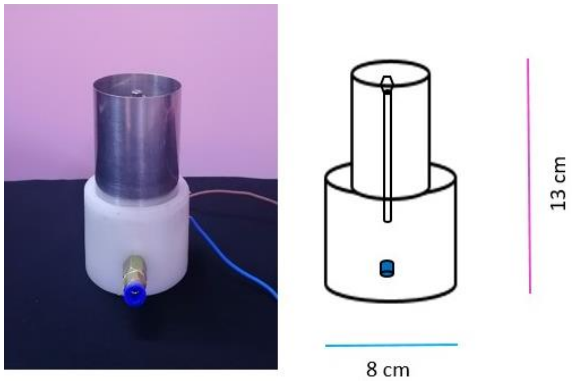

Fig. (2) Front view of1the MSGAD system

Fig. (3) Top1view of the MSGAD in operation

To pinpoint the plasma pixels within the images generated by the system, we employ digital image processing techniques for plasma torch segmentation within the MATLAB environment. The process is illustrated in Fig. (4), depicting the sequential algorithm employed to initially isolate the plasma torch pixels and subsequently convert them into a length representation.

The sequential procedure for isolating plasma pixels in the suggested technique is outlined by reading color plasma image, and then converting color plasma image to greyscale plasma image.

The plasma can be differentiated from the other aspects of the image by applying a threshold, where the specific threshold value is calculated based on the image histogram. The image histogram expresses the distribution of the color values in a digital image: it is a plot of the number of points (pixels) for each1colour value [26]. The x-axis of the graphical depiction depicts the diverse chromatic values, ranging from darker shades on the left to lighter shades on the right. Meanwhile, the y-axis corresponds to the quantity of pixels [27].

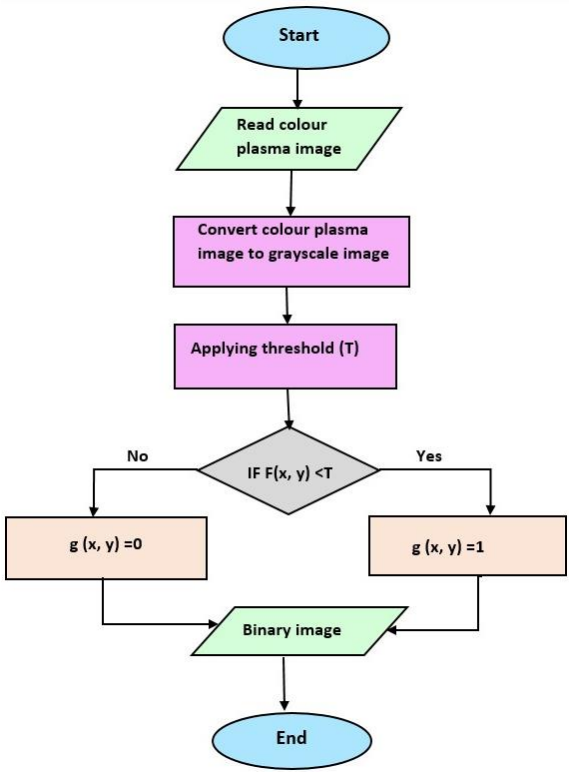

Fig. (4) The1steps of the plasma pixel1isolation algorithm

A matrix of zeros with dimensions identical to those of the original image is generated. The matrix elements are modified to a value of one if the color value of the relevant pixel in the greyscale image satisfies the threshold value. In the event that the threshold is not satisfied, the element's value will persist as zero. The outcome is a binary representation of the image, whereby each pixel is assigned a value of either zero or one. A value of one signifies the presence of plasma pixels, while a value of zero indicates the absence of plasma in the corresponding areas of the image [28]. The methodology, when applied to the matrix element denoted by matrix coordinates, can be succinctly described by the equation.

$$g\,(x,y) = \begin{Bmatrix} 1 & if\ f(x,y) < 1 \\ 0 & otherwise \end{Bmatrix} \qquad (1)$$

where g(x, y) is the output binary value for the matrix element, f (x, y) is the corresponding input greyscale pixel color value, and T is the threshold.

The algorithm employed in this research study serves the purpose of assessing plasma performance

 ISSN (print) 1813-2065, (online) 2309-1673

through the facilitation of calculations pertaining to plasma lengths, areas, and volumes.

3. Results and Discussion

The forms of waves of both voltage and current obtained from the electrical diagnostic are depicted in Fig. (5). The measurement of discharge voltage and current was conducted using a high voltage probe and a Rogowski coil. The experimental setup involved the utilization of a two channel USB oscilloscope for connectivity. As observed, the resulting voltage exhibits a smooth sinusoidal waveform devoid of spike lines. Similarly, the corresponding peak-to-peak current showcases sinusoidal characteristics accompanied by decay waveforms. The power supply operated at a frequency of approximately 9.1 kHz.

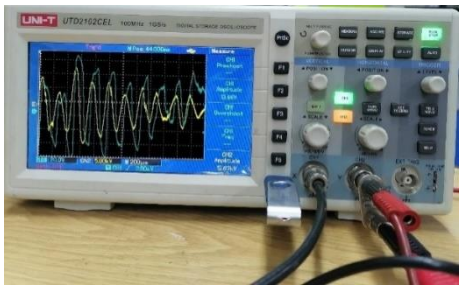

Fig. (5) Waveforms of the current (blue) with the applied voltage (yellow) of the gliding arc discharge by Digital Storage Oscilloscope

The I-V characteristic1curve was acquired in order to ascertain the operational regime of the gliding arc plasma. Figure (6) demonstrates that the voltage on the gliding arc drops as the current increases, but the gas flow and frequency remain constant. This behavior is characteristic of an arc discharge. Nevertheless, the voltage across the arc exhibits a considerable magnitude, typically measured in kV, while the current flowing through it is limited to values below 10 A. Therefore, the non-equilibrium characteristic of the arc is maintained.

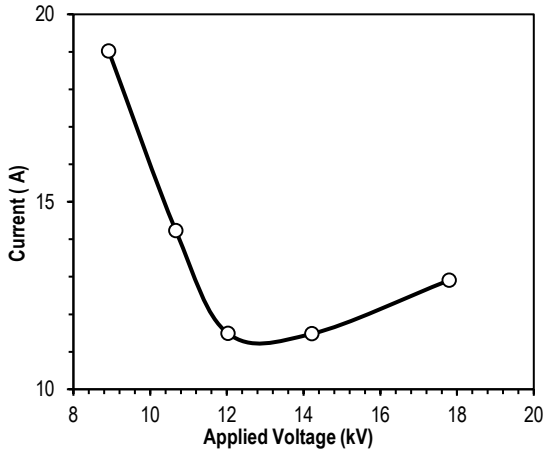

Fig. (6) I-V curves of magnetically stabilized tornado gliding arc discharge

To understand the role of gas flow and applied voltage in the arc length, area, and volume, images of the GAD have also been recorded in the presence of the magnetic field. The frequency of the arc rotation with the magnet is 9.1 kHz. This finding suggests that the external magnetic field plays a dominant role in maintaining the arc rotation in the upper zone of the GAD. Additionally, the shape and length of the plasma arc are also affected by the presence of the external magnetic field. At the beginning of the wire, we notice that the length and volume of the arc increase gradually with the increase in the gas flow rates, and the area also increases.

Table (1) The length, area, and volume of the plasma for different argon gas flow rates with magnetic coil 500 turns as calculated with the proposed plasma isolation algorithm

Flow rate (L/min)	Length (Pixel)	Area (Pixel)	Volume (Pixel)
1	13.969	134.113	4045
2	15.087	180.418	6787
3	18.035	230.788	10950
4	22.724	327.450	15330
5	32.418	441.551	18890

Table (2) The length, area, and volume of the plasma for different argon gas flow rates with magnetic coil 350 turns as calculated with the proposed plasma isolation algorithm

Flow rate (L/min)	Length (Pixel)	Area (Pixel)	Volume (Pixel)
1	12.014	123.885	3704
2	14.865	168.742	6017
3	18.894	258.761	9443
4	21.122	297.089	10267
5	29.552	329.745	11586

These findings are illustrated in figures (7, 8, 9 and 10). The length of the arc at 1 L/min is 13.969 pixels and increases gradually to reach a maximum value of 32.418 pixels at 5 L/min. The area of the arc at 1 L/min is 134.113 pixels and increases gradually to reach a maximum value of 441.551 pixels at 5 L/min. The volume of the arc at 1 L/min is 4045 pixels and increases gradually to reach a maximum value of 18890 pixels at 5 L/min, all with a magnetic coil of 500 turns. Similarly, the length of the arc at 1 L/min is 12.014 pixels and increases gradually to reach a maximum value of 29.552 pixels at 5 L/min. The area of the arc at 1 L/min is 123.885 pixels and increases gradually to reach a maximum value of 329.745 pixels at 5 L/min. The volume of the arc at 1 L/min is 3704 pixels and increases gradually to reach a maximum value of 11586 pixels at 5 L/min, all with a magnetic coil of 350 turns (see tables 1 and 2).

In a tornado arc discharge plasma system, the growth of the arc discharge between the central high voltage electrode and the grounded cylinder wall is facilitated by the presence of a magnetic field. The magnetic field plays a vital role in confining and

guiding the plasma, leading to the formation and sustained growth of the arc discharge. The stages of development of this process can be explained as follows:

Initial breakdown: The process starts with the application of a high voltage potential between the high voltage electrodes typically a central rod spiral wire and the grounded Steel cylinder wall. The electric field generated by the applied voltage initiates the breakdown of the gas within the system.

Formation of the plasma channel: As the breakdown occurs, a plasma channel begins to form between the voltage electrode and the cylinder wall. The plasma is composed of ionized gas species, electrons, and neutral atoms or molecules. Initially, the plasma channel may be relatively short and unstable.

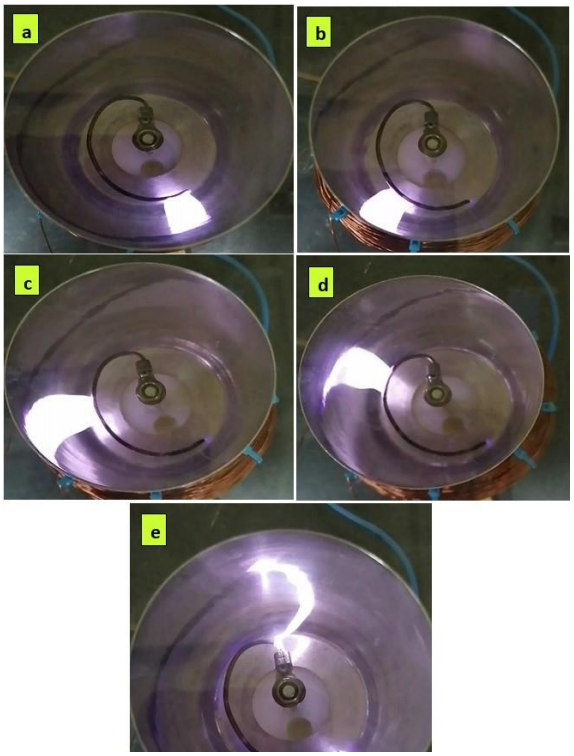

Fig. (7) The original image of the gliding arc discharge at various gas flow rate a) 1L/min, b) 2L/min, c) 3L/min, d) 4L/min and e) 5L/min with magnetic coil 500 turns

Magnetic field application: Once the plasma channel begins to form, a magnetic field is introduced into the system. This can be achieved by using electromagnets. The magnetic field is typically applied parallel to the axis of the discharge (aligned with the central rod).

Magnetic confinement: The magnetic field interacts with the electric current flowing through the plasma, resulting in the Lorentz force. The Lorentz force acts perpendicular to both the current and the magnetic field lines, causing the plasma to experience a radial force. This force helps confine the plasma column towards the axis of the discharge.

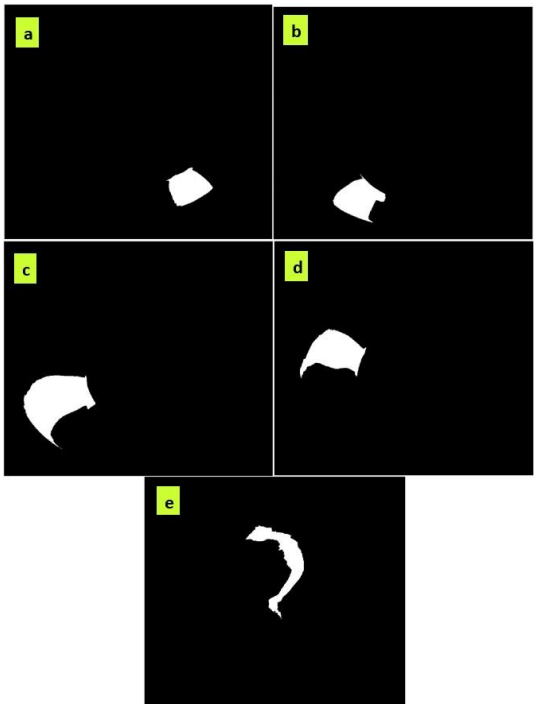

Fig. (8) The image of the gliding arc discharge using the isolation algorithm at various gas flow rate a) 1L/min, b) 2L/min, c) 3L/min, d) 4L/min and e) 5L/min with magnetic coil 500 turns

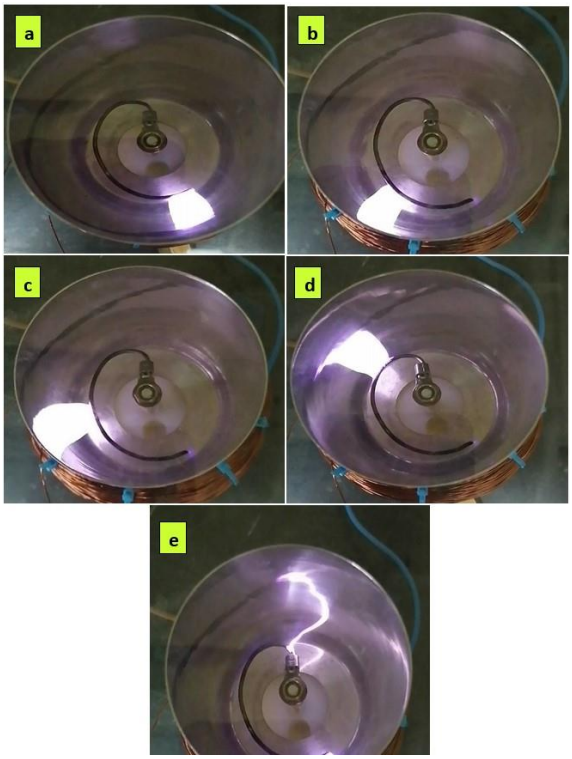

Fig. (9) The original image of the gliding arc discharge at various gas flow rate a) 1L/min, b) 2L/min, c) 3L/min, d) 4L/min and e) 5L/min with magnetic coil 350 turns

Spiral motion: Beneath the influence of the magnetic field, the confined plasma column starts to exhibit a spiral motion called as a "tornado" or "helical" motion. The Lorentz force causes the plasma to rotate

 ISSN (print) 1813-2065, (online) 2309-1673

around the axis of the discharge, resulting in the formation of a spiral-shaped plasma column. The direction and pitch of the spiral motion depend on the orientation and strength of the magnetic field.

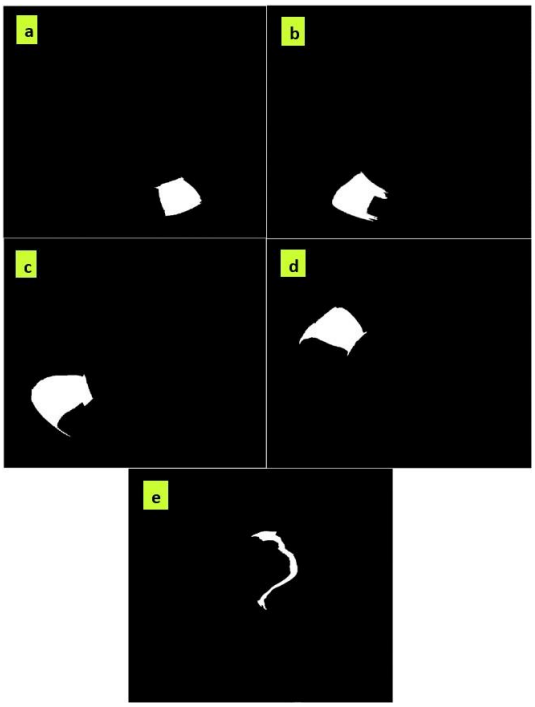

Fig. (10) The image of the gliding arc discharge using the isolation algorithm at various gas flow rate a) 1L/min, b) 2L/min, c) 3L/min, d) 4L/min and e) 5L/min with magnetic coil 350 turns

Enhanced growth and stability: The spiral motion of the plasma column enhances the growth and stability of the arc discharge. The magnetic field aids in maintaining a well-defined and extended plasma column between the voltage electrode and the cylinder wall. The spiral motion increases the length of the plasma channel, providing a larger volume for plasma reactions and energy deposition.

The growth of a magnetically stabilized gliding arc discharge can be influenced by several factors, including the gas flow rate. The gas flow rate affects the behavior and characteristics of the discharge, and ultimately impacts its growth. Here are a few ways in which the gas flow rate can influence the growth of a magnetically stabilized gliding arc discharge:

Plasma stability: The gas flow rate can affect the stability of the plasma in the discharge. An optimal gas flow rate can help maintain a stable and well-defined gliding arc, promoting sustained growth. Insufficient gas flow rates may lead to extinction of the discharge, while excessive flow rates can disrupt the stability of the plasma column.

Plasma temperature: The gas flow rate influences the temperature of the gliding arc plasma. Higher gas flow rates can enhance convective cooling of the discharge, reducing its temperature. Conversely, lower flow rates can result in higher temperatures. The temperature of the plasma affects the ionization and excitation processes within the discharge, influencing its growth and behavior.

Mass transport and reaction kinetics: The gas flow rate affects the transport of reactive species to and from the gliding arc discharge. By modifying the flow rate, the supply of precursor species or reactants can be controlled, thereby influencing the growth and characteristics of the discharge. This can be particularly relevant for processes involving surface modification or chemical reactions within the discharge.

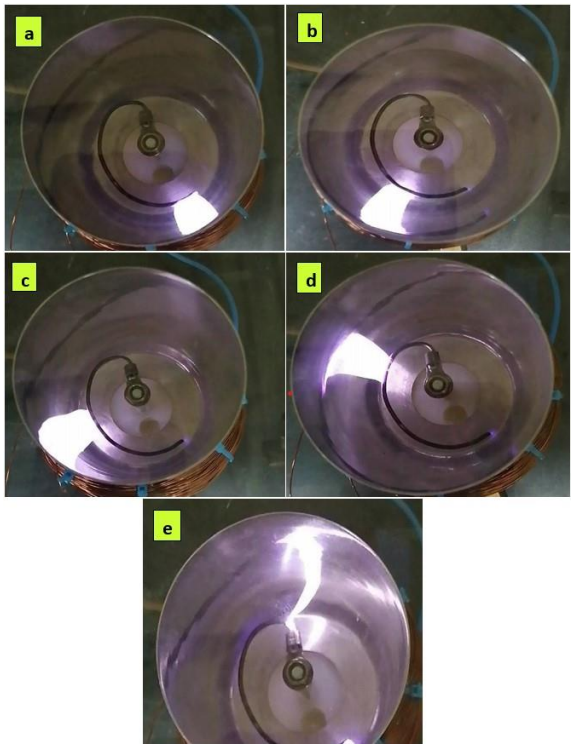

Fig. (11) The original image of the gliding arc discharge at various applied voltage a) 2 kV, b) 4 kV, c) 6 kV, d) 8 kV and e) 10 kV with magnetic coil 500 turns

Figures (11, 12, 13 and 14) represent the increase in arc length with an increase in applied voltage and constant gas flow. When the applied voltage is increased from 2 kV to 10 kV, the length of the arc increases from 12.006 pixels to 31.786 pixels, the area of the arc increases from 134.365 pixels to 384.196 pixels, and the volume of the arc increases from 4724 pixels to 16281 pixels. All of these measurements were taken with a magnetic coil of 500 turns. On the other hand, when using the magnetic coil with 350 turns, the applied voltage increased from 2 to 10 kV, resulting in an increase in the length of the arc from 10.674 to 29.526 pixels. Similarly, the area of the arc increased from 97.915 to 321.014 pixels, and the volume of the arc increased from 2172 to 12460 pixels (see tables 3 and 4).

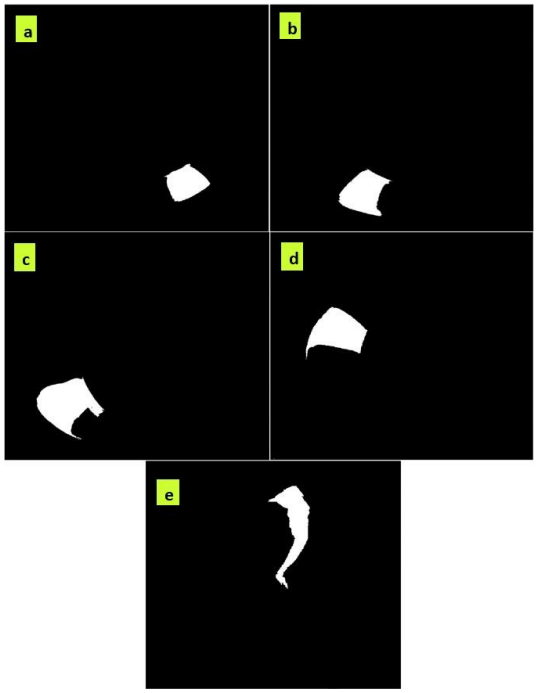

Fig. (12) The image of the gliding arc discharge using the isolation algorithm at various applied voltage a) 2 kV, b) 4 kV, c) 6 kV, d) 8 kV and e) 10 kV with magnetic coil 500 turns

Table (3) The length, area, and volume of the plasma for various applied voltage with magnetic coil 500 turns as calculated with the proposed plasma isolation algorithm

Voltage (kV)	Length (Pixel)	Area (Pixel)	Volume (Pixel)
2	12.006	134.365	4724
4	15.338	219.651	9227
6	17.814	262.55	10850
8	22.021	307.854	12790
10	31.786	384.196	16281

Table (4) The length, area, and volume of the plasma for various applied voltage with magnetic coil 350 turns as calculated with the proposed plasma isolation algorithm

Voltage (kV)	Length (Pixel)	Area (Pixel)	Volume (Pixel)
2	10.674	97.915	2172
4	16.086	158.464	8568
6	17.632	262.115	10245
8	21.758	283.883	11206
10	29.526	321.014	12460

The effect of changing the amount of high voltage on the growth of a magnetically stabilized sliding arc discharge can be significant. This effect can be summarized in the following points:

Arc length and stability: Increasing the high voltage can lead to a longer arc length in the discharge. This extended arc can contribute to enhanced plasma growth and increased energy deposition. However, excessively high voltages can also cause instabilities and disrupt the stability of the sliding arc.

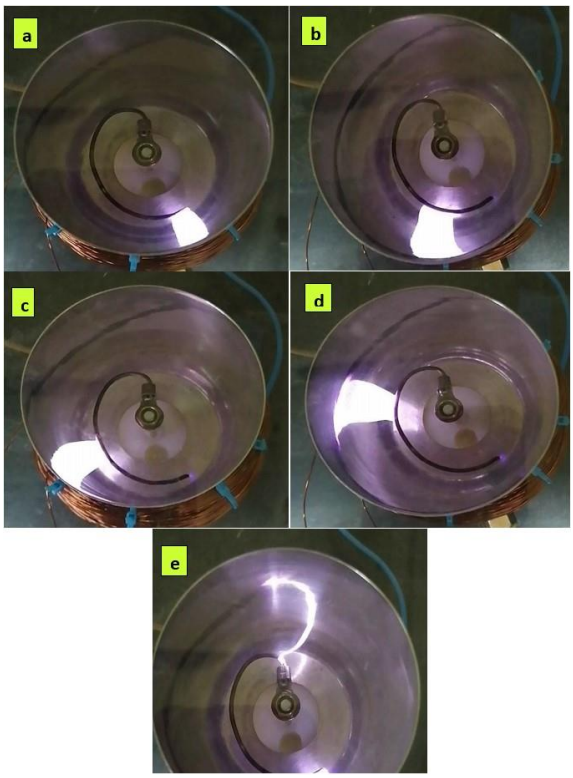

Fig. (13) The original image of the gliding arc discharge at various applied voltage a) 2 kV, b) 4 kV, c) 6 kV, d) 8 kV and e) 10 kV with magnetic coil 350 turns

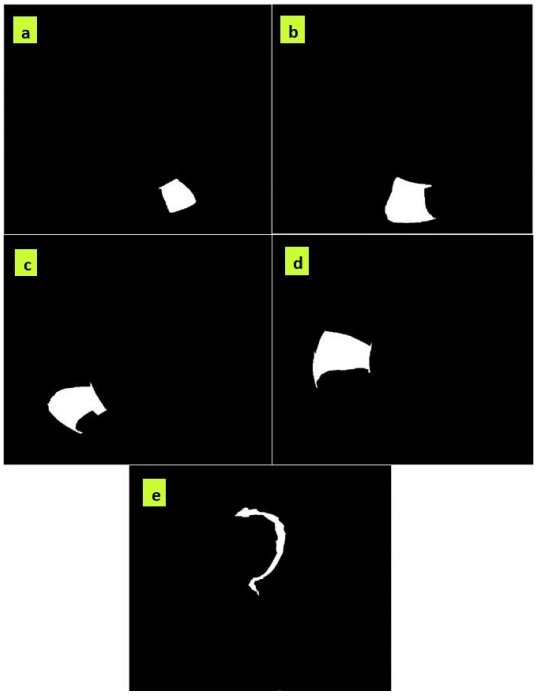

Fig. (14) The image of the gliding arc discharge using the isolation algorithm at various applied voltage a) 2 kV, b) 4 kV, c) 6 kV, d) 8 kV and e) 10 kV with magnetic coil 350 turns

Plasma temperature: Higher voltages generally result in higher plasma temperatures. This increase in temperature affects the ionization and excitation processes within the discharge, influencing the

 ISSN (print) 1813-2065, (online) 2309-1673

growth and behavior of the plasma. It can impact reaction rates and the formation of reactive species, which ultimately influence the discharge's growth characteristics.

Gas ionization: The high voltage provides the energy necessary for gas ionization in the discharge. As the voltage increases, more gas molecules become ionized, leading to a denser plasma and a potentially larger plasma volume. This increased ionization can impact the discharge growth by altering the concentration of charged particles and their interactions.

Electric field strength: The high voltage determines the strength of the electric field between the electrodes. This electric field affects the motion and behavior of charged particles within the discharge. Changes in the electric field strength can influence the distribution and transport of ions and electrons, impacting the growth patterns and dynamics of the sliding arc discharge.

Energy deposition: The amount of high voltage directly correlates with the energy deposited into the discharge. Increasing the voltage can lead to higher energy deposition, which can affect the physical and chemical processes occurring within the plasma. This energy input influences the growth rate, reactivity, and efficiency of various plasma-mediated processes.

4. Conclusions

This study examined the complex relationship between gas flow, applied voltage, and external magnetic fields on GAD plasma. We found that these elements significantly affect the arc's length, area, and volume through careful experimentation and analysis. Our findings show that the external magnetic field is crucial to arc rotation in the GAD's top zone. The association between applied voltage and arc characteristics confirms the complex interaction between electrical potential and plasma activity. The significant differences in arc dimensions under different coil turn configurations demonstrate the complex impacts of magnetic field intensity on plasma properties. This research improves our grasp of GAD phenomena and non-thermal plasma behavior theory and practice. By understanding the complicated relationship between gas movement, voltage, and magnetic fields, we can improve environmental protection, materials processing, and more.

References

[1] A. Fridman, **"Plasma Chemistry"**, Cambridge University Press (NY, 2008), pp. 200-207.

[2] W.I. Yaseen, "The Electron Temperature and the Electron Density Measurement by Optical Emission Spectroscopy in Laser Produced Aluminum Plasma in Air", *Iraqi J. Sci.*, 57(2C) (2016) 1584-1590.

[3] O.A. Hammadi et al., "Employment of Magnetron to Enhance Langmuir Probe Characteristics of Argon Glow Discharge Plasma in Sputtering System", Iraqi J. Appl. Phys., 12(4) (2016) 19-28.

[4] O.A. Hammadi, "Synthesis and Characterization of Polycrystalline Carbon Nitride Nanoparticles by Fast Glow Discharge-Induced Reaction of Methane and Ammonia", Adv. Sci. Eng. Med., 11(5) (2019) 346-350.

[5] J. Zhu et al., "Spatiotemporally resolved characteristics of a gliding arc discharge in a turbulent air flow at atmospheric pressure", *Phys. Plasmas*, 24(1) (2017) 013514-10.

[6] M.K. Khalaf, F.J. Kadhim and O.A. Hammadi, "Effect of Adding Nitrogen to the Gas Mixture on Plasma Characteristics of a Closed-Field Unbalanced DC Magnetron Sputtering System", Iraqi J. Appl. Phys., 10(1) (2014) 27-31.

[7] O.A. Hammadi, "Analysis of Secondary Electron Emission in Gas Glow Discharges Used for Thin Film Deposition Processes", Iraqi J. Appl. Phys., 16(1) (2020) 15-20.

[8] J. Sprott, "Physics Demonstrations: A Sourcebook for Teachers of Physics", Madison, WI: University of Wisconsin Press (2006).

[9] O.A. Hammadi et al., "Magnetic Field Distribution of Closed-Field Unbalanced Dual Magnetrons Employed in Plasma Sputtering Systems", Iraqi J. Appl. Phys., 12(3) (2016) 35-42.

[10] K.A. Aadim, "Spectroscopic study the plasma parameters for SnO_2 doped ZnO prepared by pulse Nd: YAG laser deposition", *Iraqi J. Phys.*, 17(42) (2019) 125-135.

[11] D. Staack et al., "Spectroscopic studies and rotational and vibrational temperature measurements of atmospheric pressure normal glow plasma discharges in air", *Plasma Sour. Sci. Technol.*, 15(4) (2006) 818-827.

[12] S. Gangoli, A. Gutsol and A. Fridman, "A non-equilibrium plasma source: magnetically stabilized gliding arc discharge: II. Electrical characterization", *Plasma Sour. Sci. Technol.*, 19(6) (2010) 065004.

[13] C. Ming, and D. Jing, "The application of non – thermal plasma generated by gliding arc discharge", *Prog. Ener. Combus. Sci.*, 14 (2012) 2-16.

[14] H. Kim, "Plasma gliding arc discharge", *Euro. Phys. J. Appl. Phys.*, 120 (2013) 423-428.

[15] T.A. Hameed and S.J. Kadhem, "Plasma diagnostic of gliding arc discharge at atmospheric pressure", *Iraqi J. Sci.*, 60(12) (2019) 2649-2655.

[16] F.A. Lazema and H.R. Humud "A low-cost gliding arc reverse vortex flow plasma system for laboratory purposes", *AIP Conf. Proc.*, 2394 (2022) 090040.

[17] O.A. Hammadi et al., "Operation Characteristics of a Closed-Field Unbalanced Dual-Magnetrons

Plasma Sputtering System", Bulg. J. Phys., 41(1) (2014) 24-33.
[18] S.P. Gangoli, A.F. Gutsol and A.A. Fridman, "A Non-equilibrium plasma source: magnetically stabilized gliding arc discharge: I. Design and diagnostics", *Plasma Sour. Sci. Technol.*, 19 (2010) 065003.
[19] A.A.-K. Hussain, and F.J. Moaen. "Diagnostics of Magnesium-Aluminum alloy plasmas produced by laser induced breakdown spectroscopy", *Iraqi J. Sci.*, 59(1A) (2018) 75-85.
[20] J. Zhu et al., "Effects of gliding arc discharge penetrating a premixed flame", *Proceedings of the European Combustion Meeting, Budapest* (2015).
[21] S.N. Mazhir et al., "The Effect of Gas Flow on Plasma Parameters Induced by Microwave", *Baghdad Sci. J.*, 15(2) (2018) 205-210.
[22] S.Y. Lu et al., "Influence of gas dynamics on arc dynamics and the discharge power of a rotating gliding arc", *Phys. Plasmas*, 19(7) (2012) 209.
[23] O.A. Hammadi, "New Technique to Synthesize Silicon Nitride Nanopowder by Discharge-Assisted Reaction of Silane and Ammonia", Mater. Res. Exp., 8(8) (2021) 085013.
[24] K. Sasujit, N. Dussadee and N. Tippayawong, "Overview of tar reduction in biomass-derived producer gas using non-thermal plasma discharges", *Maejo Int. J. Sci. Technol.*, 13(1) (2019) 42-61.
[25] S.N. Mazhir et al., "Effects of Gas Flow on Spectral Properties of Plasma Jet Induced by Microwave", *Baghdad Sci. J.*, 15(1) (2018) 81-86.
[26] A.N. Ahmed, M.J. Alwazzan and M.A. Ismael, "Study effects of pulse laser energy on human primary teeth and extraction caries area by using image processing techniques", *NeuroQuantol.*, 18(6) (2020) 36-44.
[27] M.J. Alwazzan, M.A. Ismael and M.K. Hussain, "Brain Tumour Isolation in MRI Images Based on Statistical Properties and Morphological Process Techniques", *J. Phys. Conf. Ser.*, 1279 (2019) 12018.
[28] M.J. Alwazzan, "Low cost blood vein detection system based on near-infrared LEDs and image-processing techniques", *Polish J. Med. Phys. Eng.*, 26(2) (2020) 61-67.

 ISSN (print) 1813-2065, (online) 2309-1673

IRAQI JOURNAL OF APPLIED PHYSICS
Vol. 19, No. 4C, December 2023, pp. 243-250

Characterization of ZnO-SnO_2 Nanostructures Prepared by Thermal Evaporation Technique as Gas Sensor

Abdulkareem A. Hussain
Qahtan N. Abdullah

Department of Physics, College of Education for Pure Sciences, University of Tikrit, Tikrit, IRAQ

The current study aims to prepare sensor NO_2 gas by synthesis and doping of nanocomposites of zinc oxide and tin oxide utilizing vacuum thermal evaporation technique. The structural and optical characteristics were determined and studied using x-ray diffraction (XRD), atomic force microscopy (AFM), field-emission scanning electron microscopy (FE-SEM), UV-visible spectroscopy, and Fourier-transform infrared (FTIR) analysis. At an operating temperature of 200°C, a pure ZnO sensor demonstrated a sensing response for NO_2 gas of 75.9% with an average reaction time of about 8.61 s. While doping of SnO_2 had an effect in increasing the sensitivity value of the ZnO-SnO_2 sensor at different operating temperatures

Keywords: Zinc oxide; Tin oxide; Nanocomposites; Gas sensors
Received: 02 September 2023; **Revised:** 21 September; **Accepted:** 28 September 2023

1. Introduction

Numerous dangerous gases, including CO, NO_2, NH_3, CH_4, ethanol, methanol, and benzene, are routinely produced daily from industrial and agricultural activities. They are also discharged as part of automobile exhaust emissions. Others, such as NO_2 and toluene, are detrimental to human health and the environment; when their concentrations are above a critical threshold, some become explosive when exposed to air as H_2 and CH_4. It is crucial to create high-precision gas sensors with in situ and real-time monitoring capabilities, high sensitivity, quick response, strong selectivity, and low limit of detection (LOD) [1,2]. High-performance gas sensors with high sensitivity, selectivity, and response speed are still needed to improve gas detection. SnO_2, ZnO, CuO, CdO, WO_3, and TiO_2 are metal oxides that can identify combustible, reducing, or oxidizing gases [3]. Several research teams have recently concentrated on nanocomposite materials for gas sensing applications, such as CdO-ZnO, ZnO-SnO_2, and ZnO-In_2O_3 [4,5]. Tin dioxide (SnO_2) and zinc oxide (ZnO) are valuable gas-sensing materials. They both are n-type materials, and their electrical conductivity depends on the density on the surface of pre-adsorbed oxygen ions. According to their literature review, the physical and chemical characteristics of SnO_2 and ZnO are adaptable for gas sensing applications. The synthesis process is another essential variable. Due to the synergistic effect between the two components, using a ZnO:SnO_2 composite material is a wise decision since it modifies the properties of the materials to raise the sensitivity of metal oxide gas sensors [6]. ZnO is a significant wide-bandgap semiconductor with a direct bandgap of ~3.37 eV. It is a material with great potential for UV nano-optoelectronic devices and lasers at room temperature [7]. It is widely recognized that doping significantly impacts the fundamental physical characteristics of semiconductors with certain elements, such as electrical and optical properties, which are essential for their practical use. Numerous groups have reported the creation of doped ZnO nanoparticles and nanostructured films, and they have also investigated the characteristics of these doped nanostructures in terms of electrical, optical, and sensor functions [8–11]. The choice of material has a significant impact on the behavior of the gas sensor. The sensor's material should be conductive when reacting with gases, especially at the semiconductor's surface component [12,13]. ZnO and SnO_2 are examples of n-type materials having relatively few oxygen adsorption sites that are appropriate for sensing applications to build potential barriers. In addition, adding additives to the semiconductor material may enhance the gas sensor's performance [14]. The advantages of composite sensors, including being more thermally stable, having high electron mobility, and having many hetero-contacts between the phase and the catalytic activity of the sensing matrix, can be controlled [12,15,16].

This research aims to prepare NO_2 gas sensor for pure ZnO films then doped with 7 wt.% SnO_2. These films showed different responses to gaseous sensitization at different operating temperatures.

2. Experimental Part

This paper used the vacuum thermal evaporation technique to prepare pure ZnO thin films and doping with SnO_2 by ratio (7 wt.%). They were heated-resistant in a molybdenum boat under a pressure of about 3×10^{-5} Torr. The distance between the glass

substrates and the molybdenum boat was 12 cm. The thin films in this study were deposited on glass substrates made of glass strips with a thickness of 1mm and dimensions 26×76 mm^2 after cleaning the glass substrates. Zinc powder (Zn) with a purity of 99.95 was used, mixed, and milled by an agate mill with the weight ratios of tin (Sn) with a purity of 99.95 in weight ratio of 7 wt.% of Sn. Finally, the films are extracted from the vacuum thermal evaporation after deposition and then placed in the furnace for thermal oxidation at a temperature of 450°C for two hours to obtain pure ZnO films and ZnO films doped with SnO_2.

3. Results and Discussion

In order to confirm the phase structure of the produced pure ZnO thin films, the XRD pattern in Fig. (1) shows the pure ZnO and doped with 7 wt.% SnO_2, it can be seen that the preferred orientation peaks of ZnO at (002) and angle 34.889° and that all films are polycrystalline with a hexagonal structure. Furthermore, no diffraction peaks from other impurities were detected. This figure also depicts that the intensity of the peaks increased with the doping. These results matched (JCPDS card 01-075-1526). The crystallite size (D) was calculated using the Scherrer's formula [17]:

$$D = \frac{0.9\lambda}{\beta cos\theta} \quad (1)$$

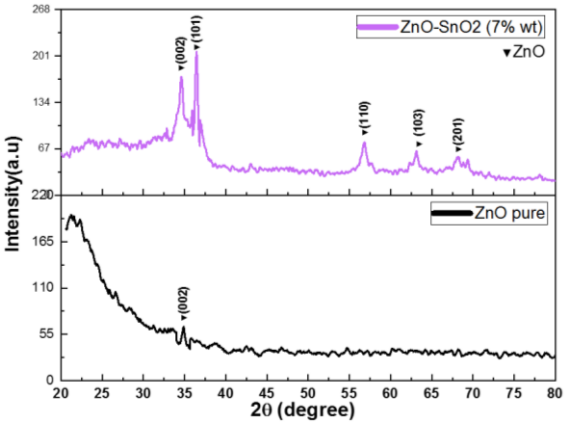

Fig. (1) The XRD patterns of pure ZnO film as well as ZnO film doped with 7 wt.% SnO_2

It was found that the crystal size decreases when doping with 7 wt.% SnO_2; the reason is stress arising from the entry and diffusion of impurity atoms in the material and their possession of sites in the crystal lattice, which causes the sites of the 2θ vertices in XRD pattern to be displaced to greater or less dependent values on the ionic diameter of the atoms of the lattice when compared with the host material in the lattice. On the other hand, the stress occurring in the crystal lattice was calculated using the equation [18]:

$$\sigma = 232.75 \frac{(C - C_\circ)}{C_\circ} \quad (2)$$

where $C_\circ$ is the lattice constant from JCPDS card, C is the lattice constant calculated in practice, and σ is the stress in the crystal lattice

It was found that the stress in the crystal lattice increases with increasing doping; the cause of stress is due to changes in the order of atoms and the random distribution of impurities within the crystal lattice or atoms have an irregular arrangement, they cause distortions in the crystal lattice and increase stress, as shown in table (1).

The surface morphology is studied using atomic force microscopy (AFM), which is crucial for gas sensor applications. Particle size and surface roughness affect how gases interact with surfaces. Figures (2) and (3) show AFM images of pure ZnO film and ZnO film doped with 7 wt.% SnO_2 on glass substrates. These surfaces contain pyramid-shaped granules with sharp edges. The diameter size of these films is 6.351 nm for pure ZnO film and 5.055 nm for doped film, with an average roughness of 233.6 nm and 100.8 nm, respectively. The decreases in grain size with increasing the doping ratio may be related to forming composite structures. Table (2) below shows our results from the atomic force microscope analysis AFM [19].

Table (2) The change in the grain size rate and surface roughness rate of pure ZnO film doped with SnO_2 (7 wt.%) using AFM analysis

Sample	Roughness Average (nm)	Root mean Square (nm)	Diameter Size (nm)
Pure ZnO	233.6	8.440	6.351
ZnO-SnO_2 (7 wt.%)	100.8	6.967	5.055

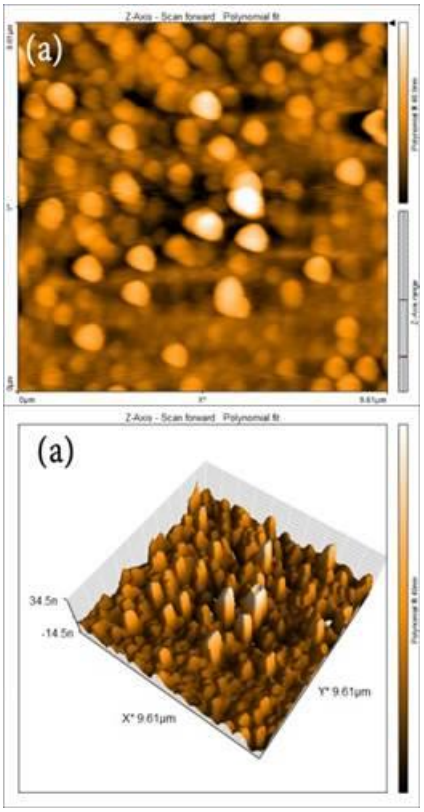

 ISSN (print) 1813-2065, (online) 2309-1673

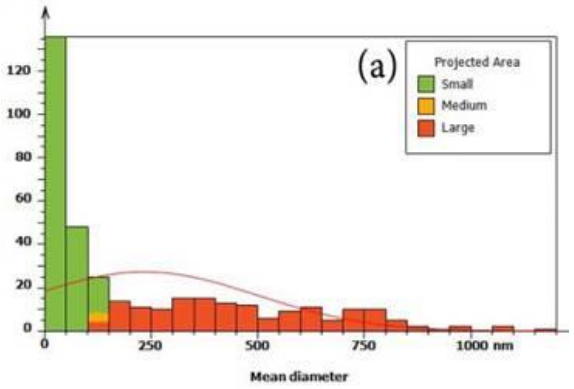

Fig. (2) Surface morphology for pure ZnO film

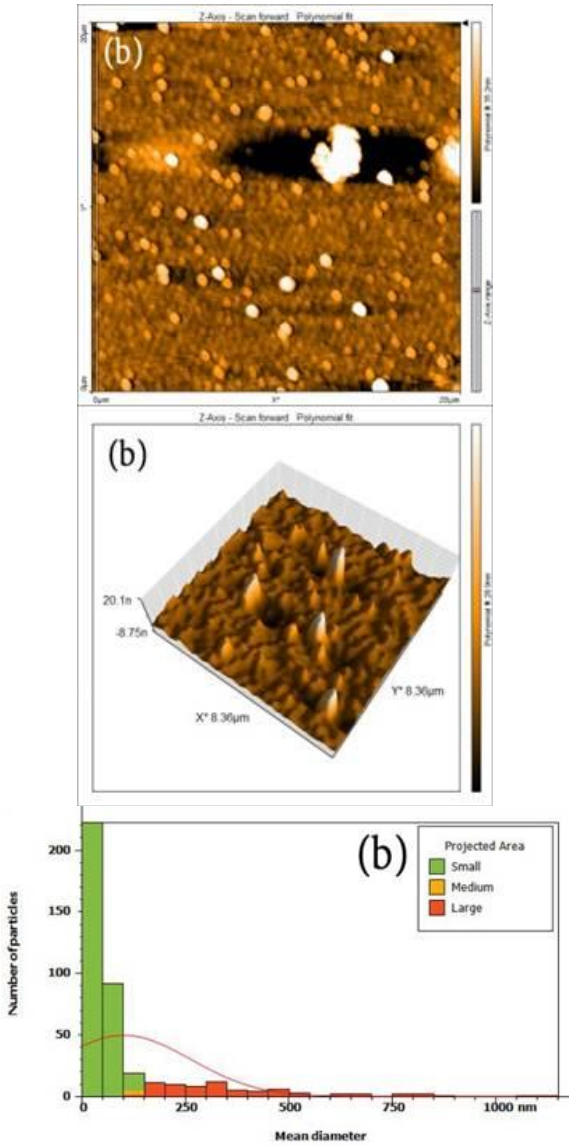

Fig. (3) Surface morphology for ZnO film doped with 7 wt.% SnO_2

Figure (4) presents the FE-SEM images of the ZnO thin films (pure and doped) by the thermal evaporation method in a vacuum. In order to determine the thickness of the prepared pure ZnO film, its thickness was measured using the cross-section technique using a scanning electron microscope. It was found that the thickness of the film was about 144 mm, as shown in Fig. (4a). The FE-SEM images show that pure ZnO films are nanostructures with stone-like shapes, with diameters ranging from 32-85 nm, as shown in Fig. (4b). The effect of doping with 7 wt.% from SnO_2 on the ZnO films led to a change in the shapes of the films' images, as they became softer and had delicate sand-like shapes, which are round granules with diameters ranging from 10-40 nm, as in Fig. (4c) [20]. On the other hand, knowing the proportions of the elements involved in the formation of these films, the analysis of the constituent elements By EDX of pure ZnO film and doped with 7 wt.% SnO_2. Figure (4d) shows that the zinc oxide film contains only oxygen and zinc and that the intensity of the zinc peak is higher than the oxygen peak. The reason may be the duration of exposure of the film to oxidation. The process of doping ratio 7 wt.% from SnO_2 on the ZnO films led to the appearance of a peak belonging to tin (Sn), and the percentage of this peak is close to the added percentage of impurities, as in Fig. (4e) [21].

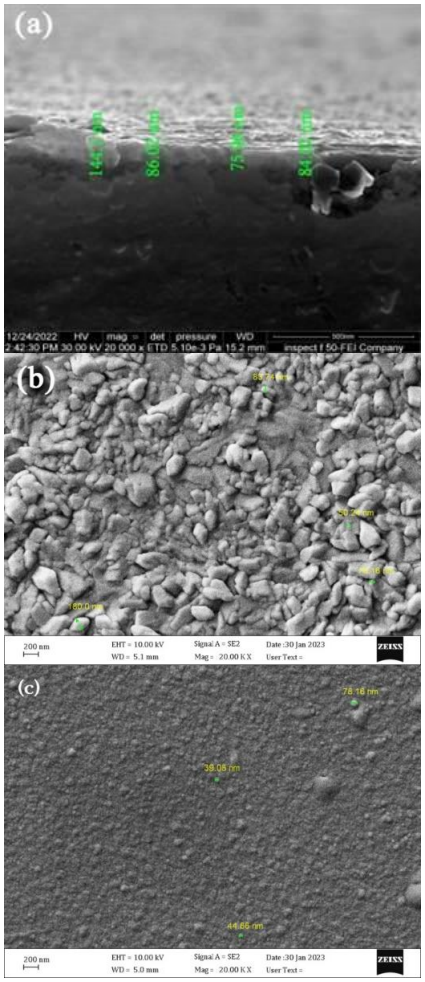

(a)

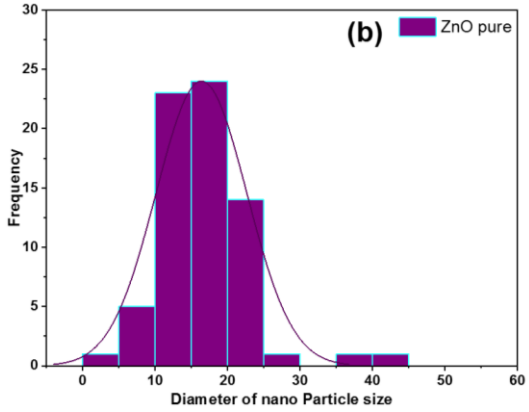

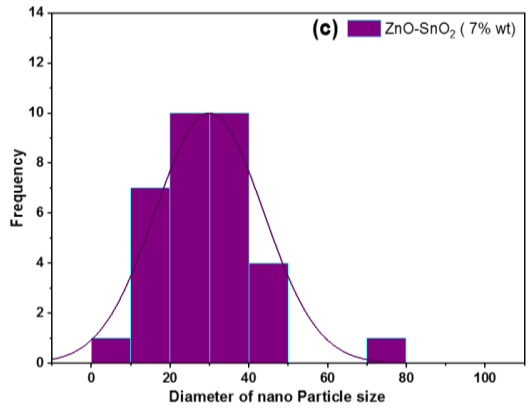

(b) and (c)

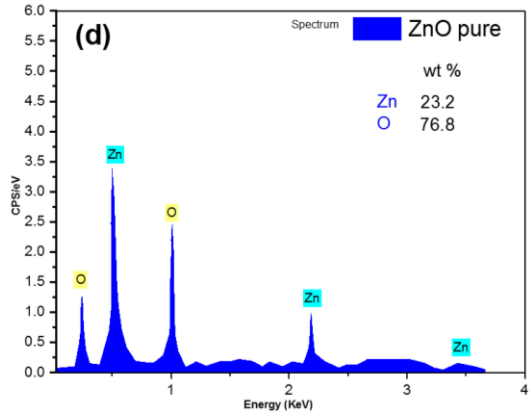

(d)

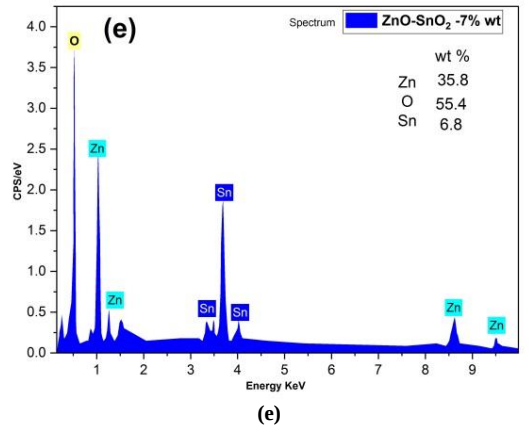

(e)

Fig. (4) (a) The cross-sectional images of pure ZnO films, (b,c) the FE-SEM images, (d,e) the EDX spectra of the pure ZnO film and ZnO film doped with 7 wt.% SnO_2

They used the thermal evaporation method in a vacuum for preparing ZnO-SnO_2 films. In order to study the optical characteristics of pure ZnO thin film and ZnO thin film doped with 7 wt.% SnO_2. These characteristics are essential in evaluating the significance of films in their employment as a gas sensor. The absorption coefficient may be readily estimated from the absorbance (A) and the film thickness (t) using the following equation (3) [22]:

$$\alpha = 2.303\, A/t \qquad (3)$$

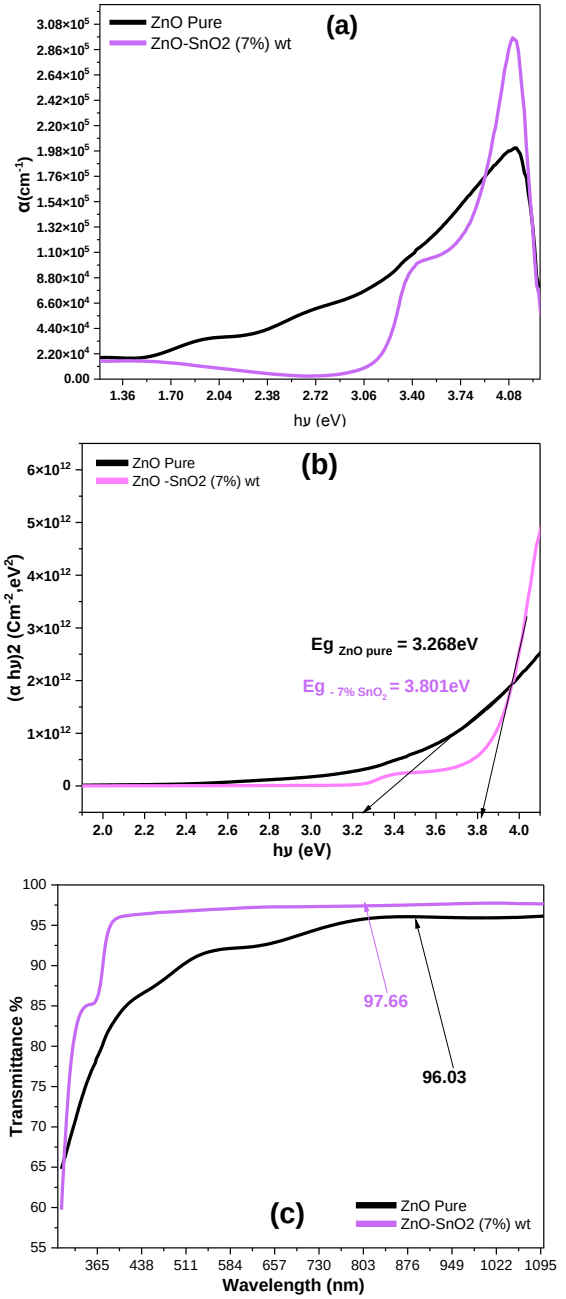

Fig. (5) (a) The absorption coefficient, (b) the optical energy gap, and (c) transmission spectra of the pure ZnO film and ZnO film doped with 7 wt.% SnO_2

It is clear from Fig. (5a), for pure ZnO that the absorption coefficient gradually increases by a small amount with increasing photon energy, and for the

 ISSN (print) 1813-2065, (online) 2309-1673

range of energies (hυ>3eV), this result helps us predict the essential absorption edge, which is attributed to the absorption processes arising from the transfer of electrons from the valence band to the conduction band. This means that the transitions from the basic absorption processes are direct transfers. As for doping, it led to an apparent decrease in the values of the absorption coefficient, especially at low photon energies, and this also appears clear through the essential absorption edge; the values of the absorption coefficient were also more significant, which suggests the occurrence of direct electronic transfers as well. This result is because the doping led to the formation (generation) of actual donor levels inside the energy gap and near the conduction band, which in turn worked to absorb low-energy photons [20]. In Fig. (5b), the band gap (E_g) of the films ranged between 3.268 to 3.801eV and also increased with the increase of the doping from 0 to 7 wt.%. Unstructured flaws may be responsible for these band gap increases by lowering the density of localized states in the band gap and so raising the energy, and this is consistent with the results of XRD, where the crystalline size decreases upon doping. Analysis of thin films can benefit from the transmittance characteristic. However, when doping with SnO_2 (7 wt.%), an increase in the transmittance was observed, as it increased sharply at the wavelength 395 nm at the central absorption edge region, which confirms that these films have a comprehensive energy gap and are of the direct type [23].

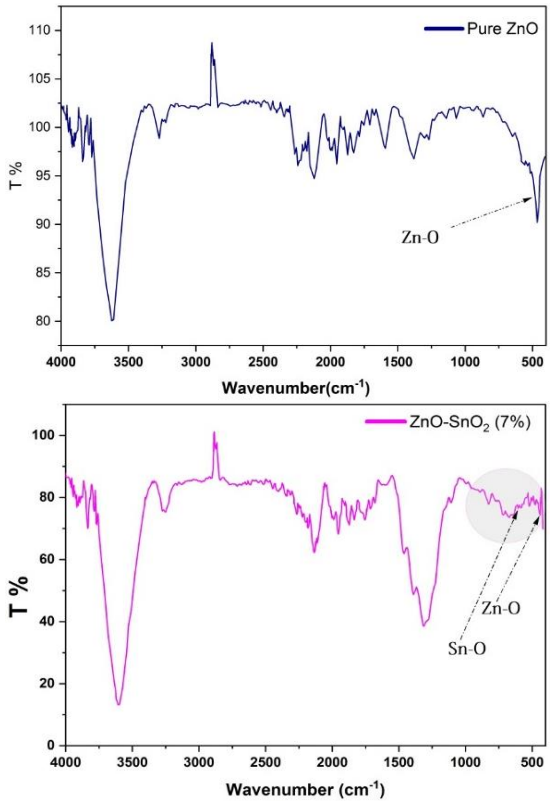

Fig. (6) FTIR spectra for (a) pure ZnO, and ZnO doped with 7 wt.% SnO_2

Figure (6a) depicts the FTIR spectra of pure ZnO nanoparticles doped with 7 wt.% SnO_2. The vibration of Zn-O bonds is reflected in high frequency bands between the region of 400-550 cm^{-1}. When doping ratio is 7 wt.%, a peak appeared that belonged to the tin oxide Sn-O bond at wave number 581 cm^{-1}. It is noted from Fig. (6b) that the peak is of low intensity, and the reason may be attributed to the small percentage of doping [24].

The gas sensitivity of pure and doped ZnO films was tested using oxidizing gas (NO_2). The main factors determining the gas sensing mechanism for thin films are the nano-distances between atoms, operating temperature, selectivity, response time, and recovery time. The sensing properties of all films were examined as a function of time to determine the sensitivity of the films to their absorption of oxidized gas, as shown in figures (7) and (8). The sensitivity to the gas increases with the temperature of the pure ZnO film within the range of degrees (25, 100, 150, and 200°C), where at a temperature of 25°C, the sensitivity was 38.9% and then gradually increases until it reaches 75.9% at temperature of 200°C. When the temperature increases, it can affect the dynamics of the chemical process. In some gas sensors, the gas reacts with the surface of the film chemically. The speed of a chemical reaction is related to temperature, as temperature increases the speed of the reaction. This can lead to increased response and recovery times, as the sensor takes longer to react to the gas and return to the original state after being exposed to the gas. On the other hand, when doping with 7 wt.% of tin oxide, we note that the sensitivity increased its values from the rest of the ratios. The reason is due to the regularity of the crystal structure, which made the membrane sensitive to these different degrees of temperature, and this was shown by the tests (XRD) for these films, where the sensitivity was 79.2% at 25°C and then increased to 80.5% at 100°C. However, the response and recovery times have not improved much at doping with SnO_2. The decrease in grain size shown in the AFM images may be the reason for the improved sensor response increase with the addition of tin oxide. The small particle size allows an immense amount of nitrogen oxide gas molecules to react with the surface of the sensor ZnO-SnO_2. However, when NO_2 gas reacts on the ZnO surface and even at lower working temperatures, it absorbs electrons from physisorbed oxygen species (O_2) and becomes desorbed as NO_2 gas molecules [25-30]. The figures below show the response and recovery times at four operating temperatures for pure ZnO and doped with SnO_2 films. Higher temperatures accelerate the reaction kinetics between gas molecules and sensing materials, leading to a faster response time of the sensor.

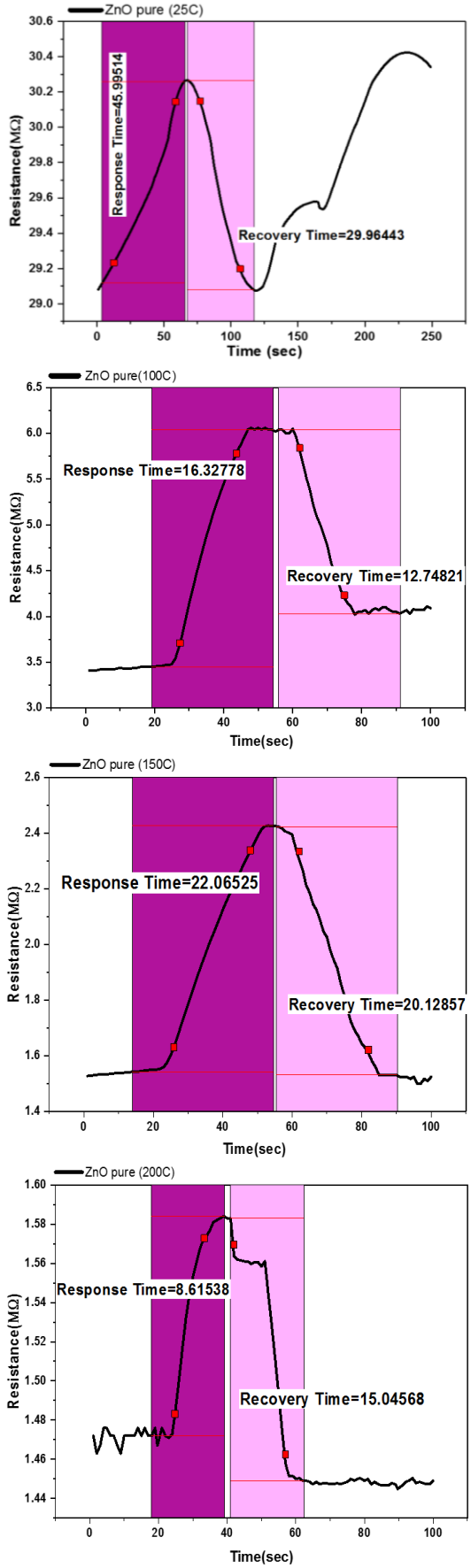

Fig. (7) The response and recovery times of pure ZnO thin film at four operating temperatures (25, 100, 150, and 200°C)

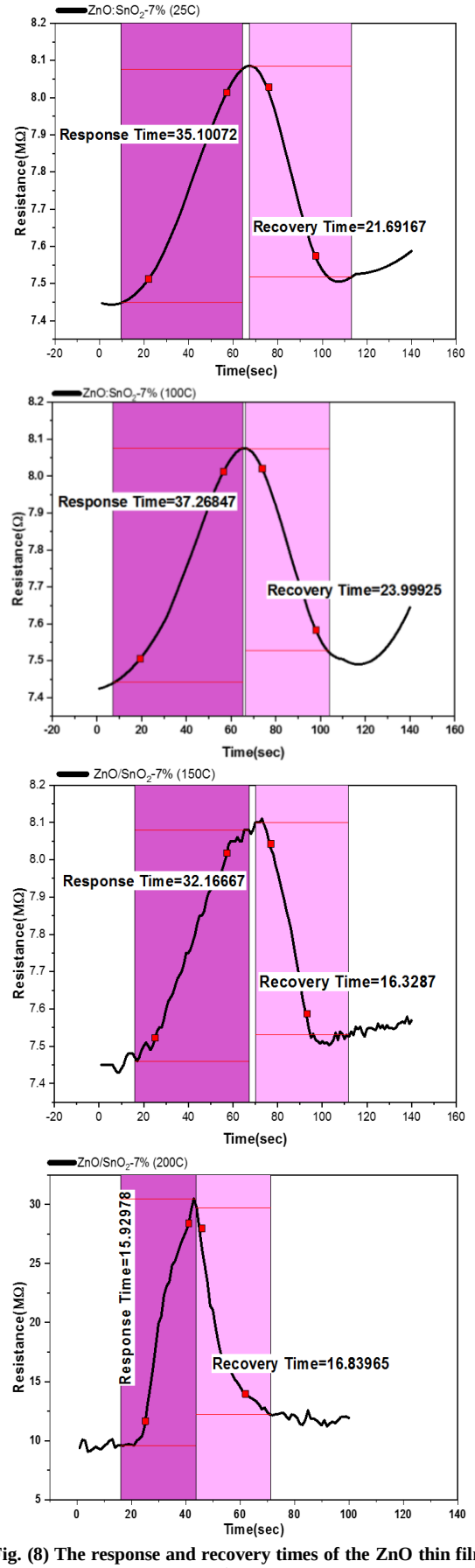

Fig. (8) The response and recovery times of the ZnO thin film doped with 7 wt.% SnO_2 at four operating temperatures (25, 100, 150, and 200°C)

 ISSN (print) 1813-2065, (online) 2309-1673

4. Conclusions

The pure ZnO as well as ZnO films doped with SnO_2 are polycrystalline with a hexagonal structure. The crystallite size decreases with increasing SnO_2 doping. The optical properties showed an increase in the value of the optical energy gap and transmittance with a decrease in the absorption coefficient for pure and doped zinc oxide films. The sensing properties of the target gas showed an increase in sensitivity when doping added for the ZnO films. Moreover, increasing the operating temperature improved both response and recovery times with an increase in the sensitivity value of the gas sensor.

References

[1] M. Jerrett et al., "Validating novel air pollution sensors to improve exposure estimates for epidemiological analyses and citizen science", *Enviro. Res.*, 158 (2017) 286-294.
[2] Z. Al Barakeh et al., "Development of a normalized multi-sensors system for low cost on-line atmospheric pollution detection", *Sens. Actuat. B: Chem.*, 241 (2017) 1235-1243.
[3] M. Batzill and U. Diebold, "The surface and materials science of tin oxide", *Prog. Surf. Sci.*, 79(2-4) (2005) 47-154.
[4] A.K. Sharma et al., "Nanostructured CdO–ZnO composite thin films for sensing application", *J. Mater. Sci. Mater. Electron.*, 31 (2020) 20932-20944.
[5] K. Zhang et al., "Ultra-sensitive ethanol gas sensors based on nanosheet-assembled hierarchical ZnO-In2O3 heterostructures", *J. Hazard. Mater.*, 391 (2020) 122191.
[6] C. Wang et al., "Metal oxide gas sensors: sensitivity and influencing factors", *Sensors*, 10(3) (2010) 2088-2106.
[7] M.H. Huang et al., "Room-Temperature Ultraviolet Nanowire Nanolasers", *Science*, 292(5523) (2002) 1897-1899.
[8] C.H. Jung et al., "Transparent amorphous In–Ga–Zn–O thin film as function of various gas flows for TFT applications", *Thin Solid Films*, 517(14) (2009) 4078-4081.
[9] E. Pál et al., "Hydrothermal synthesis of prism-like and flower-like ZnO and indium-doped ZnO structures", *Coll. Surf. Sci A: Physicochem. Eng. Aspects*, 340(1-3) (2009) 1-9.
[10] C.H. Ahn et al., "Enhancement of band-edge emission of ZnO from one-dimensional ZnO/MgZnO core/shell nanostructures", *J. Phys. D: Appl. Phys.*, 42(11) (2009) 115106.
[11] P.K. Sharma et al., "Effect of iron doping concentration on magnetic properties of ZnO nanoparticles", *J. Magn. Magn. Mater.*, 321(17) (2009) 2587-2591.
[12] G. Korotcenkov, "Metal oxides for solid-state gas sensors: What determines our choice?", *Mater. Sci. Eng. B*, 139(1) (2007) 1-23.
[13] C. Wang et al., "Metal oxide gas sensors: sensitivity and influencing factors", *Sensors*, 10(3) (2010) 2088-2106.
[14] N. Singh et al., "Chemical sensing investigations on Zn–In2O3 nanowires", *Sens. Actuat. B Chem.*, 171 (2012) 244-248.
[15] J.H. Yu and G.M. Choi, "Electrical and CO gas-sensing properties of ZnO/SnO_2 hetero-contact", *Sens. Actuat. B Chem.*, 61(1-3) (1999) 59-67.
[16] N.D.M. Sin et al., "Improvement sensitivity humidity sensor based on ZnO/SnO_2 cubic structure", *IOP Conf. Ser.: Mater. Sci. Eng.*, 46(1) (2013).
[17] D. Lu et al., "ZnO nanostructures decorated hollow glass microspheres as near infrared reflective pigment", *Ceram. Int.*, 43(12) (2017) 9164-9170.
[18] P.T. Rao et al., "Physical properties of ZnO thin films deposited at various substrate temperatures using spray pyrolysis", *Physica B: Cond. Matter*, 405(9) (2010) 2226-2231.
[19] S.M. Hanfoosh and N.K. Hassan, "Optical Properties of Mixed ZnO:Fe_2O_3 Grown via Pulsed Laser Deposition", *Iraqi J. Sci.*, 60(9) (2019) 2009-2014.
[20] S. Mu et al., "Preparation of polyimide/zinc oxide nanocomposite films via an ion-exchange technique and their photoluminescence properties", *J. Nanomater.*, 2011 (2011) 1-10.
[21] Z.H. Bakr et al., "Characteristics of ZnO–SnO_2 composite nanofibers as a photoanode in dye-sensitized solar cells", *Ind. Eng. Chem. Res.*, 58(2) (2018) 643-653.
[22] H.S. Al-Jumaili and M.N. Jasim, "Preparation and Characterization of ZnO:SnO_2 Nanocomposite Thin Films on Porous Silicon as H_2S Gas Sensor", *J. Ovonic Res.*, 15 (2019) 81-87.
[23] J.F. Mohammad and S.M. Abed, "Preparation and characterazation of aluminum doped nanocrystalline zinc oxide for solar cells applications", *J. Ovonic Res.*, 15(1) (2019) 61-67.
[24] W. Ali et al., "Effect of calcination temperature on the photoactivities of ZnO/SnO_2 nanocomposites for the degradation of methyl orange", *Mater. Chem. Phys.*, 213 (2018) 259-266.
[25] E. Oh et al., "High-performance NO_2 gas sensor based on ZnO nanorod grown by ultrasonic irradiation", *Sens. Actuat. B Chem.*, 141(1) (2009) 239-243.
[26] R.K. Sonker et al., "Low-temperature sensing of NO_2 gas using SnO_2-ZnO nanocomposite sensor", *Adv. Mater. Lett.*, 4(3) (2013) 196-201.
[27] O.A. Hamadi, N.J. Shakir and F.H. Mohammed, "Magnetic Field and Temperature Dependent Measurements of Hall Coefficient in Thermal Evaporated Tin-Doped Cadmium Oxide Thin Films", *Bulg. J. Phys.*, 37(4) (2010) 223-231.
[28] M.A. Hameed, S.H. Faisal and R.H. Turki, "Characterization of Multilayer Highly-Pure Metal Oxide Structures Prepared by DC Reactive Magnetron Sputtering Technique", *Iraqi J. Appl. Phys.*, 16(4) (2020) 25-30.

[29] A.M. Hameed and M.A. Hameed, "Highly-Pure Nanostructured Metal Oxide Multilayer Structure Prepared by DC Reactive Magnetron Sputtering Technique", *Iraqi J. Appl. Phys.*, 18(4) (2022) 9-14.

[30] A.M. Hameed and M.A. Hameed, "Spectroscopic characteristics of highly pure metal oxide nanostructures prepared by DC reactive magnetron sputtering technique", *Emer. Mater.*, 6 (2022) 627-633.

Table (1) Stress and strain values represented in the crystal lattice of ZnO thin films

Sample	a_o (Å)	a_o (Å) (Std.)	c_o (Å)	c_o (Å) (Std.)	σ Stress Residual	Strain
Pure ZnO	3.236290	3.2420	5.1908	5.1760	0.6655	0.04190
7 wt.% SnO_2	3.234789	3.2420	5.19306	5.1760	0.7671	0.04193

 ISSN (print) 1813-2065, (online) 2309-1673

IRAQI JOURNAL OF APPLIED PHYSICS
Vol. 19, No. 4C, December 2023, pp. 251-256

Characterization of Poly Methyl Methacrylate (PMMA) Nanofiber Enhanced by the Chlorophyll

Zainab J. Alhusseiny
Mohammed A. Akraa

Department of Physics, College of Education for Pure Sciences, University of Babylon, Al-Hilla, IRAQ

The objective of the study is to establish the permissible limit of the natural chlorophyll pigment added to PMMA nanofiber by presenting a statistical model. The nanofibers were produced using the electrospinning technique with pigment concentrations ranging from 0 to 1.56 wt.%. The results of viscosity, scanning electron microscopy (SEM), Fourier-transform infrared (FTIR) spectroscopy, and absorbance kinetics followed a Gaussian distribution with respect to the change in chlorophyll concentration. The unique distribution indicated that the nanofibers were homogeneous and contained chlorophyll concentrations up to 0.8 wt.%. Up to 1.6 wt.% beyond the last value of chlorophyll concentration values led to irregular electrospun fibers. The asymmetry accelerated the degradation with a percentage of 145%.

Keywords: Nanomaterials; Nanostructures; Nanotechnology; Biomolecules; Polymer blends
Received: 17 August 2023; **Revised:** 21 September 2023; **Accepted:** 28 September 2023

1. Introduction

The electrospinning technique uses electrostatic force to produce nanofibers from molten polymer or its solution. The resulting fibers are thin and have a large surface area. The process occurs at room temperature under normal atmospheric conditions. The terminal polymeric droplet undergoes deformation due to the electric field interactions when high voltage is applied to the needle's tip, which directs the polymer towards the drum. The electric field interactions directly cause this modification to occur. Several parameters affect the process, involving at first the physical properties of fluid such as elasticity and viscosity, solvent type, electrical conductivity, temperature, the tension of surface, vapor pressure, and appended salts. Secondly, process-related parameters are collector shape, spinneret geometry, the flow rate of the solution, separating distance between the needle's tip and the collecting drum, and influence voltage. Thirdly, the surrounding parameters of the temperature, ambient moisture, and speed of air [1-3]. Fong et al. found that the concentration of polymer affects the formation of beads in nanofibers. They discovered a converse relationship between polymer concentration and viscosity. POE polymer concentrations of 1-4.5 wt.% and viscosities of 1mPa.s to 1.25 Pa.s created fibers with varying degrees of bead deformation. The least viscous solution 13 mPa.s was produced at a concentration of 1 wt.% and resulted in fibers with the highest deformation of beads. Conversely, The most viscous solution (1.25 Pa.s, 4 wt.%) forms nanofibers with less beads [4]. As the viscosity of the polymeric solution increases, the gap between the beads in nanofibers increases while their diameter decreases. The viscosity has an effect on the beads' shape as well, with spherical beads gradually transforming into ones shaped like spindles as viscosity grows. Increasing viscosity or the concentration of solution affects the nanofibers' uniformity and diameter, making them larger and more consistent. The viscosity of the polymeric solution determines the concentration range for nanofibers produced by electrospinning. Lowering the viscosity of the solution leads to bead formation due to surface tension domination. Exceeding the critical limit of solution concentration produces a structure of nonstop fibers, whose morphology changes with the degree of dilution [3]. Among the many factors that determine the success of electrospinning, the polymer solution has to reach a minimum level of viscosity, which is a crucial condition, to ensure reasonable solubility. In this context, solvents play a significant role. However, the electrospinning technique requires careful selection of the solvent [5].

The limitations in solubility, average molecular weight decline, and high backbone rigidity are characteristic of conjugated polymers. These properties impede the formation of electrospinning fibers by preventing necessary entanglements. Conjugated polymers resist strength elongation and produce breaking and discontinuous jets [6]. Chlorophyll is a fascinating natural pigment that plays a crucial role in plants. It belongs to the group of conjugated polymers due to its unique porphyrin structure, which allows it to absorb electromagnetic waves and excite electrons. Chlorophyll primarily absorbs sunlight wavelengths in the red, blue, and purple ranges, which is essential for the plant's survival. Interestingly, chlorophyll is also being

studied as a potential material for use in solar cells and LED applications due to its optical properties [7].

The impact of adding chlorophyll pigment to electrospinning fibers of the PMMA matrix at different concentrations was examined in this paper. The names of the nanofiber specimens and their solutions reflected the weight ratio of chlorophyll to PMMA (pure PMMA, 0.31, 0.63, 0.94, 1.25, and 1.56 wt.%), The evaporating solvent acetone has a weight that is irrelevant. The study investigated the relationship between viscosity changes and shear flow of different solution concentrations of chlorophyll. The same specimens were analyzed using SEM and FT-IR techniques. The research also investigated how the degradation of electrospun fibers was influenced by chlorophyll concentration.

2 Method and Materials

Poly (methyl methacrylate) (PMMA) was the matrix material and chlorophyll was the pigment added to six specimens with different weight concentrations. They were made using electrospinning technique and acetone $(CH_3)_2CO$ was the solvent used. The percentage weight ratio of the chlorophyll in the solutions was (0, 0.05, 0.1, 0.15, 0.2, 0.25 wt.%). A pure PMMA dissolved in the acetone had a concentration of 16 wt.%, which was the reference specimen.

To extract chlorophyll, cleaned and dried basil leaves were put in a glass tube with a cap that had acetone in it. For two hours, the tube was left in a beaker of boiling water, making sure the water stayed hot before it cooled down. The solution in the tube was in a dark place for forty-eight hours at room temperature. They separated the leaves from the chlorophyll juice with a cotton cloth, and stored the juice in a fridge.

To determine the concentration of chlorophyll, they dried 1 mL of the juice, measured its weight before and after drying, and calculated the difference. It is found that the chlorophyll concentration was 1 g/L.

Poly (methyl methacrylate) (PMMA) with a molecular weight of 25000 type ALPHA Chemistry (Germany) was dissolved in acetone solvent at room temperature using a magnetic stirrer. The dissolution process lasted for three hours. Chlorophyll was added progressively to the solution after complete dissolution of PMMA. The weight ratio of chlorophyll to PMMA was adjusted according to the values stated in later.

Electrospinning of PMMA was performed at a weight concentration of 16 wt.%. The jet traveled 80 mm between the syringe tip and the drum. Electrospinning was carried out using 30 kV and different flow rates for other solutions with varying additive concentrations, as shown in table (1).

The samples were aged at different times (0, 22, 55, 266, and 434 hours) and concentrations (0, 0.31, 0.63, 0.94, 1.25, and 1.56 wt.%) using an oven of our design. The oven was cube-shaped and made of aluminum with sides measuring 70 cm. It was padded with synthetic wool to maintain the temperature. The heater consists of a machined 100-watt tungsten lamp and a UV lamp with specifications (Nofel Company, 15 W, Wavelength 240 Nano, C type, China). A thermostat kind RC-112E (Xuzhou Ringder Electrical Equipment Co. Ltd., China) was connected in series to the tungsten lamp to control its function such that the temperature of the oven was kept at 60°C. An o'clock and the tungsten lamp were connected to the same power supply to calculate the aging time without any missing at every potential sudden shutting down of power. The conversion of the alternation current to a direct current of about 1.5V for the o'clock was cared for (see Fig. 1).

Table (1) Electrospun of variant chlorophyll concentration versus different flow rates

Specimen Type (Additive wt.%)	Pure PMMA	0.05	0.1	0.15	0.2	0.25
Flow Rate (mL/h)	25	42	38	38	38	30

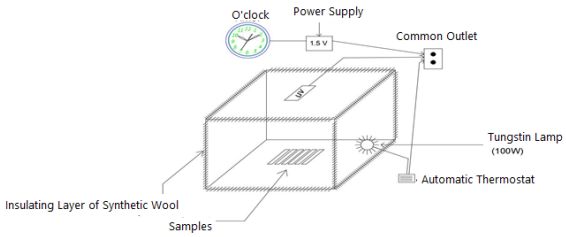

Fig. (1) The accelerated aging oven designed for the purpose of aging the electrospinning micro-nanofibers. The aging conditions are heating at 60°C, visible light of 100 W, and UVC of wavelength 240 nm

The viscosity of the solutions prepared for electrospinning injection was measured by an instrument (cone plate, Brookfield Co., Germany) and the results were analyzed and evaluated. The nanofibers produced were imaged by SEM, and analyzed by FT-IR (spectrometer, Bruker, Germany). The degradation rate of the specimens was studied as a function of chlorophyll concentration and the activation energy was calculated according to the amount of additive.

3 Results and Discussion

The rheological property of viscosity was a significant parameter to measure for six unlike samples of PMMA solution with different amounts of chlorophyll added. Two different groups were identified from the results. The first set included pure PMMA specimens, 0.31, 0.63, and 0.94 wt.%, which showed lower viscosity with higher shear flow, a phenomenon called pseudoplastic or shear thinning behavior (Fig. 2).

The rheological property in question was observed in stabilized suspensions and colloids [8]. It arises from the physical interaction between the entangled chains of polymer and the extra particles

 ISSN (print) 1813-2065, (online) 2309-1673

belonging to another phase. This interaction creates a model of two-layer, where the surface of additive particles carries a charge opposite to that of the surrounding polymer particles. By generating a long-range force, the solution becomes stabilized. The friction between the matrix polymer chains is lowered by the added particles, which enhance the shear rate. The previous figure of the primary group exhibited a style that can justify this description. However, approaching particles and layers to each other by raising the concentration of additives converts the attractive force to repulsive force. Hamaker's theory provides a good description of this interaction [9]. A repulsive force makes additives form a solid in an unstable suspension [10]. As a result, the suspension has a rising viscosity, which makes it appear shear thickening or dilatant. [8], as shown in Fig. (3). Chlorophyll accumulation in PMMA causes solute aggregation and hydro cluster convergence due to shear flow [11].

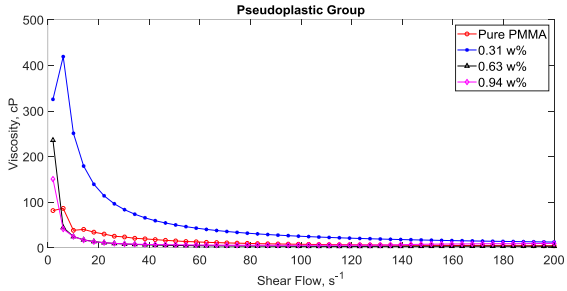

Fig. (2) Shear thinning conduct of solutions of the specimens (pure PMMA, 0.31, 0.63, and 0.94 wt.%)

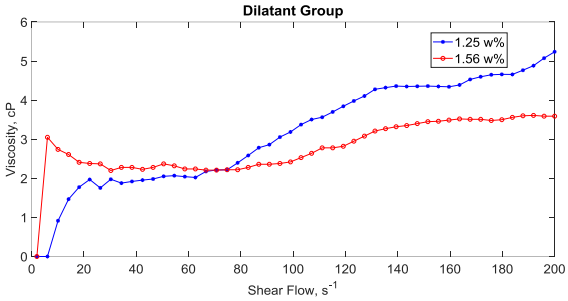

Fig. (3) Shear thickening behavior of solutions of specimens (1.25, and 1.56 wt.%)

As shown in Fig. (4), the low relative concentration of chlorophyll causes the shear thickening at its initial stage in this work. The highest obtainable viscosity that can be reached by adding chlorophyll up to ca. 0.4 wt.% is shown by the fitting curve, before a new phase of the solution begins at a chlorophyll concentration of ca. 1 wt.%.

Scanning electron microscopy (SEM), as shown in Fig. (5), scanned the electrospun fibers of different chlorophyll concentration values. The difference in the purity of the fibers is apparent. Pure PMMA and two chlorophyll specimens (0.31 and 0.63 wt.%) have no beads.

Although the last three specimens have similarities in their smearing, there are some differences that can be documented. The nanofibers at 0.94 wt.% appeared to look like perfusion wetting the nanofibers and developed an anomaly. Masses formed at nanofibers 1.25 wt.% became fewer and smaller at the nanofibers 1.56 wt.%.

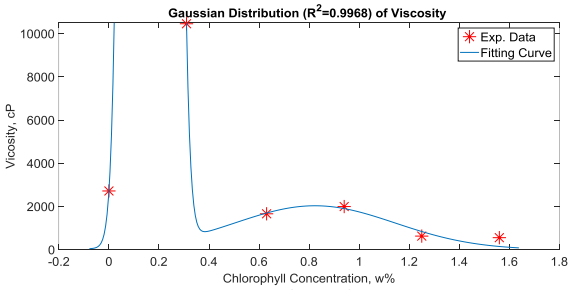

Fig. (4) Gaussian distribution of high fitting quality depicts the statistical alteration of the viscosity according to the increment of the chlorophyll weight rate percentage

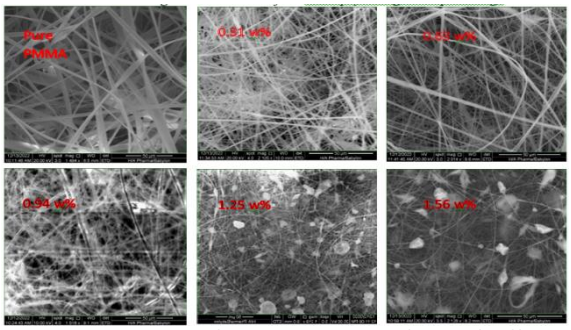

Fig. (5) SEM images of the produced nanofibers of different concentrations of chlorophyll

Chlorophyll in electro-spun nanofibers was confirmed by FT-IR. Chlorophyll traces detectable at low concentrations. The peaks of PMMA would shift if there was any physical bonding with the chlorophyll in the solution. However, as shown in Fig. (6), the PMMA molecules spectrum overshadowed the peaks of chlorophyll. The last figure displays some of the significant molecules of PMMA [12].

Similar peaks in all charts show physical interaction. Wavenumber shifts indicate PMMA-chlorophyll bonding change (Fig. 7). Curves in Fig. (7) show viscosity-dependent areas. First range: zero to 0.8 wt.% chlorophyll. Last bounds show chlorophyll amounts for pure nanofibers. PMMA molecules (-CH3, C=O, C-O) shifted to higher wavelength numbers, showing more bonding with chlorophyll [12]. The shift in wave numbers of the FTIR spectra of the electrospun nanofibers of PMMA blended with chlorophyll was due to the interaction between the PMMA chains and chlorophyll molecules. The shift in wave numbers is related to the change in the dipole moment of the PMMA chains. The best peak shifting occurred at a chlorophyll concentration of approximately 0.31 wt.%, which has the highest solution viscosity. The highest shift refers to the highest value of the force constant of physical bonds established among the PMMA and chlorophyll molecules [10]. The best molecular overlapping is

achieved in colloid or immobile suspension. Chlorophyll concentration increase caused divergent chlorophyll aggregation. Gravitational and Hamaker force isolated PMMA molecules [9]. Gradually, Viscosity decreased and new phase started in second plateau. Increasing chlorophyll concentration effectively decreased the viscosity of the blend solution, as shown in Fig. (4). The electrospinning produced extremely thin fibers that entangled in the shape of beads. The beads tended to be spherical, especially at a chlorophyll concentration of 1.25 wt.%. At a higher additive concentration of 1.56 wt.%, although the blend solution viscosity decreased and thinner fibers formed entangled fibers as beads were produced, the beads proceeded to split into thick fibers due to electric force originating from an aggregation of charges in each bead's middle. [13], Fig. (8).

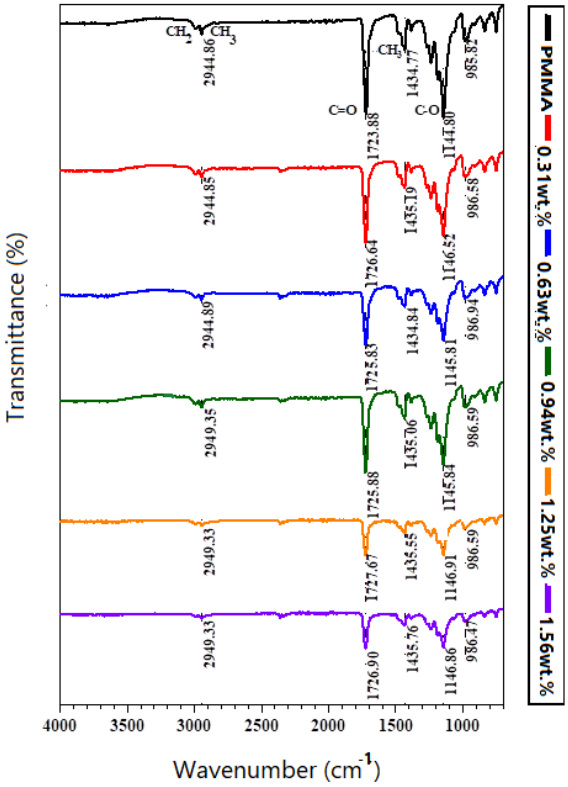

Fig. (6) FT-IR analysis of the six specimens. Shifting of peaks refers to formation of the physical bonds

The samples were subjected to accelerated degradation using a specialized oven designed for this purpose. The oven was equipped with a Tungsten lamp that emitted visible light, and UV-type C radiation, and maintained a temperature of 60°C. The samples were exposed to these conditions for different aging times of 22, 55, 151, 266, and 434 hours, in addition to the reference state of the samples with traces of aging-free. The effect of aging on the samples was evaluated by measuring the change in their absorbance, as shown in Fig. (9).

The absorbance of the samples was measured at two different positions after each aging time interval. The area under each curve of absorbance versus wavelength was calculated with error bars. The aging time affected the samples' absorbance qualitatively and quantitatively up to 55 hours, with a low amount of absorbance comparable to the following durations of 151, 266, and 434 hours. The increase in absorbance during the first 55 hours of aging time can be attributed to the appearance of new chemical groups such as the carbonyl group or any other potential type that supported the escalation of absorbance quantity. Notably, Fig.10 showed that the effect of chlorophyll concentrations up to ca. 0.8 wt.% was more stable than the occurred absorbance beyond that concentration.

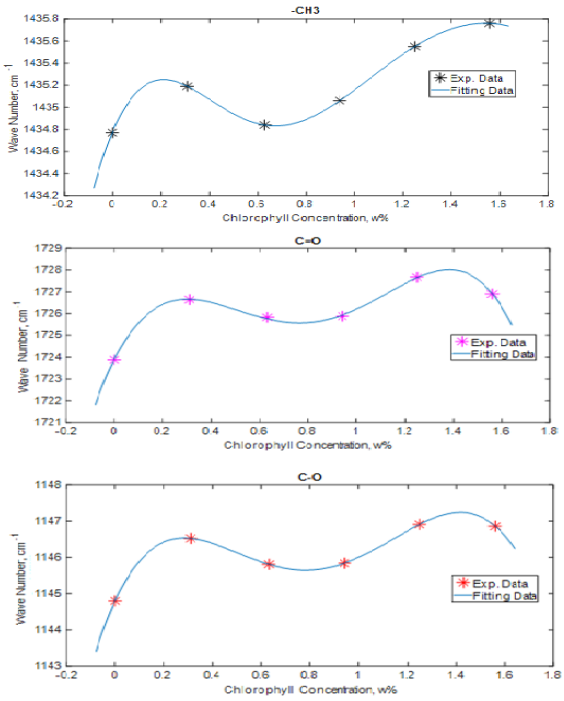

Fig. (7) The nature of Gaussian distribution nature of the shifting of molecular groups, -CH3, C=O, and C-O versus change the chlorophyll concentration

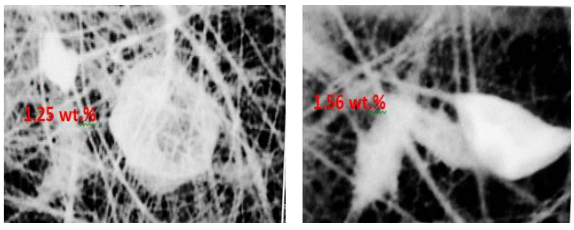

Fig. (8) The difference between beads of chlorophyll concentration 1.25 wt.% and 1.56 wt.%. The first state has a spherical shape and more density than the higher chlorophyll concentration of 1.56 wt.%. In the last case, beads converted to fibers. That is why they tended to the longitudinal shape

The rate constant, R1, is influenced by the concentration of chlorophyll up to 0.8 wt.%, which was less than that of samples containing chlorophyll beyond 0.8 wt.%, R2. The following exponential equation $A = ae^{-Kt}$ described the fitted curve that represented [14] the reaction rate. The coefficient *k*,

 ISSN (print) 1813-2065, (online) 2309-1673

which was the rate constant of the aging time *t*, can be determined. *A* represented the integrated area under the curve of absorbance versus the wavelength domain, and *a*, was the amplitude of the function. According to the values of the obtained rate constants, specimens with chlorophyll concentration greater than 0.8 wt.% have a reaction speed that was 159% higher than that of specimens with chlorophyll concentration lower than 0.8 wt.%. This increasing ratio indicated an increase in collision among the molecules of the reactants, resulting in an increased likelihood of productive collisions [14,15].

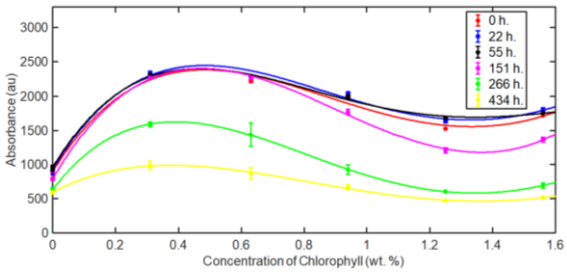

Fig. (9) The effect of chlorophyll concentrations on the samples' absorbance over different aging time durations

The activation energy of the reaction (E_a) was calculated for two cases based on the values of the rate constants. The Arrhenius Equation, given by the following form $E_a = -\ln(\frac{R}{Ro})R_gT$, can be used to determine E_a. Here, *R* is the rate constant of a sample, R_0 is the standard rate constant obtained from the value of the pure specimen of PMMA, R_g is the universal gas constant, and T is the absolute temperature [16]. The low values of chlorophyll concentrations led to an increase in activation energy by 114%, where E_{a1}=10.13 kJ/mol. The activation energy of higher chlorophyll concentrations and more rapid reaction, E_{a2}, was 8.86 kJ/mol. The decrease in activation energy value indicates weak degradation resistance of the material for high concentrations of chlorophyll (greater than 0.8 wt.%). Activation energy refers to the minimum amount of energy required to initiate a chemical reaction [16]. For a more detailed view of the effect of chlorophyll concentration, absorbance kinetics were plotted in Fig. (10). This figure shows the absorbance of each chlorophyll additive weight percent used in this study. The values were calculated using the same method as in Fig. (9) overall aging time intervals. The fitted line of absorbance kinetics for each additive concentration was obtained using two types of exponential curves: $y = ae^{-bx}$ for samples of (0.63, 0.94, 1.25 wt.%), and $y = ae^{-bx} + ce^{-dx}$ for samples of (Pure PMMA, 0.31, and 1.56 wt.%). This was based on the best goodness of the fitting curve. The R-squared values of the first group were 0.8444, 0.9115, and 0.9084 respectively, and of the second group were 0.8723, 0.92, and 0.9807, respectively.

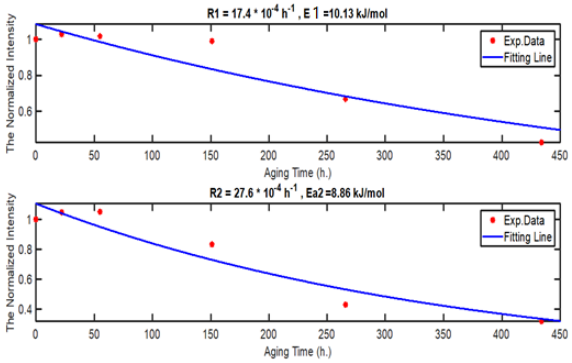

Fig. (10) The aging time of the samples affected the up and down curves of the normalized absorbance for chlorophyll concentrations up to 0.8 and above 1.6 wt.%, respectively . R and Ea represent the reaction rate constant and activation energy, respectively

The general behavior of the rate constants values of the samples as chlorophyll dependent was shown in Fig. (11). Hence, the concentration of the chlorophyll effect on the activation energy was emerged by Fig. (12).

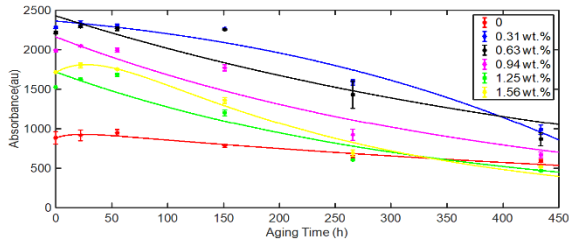

Fig. (10) The aging conditions under consideration affected the kinetics of absorbance for the six samples

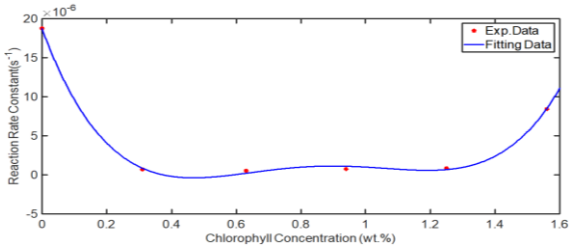

Fig. (11) The reaction rate constant changed depending on the concentrations of added chlorophyll

The final behavior of the samples' activation energy under the same employed accelerating aging conditions of 60°C and UV-C radiation depended on the chlorophyll concentration. This factor affects different other impacts such as the diameter and density of the fibers, the crystallinity of the polymer, the degree of polymerization, and the molecular weight of the polymer macromolecule. The decrease in electrospun fiber diameter creates a large surface area with respect to the bulk volume, which increases the exposure area and might decrease the activation energy. However, the high crystallinity of polymers results in high activation energy and degradation resistance [17]. Increasing the molecular weight of a polymer can increase its crystallinity. Linear polymer

chains and high molecular weight increase the crystallinity of a polymer [18].

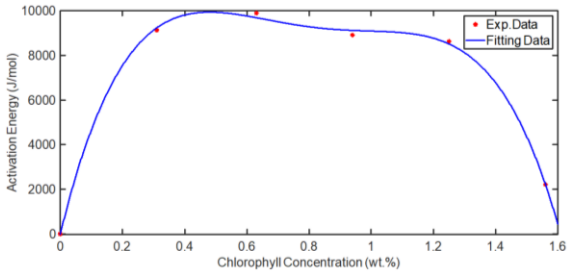

Fig. (12) The relationship between the concentration of chlorophyll and the change in activation energy suggests that chlorophyll plays a role in increasing the activation energy of the blend

4. Conclusion

The study shows that chlorophyll has specific bonds with the C-O, CH_3, and C=O groups of PMMA. The viscosity increases when the chlorophyll concentration is between 0 and 0.4 wt.%, reaching a maximum of around 0.8 wt.%. This optimal concentration results in nanofibers with minimal bead formation, indicating that higher viscosity of the polymer matrix enhances the electrospinning of chlorophyll additive. Moreover, nanofibers with a concentration of up to 0.8 wt.% chlorophyll show high thermal stability at 60°C and degradation resistance to UV-C and visible light.

Acknowledgements

Special words of thanks to Dr. Mazen Jaafar, Dr. Haider Abeis, Faculty of Pharmacy, University of Babylon; Dr. Ahmed Hashim, College of Education for Pure Science, University of Babylon; and Ms. Duha, College of Materials Engineering, University of Babylon.

References

[1] J. Jiménez Vázquez, and E.S.M. Martínez, "Collagen and elastin scaffold by electrospinning for skin tissue engineering applications", *J. Mater. Res.*, 34(16), (2019) 2819-2827.

[2] S. Pramanik, and V. Muthuvijayan, "Electrospun Nanofibrous Scaffolds for Neural Tissue Engineering" in: Electrospun Polymeric Nanofibers, R. Jayakumar, (eds), *Adv. Polym. Sci.*, 291 (2022) 229–286.

[3] F. Fadil et al., "Review on Electrospun Nanofiber-Applied Products", *Polym.*, 13(13) (2021) 2087.

[4] Y. Ding et al., "Recent Advances in Flexible and Wearable Pressure Sensors Based on Piezoresistive 3D Monolithic Conductive Sponges", *ACS Appl. Mater. Interfaces*, 11(7) (2019) 6685-6704.

[5] J. Weng et al., "Stable encapsulation of camellia oil in core–shell zein nanofibers fabricated by emulsion electrospinning", *Food Chem.*, 429 (2023) 136860.

[6] S. Majumder et al., "Understanding solubility, spinnability and electrospinning behaviour of cellulose acetate using different solvent systems", *Bull. Mater. Sci.*, 42(4) (2019) 171.

[7] R.D. Sandiningtyas, and V. Suendo, "Isolation of chlorophyll a from spinach and its modification using Fe^{2+} in photostability study", *Proc. 3th Int. Conf. Math. Nat. Sci.*, 2010 (2010) 859-873.

[8] T. Tadros, **"Encyclopedia of Colloid and Interface Science"**, Springer (Berlin/Heidelberg, 2013) 117-145.

[9] W.H. Boersma, J. Laven and H.N. Stein, "Shear thickening (dilatancy) in concentrated dispersions", *AIChE J.*, 36(3) (1990) 321-332.

[10] P. Atkins, and J. Paula, **"Physical Chemistry"**, 9th ed., W.H. Freeman Co. (NY, 2010) 556.

[11] M. Zarei and J. Aalaie, "Application of shear thickening fluids in material development", *J. Mater. Res. Technol.*, 9(5) (2020) 10411-10433.

[12] D.L. Pavia et al., **"Introduction to Spectroscopy"**, Cengage Learning (2014) 31-87.

[13] Y. Liu et al., "Progress in Electrospun Fibers for Manipulating Cell Behaviors", *Adv. Fiber Mater.*, 5 (2023) 1241–1272.

[14] T. Chu and K. Han, "Reaction Rate Constant Computations: Theories and Applications", *Roy. Soci. Chem.*, 6 (2013) 1-33.

[15] M.A. Akraa, A.S. Hasan and M.J.H. Kadhim, "Spectroscopy characterization of ethylene vinyl acetate degradation by different kinds of accelerated aging", *Baghdad Sci. J.*, 17(3) (2020) 0795-0795.

[16] M. Samperi, L. Perez-Garcia and D.B. Amabilino, "Quantification of energy of activation to supramolecular nanofibre formation reveals enthalpic and entropic effects and morphological consequence", *Chem. Sci.*, 10(44) (2019) 10256-10266.

[17] C.J. Shine, P.E. McHugh and W. Ronan, "Impact of Degradation and Material Crystallinity on the Mechanical Performance of a Bioresorbable Polymeric Stent", *J. Elast.*, 145(1-2) (2021) 243-264.

[18] D.E. Chung and I.C. Um, "Effect of molecular weight and concentration on crystallinity and post drawing of wet spun silk fibroin fiber", *Fibers Polym.*, 15 (2014) 153-160.

 ISSN (print) 1813-2065, (online) 2309-1673

IRAQI JOURNAL OF APPLIED PHYSICS
Vol. 19, No. 4C, December 2023, pp. 257-262

Zainab A. Kadem
Ahmed B. Sharba
Jassim M. Jassim

Department of Laser Physics,
College of Science for Women
University of Babylon,
Hilla-Najaf Road,
Babylon, IRAQ

Fast-attenuation Magnetic Fluid-based Filters with Stable and Variable Spectra

Optical filters are among the most important tools used in all fields of photonics and lasers. In this work, four types of magnetic liquids-based optical filters with different specifications have been designed and studied. The control of these filters is fully reversible. The first type depends on magnetic fluid containing Fe_3O_4 nanoparticles only. Two other kinds of filters were designed by adding non-magnetic solutes or nanoparticles to the magnetic fluid. These two filters are of controllable transmittance and changing spectral shape. The fourth type of tunable filter is designed with a perfectly flat and stable spectrum over a wide range of wavelengths by synthesizing Fe_3O_4 particles that are completely tied to copper nanoparticles. The results of this work can be invested in the field of designing pioneering filters for optical fields and communications applications.

Keywords: Attenuation; Optical filter; Magnetic nanoparticles; External magnetic field
Received: 03 September 2023; **Revised:** 21 September; **Accepted:** 28 September 2023

1. Introduction

Optical filters play an important role in various fields such as communications, imaging, spectroscopy, and sensing. They enable light manipulation for a wide range of applications. Optical filters are designed to selectively transmit or reflect specific wavelengths of light based on their properties [1, 2]. Recent advances have introduced a new class of optical filters that can be controlled by an external magnetic field using modern nanofabrication techniques [3]. This functionality has been achieved by fabricating specific magnetic nanoparticles, such as magnetite (Fe_3O_4), dispersed in nonmagnetic fluids [4]. These particles are characterized by high magnetic orientation stability in response to an external magnetic field, which allows precise control of their optical properties. In addition, when the magnetic field is removed, the liquid and particles of the magnetic fluids fully recover their initial properties. This innovative technology provides unprecedented versatility and tunability in optical filters and opens up exciting possibilities in optical device design and applications [5-7].

The magnetic field-controlled optical filters considered in this work belong to the category of optically tunable filters, which is a subclass of general optical filters [8]. In spectral and interference experiments involving different wavelengths of light, it may be necessary to replace the filters for many reasons, e.g., changing the source, the wavelength is constantly changing, or for spectral shaping. In order to avoid the filter replacement problems, adjustable magnetic fluid-based optical filter can be used [9]. Adjusting optical filters is an important progress in the field of light control. It opens a new way for various applications that require flexibility and precise modification in the properties of optical filters [10, 11].

The design and the performance of the magnetic fluid-based optical filters have been a topic for a large number of studies, e.g. [12-17]. Ferro-fluid optical filters were proposed for the applications of hybrid thermal photovoltaic cells (PV/T) using a new magnetic electrolyte nanofluid (ENF) [12]. There are filters designed using Monte Carlo optimization depending on mixing nanoparticles in liquids [13]. Thanks to this technology, optical filters with excellent performance have been achieved with performance very close to conventional filters with a deviation of less than 15% in the transmittance. The main motivation behind these liquid filters is the possibility of being pumped in and out of the system to meet transient needs in many applications [13].

In this work we discuss the design of different optical filters using the magnetic nanomaterial Fe_3O_4 alone and mixed with other material. The filters designed in this work depend mainly on causing spatial changes in the concentration of the dispersed particles. This requires relatively bulk samples that allow physical movement of the magnetic material within the sample in response to an external magnetic field.

2. Experimental part

In this work, several samples have been adopted to design optical filters with different preparation methods. All the prepared samples contained Fe_3O_4 nanoparticles. Fe_3O_4 nanoparticles were prepared chemically according to the procedure described in [18,19]. After the preparation process, we exposed the material to ultrasound waves to break up the agglomerated nanoparticles using a sonication probe with a power of 160 watts for 5 minutes.

To prepare this sample, methylene blue (MB) dye was dissolved in methanol containing suspended Fe_3O_4 particles. The ratio of the dissolved dye concentration to the suspended nanoparticle concentration was chosen depending on the required shape of the absorption spectrum of the mixture. The initial concentration of MB in this work is chosen to be 0.018 mM.

These samples were prepared by mixing silver nanoparticles with Fe_3O_4 particles. For this sample, both types of nanoparticles were prepared separately. The Fe_3O_4 particles were prepared by the chemical method mentioned above. The silver nanoparticles were prepared by using the pulsed laser ablation technique. In this process, a 1 cm diameter silver disc immersed in water and fired with multiple pulses of Nd:YAG laser at 1064 nm with 100 mJ pulse energy. After that, the resulting silver nanoparticles were mixed with Fe_3O_4 nanoparticles suspended in water. The mixing ratio depends on the shape of the desired absorption spectrum or the required transmittance of the optical filter at specific wavelength.

To prepare this sample, pulsed laser ablation was used in several stages. First, the synthesized Fe_3O_4 nanoparticles were dried using an oven at 100 °C. Then, the resulting powder was compressed into a circular disc by using a mechanical piston with a pressure of (10MPa). This disc was placed in methanol and exposed to 5 Hz Nd:YAG laser pulses at 100 mJ. The particles generated by using this way were, in terms of optical and magnetic properties, similar to the particles dispersed by using the sonication probe. Second, the Fe_3O_4 disk was removed from the liquid and replaced with a high purity copper disk. The laser ablation process was repeated to generate the copper nanoparticles in the same liquid containing the Fe_3O_4 nanoparticles. By using this method, the generated copper nanoparticles were completely bound to the Fe_3O_4 nanoparticles. The proof of this will be shown later. The ratio of generated Cu particles to Fe_3O_4 particles depends on the desired shape of the transmittance spectrum of the final sample. This ratio is controlled by controlling the number of laser pulses used to prepare each type of material.

Optical measurements were performed for assessing the performance of the prepared samples to work as optical filters. The linear transmittance variations was studied by measuring the transmitted power of a laser beam at 532 nm passing through a 1 cm thick cell containing Fe_3O_4 nanoparticles. This cell is surrounded by two coils for generating magnetic field on both sides of the cell as shown in Fig. (1). These two coils are supplied with current from two separate sources and each generates a magnetic field of 50 mT.

To study the change in the transmission spectrum of the samples under study, a Spectra Academy UV-VIS spectrometer provided by (K-MAC Co. ltd) was used with two magnets added to both sides of the sample cell as shown in Fig. (2). The Spectra Academy device consists of a broadband source (200-900 nm) and an imaging spectrometer. Therefore, the absorption or transmission spectra of the samples can be directly measured and viewed in live mode.

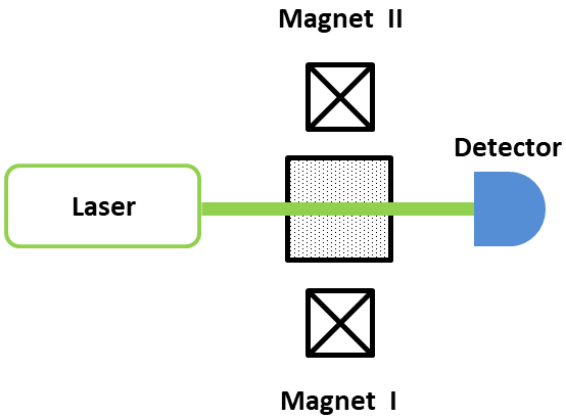

Fig. (1) Experimental setup for measuring the changes of the linear transmittance

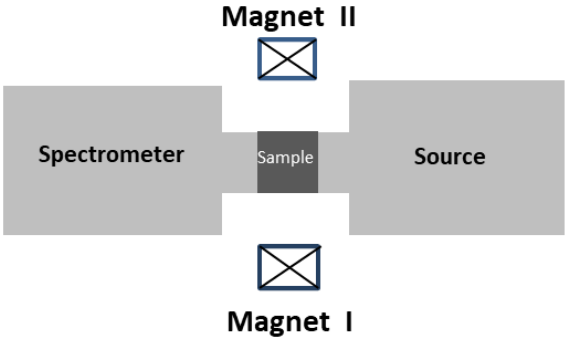

Fig. (2) Experimental setup for measuring the variations of the transmission spectra of the designed filters under the action of external magnetic field

3. Results and Discussion

The TEM examination, shown in Fig. (3), indicates that the Fe_3O_4 nanoparticles have irregular shapes with sizes ranging from 5 to 50 nm. These particles connected to each other forming tangled chains due to their magnetic properties. These chains have random orientations in the absence of an external magnetic field.

The Fe_3O_4 particles have a high-purity crystalline structure (JCPDS card no. 26-1136), as can be deduced from the XRD examination shown in Fig. (4).

The linear optical transmittance of any magnetic fluid depends on the wavelength of the transmitted radiation and the concentration of the nanomaterial. Therefore, the transmittance can be changed by controlling the concentration of suspended nanoparticles. This can be done in ferromagnetic fluids by using an external magnetic field [20]. The amount and speed of change in the transmittance is determined by the viscosity of the liquid, the initial concentration of the nanoparticles, and the strength

 ISSN (print) 1813-2065, (online) 2309-1673

of the magnetic field used. On the other hand, the direction of the change of transmittance (increase or decrease) depends directly on the direction of change in the concentration of the nanomaterial (increase or decrease) in the beam path. Figure (5) presents two trajectories of transmittance change in two different regions within the same sample cell, one at the center of the cell and the other at the edge of the cell.

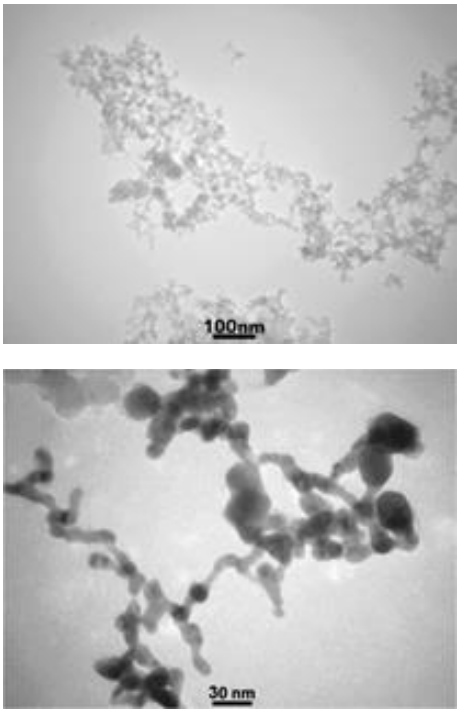

Fig. (3) TEM images of Fe_3O_4 nanoparticles

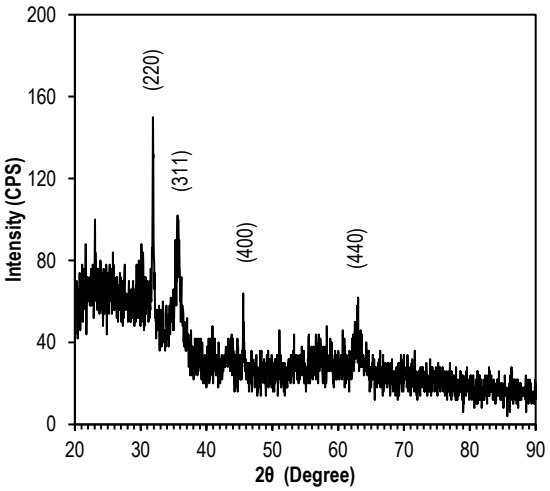

Fig. (4) XRD pattern of Fe_3O_4 nanoparticles

In the center of the cell, Fe_3O_4 particles are attracted towards the magnetic poles at both ends of the cell. This always leads to reduce the concentration of the particles. Therefore, the transmittance of the sample through this region always increases. At the edge of the cell, the particles gather due to the magnetic pole at that end. This leads to reduce the linear transmittance through the edge of the sample.

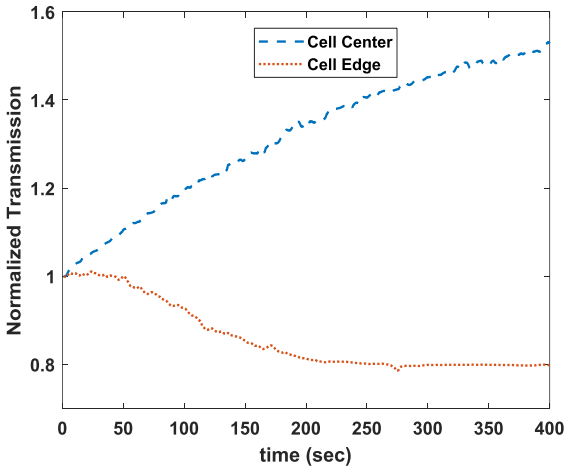

Fig. (5) The linear transmittance change of a sample of Fe_3O_4 nanoparticles suspended in methanol when a magnetic field of 50 mT is applied

It should be noted that, since the magnetic nanoparticles can be moved away from or towards any region within the sample, the change in transmittance is adjustable in two directions (increase and decrease). Figure (6) shows different trajectories of the optical transmittance changes induced by two magnetic fields placed on the opposite sides of the sample, as shown in the experimental setup (Fig. 1). In this setup, the laser beam passes at the edge of the cell close to the magnet I and the two magnets were operated in three arrangements.

Arrangement A: Both magnets I and II work together
Arrangement B: Magnet II operates for 100 seconds, followed by magnet I working for the rest of the time
Arrangement C: Magnet II operates for 100 seconds, followed by magnet I working for the next 150 seconds, then magnet II operates for the rest of the time.

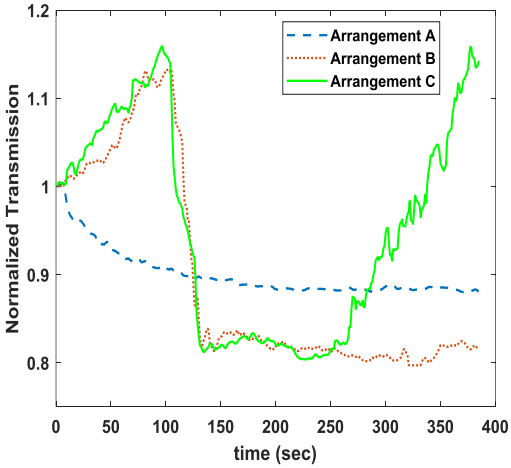

Fig. (6) The linear transmittance change of a sample of Fe_3O_4 nanoparticles suspended in methanol when a 50 mT magnetic field is applied alternately on both ends of the cell

In this work, we used two identical solenoids and they wired such that neighboring magnetic poles are different (north and south). In addition, since the sample cell is placed halfway between the two solenoids, the magnetic field distribution through the cell can be considered uniform. We notice from the figure that when both magnets work together, the transmittance decreases due to the gathering of nanoparticles at the edge of the sample. As for the arrangement (B), when magnet II works far from the laser beam, the particles move away from the laser beam leading to increase the transmittance. However, when magnet II is turned off and magnet I, which is near the beam path, is turned on, the nanoparticles concentration in the beam path increases. This leads to a sharp and rapid decrease in optical transmittance. For this arrangement, the stability of the transmittance at a certain value suggests that all particles in the liquid are collected in the path of the laser beam. Finally, arrangement (C), since the magnets were operated alternately, alternating changes in the optical transmittance have happened.

This experiment, as shown in Figure (6), demonstrates the possibility of using magnetic nanomaterial to design attenuation optical filters that can be quickly and accurately controlled in both directions. The steep slope of the curves shown in the figure proves the possibility of rapidly changing the transmittance of the filter. It is also possible to adjust the speed of change by adjusting the viscosity of the liquid and the intensity of the magnetic field used. The extent of the transmittance change, hence the extent of filter control, depends mainly on the initial concentration of nanoparticles. It can include a very large controlling the range.

The tuning property can be employed in the applications of optical filters as it has been studied in many previous works, e.g. [12-17]. A sample of nanomaterial can be a continuously changing or passive optical filter working at a certain wavelength. In addition, it is also possible to design an optical filter with transmittance spectrum that can be easily formed according to the required application. This can be achieved by using mixtures of magnetic nanomaterial with other materials, which can be magnetic, non-magnetic, organic, or other materials. The shape of the transmittance spectrum can be formed by controlling the concentrations ratio of magnetic nanomaterial and the other additives. In this work, four types of controllable optical filters were designed by using Fe_3O_4 nanomaterial alone and mixed with different materials.

Figure (7) shows the change in the spectrum of the transmittance of Fe_3O_4 when a magnetic field is applied to one end of the sample shown in Figure (2). In this experiment, a weak magnetic field (5 mT) was used. Therefore, the change in the spectrum was relatively slow.

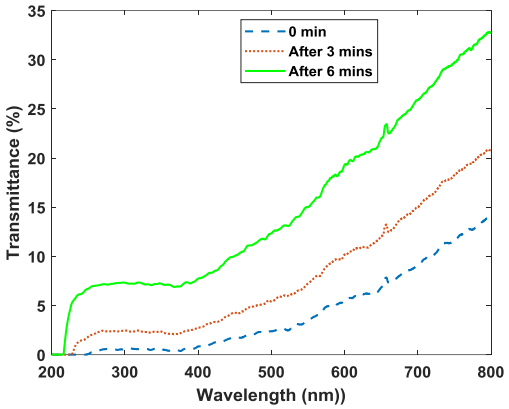

Fig. (7) The change of the linear transmittance spectrum of a sample of Fe_3O_4 nanoparticles suspended in methanol when a magnetic field is applied

We notice from the figure that the whole transmittance changes due to the local concentration changes induced by the magnetic field. However, the shape of the spectrum is fixed and determined by the optical properties of the magnetic material. This sample can be considered as an attenuation filter that can be controlled in a very wide range at all wavelengths covered by this spectrum.

Another example of fabricating an optical filter with adjustable spectrum is achieved by adding Methylene Blue dye (MB) to the liquid containing the Fe_3O_4 nanomaterial. The transmission spectrum of this mixture is shown in Figure (8). MB was also adopted in [11] to design an optical filter with slightly different mixture.

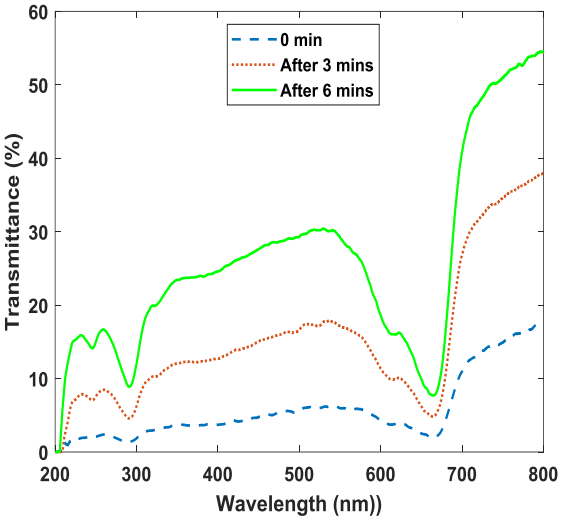

Fig. (8) The magnetic field-induced changes of the linear transmittance spectrum of a sample of Fe_3O_4 nanoparticles suspended in methanol containing MB dye

It can be seen that before applying the external magnetic field, the transmittance spectrum is composed of the sum of the transmittance spectrum of Fe_3O_4 particles and the transmittance spectrum of MB dye. After applying the magnetic field, the local concentration of Fe_3O_4 particles decreases leading to

 ISSN (print) 1813-2065, (online) 2309-1673

increase the transmittance and change the shape of the spectrum simultaneously. This type of filter, using a variety of materials, is of a very high importance in applications that require a directly and accurate shaping of the spectrum of transmitted radiation such as the spectral applications and laser pulses shaping.

Another type of filter can be manufactured by mixing non-magnetic nanomaterial with Fe_3O_4 particles. The transmittance change shown in Fig. (9) is an example of this type of filters. This filter was produced by adding silver nanoparticles to the magnetic fluid. The shape of the initial spectrum can be controlled by controlling the ratio of the mixed concentrations.

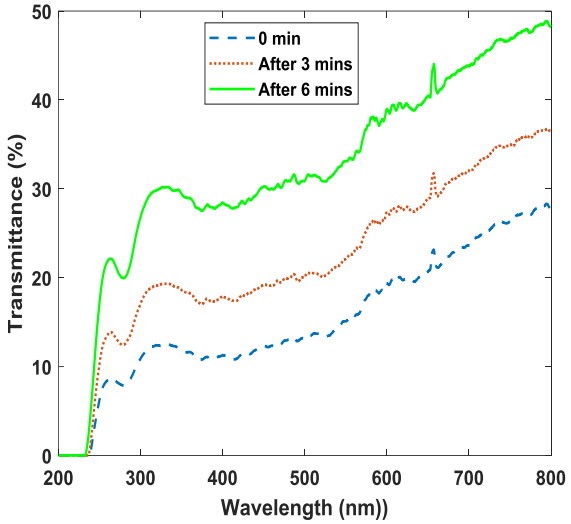

Fig. (9) The magnetic field-induced changes of the linear transmittance spectrum of a mixture of Fe_3O_4 nanoparticles and silver particles suspended in water

In this kind of mixtures, there are three different types of particles in the liquid; silver nanoparticles, Fe_3O_4 nanoparticles, and silver nanoparticles physically bound to the Fe_3O_4 nanoparticles. The last type of particles can be formed in the liquid by the agglomeration of the nanoparticles. When a magnetic field is applied, the last two types of particles are attracted to the field causing a change in the shape and the value of the optical transmittance. However, it can be seen from Figure (9) that the change in the shape of the transmission spectrum is hardly noticed. This indicates that a large percentage of the silver particles are interconnected with the iron oxide particles, which causes them to move with the iron oxide particles due to the external magnetic field. This kind of bounding between the particles is not fully reliable because the particles can be agglomerated or broken up by sonication and other external and internal effects.

The last kind of filters designed in this work is a filter with a stable and equal spectrum for all wavelengths within a very wide range, starting from the ultraviolet region and extending beyond the near infrared region. This filter was designed for the first time by synthesizing hybrid nanoparticles using pulsed laser ablation method. The iron oxide particles covered with copper particles with a ratio that insures producing a flat transmittance spectrum, as shown in Figure (10). This figure presents the difference between the transmittance spectrum of bare iron oxide particles and those covered with copper particles.

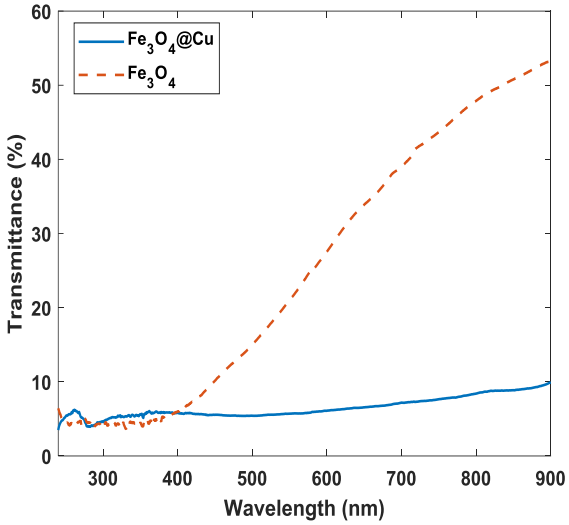

Figure 10: Transmittance spectrum of Fe_3O_4 and Fe_3O_4@copper nanoparticles.

The bonding between the magnetic and nonmagnetic particles ensures that they move together with the action of the magnetic field. This can be seen in Figure (11), which shows the magnetic field-induced changes in the transmittance with a perfectly stable spectrum shape over a wide spectral range.

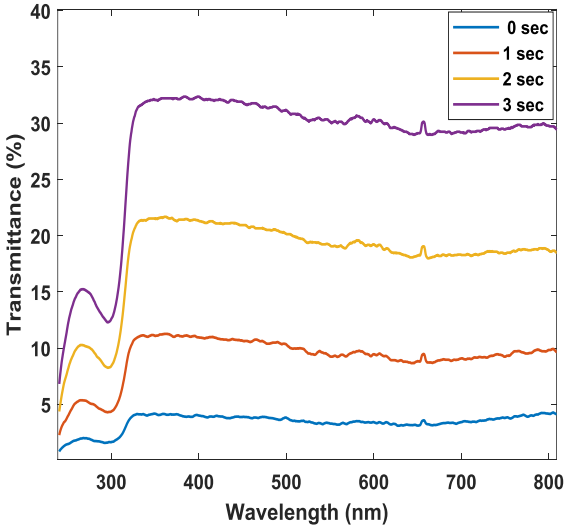

Fig. (11) The magnetic field-induced changes of the linear transmittance spectrum of Fe_3O_4 nanoparticles covered with copper particles suspended in methanol

The result shown in Fig. (11) indicates many important observations. The most important of which is that; first, the transmittance value of this filter can

be changed from 5% to 32% in only three seconds. Although this time scale is very long for photonics applications, it is, for example, much shorter than any time needed for replacing a passive filter in any optical system. Second: the extent of the change can be increased to reach 100% over a slightly longer time. Third: the speed of change can be increased to a very high value by using an external magnetic field with a higher intensity. Fourth: the ideal stability of the transmittance spectrum proves that all the copper and Fe_3O_4 particles are tied to each other. Fifth: this model can be of a very high value as it represents a very accurate and fast attenuation filter that can be used in the field of broadband and neutral filters.

It is worth mentioning that all the magnetic-induced optical changes observed in this work are due to the spatial changes in the concentration of the nanoparticles. In other words, we could not detect any direct influence of the magnetic field on the optical or the spectral properties of the samples.

4. Conclusion

The designed filters in this work have transmittance with value and spectral shape that can be controlled freely in two opposite directions (increase or decrease) by using magnetic fields distributed around the filter. The transmission spectrum of filters made of unconnected hybrid nanoparticles can change via agglomeration and dispersion. However, an optimally controllable and highly reliable filter is designed based on magnetic material tightly connected to copper nanoparticles. This filter is an example of controllable filters with fixed spectra defined by the optical properties of the material used. The filters designed in this work can have a very high value in the field of photonics and communications.

References

[1] L. Martinu and D. Poitras, "Plasma deposition of optical films and coatings: A review", *J. Vac. Sci. Technol. A*, 18(6) (2000) 2619-2645.
[2] A.G. Imenes and D.R. Mills, "Spectral beam splitting technology for increased conversion efficiency in solar concentrating systems: a review", *Sol. Ener. Mater. Sol. Cells*, 84(1-4) (2004) 19-69.
[3] R.A. Taylor, T. Otanicar and G. Rosengarten, "Nanofluid-based optical filter optimization for PV/T systems", *Light: Sci. Appl.*, 1(10) (2012) e34-e34.
[4] R.E. Rosensweig, "Magnetic fluids", *Annual Rev. Fluid Mech.*, 19(1) (1987) 437-461.
[5] J. Henzie et al., "Nanofabrication of plasmonic structures", *Annual Rev. Phys. Chem.*, 60 (2009) 147-165.
[6] R. Taylor et al., "Small particles, big impacts: A review of the diverse applications of nanofluids", *J. Appl. Phys.*, 113(1) (2013) 1.
[7] J.M. Jassim, Y.H. Khadim and M.M.M. Al-Sultani, "Study of linear and non-linear optical properties for the thin films of laser dye- Fe_3O_4 nanoparticles doped PMMA thin films", *J. Eng. Appl. Sci*, 13(22) (2018) 9511-9518.
[8] I. Libon et al., "An optically controllable terahertz filter", *Appl. Phys. Lett.*, 76(20) (2000) 2821-2823.
[9] J. Philip et al., "A tunable optical filter", *Measur. Sci. Technol.*, 14(8) (2003) 1289.
[10] J. De Vicente, D.J. Klingenberg and R. Hidalgo-Alvarez, "Magnetorheological fluids: a review", *Soft Matter*, 7(8) (2011) 3701-3710.
[11] B.M. Berkovsky, V.F. Medvedev and M.S. Krakov, **"Magnetic Fluids: Engineering Applications"**, Oxford University Press (1993).
[12] J. Jin and D. Jing, "A novel liquid optical filter based on magnetic electrolyte nanofluids for hybrid photovoltaic/thermal solar collector application", *Solar Energy*, 155 (2017) 51-61.
[13] R.A. Taylor et al., "Feasibility of nanofluid-based optical filters", *Appl. Opt.*, 52(7) (2013) 1413-1422.
[14] J. Zeng and Y. Xuan, "Tunable full-spectrum photo-thermal conversion features of magnetic-plasmonic Fe_3O_4/TiN nanofluid", *Nano Energy*, 51 (2018) 754-763.
[15] Z.S. Kochnev, Y.V. Kistenev and A.V. Borisov, "Magnetically Tunable Bandpass Filter of Teraherz Radiation", *Russian Phys. J.*, 65(10) (2023) 1667-1675.
[16] E.S. Savelyev et al., "Development of an automated prototype of THz filter based on magnetic fluids", *in XV Int. Conf. on Pulsed Lasers and Laser Applications, SPIE*, 12086 (2021) 495-499.
[17] Z.S. Kochnev, Y.V. Kistenev and A.V. Borisov, "Model of Terahertz Bandpass Filter Based on Ferrofluids", *Russian Phys. J.*, 65(12) (2023) 2045-2051.
[18] T. Ahn et al., "Formation pathways of magnetite nanoparticles by coprecipitation method", *The J. Phys. Chem. C*, 116(10) (2012) 6069-6076.
[19] M.S. Al-Samak and J.M. Jassim, "Dye-Doped Fe_3O_4 Nanoparticles for Magnetically Controlling Random Laser Parameters at Visible Wavelengths: Literature Review and Experiment", *Indonesian J. Sci. Technol.*, 7(3) (2022) 497-510.
[20] S. Malynych and I. Moroz, "Time dependent magnetically induced variations in optical transmission of magnetite nanoparticle aqueous suspension", *Open Phys.*, 10(1) (2012) 159-165.

 ISSN (print) 1813-2065, (online) 2309-1673

IRAQI JOURNAL OF APPLIED PHYSICS
EDITORIAL BOARD

COPYRIGHT RELEASE FORM
IRAQI JOURNAL OF APPLIED PHYSICS (IJAP)

We, the undersigned, the author/authors of the article titled

……
……
……
……
……

that is submitted to the Iraqi Journal of Applied Physics (IJAP) for publication, declare that we have neither taken part or full text from any published work by others, nor presented or published it elsewhere in any other journal. We also declare transferring copyrights and conduct of this article to the Iraqi Journal of Applied Physics (IJAP) after accepting it for publication.
The authors will keep the following rights:

1. Possession of the article such as patent rights.
2. Free of charge use of the article or part of it in any future work by the authors such as books and lecture notes after informing IJAP editorial board.
3. Republishing the article for any personal purposes of the authors after taking journal permission.

To be signed by all authors:

Signature:……..date: ……
Printed name: ……

Signature:……..date: ……
Printed name: ……

Signature:……..date: ……
Printed name: ……

Signature:……..date: ……
Printed name: ……

Correspondence author:……..……..
……
Address:……..……
……
Telephone:……..……..email: ……

Note: Complete and sign this form and mail it to the below address with your finally revised manuscript

The Iraqi Journal of Applied Physics
P. O. Box 88052, Baghdad 12631, IRAQ
www.iraqiphysicsjournal.com
Email: info@iraqiphysicsjournal.com
Email: editor_ijap@yahoo.co.uk
Email: ijap.editor@gmail.com

IRAQI JOURNAL OF APPLIED PHYSICS

Volume (19) Issue (4C) December 2023

CONTENTS